Cellulose nanocrystals as versatile support for catalysis

A thesis submitted to McGill University
In partial fulfilment of the requirements of the degree of Doctor of Philosophy
By
Madhu Kaushik
October 2015

Centre for Green Chemistry and Catalysis, Department of Chemistry
McGill University, Montreal, Quebec, Canada

The low lands call, I am tempted to answer.
They are offering me a free dwelling, without having to conquer.

The massive mountain makes its move, beckoning me to ascend.
A much more difficult path, to get up the slippery bend.

I cannot choose both, I have a choice to make.
I must be wise, this will determine my fate

I choose, I choose the mountain, with all its stress and strain.
Because only by climbing, can I rise above the plane!

I choose the mountain, and I will never stop climbing
I choose the mountain, and I shall forever be ascending

I choose the mountain!

\- *Howard Simon*

Abstract

The ever-growing world population has changed the dynamics between the demand and supply of food, materials and energy, which, in turn, has challenged us to introduce sustainable alternatives across the diverse spectrum of human needs. Therefore, as a synthetic chemist, I was particularly interested in proposing sustainable catalysis, thereof. Cellulose nanocrystals (CNCs), termed as 'the sustainable material of 21st century' by the Technical Association of Pulp and Paper Industries, proved to be an interesting template for deposition of metal nanoparticles. The dissertation begins with introducing the family of crystalline cellulose in the nano-domain, hereby referred to as nanocelluloses, which includes cellulose nanocrystals, cellulose nanofibers and bacterial cellulose nanofibers. In the first chapter the applications of nanocelluloses in catalysis is reviewed, with emphasis on their role as support for metal nanoparticles. Next, the importance for characterisation of the CNCs and their metal-hybrid composites is highlighted. This work presents a robust and reproducible method to image CNCs by transmission electron microscopy (TEM), without the need for staining. In the following chapter, we establish the role of CNCs in the enantioselective hydrogenation of prochiral ketones, using Pd metal. By a careful choice of substrate, we could achieve enantiomeric excesses (ees) of up to 65%, which is unprecedented for a system where the chirality is solely carried by the unmodified biomass support. By using high-end microscopy techniques, namely cryo-TEM and tomography in conjunction with a direct detection device (DDD) camera, we demonstrated that palladium was present in the catalyst as sub nanometric patches, in direct contact with their low-density support. In addition, we constructed the 3D tomograms of CNCs and the CNC-metal hybrid composite. Conceptually, these results offer an opportunity to use cellulose, in the form of the highly crystalline CNC, directly in asymmetric catalysis. The subsequent chapter presents a highly atom-economical synthetic method to access nanocatalysts from bulk metal. A water suspension of cellulose nanocrystals was exposed to an Ag wire, under air and light exposure. In 2 weeks, Ag nanoparticles of size 1.3 ± 0.3 nm were deposited onto the biopolymer. These species were active for the hydrogenation of aldehydes, 4-nitrophenol, alkenes and alkynes. Specifically this work is the first example of the reduction of nitroarene using H_2 as an atom economical reducer, using Ag as a catalyst. The ensuing chapter describes the synthesis of Ru nanoparticles from $RuCl_3$ under mild H_2 pressure within a suspension of cellulose nanocrystals. X-ray photoelectron spectroscopy and TEM revealed that the small Ru (0) nanoparticles (3.3 ± 1 nm) were deposited onto their cellulosic support. This hybrid proved to be a highly efficient arene hydrogenation catalyst operational at 4 bars and room temperature, conditions rivaling in mildness with the best published works. Finally, a perspective is presented on the directions which could be taken in the future to widen the applications of CNCs in catalysis.

Resumé

La croissance constante de la population affecte la dynamique entre l‘offre et la demande des ressources en nourriture, matières premières et énergie, ce qui à son tour nous enjoint à mettre en œuvre des altératives durables pour l’étendue des besoins humains. En conséquence, en tant que chimiste de synthèse, j’étais particulièrement intéressée par l’idée de proposer de nouveaux modèles catalytiques durables. Les nanocristaux de cellulose (NCCs), désignés comme le « matériau durable du 21ème siècle » par l’association technique des industries des pâtes et papiers, se sont avérés être d’excellents supports de catalyseurs. Ce manuscrit commence par l’introduction de la famille de la cellulose cristalline dans le domaine nanométrique, appelée de façon générique nanocellulose, et qui comprend les nanocristaux de cellulose, les nanofibres de cellulose et les nanofibres de cellulose bacterienne. Dans le premier chapitre, les applications des nanocelluloses en catalyse sont passées en revue, avec un accent sur leur rôle comme support de nanoparticules de métaux. Ensuite l’importance de la caractérisation des NCCs et de leur composites hybrides avec des métaux est mis en évidence. Ce travail présente une méthode reproductible pour visualiser les NCCs par microscopie électronique à transmission (MET) sans avoir recours à la teinture. Dans le chapitre suivant, nous établissons le rôle des NCCs dans l’hydrogénation de cétones chirales, catalysée par le palladium. En choisissant avec attention le substrat, on peut obtenir un excès énantiomérique de plus de 65%, ce qui est une première pour des systèmes où la chiralité est présente uniquement au niveau du support issu de la biomasse et non-modifié. En utilisant des techniques de microscopie avancées, telles que le MET-cryo et la tomographie en conjonction avec une caméra « direct detection device (DDD) », nous avons démontré que le palladium était présent sur le catalyseur sous forme de patches de taille sous nanométrique, eux-mêmes en contact direct avec leur support de basse densité. De plus, nous avons reconstruit des tomogrammes en 3 dimensions des NCCs et des composites hybrides NCCs-métal. Conceptuellement, ces résultats montrent l’opportunité d’utiliser la cellulose, sous sa forme NCC hautement cristalline, directement en catalyse asymétrique. Le chapitre suivant présente une méthode synthétique hautement atome-économique pour accéder à des nanocatalyseurs à partir de métal macroscopique. Une suspension aqueuse de cellulose a été exposée à un fil d’argent, à l’air et à la lumière du soleil. En deux semaines des nanoparticles d’argent de taille 1.3 ± 0.3 nm se sont déposés sur le biopolymère. Ces espèces sont actives pour l’hydrogénation des aldéhydes, du 4-nitrophénol, des alcènes et des alcynes. En particulier, ce travail est le premier exemple de réduction des nitroarènes avec l’H2 comme réducteur atome économique, avec l’argent comme catalyseur. Ensuite vient un chapitre qui décrit la synthèse de nanoparticules de ruthénium à partir de RuCl3, réduit sous basse pression de H2 dans une suspension de NCCs. La spectroscopie photo-électronique aux rayons X et le MET ont révélé que de petites nanoparticules de Ru(0) (3.3 ± 1 nm) se sont déposées sur le support cellulosique. Cet hybride s’est révélé très efficace pour l’hydrogénation des arènes à 4 bars et à température ambiante, des conditions qui rivalisent avec les plus douces publiées. Enfin, une perspective est présentée sur les directions qui pourraient être prises dans le futur pour ouvrir de nouvelles applications aux NCCs en catalyse.

Dedicated to Kapil, my husband, who taught me to fly …

Acknowledgements

I would always associate McGill University and Montreal with inspiring mentors, excellent peers, loving friends and incredible learning opportunities.

Foremost, I thank Dr. Audrey Moores for shepherding my PhD to completion, for advice, suggestions, patience, motivation and unconditional support. My initial ecstatic state of getting an admission into McGill University only lasted until a few weeks, after which the cultural differences, harsh winters and the ‘missing family’ mode set in. I became unsure of my decision of coming to Montreal. I was scared, clueless, missing my family, coping with my first winters and wondering if I could fit into the new culture. It was then, when Dr. Moores reassured me of my own strengths through my struggle. Under her mentorship, I became an independent scientist with critical thinking and improved communication skills. Because of her guidance and finesse, I have achieved the confidence of taking up new challenges, both in professional and personal life.

I thank all the agencies that have provided funding for my project and financial support to the Moores group: McGill University, the Canada Foundation for Innovation (CFI), the Fonds de Recherche sur le Nature et les Technologies (FQRNT), the Canada Research Chairs (CRC), the Green Chemistry-NSERC Collaborative Research and Training Experience (CREATE) Program, and Natural Sciences and Engineering Council of Canada (NSERC). In addition, I thank FP Innovations for providing me cellulose nanocrystals for my research. A very big thank you to Dr. Nicolas Moitessier, Chantal, my review committee and the administrative staff for the support they gave throughout the program. I thank my collaborators: Dr. Li, Dr. van de Ven, Dr. Vali, Kaustuv, and Wei. I am indebted to all those in the McGill University who helped my research by loaning chemicals, explaining laboratory techniques, training on instruments, discussing ideas, giving me feedback, or just giving me hope to survive through the graduate school.

I am grateful to the Moores group members, both past and present, who took amazing care of me both professionally and personally. Special thanks to Ciprian for holding my hands when I took my first steps into the graduate school. He introduced me to my project, lab, instruments and people around me. I thank the ‘extraordinary’ Monika, who made all the difference to my sanity both on and off the road. She inspired me to work harder, think critically and set high standards for excellence. I owe my success to her honest, crisp and downright humbling feedbacks. I thank the ‘kind-hearted’ Mary, who is forever ready to listen to all my stories and accompany me to Bollywood movies. I am thrilled to have a friend and accomplice like Alain, who is so insightful, talented, and patient with my whining (both of research and French). I also owe many happy memories: nail and henna nights, Bollywood dance parties, pranks, etc. to Monika, Alain, Mary, and Janane. You guys make Montreal a wonderful place. I thank Luis and Michael for their invaluable inputs and encouraging words. I thank Reuben, to believe in my chemistry as well as my cooking skills. I thank Mitra and Huizhi, for their perspectives into material chemistry.

My undergraduate students, Kade, Charles, Hava and Luca, amazed me by their hard work on the projects we worked together. I thank my marvellous friends from the neighbouring lab: Janane, Aurélie and Donatien. I thank Janane who made me laugh with his distinct sense of humour and danced with me to Bollywood tunes. I shall be forever indebted to Anjali and Rishi for being my guardian angels, who inspired me to apply for graduate studies and helped me in the application process, planning my travel and settling in Montreal. I thank Aaron and Mandy, who were my first friends in Montreal. I am in debt to all my wonderful friends, who were not chemists and hence, totally clueless, when I ranted about my lab adventures, failed reactions and frustrations in general: Ekta, Vaibhav, Surbhi, Sushma Aunty, Rahul, Gagan, Bikram, Poonam, and Rashi. You all make my life brighter and happier.

I am grateful to Kapil, my husband, best friend and philosopher, who knocked me off my feet the day I met him. I thank him for teaching me to dream like a queen and then work smart with a smile to achieve them. He has the ability (or the lunacy!) to smile while dealing with my craziness, awkward silences, mysterious moods and impossible dreams. I cannot fully convey how much I appreciate your standing by me through the challenging times. I also thank him for making me a part of his wonderful family: Pappaji, Pitaji, Ammi, Ravinder, Binni, Surinder, Suanne, Shanky and Sunny. I am truly blessed and fortunate to have you all.

My special gratitude to my Daddy and Mumma, who taught me the life skills and gave me the freedom to make my own choices. I learnt the power of persistence and resilience from my father. Whereas, my mother instilled in me fearlessness, courage and independence. Their irrational and unbreakable faith in my capabilities have kept me on my toes. I thank my siblings: Punnu and Milli, who have pioneered the task of humbling me and breaking my delusions about my glorious self. You are my life support systems. I thank Ajay and Miththu, who have willingly accepted me as their own and showered on me their affection and care.

As an undergraduate student with chemistry major, it was my most fervent dream, to pursue a PhD in chemistry from a world class institute. And now, when this dream is almost near its realization, I thank all my family, friends and mentors who have encouraged me along the way. I shall not be able to mention all of you here, but many thanks to each one of you.

Thesis Overview and Contribution of Authors

This thesis is composed of 6 manuscripts written primarily by the author and co-written by Audrey Moores, who acted as the research supervisor. Each citation is listed below, followed by a detailed explanation of each author's contributions.

1. **Chapter 1:**

   Madhu Kaushik and Audrey Moores. Review: Cellulose nanocrystals as versatile supports for catalysis. *Green Chem*. Manuscript in preparation.

   The author wrote the manuscript. Audrey Moores designed and edited the manuscript.

2. **Chapter 2:**

   Madhu Kaushik, Wei C. Chen, Theo G. M. van de Ven and Audrey Moores. An improved methodology for imaging cellulose nanocrystals by transmission electron microscopy. *Nord. Pulp Pap. Res. J.* 2014, 29, 77-81.

   The author collected all data and wrote the manuscript. Wei C. Chen helped in synthesizing never-dried cellulose nanocrystals, pH-dependent studies and writing those experiments. Theo G. M. van de Ven reviewed the manuscript. Audrey Moores directed the design of experiments and edited the manuscript.

3. **Chapter 3:**

   Madhu Kaushik, Kaustuv Basu, Charles Benoit, Ciprian M. Cirtiu, Hojatallah Vali and Audrey Moores. Cellulose Nanocrystals as chiral inducers: Enantioselective cataly-sis and Transmission Electron Microscopy 3D Characterization. *JACS*, 2015, 137, 6124-6127.

   Madhu Kaushik collected all data and wrote the manuscript. Author trained Charles Benoit for all laboratory techniques involved in the paper. Charles Benoit helped in collection of data. Ciprian M. Cirtiu demonstrated the proof of concept experiment. Kaustuv Basu designed TEM experiments, helped in collection of TEM images and their interpretations. Hajotallah Vali specifically gave insights on design of TEM experiments and reviewed the manuscript in general. Audrey Moores coordinated between the collaborators, designed experiments and edited the manuscript.

4. Chapter 4:

Madhu Kaushik, Alain Li, Reuben Hudson, Mitra Masnadi, Chao-Jun Li and Audrey Moores. Reversing aggregation: Direct synthesis of nanocatalysts from bulk metal. Cellulose nanocrystals as active support to access efficient hydrogenation silver nanocatalysts. *Green Chem*. 2015, DOI: 10.1039/C5GC01281C.

Madhu Kaushik compiled all data and wrote the manuscript. Author trained Alain Li for all laboratory techniques involved in the paper. Alain Li helped in collection of data, discussing results and reviewing the manuscript. Reuben Hudson intellectually contributed to the design of experiments. Mitra Masnadi conducted the XPS experiments and discussed the results. Chao-Jun Li gave insights on experiments and reviewed the manuscript. Audrey Moores coordinated between the collaborators, designed experiments and edited the manuscript.

5. Chapter 5:

Madhu Kaushik, Hava M. Friedman, Mary Bateman and Audrey Moores. Cellulose nanocrystals as non-innocent supports for the synthesis of ruthenium nanoparticles and their application to arene hydrogenation. *RSC adv*. 2015, 5, 53207-53210.

Madhu Kaushik compiled all data and wrote the manuscript. Author trained Hava M. Friedman for all laboratory techniques involved in the paper. Hava M. Friedman and the author shared equally in collection of data. Mary Bateman helped in collection of ICP data. Audrey Moores directed the design of experiments and edited the manuscript.

6. Chapter 6:

This chapter includes the concluding remarks and future perspective of the research work included in the thesis.

7. Appendix: TEM Chapter

Madhu Kaushik, Jean-Luc Putaux, Carole Fraschini, Gregory Chauve and Audrey Moores, in The Transmission Electron Microscope, Intech, 2015, ch. Transmission Electron Microscopy for the Characterization of Cellulose Nanocrystals, Published September 2015, (http://www.intechopen.com/books/the-transmission-electron-microscope-theory-and-applications/transmission-electron-microscopy-for-the-characterization-of-cellulose-nanocrystals)

Madhu Kaushik compiled all data and wrote the manuscript. Jean-Luc Putaux collected data, references and wrote large sections of the chapter. Gregory Chauve and Carole Fraschini helped to collect references, write introduction and review the chapter. Audrey Moores directed the design of chapter and edited the manuscript.

Table of contents

Contents

List of figures

List of schemes

List of tables

1 Introduction

This chapter is based on the review of applications of cellulose nanocrystals (CNCs) in catalysis, which is a manuscript in preparation to be submitted soon.

Review: Nanocelluloses as versatile supports for metal nanoparticles and their applications in catalysis.

Madhu Kaushik and Audrey Moores. *Green Chem*. Manuscript in preparation.

The chapter begins with introducing CNCs, their synthesis and applications in general. Thereafter, it specifically covers the applications of CNCs in catalysis.

1.1 Abstract

Nanocelluloses derived from the biopolymer cellulose are a relatively new class of sustainable functional nanomaterials. They have been extensively applied in polymer and paper industry to produce super capacitors, pH-responsive reversible flocculants, aerogels, sensors, pharmaceuticals, chiral materials and catalysts. This review will focus on the applications of nanocelluloses in catalysis. The first part illustrates their use as support, stabilizer and/or reducing agent role in the synthesis of various metal nanoparticle. Subsequently, the applications of these metal-hybrid nanocellulose composites in catalysis are reviewed. Finally, catalysis involving nanocelluloses without the use of metal nanoparticles are included.

1.2 Introduction

The term “nanocelluloses” broadly defines a class of nanomaterials obtained in top-down approaches from vegetal or bacterial cellulose. Cellulose is the most abundant biopolymers on earth and a polymer of cellobiose, a dimer of glucose where each molecule of glucose is joined by a β-1,4-glycosidic linkage (Figure 1.1). In nature, these cellulose chains are assembled in microfibrils, which are further bundled into macrofibers and fibers. Within the microfibrils ordered crystalline regions alternate with disordered amorphous regions. Upon hydrolysis, the glycosidic linkages in the disordered regions, which are more accessible and reactive, are preferentially cleaved, freeing up nano-sized and highly crystalline cellulose materials, or nanocelluloses. The most common hydrolysis method uses sulfuric acid, because it introduces a small number of sulfate ester groups on the nanocellulose surfaces, making them easily dispersible in water.[1-3] Cellulose crystallites were isolated for the first time in the late 1940s *via* this method from cotton.[4] Soon after, Rånby showed that stable colloidal suspensions of these negatively charged cellulose particles could be obtained.[5, 6] Other synthetic techniques include mechanical refining and HCl or enzymatic hydrolysis, which do not affect their surface chemistry.[7]

Nanocelluloses are rod-like or ribbon-like objects with a length typically ranging from 50-1000 nm and a width varying from 3-50 nm, and therefore have high length-to-width (aspect) ratios (10 to 100).[8-12] Their morphology largely depends on the cellulose source and the conditions of preparation (type and concentration of acid, acid-to-cellulose ratio, reaction time and temperature). They have been produced from a wide variety of sources,[13] such as wood, cotton, bamboo,[14] bacteria,[15] algae, tunicates,[16] eucalyptus,[14] spruce bark,[17] soy husk,[18] etc. The size and morphology of nanocellulose have been well-defined and extensively studied[19] because they both influence their colloidal and macroscopic properties such as suspension rheology, phase separation concentration, liquid crystal behavior, orientation under electric or magnetic field and mechanical reinforcement ability in nanocomposites.[8, 17] They have a high specific surface area,[20] high aspect ratio, high crystalline order and chirality, superior mechanical strength, and controllable surface chemistry.[9, 10, 21-23] In addition, they are cheaply synthesized, renewable, biodegradable, non-toxic,[24-27] thermally stable and accessible industrially in large scale.[28]

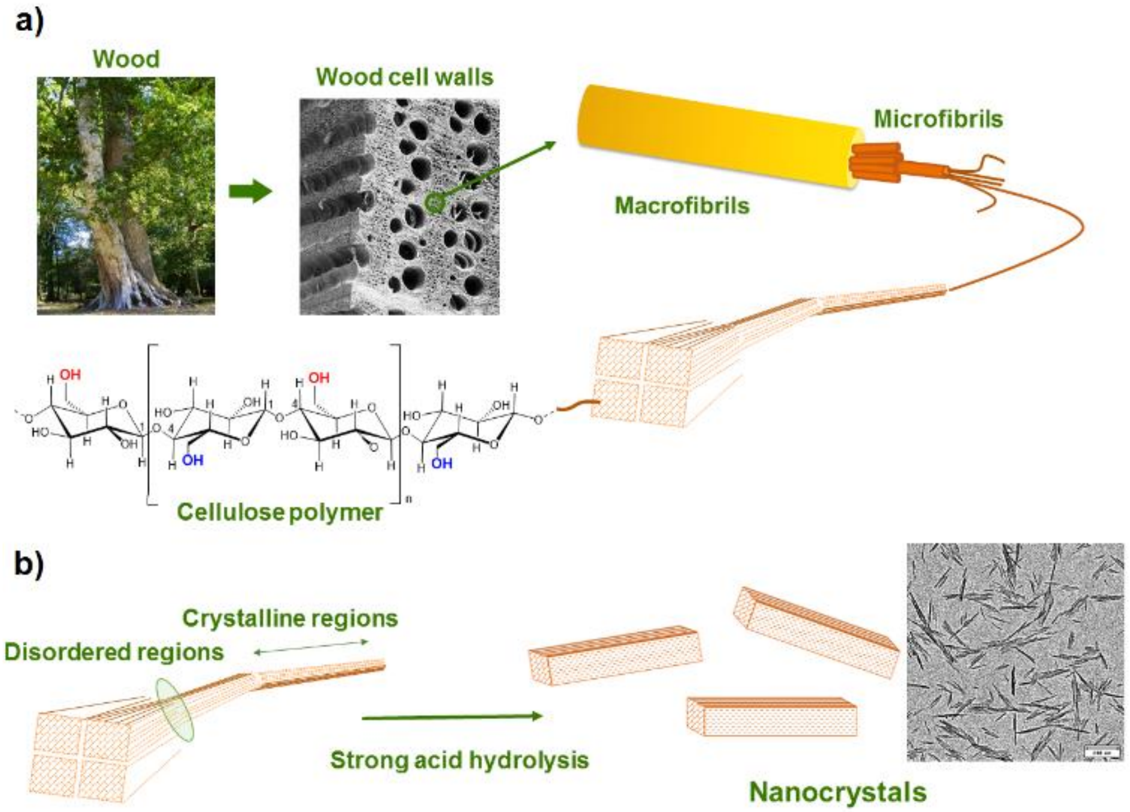

Figure 1.1 a) Structural hierarchy of the cellulose fiber component from the tree to the anhydroglucose molecule. b) Preparation of nanocrystals by selective acid hydrolysis of cellulose microfibrils.

In 1959, Marchessault *et al.* first demonstrated that colloidal suspensions of CNCs spontaneously organize into a chiral nematic phase above a certain critical concentration.[29] Consequently, CNCs have been used to produce iridescent and birefringent films[30, 31] for biotemplating to produce chiral mesoporous silica[32-35] and carbon[36], titania films[37-39] and gold nanoparticle films with chiral plasmonic properties.[40, 41] Their high mechanical strength have been exploited since the mid 1990's when it was shown that CNCs were efficient reinforcing fillers in latex-based polymer matrices, leading to applications in polymer and plastic manufacturing.[9, 16, 42, 43] More recently, they have been used for producing hydrogels,[44] aerogels,[45, 46] shape memory polymers,[47] sensors,[48] and pH-responsive flocculants.[49, 50] As a consequence, nanocelluloses have been applied to the paper, cosmetics, food, pharmaceuticals and biomedical industries.[51-53] Several review articles and book chapters have been published over the last years that detail the various properties and applications of nanocelluloses.[8-10, 19, 21-23, 54-68]

A key feature in the development of novel catalysts resides in the importance of engineering an easy recovery step.[69] Among the many applications of nanocelluloses, their use in the design of such recyclable catalysts is appealing for a number of reasons: 1) The high surface area, thermal stability and functionalizable surface makes them interesting supports; 2) The natural surface chemistry of nanocellulose, mostly composed of hydroxy and sulfate ester groups, their crystallinity and chiral properties play a role in their ability to reduce metal species or to participate in catalytic events; 3) Nanocellulose suspensions in water are very stable and confer enhanced stability to catalysts supported by them. They afford avenues for the generation of biphasic catalytic systems akin to, for instance, ionic liquids;[70, 71] 4) Finally nanocelluloses are bio-sourced, biodegradable, non-toxic, and available industrially in large scale. The most developed approach has been to use nanocelluloses as support for metal nanoparticles (NPs). Other examples include the grafting of organometallic species or the chemical modification of the nanocelluloses to afford organocatalysts. In the following sections, we introduce the nanocelluloses nomenclature and their various properties. Then we detail how nanocelluloses are used to produce supported metal NPs and review the use of these hybrid systems in catalysis. At last, other use of nanocelluloses in catalysis are covered.

1.3 Nanocellulose Nomenclature

In the literature, a wide range of nomenclature are used to categorize these nanocelluloses, for example, nanocrytallites of cellulose (NCCs), nanocrytalline cellulose (NCCs), cellulose nanocrystals (CNCs), cellulose nanowhiskers (CNWs), cellulose nanofibers (CNFs), nanofibrillated cellulose (NFCs), nanofibrous cellulose (NFCs), bacteria cellulose, bacterial cellulose and/or bacterial nanocellulose (BCNs). In the past, attempts have been made to rationalize the use of these terms based on their morphology and synthetic procedure.[8, 10, 19, 64, 68] We have summarized the nomenclature of nanocelluloses in Table 1.1 based on their size distribution and method of preparation.

Table 1.1 Nomenclature and size distribution of nanocelluloses.

Nomenclature	Abbreviations	Size distribution (nm)	Mode of preparation (sources)	References*
Cellulose nanocrystals, Nanocrystalline cellulose, Nanocrytallites of cellulose, Crystalline cellulose, Cellulose nanowhiskers	CNCs, NCCs, CNXLs, XNLs, CNWs	Length: 50 – 500 Width: 3 – 15	Acid hydrolysis (Wood, Cotton, Rice, Ramie, Sisal, Tunicates)	7, 72-80
Cellulose nanofibers, Nanofibrillated cellulose, Nanofibrous cellulose	CNFs NFCs	Length: 50 – 3000 Width: 5 – 50	Mechanical treatment (Wood, Microcrystalline cellulose, Tunicates)	7, 72, 73, 81-86
Bacteria cellulose, Bacterial cellulose, Bacterial nanocellulose, Bacteria nanofiber	Bacteria CNs BNCs, BNFs	Length: 200 – 3000 Width: 10 – 75	Bacteria	7, 87-89

** Proposed references are representative examples and do not constitute an exhaustive list*

We have broadly categorized the nanocelluloses into three categories in Table 1.1: (i) nanocrytallites of cellulose (NCCs), nanocrytalline cellulose (NCCs), cellulose nanocrystals (CNCs) and/or cellulose nanowhiskers (CNWs), which are produced from acid hydrolysis and are typically shorter in length, narrower in width and higher in crystallinity; (ii) cellulose nanofibers (CNFs), nanofibrillated cellulose (NFCs) and/or nanofibrous cellulose (NFCs), which are those obtained from mechanical treatment and are frequently longer, wider and lower in crystallinity, and (iii) bacterial cellulose and/or bacterial nanocellulose (BCNs), which are derived from bacteria, and are the longest and widest in the family. It is essential to introduce a standard nomenclature for the family of nanocelluloses. Some attempts in this directions have been taken by the Technical Association of Pulp and Paper Industries (TAPPI).[90] However, there is no set definition for each sub-set yet, and the literature reveals that various nanocelluloses co-exist in the broad and overlapping material space. In our review, the applications of all forms of nanocelluloses in catalysis shall be included.

1.4 Nanocelluloses as support for metal NPs

Applications of nanocellulose as a metal NP support as attracted a lot of attention in the past decade. Metal NPs possess properties which are unique and distinct from those of their bulk or molecular counterparts.[91] Metal NPs are thermodynamically unstable and tend to aggregate to form bulk metal without the use of capping agents, ligands or supports in their synthesis. Because of their high surface area, reductive surface functional groups and water suspendability, nanocelluloses are attractive supports for metal NPs. The following section shall review the synthesis of metal NPs in detail. Table 1.2 gives a list of metal NP-nanocellulose hybrid composites with non-catalytic applications, whereas Table 1.3 lists metal NP-nanocellulose hybrid composites with applications in catalysis.

Table 1.2 Metal, alloy and oxide NPs – nanocellulose hybrid composites with non-catalytic applications. Metal, alloys and oxides are listed in alphabetical order.

Metal/oxide NP (size in nm)	**Precursor (synthesis of NPs)**	**Nanocellulose used**	**Application**	**Reference**
Ag NPs (~7)	$AgNO_3$ (reduction by dopamine hydrochloride)	Polydopamine coated CNCs	Antibacterial activity	92
Ag NPs (10 – 80)	$AgNO_3$ (reduction by $NaBH_4$)	Amine grafted CNCs	-	93
Ag NPs (2 – 3)	$AgNO_3$ (reduction by $NaBH_4$)	CNCs with varied sulfur content	-	94
Ag NPs (6.3 ± 3.1)	$AgNO_3$ (reduction by $NaBH_4$)	TEMPO-oxidised CNFs	Antibacterial activity	95

Ag NPs (spherical: 1 – 10; dendritic: 5 – 10 µm)	$AgNO_3$ (reduction by CNCs)	CNCs	Antibacterial activity	96
Ag NPs (3 – 4)	$AgNO_3$ (reduction by CNFs)	TEMPO-oxidised CNFs	Aerogels	46
Ag NPs (5 – 14)	$AgNO_3$ (reduction by $NaBH_4$)	Bacteria CNFs	Antibacterial activity	97
Ag NPs (17.1 ± 5.9)	$AgNO_3$ (reduction by bacterial CNFs)	Bacteria CNFs	Antibacterial activity	98
Ag NPs (10 – 15)	$AgNO_3$ (reduction by $NaBH_4$)	TEMPO-oxidised CNCs	Antibacterial activity	99
Ag NPs (<10)	$AgNO_3$ (reduction by $NaBH_4$)	TEMPO-oxidised CNCs	DNA biosensor	100
Ag NPs (20 – 45)	$AgNO_3$ (reduction by aldehyde groups on CNC surface)	Periodate-oxidised surface CNCs	Antibacterial activity	101
Ag nanoclusters (size not reported)	$AgNO_3$ (reduction by $NaBH_4$)	CNFs (Polymethacrylic acid (PMAA) used as stabiliser)	Antibacterial activity	102
Ag NPs (8 – 15)	$AgNO_3$ (reduction by triethanolamine)	Bacteria CNFs (triethanolamine as complexing agent)	Antibacterial activity	103
Ag NPs (~ 30)	$AgNO_3$ (reduction by NH_2NH_2, NH_2OH, ascorbic acid)	Bacteria CNFs (polyvinylpyrrolidone (PVP) and gelatin used as additional stabilisers)	Antibacterial activity	104
Ag NPs (10 – 20)	$AgNO_3$ (reduction by CNFs)	TEMPO-oxidised bacteria CNFs	-	105
Ag NPs (size not reported)	$AgNO_3$ (reduction by sodium citrate)	Bacteria CNFs (sodium citrate as additional stabiliser)	Substrate enhanced raman scattering (SERS) substrates	106
AgCl NPs (size not reported)	$AgNO_3$ and NaCl	Bacteria CNFs	Antibacterial activity	107
Ag-Au alloy NPs (3 – 7)	$AgNO_3$ and $HAuCl_4$ (reduction by $NaBH_4$)	CNCs (capping agent used: sodium citrate)	-	108
Ag-ZnO NPs (9 – 35)	$AgNO_3$ and $Zn(AcO)_2\cdot 2H_2O$ (reduction by CNCs)	CNCs	Antibacterial activity	109
Au NPs (~10)	$HAuCl_4$ (reduction by citrate ions and surface of CNFs)	Wood or bacteria CNFs	Security paper making:	110

			optical properties	
CdS NPs (~8)	$Cd(NO_3)_2.5H_2O$ and Na_2S	Bacterial CNFs	-	111
$Cu_{0.5}Co_{0.5}Fe_2O_4$ NPs (13.5)	$FeCl_3$, $CoCl_2$, $CuCl_2$ (reduction by CNCs)	CNCs	-	112
Fe_3O_4 (5.9 – 14.1)	$FeSO_4{\cdot}7H_2O$ (reaction in NaOH)	CNCs (PDDA, PVP, SiO_2 and β-cyclodextrins used as additional stabilisers)	Adsorption of pharmaceutical residues	113
Ni NPs (5-12)	$Ni(NO_3)_2$ (reduction by CNCs)	CNCs	-	114
Pt NPs (5 – 30)	H_2PtCl_6 (CNCs as reducers in $scCO_2$)	CNCs	-	115
Se NPs (10 – 20)	H_2SeO_3 and Na_2SeO_3 (reduction by CNCs)	CNCs	-	116
TiO_2 NPs (Length: 26 ± 3; Breadth: 16 ± 2)	Commercial TiO_2 NPs adsorbed on the CNF surface	CNFs	-	117

1.4.1 Synthesis of metal NPs

Nanocelluloses were first used as template for synthesizing metal NPs in 2003, when Woodward and coll. precipitated Pd, Au and Ag from their metal precursors onto bacterial CNFs, without the use of any external reducing agent.[118] The next example in literature came in 2007 with the synthesis of Se and Ni NPs by Exarhos and coll.[114, 116] Ni NPs of 5 to 12 nm on carbon were prepared by the thermal treatment (400-500°C) of $Ni(NO_3)_2$ in the presence of CNCs acting as the source of carbon. Thermal reduction of CNC at lower temperatures with Se precursors was used in the synthesis of Se NPs onto rod-like carbon structures. Following these preliminary works, the use of nanocelluloses for metal NPs gradually increased. There are mainly three approaches in the synthesis of metal NPs, shown in Figure 1.2.

The first and most common approach is to use an external reducing agent to reduce a metal precursor into metal NP on the nanocellulose surface. Ag NPs have been synthesized on various types of nanocelluloses by reducing $AgNO_3$ with $NaBH_4$.[93-95, 97, 99, 100, 102-104, 119, 120] Laine and coll. studied the effect of the number of sulfate ester on the CNC surface on NP formation and nucleation of Ag NPs by borohydride reduction. CNCs, with a minimum quantity of sulfate, proved to be vital for the nucleation of small, monodisperse Ag NPs. [94] Other external reducing agents like triethanolamine, NH_2NH_2, NH_4OH and ascorbic acid have also been used for reducing Ag salts into Ag NP.[103, 104] Au NPs have been synthesized from $HAuCl_4$ onto nanocelluloses by using external reducing agents ($NaBH_4$[110, 121-124] and poly(ethyleneimine[125, 126]) as well. Schlesinger *et al.* demonstrated that the size of Au NPs increases with increasing concentration of the metal salt solution.[121] Borohydride reduction has also been applied towards synthesizing Pd NPs,[127] Ru NPs,[120] CuO[128] NPs, and alloy NPs, including Au-Pd,[129] Pd-Cu,[130] and Au-Ag.[108] In case of alloy NPs, varied size distributions could be achieved by varying the ratio of the two metal precursor used. A more atom-economical alternative to borohydride reduction is the use of H_2 gas as a reducer of metal precursors. Our group applied this approach to synthesize Pd NPs[131, 132] and Ru NPs[133] onto CNCs. Notably, in the latter, CNCs not only act as supports for NPs but also participate in the reduction of Ru(III) to Ru (0). It is the first reported study where the $RuCl_3$ could be reduced to Ru (0) NPs without using strong reducing agents like $NaBH_4$, which shows the positive role of CNC in the sustainable synthesis of metal NPs. CNCs are believed to act in synergy with H_2 to perform the reduction under mild conditions of room temperature and 4 bars H_2.

The second approach for using nanocellulose as bio-templates for metal NPs is to modify their surface by attaching chemical groups that have reducing/coordinating capabilities, and using these modified nanocelluloses to form metal NPs from their metal salts, without the use of any external reducing agent. Tam and coll. used polydopamine-coated CNCs to generate Ag NPs from $AgNO_3$, where the Ag ions were reduced by dopamine.[92, 134] Interestingly, they used β-cyclodextrin as an additional capping agent in one synthesis and only polydopamine-coated CNCs in the other.[134] Periodate-oxidised CNCs have also been used in the formation of Ag NPs from Ag (I) salt, where the aldehyde groups on the CNC surface have been proposed to act as reducing agents.[101] Au NPs have also been synthesized from their metal salt using surface-modified nanocelluloses as reductants. Tam and coll. grafted PAMAM (poly(amidoamine)-dendrimer onto CNCs, and the amine groups were used for reducing $HAuCl_4$ into Au NPs. [135] The size distributions of Au NPs were broader when using CNC-PAMAM as a reducing agent compared to conventional borohydride reduction, and the greater the PAMAM loading was, the more polydisperse the resulting Au NPs were. It was rationalized that PAMAM was a very active reducing agent, thus causing rapid $HAuCl_4$

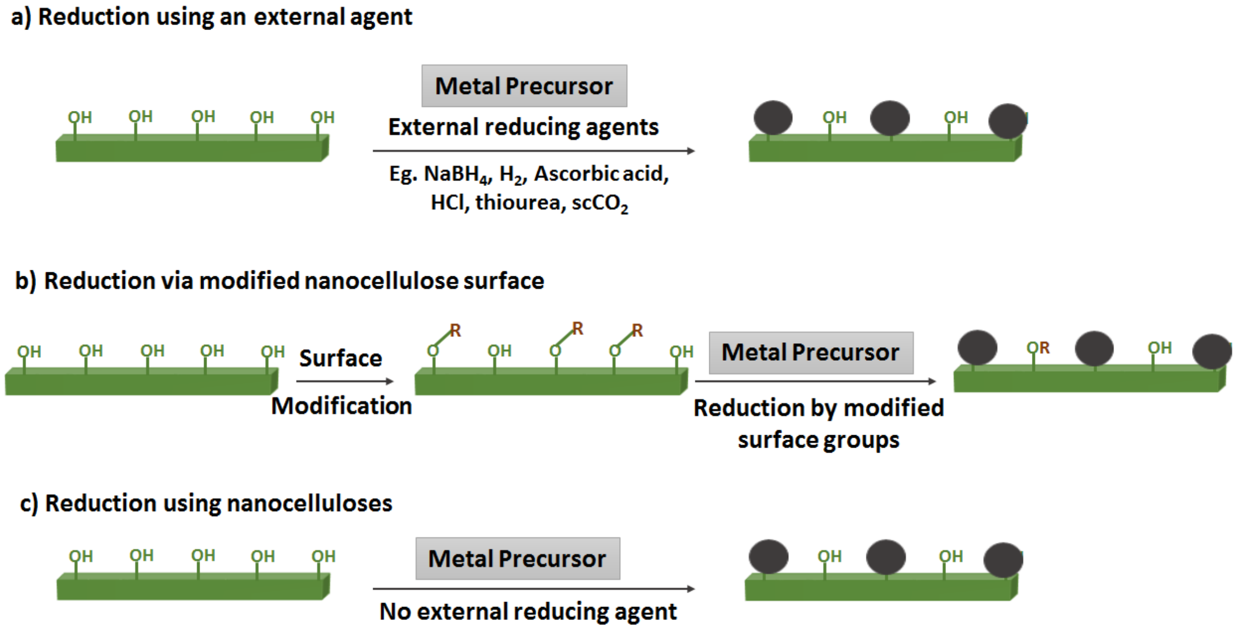

Figure 1.2 Three approaches for synthesis of metal NP-nanocellulose hybrid composite: a) reduction using an external agent, b) reduction via modified nanocellulose surface, and c) reduction using nanocelluloses.

reduction and seeding and poor growth control. Huang *et al.* used the HS-functionalized CNCs for reducing $HAuCl_4$ to Au NPs.[136]

The third approach, and the simplest, is to use the surface hydroxyl groups on the nanocelluloses itself for reducing metal precursors into metal NPs. In this method, the nanocelluloses act as both support and reducers for the generation of NPs. Through this approach, Ag NPs,[46, 96, 105, 137] AgCl NPs,[107] Au NPs,[138] Pd NPs,[139, 140] Pt NPs,[115, 141, 142] $Cu_{0.5}Co_{0.5}Fe_2O_4$ NPs,[112] Fe_3O_4 NPs,[113] Se NPs,[116] Ni NPs[114] and Fe[143] NPs have been synthesized. Remarkably, Thielemans and coll. synthesized Pd NPs supported on to CNCs in a one-pot synthesis in sub-critical and supercritical CO_2 from $Pd(hexafluoroacetylacetonate)_2$ ($Pd(hfac)_2$).[140] The advantage of using supercritical CO_2 was that at the end of the reaction, dry Pd NPs supported onto CNCs were obtained simply by venting out the CO_2. Pressure (240−2200 psi), reaction time (2−17 h), and weight ratio of the precursor $Pd(hfac)_2$ to CNCs (1−4% w/w) affected the size of the Pd NPs obtained. These results show that the diameter of Pd NPs varied between 6 and 13 nm. The smaller NPs were attached on the CNCs, while NPs with diameters above 13 nm appeared not to remain attached to the CNC surface. In another work, Thielemans and coll. synthesized Pt NPs supported onto CNCs in supercritical CO_2/water system, where they reduced H_2PtCl_6 into Pt in aqueous solution using CNCs as reducing agent. They reported an interesting phenomena that the reaction only proceeded when water was in contact with supercritical CO_2.[115] Recently, our group described a highly atom economical synthesis of Ag NPs onto the CNCs directly from bulk Ag metal in presence of light, water and CNC suspension. In this study, CNCs played a key role as high surface support and *in situ* reducers to drive the depletion of Ag from a metal wire and afford 1.3 nm ± 0.3 nm Ag NPs.

The mechanism of binding metal NPs onto nanocelluloses have not been studied in much detail. Unmodified nanocelluloses have a hydrophillic surface covered with hydroxyl groups. The most classically used nanocellulose rely on a sulfuric acid digestion, which also leaves sulfate esters, at the surface. When the surface is fully oxidized using

TEMPO, carboxylate functionalities are introduced. All these oxygen containing moieties are very effective metal center stabilizers *via* the formation of dative bonds.[128, 138, 139, 141] Thiols being known for their strong affinity for metal surfaces, especially for gold, SH-functionalized CNCs were used to effectively stabilize Au NPs.[136] Interestingly, CNCs are very efficient towards the formation of small metal NPs and their stabilization, notably under catalytic conditions.[132, 133]

1.4.2 Characterization of metal NP-nanocellulose hybrid composites

Visualization of metal NP-nanocellulose hybrid composites is an essential part of the bio-templating metals onto nanocellulose surfaces. Transmission electron microscopy (TEM), cryo-TEM, atomic force microscopy (AFM), and field emission gun scanning electron microscopy (FEG-SEM) are a few visualization techniques. The most widely used technique is TEM, along with its analytical tools. TEM observation of hybrid organic-inorganic systems is very difficult because nanocelluloses and metal NPs have very different sensitivity to beam damage and density.[144, 145] While metallic NPs are very stable, nanocelluloses are quickly damaged in the microscope, resulting in a significant loss of contrast and recognizable morphology. Moreover, a large defocus has to be applied to visualize the little dense cellulose. When metal NPs are image simultaneously, this leads to an overestimation of their size. Consequently, only a few TEM images are available in the literature where nanocelluloses and supported metal NPs could be seen simultaneously with clarity.[145] To overcome this issue, negative staining could be applied, which outlines the CNCs with precision. However, this technique is not compatible with metal NPs are smaller than 3-4 nm, they will not be distinguished. Recent results demonstrated that highly sensitive direct detection device (DDD) cameras associated with phase plates allowed simultaneous observation of CNCs and sub-nanometer thick Pd patches at their surface. In this experiment, the organic and inorganic phases were observed together at near-focus conditions.[132]

Alongside visualization of metal NPs, it is very important to validate the chemical nature of the NPs seen in the images. This analysis can be done in TEM by using energy dispersive X-ray spectroscopy (EDX), which allows for quantitative measurement of chemical composition. Furthermore, it is vital to evaluate the oxidation state of the metal NPs, especially in the context of catalysis. For this, the most common technique used is X-ray photoelectron spectroscopic (XPS) analysis. In addition, thermogravimetric analysis (TGA) is done to monitor the thermal stability of these hybrid composites. Usually, the thermal stability of the modified nanocelluloses composites are higher than nanocelluloses alone.[146] Furthermore, X-ray powder diffraction (XRD) experiments are carried out to determine any change in crystallinity within the nanocelluloses after the modification. Usually no significant change in the crystallinity of the nanocelluloses is observed.[134] Inductive coupled plasma (ICP) coupled with atomic emission spectroscopy (AES) or mass spectroscopy (MS) as detection methods is also conducted to determine the metal loading within the synthesized hybrid materials. The same methods are also used to study the leaching of metal NPs in catalytic product, which is essential for determining the robustness and heterogeneous nature of the catalytic system.[127, 128, 133, 147, 148]

1.5 Catalysis by metal NP-nanocellulose hybrid composites

NP catalysis has gained momentum in the recent years as they provide a bridge between the homogeneous and heterogeneous catalytic systems. [149] They bridge the efficacy, selectivity, and moderate reaction conditions of homogeneous systems to the easy separation, recyclability and affordability of heterogeneous systems. Metal NP-nanocellulose hybrid composites have been more and more applied towards catalysis, especially in the last 5 years. Nanocelluloses provides interesting properties compared to conventional supports and thus afford novel catalytic system, with unique features, notably in terms of NP stability, NP reactivity and selectivity (*vide infra*), but also with the goal of afford sustainable alternatives to known methods. Besides catalysis, they have been used for antibacterial applications,[92, 95-99, 101-104, 107, 109, 150] aerogels,[46] DNA biosensors,[100] substrate enhanced raman scattering (SERS) substrates,[106] security paper making: optical properties,[110] and adsorption of pharmaceutical residues.[113] These are listed in Table 1.2, but are not further discussed as they are beyond the scope of the present review. In the following section, we shall evaluate the catalytic applications of the metal NP-nanocellulose hybrid composites, which have been summarized in Table 1.3.

Table 1.3 Metal/oxide NP – nanocellulose hybrid composites with catalytic applications. Metal, alloys and oxides are listed in alphabetical order.

Metal/oxide NP (size in nm)	**Precursor (synthesis of NPs)**	**Type of nanocellulose used (additional capping agent or support used, if any)**	**Catalytic reaction**	**Reference**
Ag NP (~ 10)	$AgNO_3$ (reduction by dopamine)	Polydopamine-coated CNCs (β-cyclodextrin agent used as additional capping agent)	Reduction of 4-nitrophenol	134
Ag NPs (~ 6.2)	$AgNO_3$ (reduction by $NaBH_4$)	NFCs (poly(amidoamine), PAMAM, dendrimer)	Reduction of Rhodamine B (decoloration of the dye)	119
Ag NPs (4.0 ± 2.0)	$AgNO_3$ (reduction by $NaBH_4$)	TEMPO-oxidised CNFs	Aza-Michael reaction	120
Ag NPs (10 to 50)	$AgNO_3$ (reduction by CNC)	CNFs	Electrocatalysis: reduction of oxygen	137
Au NPs (4.5 ± 0.4, 5.6 ± 0.6, 7.1 ± 0.6)	$HAuCl_4$ (reduction by $NaBH_4$)	CNCs modified into mesoporous photonic cellulose by co-templating with urea/formaldehyde resin	Biosensor (undergo color changes on exposure to 2-mercaptoethanol)	121
Au NPs (2 – 4)	$HAuCl_4$ (reduction with and without $NaBH_4$)	PAMAM dendrimer-grafted CNCs	Reduction of 4-nitrophenol	135
Au NPs (30.5 ± 13.4)	$HAuCl_4$ (reduction by CNCs)	CNCs	Reduction of 4-nitrophenol	138
Au NPs (2 – 3)	$HAuCl_4$ (reduction by -HS groups on the CNC surface)	HS-functionalized CNC	Alkyne-Aldehyde-Amine-coupling	136
Au NPs (2.95 ± 0.06)	$HAuCl_4$ (reduction by $NaBH_4$)	Poly(diallyldimethyl ammonium chloride) (PDDA)-coated carboxylated CNCs	Reduction of 4-nitrophenol	123
Au NPs (~9)	$HAuCl_4$ (reduction by poly(ethyleneimine)	Bacteria CNFs (Heme proteins: horseradish peroxidase, hemoglobin and myoglobin immobilised onto CNFs)	Electrocatalysis: reduction of H_2O_2	151
Au NPs (~9)	$HAuCl_4$ (reduction by poly(ethyleneimine)	Bacteria CNFs: poly(ethyleneimine) used as linking agent	Electrocatalysis: reduction of H_2O_2 in biosensers	125
Au NPs (<5)	$HAuCl_4$ (reduction by $NaBH_4$)	CNFs	Reduction of 4-nitrophenol	124
Au NPs (2 – 7)	$HAuCl_4$ (reduction by $NaBH_4$)	TEMPO-oxidised CNFs	Enzyme immobilisation: bio-catalysis	152

Au-Pd NPs (4 – 9)	$HAuCl_4.3H_2O$ and $[Pd(NH_3)_4]\cdot Cl_2$ (reduction by $NaBH_4$)	TEMPO-oxidised CNFs	Reduction of 4-nitrophenol	129
CdS NPs (10 – 20)	$CdCl_2$ (thermal treatment in presence of thiourea)	Bacteria CNFs	Photocatalysis: methyl orange (MO) degradation	153
Cu NPs (~5)	$CuCl_2$ (reduction by ascorbic acid)	TEMPO-oxidised CNFs	Reduction of 4-nitrophenol	154
CuO NPs (~7)	$CuSO_4$ (reduction by $NaBH_4$)	CNCs	Reduction of 4-nitrophenol	128
Cu-Pd NPs (Pd = ~3.7; Cu = ~4.0)	$PdCl_2$ and $CuCl_2$ (reduction by KBH_4)	Bacteria CNFs	Water denitrification: nitrate reduction	130
Fe NPs	$FeCl_3$ (reduction by H_2)	CNCs from bamboo pulp	Methylene blue degradation, Reduction of 4-nitrophenol	143
Pd NPs (1 – 7)	$PdCl_2$ (reduction by CNCs)	CNCs	Reduction of methylene blue and 4-nitrophenol	139
Pd NPs (~20)	$PdCl_2$ (reduction by KBH_4)	Bacteria CNFs	Heck Reaction	127
Pd NPs (3.6 ± 0.8)	$PdCl_2$ (reduction by H_2)	CNCs	Hydrogenation of phenol; Heck coupling	131
Pt NPs (11 – 101)	H_2PtCl_6 (reduction by wood nanomaterial)	Wood nanomaterials	Reduction of 4-nitrophenol	141
Pt NPs (~2)	H_2PtCl_6 (reduction by CNCs)	CNCs; carbon black as additional support	Electrocatalyst for oxygen electroreduction	142
Pt NPs (3 – 4)	H_2PtCl_6 (Reduction by $NaBH_4$ and HCHO)	Bacteria CNFs	Electrocatalysis: oxidation of hydrogen in fuel cells	150
Ru NPs (8.0 ± 2.0)	$RuCl_3$ (reduction by $NaBH_4$)	TEMPO-oxidised CNFs	Aerobic oxidation of benzyl alcohol	120
TiO_2 NP (4.3 – 8.5)	$Ti(OBu)_4$ (thermal treatment)	Bacteria CNFs	Photocatalysis: Methyl Orange degradation	155

1.5.1 Reductions

Metal NP-nanocellulose hybrid composites have been widely applied towards the reduction of 4-nitrophenol to 4-aminophenol (Scheme 1.1a). This reaction has been successful using Au NPs,[123, 124, 135, 138] Ag NPs,[134] Pd NPs,[139] Au-Pd NPs,[129] Pt NPs,[141] Cu NPs[154] and CuO NPs.[128] This reduction reaction with metal NPs supported onto nanocelluloses in presence of $NaBH_4$ occurs at room temperature, reaching completion between 15-30 mins, and giving excellent conversions of 95-100%. The turn over frequencies (TOFs) for the reduction of 4-nitrophenol to 4-aminophenol by metal NPs supported onto nanocelluloses were much higher than metal NPs supported onto other polymer supports. The higher TOFs were because of the highly dispersed metal NPs, which were exposed on the nanocellulose surface, allowing effective contact with the reactants.[123, 124, 128, 135, 138]

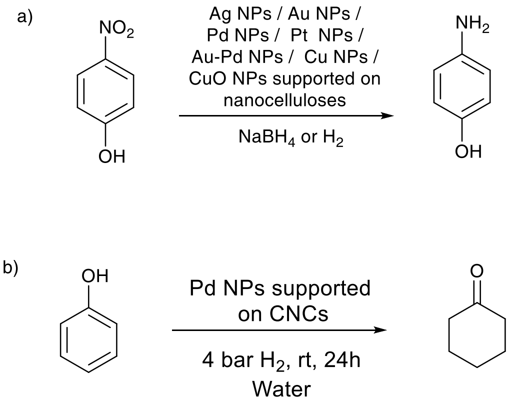

Scheme 1.1 Reduction reactions by metal NP-nanocellulose hybrid composites: a) reduction of 4-nitrophenol, b) hydrogenation of phenol.

4-nitrophenol reduction has been postulated to follow the Langmuir-Hinshelwood mechanism. Metal hydrides are formed when borohydride ions react with metal NPs on the metal surface, with the simultaneous adsorption of nitrophenolate ions. The rate-determining step is the electron transfer from the borohydride ion to the 4-nitrophenolate ion, through the metal NP surface. This reduces the 4-nitrophenolate ion into a 4-aminophenolate ion. Finally, H^+ and 4-aminophenolate ions desorb from the metal surface to produce 4-aminophenol.[123] Tam and coll. carried the reduction 4-nitrophenol with Ag

NPs supported onto poly(dopamine)-coated CNCs. They compared the efficiency of 4-nitrophenol reduction with Ag NPs to Au, Pd and Cu NPs.

The reduction with Ag NPs had higher TOFs compared to others. Interestingly, they could accelerate the catalytic process with further incorporation of β-cyclodextrin into the system due to host−guest interactions between 4-nitrophenol and cyclodextrins. Huang and coll. inferred that the catalytic activity for the reduction of 4-nitrophenol depends on the metal NP size, that is, smaller Pt NPs exhibited enhanced catalytic activities.[141] They used varied sizes of Pt NPs for the reaction and the catalytic activities of the Pt particles followed the order of: spherical Pt NPs (2.3 ± 0.5 nm) > spherical Pt nanoclusters (21.5 ± 5.2 nm) > Pt NPs (4.5 ± 0.8 nm) > cubic Pt NPs (15.9 ± 2.9 nm). Even though the size of spherical Pt nanoclusters was larger than that of the cubic Pt NPs, the kinetic data indicated that the Pt clusters were catalytically more active than the cubic Pt NPs. This could be explained on the following account: the nanoclusters were composed of more than 50 particles with an average diameter of about 3.0 nm; the larger percentage of edge and corner atoms in structures might have increased their catalytic activities. In recent report, Fe supported on CNCs was also demonstrated to be apt for this reaction.[143]

Ramaraju *et al.* studied the decoloration of rhodamine B dye by Ag NPs supported onto CNFs, additionally stabilized by PAMAM dendrimer. The dye was reduced by $NaBH_4$ in the presence of Ag NPs acting as catalysts.[119] They explained the catalytic mechanism as follows: the nucleophilic borohydride ion donates its electrons to Ag NPs and the electrophillic Rhodamine B captures electrons from the Ag NPs. Therefore, Ag NPs serve as a catalytic electron relay for the redox reduction degradation of Rhodamine B. Without metal NPs, potential difference between the borohydride ion and the dye is too high and there is no electron transition. The similar reduction of methylene blue with $NaBH_4$ was reported with Pd[139] and very recently with less toxic and earth-abundant Fe[143] on nanocellulose. Interesting, in the latter example, the CNCs were shown to preserve the zero-valent Fe against oxidation, to make the FeNPs-CNCs hybrids more performant that the classic nano-sized zero-valent Fe systems. This example could prove appealing for real-world water remediation. The reduction of nitrates for water denitrification was also reported with Cu-Pd NPs on bacterial CNFs.[130]

Hydrogenation of C-C and C-O multiple bonds is a very active research field, with applications in all chemical industries, from petro chemistry to pharma, and nanocellulose hybrids offer interesting examples (Scheme 1.1b). Pd NPs supported onto CNCs were first described by us for the hydrogenation of phenol at 4 bars H_2, room temperature, in water for 2h (Scheme 1.1b).[131]

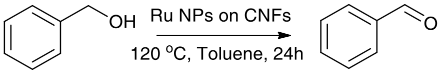

Scheme 1.2 Oxidation of benzyl alcohol using Ru NPs supported on CNFs as catalysts.

1.5.2 Oxidations

Ru NPs supported onto CNFs have been used for catalyzing the oxidation of benzyl alcohol to benzaldehyde at 120°C for 24h with 89% yields (Scheme 1.2).[120] These results proved superior to catalysis done by Ru NPs supported onto titania or alumina. In the proposed mechanism, Ru NPs formed the Ru^{II} =O species with the help of atmospheric oxygen. This is followed by the assistance of formed Ru-oxo species in the formation of benzaldehyde from benzyl alcohol. The system was recyclable up to 4 cycles.

1.5.3 Coupling Reactions

Heck coupling reactions (Scheme 1.3a) using Pd NPs supported onto nanocelluloses have been studied by various research groups. Our group demonstrated that Heck coupling reactions using model substrates, styrene and iodobenzene, could be carried out efficiently by Pd NPs supported onto CNCs in a 1:1 mixture of water–acetonitrile at 100°C. Using K_2CO_3 as a base, 75% of iodobenzene was converted in stilbene within 24 h, at a molar ratio iodobenzene/Pd of 170/1. Zhou *et al.* carried out the similar Heck coupling reactions in DMF and triethylamine at 120°C for 10h, using Pd NPs supported onto bacterial CNFs.[127] They also expanded the scope of the reaction to other aryl halides and acryl acetates. The catalyst was recyclable up to 5 cycles with no significant metal leaching. In this study, Pd leaching was studied by ICP-AES analysis before and after the fifth reaction cycle. The Pd concentration was found to be 8.12% after the fifth cycle. However, no Pd metal was detected in the final coupling product, indicating possible Pd loss during the workup. Thielemans and coll. have also used Pd NPs supported onto CNCs for the Heck coupling reactions at 100 – 130°C, for 16h, with

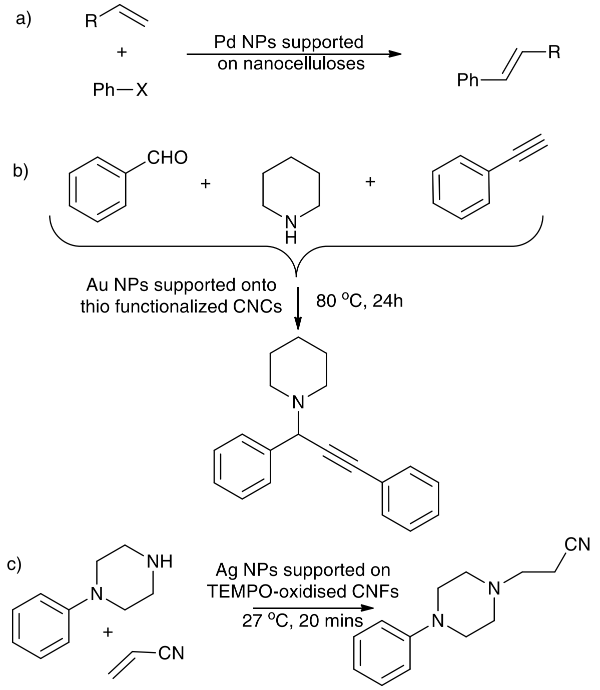

Scheme 1.3 a) Heck coupling reaction with Pd NPs supported onto nanocelluloses, b) A-3 coupling reaction with Au NPs onto CNCs, and c) aza-Michael reaction with Ag NPs onto CNFs.

good yields.[140] Huang *et al.* carried out an A3-coupling reaction (coupling of aldehyde-alkyne-amine) utilising Au NPs supported onto thiol-functionalized CNCs (Scheme 1.3b). The system exhibited excellent activity both in water and without solvent at 80°C for 24h, with high promiscuity towards a variety of reactants.[136] The catalyst was recyclable up to 11 cycles. A different study reported the first aza-Michael reaction (Scheme 1.3c) of 1-phenylpiperazine with acrylonitrile using the Ag NPs supported onto TEMPO-oxidized CNFs at 27°C, for 20 mins with 99 % yields and 100 % selectivities.[120] This system was recyclable up to 4 cycles.

1.5.4 Electrocatalysis

Evans *et al*. demonstrated one of the earliest applications for metal NP-nanocellulose hybrid composites in electrolysis in 2003.[118] They used Pd supported onto bacterial CNFs as catalysts for H_2 evolution when incubated with sodium dithionite. This result demonstrated the potential application of bacterial CNFs for anodic oxidation of H_2 and therefore, their aptness in energy conversion devices. Experimental data also showed that bacterial CNFs possessed greater thermal stability and lower H_2 crossover characteristics compared to Nafion 117-based proton exchange membrane (PEM) fuel cells, which are the most prevalent. Another study revealed that Pt NPs supported on bacterial CNFs possessed high electrocatalytic activity in H_2 oxidation reactions.[150] The single cell performance of Pt NPs supported on bacterial CNFs was tested at 20, 30, and 40°C under non-humidified conditions. In addition, matrix proton conductivity could be improved by doping bacterial CNF pellicles with proton or inorganic acids, increasing the current density. Johnson *et al.* studied Pt NPs supported onto CNFs in electrocatalysis for oxygen electroreduction.[142] Their results were comparable to state-of-the-art Johnson Matthey Pt/C. In another work, they used Ag NPs supported onto CNFs for electrocatalytic oxygen reduction.[137] The electrocatalytic oxygen reduction reaction is a cathode reaction in alkaline fuel cells, and silver is a better cathode material for alkaline fuel cells because it has an activity almost equal to that of platinum but is significantly less expensive.

1.5.5 Photocatalysis

Photocatalysis provides an efficient way of degrading dyes accumulated in the environment, mainly in water. Metal NP-nanocellulose hybrid composites have been used as photocatalysts for degradation of a model pollutant, methyl orange (MO). CdS supported onto bacterial CNFs demonstrated high-efficiency photocatalysis with 82% MO degradation after 90 min irradiation and recyclability up to 5 times.[153] Similar results were also shown with TiO_2 supported onto bacterial CNFs for degradation of MO.[155] Doping the catalyst with nitrogen enhanced its photocatalytic activity. Notably, both catalysts resulted in better photocatalytic activity than the commercially available ones.

1.5.6 Biosensing and Enzyme Immobilisation

Due to their excellent biocompatibility and limited toxicity, metal NP-nanocellulose hybrid composites provide an excellent route for making biosensors and enzyme immobilization. Wang *et al.* developed a high performance biosensor based on Au NP-nanocellulose hybrid composites.[151] Heme proteins such as horseradish peroxidase, hemoglobin and myoglobin were immobilized on the surface of Au NP–bacterial CNF nanocomposites. Heme proteins are important peroxidases that contain iron heme prosthetic groups in their polypeptide pockets, and can catalyze the oxidation of substrates when activated by peroxides. Therefore, to check the bioactivity of these heme proteins, H_2O_2 is often selected as a target compound. The immobilized heme proteins showed electrocatalytic activities towards the reduction of H_2O_2 in the presence of the mediator hydroquinone. The response of the developed biosensor to H_2O_2 was related to the amount of Au NPs in the Au NP–bacterial CNF nanocomposite. In another study, the Au NP–bacterial CNFs were used for fabrication of a horseradish peroxidase biosensor, which was highly sensitive H_2O_2 with a detection limit lower than 1 μM.[125]

Thiol sensors serve as markers for the diagnosis of metabolic diseases like skin lesions, edema, liver damage and pancreatitis. Mac Lachlan and coll. used Au NP-nanocellulose composites for sensing 2-mercaptoethanol.[121] The Au-loaded mesoporous photonic cellulose films exhibited large color changes upon exposure to 2-mercaptoethanol. These results indicated that the mesoporosity of the host matrix renders the NPs accessible to analytes, and alluded to the use of Au NP-loaded mesoporous photonic cellulose for novel sensors.

Luong and coll. used Au NPs supported onto CNCs for the immobilization of enzymes, cyclodextrin glycosyl transferase (CGTase) and alcohol oxidase.[152] This catalytic platform exhibited significant biocatalytic activity with excellent enzyme stability and without apparent loss of the original activity. The recovered specific activities were ~70% and 95% for CGTase and alcohol oxidase, respectively. This strategy provides a novel platform for the scale-up of enzyme-catalyzed processes at the industrial level with improved performance, homogeneity, reusability, and cost effectiveness.

1.6 Other types of catalysis

In recent years, a few examples in the literature have emerged where the nanocelluloses have been applied for catalysis without the use of metal NPs. In this section we shall summarize various catalytic systems using nanocelluloses, without metal NPs (Table 1.4).

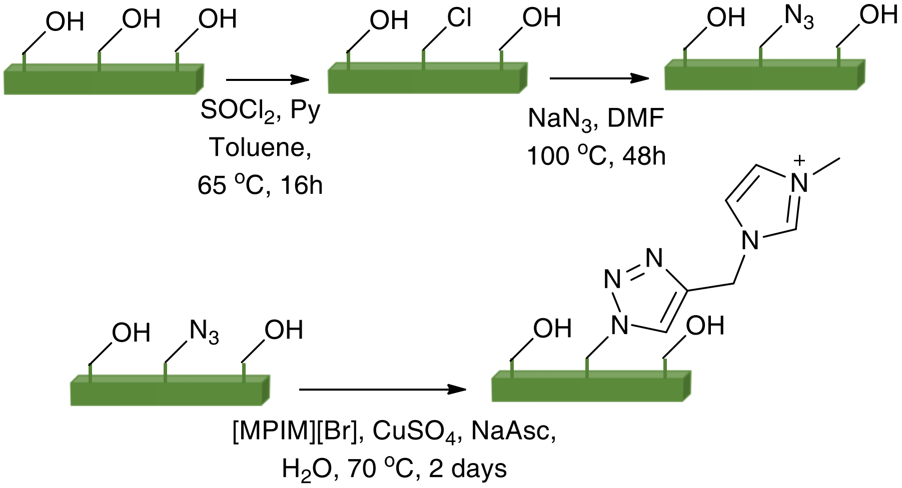

Scheme 1.4 Surface modifications of CNCs.

Thielemans and coll. modified the surface of CNCs using copper (I) catalyzed azide–alkyne cycloaddition to graft an imidazolium salt (Scheme 1.4).[156] The modified CNCs were then examined for their potential application in ion-exchange reactions. The ion exchange capability of modified CNCs was tested by suspending them in an aqueous solution of lithium bis(trifluoromethanesulfonyl)imide overnight. The bromide anion was successfully exchanged with bistriflimide. This work demonstrates a method to immobilize imidazolium salts, producing a heterogeneous system in which the anion can be easily exchanged, and hence, provides an opportunity for synthesizing a wide variety of catalytic and ion-exchange systems.

Table 1.4 Catalysis by nanocelluloses without the metal NPs.

Catalyst system	**Precursor (Synthesis of catalyst)**	**Catalytic reaction**	**Reference**
CNC-Rh_2 (TEMPO-oxidised CNCs used)	$Rh_2(OOCCF_3)_4$ (ligand exchange)	Cyclopropanation of styrene	146
Mesoporous α-Fe_2O_3 (CNCs as support)	$FeCl_3$ (sol-gel method)	Photo-degradation of methylene blue	157
Copper-tetrasulfonate PC grafted on CNCs	Phthalocyanine (PC) (electrostatic interaction and H-bonding between cationic CNC and anionic sulfonate Cu-PC)	Aerobic oxidation of alcohols and alkyl arenes	147
Co (II) species on ethylenediamine-functionalized CNCs	$CoCl_2$	Oxidation of benzyl alcohols	158
HCl-treated CNFs	-	Chirality-specific hydrolysis of amino-acids	159
HCl-treated CNFs	-	Hydrolysis of esters, monophosphate, amide, and ether bonds: decomposition of coat protein of model viruses	160
Imidazolium-grafted CNCs	-	Ion-exchange reactions	156

Wada and coll. presented the hydrolytic activities of CNFs through their latest work. They used the abundant nucleophillic hydroxyl groups on the surface of HCl treated-CNFs for hydrolysis of esters, as well as monophosphate, amide, and ether bonds (Scheme

1.5a).[160] They incubated small organic substrates with CNFs under mild conditions (10 mM HEPES buffer solution, pH 7.4, 30°C, atmospheric pressure) for examining the hydrolytic activities of CNFs. The order of the hydrolysis rates was estimated to be ester > monophosphate > amide bonds. On the other hand, CNFs could not hydrolyse the ether bonds. The crystalline nanofiber structure of cellulose was essential for their hydrolytic activities. When CNFs obtained from green algae (Cladophora) (which had similar diameters and lengths as those obtained from tunicates) were used under the same reaction conditions, similar activities were observed. This observation suggested that the hydrolytic activities were independent of the crystal polymorphs of CNFs. On the other hand, CNFs obtained from cotton and wood, which have smaller diameters and lengths, showed decreased hydrolytic activities than those from tunicates and green algae, suggesting that the hydrolytic activities were strongly dependent on the cellulose source and their sizes. Following these results, they applied the hydrolytic abilities of CNFs to the decomposition of coat protein of the model virus, filamentous M13 bacteriophage. CNFs could decompose the coat proteins, followed by a drastic decrease in virus' infection capabilities of host cells. Through their work, they anticipated that the CNFs could lead to a novel class of artificial enzymes and called them cellizymes. In a different study, they used CNFs for chirality-specific hydrolytic activities for model amino acid substrates with activated amide bonds (Scheme 1.5a).[159] The resulting chiral specificities significantly correlated with the amino acid species and crystal structures of the CNFs.

In an interesting study, Co (II) was immobilised using its coordination to amine-functionalized nanocellulose to obtain a heterogeneous catalyst for the oxidation of various primary and secondary benzylic alcohols to their corresponding aldehydes and ketones, in o-xylene at room temperature, with good yields and recyclability.[158] A low loading of Co (II) (1.04 wt %) could be afforded because of distribution of cobalt on the nanocelluloses with high surface area. Another heterogeneous catalyst was devised by grafting copper tetrasulfonate phthalocyanine (Cu-PC) onto CNCs for selective aerobic oxidation of benzylic alcohols to corresponding ketones under mild conditions with good yields.[147] The grafting was due to electrostatic interactions and H-bonding between cationic CNC and anionic sulfonate Cu-PC. The system was recyclable up to 7 times and showed no leaching of Cu during the catalysis. Liang *et al.* synthesized mesoporous α-

Fe_2O_3 via sol–gel methods using CNCs as template and studied its photo-catalytic properties.[157] The prepared α- Fe_2O_3 catalyst was used for the photo degradation of methylene blue, and the results revealed that α- Fe_2O_3 on CNC templates had improved photo-catalytic activity than that of samples prepared without CNCs. Liu *et al.* recently designed yet another heterogeneous catalyst using CNCs for cyclopropanation.[146] To prepare the catalyst, the CNCs were synthesized by TEMPO-mediated oxidation of microcrystalline cellulose, transforming the primary hydroxyl groups at C6 position to carboxyl groups. The diRhodium (II) moieties were then anchored on the surface of CNCs by a ligand exchange between $Rh_2(OOCCF_3)_4$ and carboxyl groups to give the CNC-Rh_2 catalyst. Cyclopropanation of styrene with ethyl diazoacetate (Scheme 1.5b) catalyzed by heterogeneous CNC-Rh_2 catalyst at room temperature gave excellent yields. Remarkably, the study also concluded that the contribution of physisorbed $Rh_2(OOCCF_3)_4$ on CNCs to the reaction was negligible in comparison to its covalently immobilized counterpart.

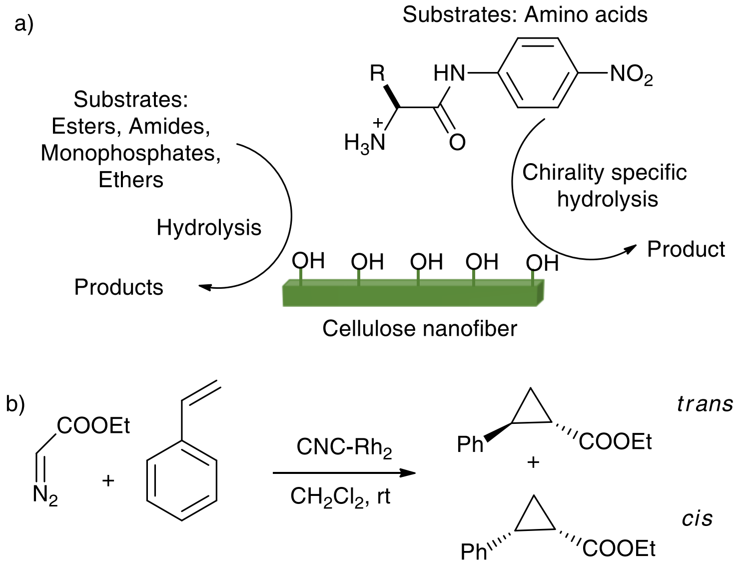

Scheme 1.5 a) Hydrolytic activities of HCl-treated CNFs, and b) Cyclopropanation by the heterogeneous catalyst CNC-Rh_2.

1.7 Conclusion

Nanocelluloses, comprising the whole class of crystalline celluloses in the nano-domain (CNCs, CNFs and bacterial CNFs) have proved to be a versatile support for metal

NPs. Their high surface area, thermal stability, non-toxicity and inexpensiveness provide researchers a sustainable template for metal NPs. Moreover, the hydroxyl groups on its surface has been utilised in the recent years for reducing metal precursors, and hence, opening a greener approach for metal NP synthesis, without the use of any external reducing agents. The metal NP-nanocellulose hybrid composites have found diverse applications in paper, polymer, plastics, chiral templating, flocculants, aerogels, hydrogels, drug delivery, cosmetics, pharmaceutics and catalysis. This review focussed on the role of nanocelluloses in catalysis. The catalysis performed by nanocelluloses has given highly promising results in heterogeneous systems, where the catalysts are recyclable multiple times. Recently, researchers have demonstrated that these nanocelluloses could act as chiral recognition centres in chirality specific hydrolysis of amino acids. Over the years, the characterisation techniques for these nanocelluloses and their modified hybrids have improved. These advances will heavily steer the catalytic applications of nanocelluloses in the coming years.

The following chapter shall demonstrate the work done on the characterisation of CNCs as the first step towards using them for supports in synthesis of metal NPs and their applications in catalysis. After that, the following three chapters focus on the deposition of Pd NP, Ag NP and Ru NP, respectively, and their applications. In each of these work, we prove that the nanocellulose suspensions in water provide us a robust system in which biphasic catalysis can be explored. These suspensions provide an ionic liquid-like environment to the metal NPs and metal salts in them. In end, the thesis concludes by discussing the future perspectives in the use of CNCs.

1.8 References

1. X. M. Dong, T. Kimura, J.-F. Revol and D. G. Gray, *Langmuir*, 1996, **12**, 2076.
2. O. van den Berg, J. R. Capadona and C. Weder, *Biomacromolecules*, 2007, **8**, 1353.
3. S. Beck, J. Bouchard and R. Berry, *Biomacromolecules*, 2012, **13**, 1486.
4. R. F. Nickerson and J. A. Habrle, *Ind. Eng. Chem. Res.*, 1947, **39**, 1507.

5. B. G. Rånby, *Acta Chem. Scand.*, 1949, **3**, 649.
6. B. G. Rånby, *Discuss. Faraday Soc.*, 1951, **11**, 158.
7. I. A. Sacui, R. C. Nieuwendaal, D. J. Burnett, S. J. Stranick, M. Jorfi, C. Weder, E. J. Foster, R. T. Olsson and J. W. Gilman, *ACS Appl. Mater. Interfaces*, 2014, **6**, 6127.
8. S. J. Eichhorn, A. Dufresne, M. Aranguren, N. E. Marcovich, J. R. Capadona, S. J. Rowan, C. Weder, W. Thielemans, M. Roman, S. Renneckar, W. Gindl, S. Veigel, J. Keckes, H. Yano, K. Abe, M. Nogi, A. N. Nakagaito, A. Mangalam, J. Simonsen, A. S. Benight, A. Bismarck, L. A. Berglund and T. Peijs, *Journal of Material Science*, 2009, **45**, 1.
9. Y. Habibi, L. A. Lucia and O. J. Rojas, *Chem. Rev.*, 2010, **110**, 3479.
10. R. J. Moon, A. Martini, J. Nairn, J. Simonsen and J. Youngblood, *Chem. Soc. Rev.*, 2011, **40**, 3941.
11. N. Lin, J. Huang and A. Dufresne, *Nanoscale*, 2012, **4**, 3274.
12. C. Salas, T. Nypelö, C. Rodriguez-Abreu, C. Carrillo and O. J. Rojas, *Curr. Opin. Colloid Interface Sci.*, 2014, **19**, 383.
13. C. Fraschini, G. Chauve, J.-F. L. Berre, S. Ellis, M. Méthot, B. O’Connor and J. Bouchard, *Nordic Pulp and Paper Res. J.* , 2014, **29**, 31.
14. B. S. Brito, F. V. Pereira, J.-L. Putaux and B. Jean, *Cellulose*, 2012, **19**, 1527.
15. M. Lopez, H. Bizot, G. Chambat, M.-F. Marais, A. Zykwinska, M.-C. Ralet, H. Driguez and A. Buléon, *Biomacromolecules*, 2010, **11**, 1417.
16. V. Favier, H. Chanzy and J. Cavaille, *Macromolecules*, 1995, **28**, 6365.
17. M. Le Normand, R. Moriana and M. Ek, *Carbohydr. Polym.*, 2014, **111**, 979.
18. H. A. Silvério, W. P. F. Neto, N. O. Dantas and D. Pasquini, *Industrial Crops and Products*, 2013, **44**, 427.
19. D. Klemm, F. Kramer, S. Moritz, T. Lindström, M. Ankerfors, D. Gray and A. Dorris, *Angew. Chem. Int. Ed.*, 2011, **50**, 5438.
20. G. Morandi, L. Heath and W. Thielemans, *Langmuir*, 2009, **25**, 8280.
21. W. Wu and L. Zhang, *Progress in Chemistry*, 2014, **26**, 403.
22. K. Y. Qiu and A. N. Netravali, *Polymer Reviews*, 2014, **54**, 598.

23. N. Lin, J. Huang and A. Dufresne, *Polysaccharide Nanocrystals‐Based Materials for Advanced Applications*, Wiley-VCH, Weinheim, 2014.
24. M. Roman, *Ind. Biotechnol.*, 2015, **11**, 25.
25. N. Yanamala, M. T. Farcas, M. K. Hatfield, E. R. Kisin, V. E. Kagan, C. L. Geraci and A. A. Shvedova, *ACS Sustainable Chem. Eng.*, 2014, **2**, 1691.
26. K. Kümmerer, J. Menz, T. Schubert and W. Thielemans, *Chemosphere*, 2011, **82**, 1387.
27. T. Kovacs, V. Naish, B. O'Connor, C. Blaise, F. Gagné, L. Hall, V. Trudeau and P. Martel, *Nanotoxicology*, 2010, **4**, 255.
28. S. Kalia, S. Boufi, A. Celli and S. Kango, 2014, **292**, 5.
29. R. H. Marchessault, F. F. Morehead and N. M. Walter, *Nature*, 1959, **184**, 632.
30. J.-F. Revol, L. Godbout, X.-M. Dong, D. G. Gray, H. Chanzy and G. Maret, *Liq. Cryst.*, 1994, **16**, 127.
31. J. F. Revol, H. Bradford, J. Giasson, R. H. Marchessault and D. G. Gray, *Int. J. Biol. Macromol.*, 1992, **14**, 170.
32. K. E. Shopsowitz, H. Qi, W. Y. Hamad and M. J. MacLachlan, *Nature*, 2010, **468**, 422.
33. J. A. Kelly, K. E. Shopsowitz, J. M. Ahn, W. Y. Hamad and M. J. MacLachlan, *Langmuir*, 2012, **28**, 17256.
34. K. E. Shopsowitz, J. A. Kelly, W. Y. Hamad and M. J. MacLachlan, *Adv. Funct. Mater.*, 2014, **24**, 327.
35. H. Qi, K. E. Shopsowitz, W. Y. Hamad and M. J. MacLachlan, *J. Am. Chem. Soc.*, 2011, **133**, 3728.
36. K. E. Shopsowitz, W. Y. Hamad and M. J. MacLachlan, *Angew. Chem. Int. Ed.*, 2011, **50**, 10991.
37. D. Zhang and L. Qi, *Chem. Commun.*, 2005, **41**, 2735.
38. Y. Shin and G. J. Exarhos, *Mater. Lett.*, 2007, **61**, 2594.
39. A. Ivanova, D. Fattakhova-Rohlfing, B. E. Kayaalp, J. Rathouský and T. Bein, *J. Am. Chem. Soc.*, 2014, **136**, 5930.
40. A. Querejeta-Fernández, G. Chauve, M. Methot, J. Bouchard and E. Kumacheva, *J. Am. Chem. Soc.*, 2014, **136**, 4788.

41. M. G. Campbell, Q. Liu, A. Sanders, J. S. Evans and Smalyukh, II, *Materials*, 2014, **7**, 3021.
42. V. Favier, G. Canova, J. Cavaillé, H. Chanzy, A. Dufresne and C. Gauthier, *Polym. Adv. Technol.*, 1995, **6**, 351.
43. A. Dufresne, *Can. J. Chem.*, 2008, **86**, 484.
44. J. Yang, C.-R. Han, J.-F. Duan, M.-G. Ma, X.-M. Zhang, F. Xu, R.-C. Sun and X.-M. Xie, *J. Mater. Chem.*, 2012, **22**, 22467.
45. X. Yang and E. D. Cranston, *Chem. Mater.*, 2014, **26**, 6016.
46. H. Dong, J. F. Snyder, D. T. Tran and J. L. Leadore, *Carbohydr. Polym.*, 2013, **95**, 760.
47. Y. Liu, Y. Li, G. Yang, X. Zheng and S. Zhou, *ACS Appl. Mater. Interfaces*, 2015, **7**, 4118.
48. S. Eyley, S. Shariki, S. E. C. Dale, S. Bending, F. Marken and W. Thielemans, *Langmuir*, 2012, **28**, 6514.
49. K. H. M. Kan, J. Li, K. Wijesekera and E. D. Cranston, *Biomacromolecules*, 2013, **14**, 3130.
50. S. Eyley, D. Vandamme, S. Lama, G. Van den Mooter, K. Muylaert and W. Thielemans, *Nanoscale*, 2015, **7**.
51. M. Jorfi and E. J. Foster, *J. Appl. Polym. Sci.*, 2015, **132**, 41719.
52. V. Incani, C. Danumah and Y. Boluk, *Cellulose*, 2013, **20**, 191.
53. A. Isogai, *Journal of Wood Science*, 2013, **59**, 449.
54. M. Giese, L. K. Blusch, M. K. Khan and M. J. MacLachlan, *Angew. Chem. Int. Ed.*, 2015, **54**, 2888.
55. H. Wei, K. Rodriguez, S. Renneckar and P. J. Vikesland, *Environ. Sci. Nano*, 2014, **1**, 302.
56. J. Huang, P. R. Chang and A. Dufresne, *Polysaccharide Nanocrystals: Current Status and Prospects in Material Science*, Wiley-VCH, Weinheim, 2014.
57. F. Hu, S. Fu, J. Huang, D. P. Anderson and P. R. Chang, *Structure and Properties of Polysaccharide Nanocrystals*, Wiley-VCH, Weinheim, 2014.
58. Y. Habibi, *Chem. Soc. Rev.*, 2014, **43**, 1519.
59. S. Eyley and W. Thielemans, *Nanoscale*, 2014, **6**, 7764.

60. K. Missoum, M. N. Belgacem and J. Bras, *Materials*, 2013, **6**, 1745.
61. E. Lam, K. B. Male, J. H. Chong, A. C. W. Leung and J. H. T. Luong, *Trends Biotechnol.*, 2012, **30**, 283.
62. H. Khalil, A. H. Bhat and A. F. I. Yusra, *Carbohydr. Polym.*, 2012, **87**, 963.
63. E. C. Ramires and A. Dufresne, *TAPPI Journal*, 2011, **10**, 9.
64. S. J. Eichhorn, *Soft Matter*, 2011, **7**, 303.
65. S. Padalkar, J. R. Capadona, S. J. Rowan, C. Weder, Y.-H. Won, L. A. Stanciu and R. J. Moon, *Langmuir*, 2010, **26**, 8497.
66. P. Lu and Y.-L. Hsieh, *Carbohydr. Polym.*, 2010, **82**, 329.
67. M. A. S. Azizi Samir, F. Alloin and A. Dufresne, *Biomacromolecules*, 2005, **6**, 612.
68. H. Charreau, M. L Foresti and A. Vazquez, *Recent patents on nanotechnology*, 2013, **7**, 56.
69. D. J. Cole-Hamilton and R. P. Tooze, *Catalyst separation, recovery and recycling: chemistry and process design*, Springer, The Netherlands, 2006.
70. D. J. Cole-Hamilton, 2003, **299**, 1702.
71. J. Dupont, G. S. Fonseca, A. P. Umpierre, P. F. Fichtner and S. R. Teixeira, 2002, **124**.
72. L. Heux, G. Chauve and C. Bonini, *Compos. Interfaces*, 2000, **16**, 8210.
73. S. Elazzouzi-Hafraoui, Y. Nishiyama, J.-L. Putaux, L. Heux, F. Dubreuil and C. Rochas, *Biomacromolecules*, 2008, **9**, 57.
74. P. Lu and Y.-L. Hsieh, *Carbohydr. Polym.*, 2012, **87**, 564.
75. N. Johar, I. Ahmad and A. Dufresne, *Industrial Crops and Products*, 2012, **37**, 93.
76. M. S. Peresin, Y. Habibi, J. O. Zoppe, J. J. Pawlak and O. J. Rojas, *Biomacromolecules*, 2010, **11**, 674.
77. Y. Habibi, A.-L. Goffin, N. Schiltz, E. Duquesne, P. Dubois and A. Dufresne, *J. Mater. Chem.*, 2008, **18**, 5002.
78. A. Junior de Menezes, G. Siqueira, A. A. S. Curvelo and A. Dufresne, *Polymer*, 2009, **50**, 4552.
79. N. L. Garcia de Rodriguez, W. Thielemans and A. Dufresne, *Cellulose*, 2006, **13**, 261.

80. N. Duran, A. Paula Lemes and A. B Seabra, *Recent patents on nanotechnology*, 2012, **6**, 16.
81. J. Araki, M. Wada, S. Kuga and T. Okano, *Journal of Wood Science*, 1999, **45**, 258.
82. D. Bondeson, A. Mathew and K. Oksman, *Cellulose*, 2006, **13**, 171.
83. R. J. M. Michael T. Postek, Alan W. Rudie, Michael A. Bilodeau, *Production and Applications of Cellulose Nanomaterials*, Technical Association of Pulp and Paper Industry, TAPPI, Peachtree Corners, GA, August 01, 2013.
84. J. R. Capadona, K. Shanmuganathan, S. Trittschuh, S. Seidel, S. J. Rowan and C. Weder, *Biomacromolecules*, 2009, **10**, 712.
85. F. Kimura, T. Kimura, M. Tamura, A. Hirai, M. Ikuno and F. Horii, *Langmuir*, 2005, **21**, 2034.
86. M. N. Anglès and A. Dufresne, *Macromolecules*, 2000, **33**, 8344.
87. M. Roman and W. T. Winter, *Biomacromolecules*, 2004, **5**, 1671.
88. M. Grunert and W. T. Winter, *J. Polym. Environ.*, 2002, **10**, 27.
89. J. Araki and S. Kuga, *Langmuir*, 2001, **17**, 4493.
90. Technical Association of Pulp and Paper Industries (TAPPI), www.tappi.org.
91. D. Astruc, *Nanoparticles and catalysis*, John Wiley & Sons, 2008.
92. Z. Shi, J. Tang, L. Chen, C. Yan, S. Tanvir, W. A. Anderson, R. M. Berry and K. C. Tam, *J. Mater. Chem. B*, 2015, **3**, 603.
93. F. Hoeng, A. Denneulin, C. Neuman and J. Bras, *J. Nanopart. Res.*, 2015, **17**, 1.
94. A. R. Lokanathan, K. M. A. Uddin, O. J. Rojas and J. Laine, *Biomacromolecules*, 2014, **15**, 373.
95. M. S. Wang, F. Jiang, Y. L. Hsieh and N. Nitin, *J. Mater. Chem. B*, 2014, **2**, 6226.
96. R. Xiong, C. Lu, W. Zhang, Z. Zhou and X. Zhang, *Carbohydr. Polym.*, 2013, **95**, 214.
97. G. Yang, J. Xie, F. Hong, Z. Cao and X. Yang, *Carbohydr. Polym.*, 2012, **87**, 839.
98. G. Yang, J. Xie, Y. Deng, Y. Bian and F. Hong, *Carbohydr. Polym.*, 2012, **87**, 2482.
99. H. Liu, J. Song, S. Shang, Z. Song and D. Wang, *ACS Appl. Mater. Interfaces*, 2012, **4**, 2413.

100. H. Liu, D. Wang, Z. Song and S. Shang, *Cellulose*, 2011, **18**, 67.
101. N. Drogat, R. Granet, V. Sol, A. Memmi, N. Saad, C. Klein Koerkamp, P. Bressollier and P. Krausz, *J. Nanopart. Res.*, 2011, **13**, 1557.
102. I. Diez, P. Eronen, M. Osterberg, M. B. Linder, O. Ikkala and R. H. Ras, *Macromolecular Bioscience*, 2011, **11**, 1185.
103. H. S. Barud, T. Regiani, R. F. Marques, W. R. Lustri, Y. Messaddeq and S. J. Ribeiro, *Journal of Nanomaterials*, 2011, **2011**, 1.
104. L. Maria, A. L. Santos, P. C. Oliveira, A. S. Valle, H. S. Barud, Y. Messaddeq and S. J. Ribeiro, *Polimeros*, 2010, **20**, 72.
105. S. Ifuku, M. Tsuji, M. Morimoto, H. Saimoto and H. Yano, *Biomacromolecules*, 2009, **10**, 2714.
106. P. A. Marques, H. I. Nogueira, R. J. Pinto, C. P. Neto and T. Trindade, *J. Raman Spectrosc.*, 2008, **39**, 439.
107. W. Hu, S. Chen, X. Li, S. Shi, W. Shen, X. Zhang and H. Wang, *Mater. Sci. Eng., C*, 2009, **29**, 1216.
108. Y. Shin, I.-T. Bae, B. W. Arey and G. J. Exarhos, *J. Phys. Chem. C*, 2008, **112**, 4844.
109. S. Azizi, M. B. Ahmad, M. Z. Hussein and N. A. Ibrahim, *Molecules*, 2013, **18**, 6269.
110. R. J. Pinto, P. A. Marques, M. A. Martins, C. P. Neto and T. Trindade, *J. Colloid Interface Sci.*, 2007, **312**, 506.
111. X. Li, S. Chen, W. Hu, S. Shi, W. Shen, X. Zhang and H. Wang, *Carbohydr. Polym.*, 2009, **76**, 509.
112. C. Tian, S. Fu and L. A. Lucia, *Cellulose*, 2015, **22**, 1.
113. L. Chen, R. M. Berry and K. C. Tam, *ACS Sustainable Chem. Eng.*, 2015, **2**, 951.
114. Y. Shin, I.-T. Bae, B. W. Arey and G. J. Exarhos, *Mater. Lett.*, 2007, **61**, 3215.
115. K. Benaissi, L. Johnson, D. A. Walsh and W. Thielemans, *Green Chem.*, 2010, **12**, 220.
116. Y. Shin, J. M. Blackwood, I.-T. Bae, B. W. Arey and G. J. Exarhos, *Mater. Lett.*, 2007, **61**, 4297.

117. C. Schütz, J. Sort, Z. Bacsik, V. Oliynyk, E. Pellicer, A. Fall, L. Wågberg, L. Berglund, L. Bergström and G. Salazar-Alvarez, *PLoS ONE*, 2012, **7**, 45828.
118. B. R. Evans, H. M. O'Neill, V. P. Malyvanh, I. Lee and J. Woodward, *Biosens. Bioelectron.*, 2003, **18**, 917.
119. B. Ramaraju, T. Imae and A. G. Destaye, *Applied Catalysis a-General*, 2015, **492**, 184.
120. M. Gopiraman, H. Bang, G. Yuan, C. Yin, K.-H. Song, J. S. Lee, I. M. Chung, R. Karvembu and I. S. Kim, *Carbohydr. Polym.*, 2015, **132**, 554.
121. M. Schlesinger, M. Giese, L. K. Blusch, W. Y. Hamad and M. J. MacLachlan, *Chem. Commun.*, 2015, **51**, 530.
122. O. Eisenhut and E. Kuhn, *Angew. Chem.*, 1942, **55**, 198.
123. E. Lam, S. Hrapovic, E. Majid, J. H. Chong and J. H. T. Luong, *Nanoscale*, 2012, **4**, 997.
124. H. Koga, E. Tokunaga, M. Hidaka, Y. Umemura, T. Saito, A. Isogai and T. Kitaoka, *Chem. Commun.*, 2010, **46**, 8567.
125. T. Zhang, W. Wang, D. Zhang, X. Zhang, Y. Ma, Y. Zhou and L. Qi, *Adv. Funct. Mater.*, 2010, **20**, 1152.
126. W. Wang, H. Y. Li, D. W. Zhang, J. Jiang, Y. R. Cui, S. Qiu, Y. L. Zhou and X. X. Zhang, *Electroanalysis*, 2010, **22**, 2543.
127. P. Zhou, H. Wang, J. Yang, J. Tang, D. Sun and W. Tang, *Ind. Eng. Chem. Res.*, 2012, **51**, 5743.
128. Z. H. Zhou, C. H. Lu, X. D. Wu and X. X. Zhang, *RSC Adv.*, 2013, **3**, 26066.
129. A. Azetsu, H. Koga, A. Isogai and T. Kitaoka, *Catalysts*, 2011, **1**, 83.
130. D. Sun, J. Yang, J. Li, J. Yu, X. Xu and X. Yang, *Appl. Surf. Sci.*, 2010, **256**, 2241.
131. C. M. Cirtiu, A. F. Dunlop-Brière and A. Moores, *Green Chem.*, 2011, **13**, 288.
132. M. Kaushik, K. Basu, C. Benoit, C. C. M., H. Vali and A. Moores, *J. Am. Chem. Soc.*, 2015, **137**, 6124.
133. M. Kaushik, H. M. Friedman, M. Bateman and A. Moores, *RSC Adv.*, 2015, **5**, 53207.

134. J. Tang, Z. Shi, R. M. Berry and K. C. Tam, *Ind. Eng. Chem. Res.*, 2015, **54**, 3299.

135. L. Chen, W. Cao, P. J. Quinlan, R. M. Berry and K. C. Tam, *ACS Sustainable Chem. Eng.*, 2015, **3**, 978.

136. J.-L. Huang, D. G. Gray and C.-J. Li, *Beilstein J. Org. Chem.*, 2013, **9**, 1388.

137. L. Johnson, W. Thielemans and D. A. Walsh, *J. Mater. Chem.*, 2010, **20**, 1737.

138. X. D. Wu, C. H. Lu, Z. H. Zhou, G. P. Yuan, R. Xiong and X. X. Zhang, *Environ. Sci. Nano*, 2014, **1**, 71.

139. X. Wu, C. Lu, W. Zhang, G. Yuan, R. Xiong and X. Zhang, *J. Mater. Chem. A*, 2013, **1**, 8645.

140. M. Rezayat, R. K. Blundell, J. E. Camp, D. A. Walsh and W. Thielemans, *ACS Sustainable Chem. Eng.*, 2014, **2**, 1241.

141. X. B. Lin, M. Wu, D. Y. Wu, S. Kuga, T. Endo and Y. Huang, *Green Chem.*, 2011, **13**, 283.

142. L. Johnson, W. Thielemans and D. A. Walsh, *Green Chem.*, 2011, **13**, 1686.

143. P. Dhar, A. Kumar and V. Katiyar, *Cellulose*, 2015.

144. M. Kaushik, W. C. Chen, T. G. M. van de Ven and A. Moores, *Nordic Pulp and Paper Res. J.* , 2014, **29**, 77.

145. M. Kaushik, J.-L. Putaux, C. Fraschini, G. Chauve and A. Moores, in *The Transmission Electron Microscope*, ed. M. Khan, Intech, 2015, ch. Transmission Electron Microscopy for the Characterization of Cellulose Nanocrystals, pp. 129-163.

146. J. Liu, A. Plog, P. Groszewicz, L. Zhao, Y. Xu, H. Breitzke, A. Stark, R. Hoffmann, T. Gutmann and K. Zhang, *Chem. Eur. J.*, 2015, **21**, 12414.

147. P. Chauhan and N. Yan, *RSC Adv.*, 2015, **5**, 37517.

148. M. Kaushik, A. Y. Li, R. Hudson, M. Masnadi, C.-J. Li and A. Moores, *Green Chem.*, 2015.

149. D. Astruc, F. Lu and J. R. Aranzaes, *Angew. Chem. Int. Ed.*, 2005, **44**, 7852.

150. J. Yang, D. Sun, J. Li, X. Yang, J. Yu, Q. Hao, W. Liu, J. Liu, Z. Zou and J. Gu, *Electrochim. Acta*, 2009, **54**, 6300.

151. W. Wang, T. J. Zhang, D. W. Zhang, H. Y. Li, Y. R. Ma, L. M. Qi, Y. L. Zhou and X. X. Zhang, *Talanta*, 2011, **84**, 71.
152. K. A. Mahmoud, K. B. Male, S. Hrapovic and J. H. T. Luong, *ACS Appl. Mater. Interfaces*, 2009, **1**, 1383.
153. J. Yang, J. Yu, J. Fan, D. Sun, W. Tang and X. Yang, *J. Hazard. Mater.*, 2011, **189**, 377.
154. R. Bendi and T. Imae, *RSC Adv.*, 2013, **3**, 16279.
155. D. Sun, J. Yang and X. Wang, *Nanoscale*, 2010, **2**, 287.
156. S. Eyley and W. Thielemans, *Chem. Commun.*, 2011, **47**, 4177.
157. H. Liang, K. Liu and Y. Ni, *Mater. Lett.*, 2015, **159**, 218.
158. A. Shaabani, S. Keshipour, M. Hamidzad and M. Seyyedhamzeh, *J. Chem. Sci.*, 2014, **126**, 111.
159. T. Serizawa, T. Sawada and M. Wada, *Chem. Commun.*, 2013, **49**, 8827.
160. T. Serizawa, T. Sawada, H. Okura and M. Wada, *Biomacromolecules*, 2013, **14**, 613.

2 Characterisation of cellulose nanocrystals by transmission electron microscopy

Visualisation of CNCs and the metal-hybrid composites of CNCs is vital for characterisation while applying them for catalysis. Imaging CNCs by transmission electron microscopy (TEM) is challenging, as they are susceptible to electron beam damage because of their reduced electron density as compared to the metal nanoparticles. Therefore, the first part of the research focussed on standardisation of the preparation of TEM samples and microscopic techniques.

This chapter is adapted from a published article, whose citation appear below, which is reprinted with permission from the Nordic Pulp and Paper Journal and all co-authors.

Madhu Kaushik, Wei C. Chen, Theo G. M. van de Ven and Audrey Moores. An improved methodology for imaging cellulose nanocrystals by transmission electron microscopy. *Nord. Pulp Pap. Res. J.* 2014, 29, 77-81.

Note: In addition to this work, a review was written on the use of transmission electron microscopy for the characterisation of CNCs, which was published as a book chapter, whose citation appears below. Due to its length, this book chapter appears as an appendix at the end of the thesis..

Madhu Kaushik, Jean-Luc Putaux, Carole Fraschini, Gregory Chauve and Audrey Moores, in The Transmission Electron Microscope, Intech, 2015, ch. Transmission Electron Microscopy for the Characterization of Cellulose Nanocrystals, Published September 2015, (http://www.intechopen.com/books/the-transmission-electron-microscope-theory-and-applications/transmission-electron-microscopy-for-the-characterization-of-cellulose-nanocrystals)

2.1 Abstract

Although transmission electron microscopy (TEM) is a method of choice for the analysis of cellulose nanocrystals (CNCs), it is still a challenging technique to use due to the low electron density and aggregation issues associated with this material. This work presents a robust and reproducible method to image CNCs by TEM, without the need for staining. It is demonstrated that low pH and hydrophilic TEM grids favored high dispersion of the sample for optimal imaging. Electron beam and voltage settings are also discussed. Three distinct types of CNCs are analyzed: never-dried, freeze-dried and spray-dried CNCs. Although a few reports accounted for mushroom structures, we demonstrate herein that, regardless of the sample history, this nanomaterial is always rod-shaped. The rods were measured to be 9.7 ± 4.4 nm in width and 216 ± 82 nm in length. By dismissing the use of heavy metal staining, multi-component systems, for instance, palladium nanoparticles onto CNCs, could be imaged by TEM.

2.2 Introduction

Cellulose Nanocrystals (CNCs) are derived from the renewable polymer, cellulose, through acid hydrolysis by concentrated sulphuric acid, first reported by Ranby.[1] This material has well-defined size and morphology,[2] high specific surface area,[3] high aspect ratio, high crystalline order and chirality, superior mechanical strength, and controllable surface chemistry.[4] In addition, CNCs are relatively cheap, renewable, biodegradable, non-toxic,[5, 6] and accessible industrially in large scale. These properties of CNCs have made them applicable in diverse fields, for example, production of iridescent and birefringent films,[7] reinforcing fillers in plastics and polymers,[4, 8, 9] support for nanoparticles,[10, 11] and paper, food, cosmetic and pharmaceutical industry.[4] The knowledge of exact size and morphology of CNCs plays a very important role in the development of all these applications. In addition, the development of several processes for the production of CNCs (*vide infra*), calls for a systematic and robust method of analyzing these properties.[2] Scanning electron microscopy (SEM), transmission electron microscopy (TEM) and atomic force microscopy (AFM) are the classical techniques used to determine the shape and size of these nanocrystals. In this context, TEM offers several advantages: its resolution is well adapted for the imaging of CNCs, it is a milder technique than SEM in terms of flux of electrons received by the sample, it allows visualization of individual particles, and the sampling techniques are easy, reproducible, and tunable depending on the selected TEM grids. However, despite the ubiquitous use of TEM for CNC characterization, there are still challenges associated with its use. This paper proposes a straightforward method of imaging CNCs by TEM, without staining. In doing so, we explored the properties of CNCs in terms of drying process, of pH, and functionalization, and demonstrated that the size and shape of CNCs are robust features.

CNCs, being organic matter, are not as electron dense as metal nanoparticles, and are susceptible to burning upon long electron beam exposure. Hence, TEM imaging of CNCs has often involved negative staining with uranyl acetate,[12] a relatively expensive and toxic heavy metal salt.[13] Staining poses aggregation problem in the drying step. In addition, when characterizing CNC-containing hybrid structures (for instance CNC-supported metal nanoparticles), staining interferes with accurate image analysis.[10] A few unstained images have been reported in the past, but they suffered from poor contrast and no systematic method has been reported.

Herein, we report a method for taking TEM images of CNCs in detail, covering various aspects of ascertaining high quality images, such as method of preparation of TEM grids, dispersion of CNCs on the grid, types of TEM grids used, low dose versus high resolution (HR) TEM, and preventing damage to the CNC sample under electron beam while using a high resolution and/or high voltage TEM. This work also looks into morphology differences depending on the drying method. The size and morphology of this biopolymer depends on the source of cellulose and method of preparation, where the key conditions include: the type and concentration of the acid used for hydrolysis, reaction time and temperature, and method of drying.[2, 4] The usual methods of drying[14] used for the preparation of CNCs are: (1) oven drying, (2) freeze drying (FD), (3) supercritical drying (SCD), and (4) spray-drying (SD). It has been reported that freeze-dried CNCs are fibre/rod-like whereas spray-dried CNCs are spherical or mushroom shaped.[14-17] We investigated in detail TEM sampling and imaging for CNC samples with distinct drying history. We compared never-dried samples (samples that were not dried after synthesis), spray-dried and freeze-dried samples. We demonstrated that all samples possess the same nanorod morphology, provided they are dispersed properly.

2.3 Materials and methods

2.3.1 Materials and equipments

Never-dried CNCs were prepared from wood pulps (Q90 and bHKP, FPInnovations). FPInnovations also provided dried CNC samples: freeze-dried and spray-dried, the freeze-drying or spray-drying process being performed by FPinnovations. No further treatment was performed before imaging on these samples, unless specified otherwise. For the manipulation of pH, hydrochloric acid (0.01M) was provided by Fluka Analytical. To redisperse dried CNC samples in suspension, the Sonics & Materials Inc. Vibra-Cell VC1500 ultrasonicator (220V, 15A, 1500W, 20 kHz) was used. The Metrohm Titrando (836 base, 804 Ti stand, and 802 stirrer) autotitrator was used for attaining various pH values. The transmission electron microscopy (TEM) samples were deposited on 400 mesh copper grids coated with silicon monoxide, formvar, and carbon. All three were supplied by Electron Microscopy Sciences. The analyses were performed on the Tecnai 12 microscope (FEI electron optics) equipped with a Lab6 filament at 120kV, equipped with Gatan 792 Bioscan 1k x 1k Wide Angle Multiscan CCD Camera (Gatan Inc.); and FEI G2 F20 Cryo-S/TEM microscope (FEI, Inc) at 200kV, equipped with Gatan Ultrascan 4k x 4k Digital (CCD) Camera System at different magnifications corresponding to different pixel size (defocus level ranging from − 2.5 to − 4.5 μm). High pressure reactions were performed on Parr Instrument 5000 Series Multiple Reactor System.

2.3.2 Preparation of CNCs for never-dried samples

Based on the method developed by Dong et al.,[18] CNCs were prepared from wood pulp. A 500 mL aqueous solution of H_2SO_4 (60% w/w) was preheated to 45ºC and stirred with an overhead rotating paddle at 200 RPM. To this solution, a 100 mL suspension of Q90 and bHKP wood pulp (obtained as wet pulp samples from the manufacturer) at a 1:1 volume ratio were added. After 60 minutes, the suspension turned beige in colour. To quench this reaction, 1 L of water was added. By centrifugation, the supernatant was removed and more fresh water was added to repeat the washing. After four washings by centrifugation, the sediments became more loosely packed. At this stage, the sediments were collected and dialyzed with deionised water for 5 days under constant stirring. The resulting suspension was cast into films and weighed to determine the concentration of CNCs in water.

2.3.3 Sample preparation for TEM imaging

In the case of never-dried CNCs, the samples were already suspended in water. As for freeze-dried and spray-dried CNCs, samples were weighed and mixed with a known amount of deionised water. All three types of CNCs were dispersed uniformly in water by ultrasonication at 60% output, for about 20-25 seconds, until turbidity was visibly reduced and no macroscopic particles could be seen. Their concentrations ranged between 0.1% w/w and 0.3% w/w. The samples were either used as is (pH 5-6) or the pH of the samples was set to 3.5 by autotitration. One drop of each sample was then deposited onto either a carbon, formvar, or silicon monoxide coated grid. After 1 minute, the water drop was removed by dabbing with a tissue paper. CNC single rod size was determined by manually measuring 1000 single rods with the help of imageJ software (version 1.48e). For comparison purposes, never-dried CNCs at pH 3.5 were stained with uranyl acetate and imaged. The staining was done according to the protocols already available in the literature.[19]

2.3.4 Synthesis of Pd nanoparticles onto CNCs (PdNPs@CNCs)

This method was adapted from Cirtiu *et.al*.[10] A suspension of 500 mg of CNCs in 50 mL HCl solution at pH 2 was mixed with 50 mL of saturated $PdCl_2$ acidic solution (pH adjusted to 2 with dilute HCl). The mixture was stirred for 10 min to homogenize the suspension. The final concentration of $PdCl_2$ was 0.75×10^{-3} M, while the CNC concentration in the mixture was 0.5% w/w. Then, the mixture was placed under 4 bars of hydrogen gas for 2 hours at room temperature to obtain PdNPs@CNCs.

2.3.5 Low dose and high resolution transmission electron microscopy

The low dose and high resolution (HR-TEM) transmission electron microscopy were carried out on FEI G2 F20 Cryo-STEM microscope (FEI, Inc) at 200 kV. At this high voltage, the CNCs are more prone to damage by the electron beam. Therefore, it is advisable to use the microscope at low dose TEM for organic polymers. Low-dose imaging is carried out by locating an area of interest on the grid surface and determining the appropriate focus without significantly exposing the location to be imaged to high electron beam. This microscope has preinstalled low dose software, which was used to get the TEM image of freeze-dried CNCs on carbon grid at pH 5-6. An image with good focus and contrast can also be achieved without using the low dose software. Using the HR-TEM, the intensity of the electron beam was lowered to reduce the number of electrons striking the sample and the objective aperture was reduced from 100 to 40, to get a better contrast, where necessary, for some of the samples.

2.4 Results

For this work, we imaged CNCs while varying the following parameters: drying history, pH of the suspension and TEM grids. CNC suspensions were synthesized in the lab, sampled directly and referred to as “never-dried”. Freeze-dried and spray-dried CNCs were ordered from FPinnovations and resuspended prior to sampling. All our TEM observations are summarized in Table 2.1.

Grid type	**Carbon grid**		**Formvar grid**		**Silicon monoxide Grid**	
pH	**3.5**	**5-6**	**3.5**	**5-6**	**3.5**	**5-6**
Never-dried	Single rods and small clusters	A few single rods and many clusters	Small clusters	Dense aggregates, clambered together	Mostly single rods	Many rods and rod bundles
Spray-dried	Few single rods and many aggregated bundles	Aggregated bundles/clusters	CNCs clumped together to form mushroom-like aggregates	CNCs clumped together to form mushroom-like aggregates	Mostly single rods	Clusters, not very thick
Freeze-dried	Small clusters, very few single rods	Mostly large clusters	Dense aggregates, clambered together	Dense aggregates, clambered together	Small clusters of rods	Small clusters of rods

Table 2.1 Summary of results from TEM images of CNCs depending on sample type, grid type and pH.

2.4.1 Optimization of dispersion conditions for TEM imaging: pH and grid type

In a first step, optimization of imaging conditions was performed on never-dried CNCs samples. Their pH values ranged between 5 and 6. At this pH and concentration, TEM images feature individual rods and aggregated ones (Figure 2.1 Never-dried sample on carbon grid: Top at pH 5-6; Bottom at pH 3.5, Table 2.1). In order to improve dispersion, the pH was lowered to 3.5 using dilute hydrochloric acid (0.01N). The larger aggregates came apart, smaller bundles were observed and individual CNCs could be seen in larger proportion.

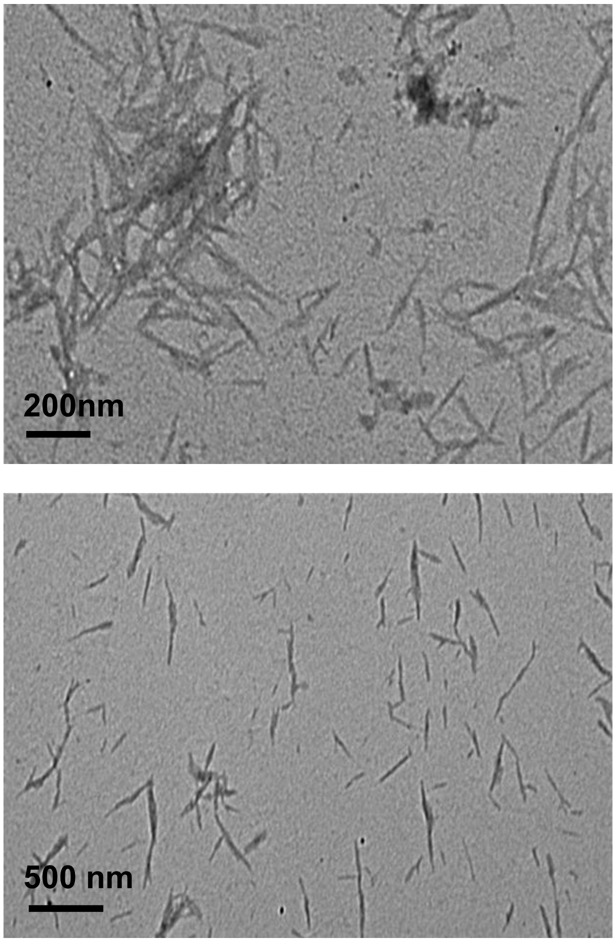

Figure 2.1 Never-dried sample on carbon grid: Top at pH 5-6; Bottom at pH 3.5

CNCs were also imaged using three different types of grid coating: carbon, formvar and silicon monoxide. Imaging was impacted by this parameter as well. The formvar grids have a hydrophobic surface. With them, single rods came together in large aggregates and were no longer observable individually. On the carbon grid, dispersion improved. On the hydrophilic silicon monoxide coated grids, the dispersion was maximized. Figure 2.1 and Figure 2.2 compares never-dried CNCs at pH 5-6 on the three types of grids and clearly show this trend.

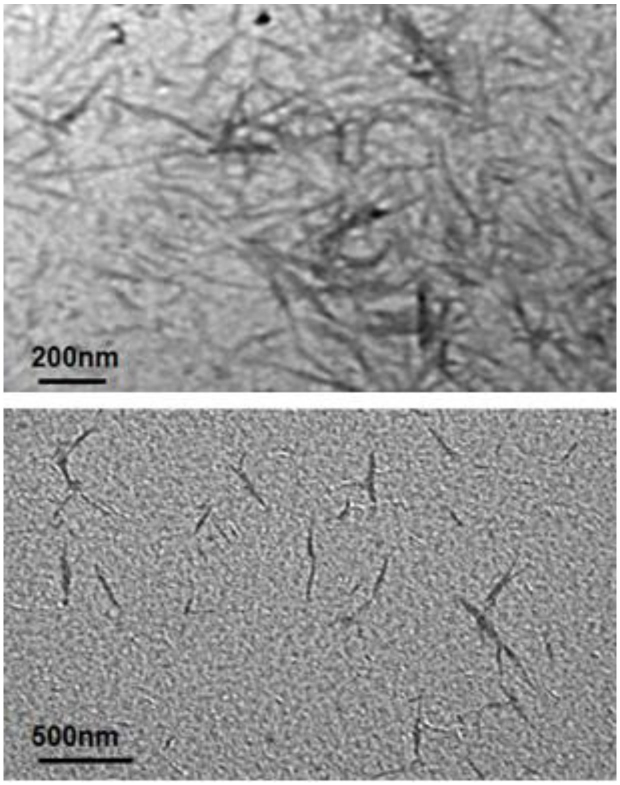

Figure 2.2 Never-dried CNCs at pH 5-6: on formvar grid (top); silicon monoxide grid (bottom).

Figure 2.3 summarizes the size distribution, in length and in width, of the CNC bundles/rod of never-dried CNCs at pH 3.5 on different type of grids, based on manual counting of 200 particles of each type. Their average length and width is provided in Table 2.2. Both histograms and average values show a clear trend: the more hydrophilic the grid, the smaller the particles measured, both in length and in width. For instance, silicon monoxide grids featured a CNC length of 149 nm, while this value is 211 for carbon coated ones and 250 for formvar. The trend is even more pronounced for CNC width with values of 5.2, 8.8 and 19.1 nm for silicon monoxide, carbon and formvar coating respectively. This is consistent with the fact that bundles composed of a small number of CNC rods are more numerous in a hydrophobic environment. This phenomenon is more visible when looking at the CNC width compared to length, because high aspect ratio CNCs favorably aggregate laterally.

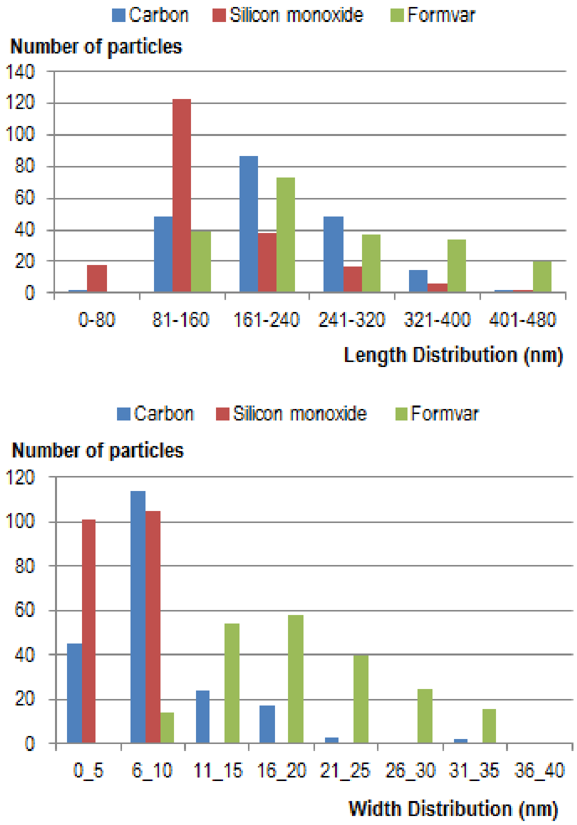

Figure 2.3 Length and width distribution of CNCs bundles/rod of never-dried CNCs at pH 3.5 on different type of grids, based on the counting of 200 particles on each type of grid.

To compare our methodology with the earlier methods of staining and then imaging the CNCs, we also counted approximately 200 single rods after staining the never-dried CNCs at pH 3.5 on carbon grid. TEM images and a histogram for size distribution in this case have been included in the appendix (Figure 2.9 to Figure 2.16). The average width and length came out to be 9.1 ± 3.2 nm and 248 ± 72 nm, respectively. These values are comparable, but both higher than the values obtained in this article without staining (Table 2.2). Also, in stained samples, we observed more large clusters than unstained samples, confirming that staining favors aggregation.

2.4.2 The impact of CNC drying history on TEM imaging

Figure 2.4 compares the never-dried, freeze-dried and spray-dried samples on carbon grid, at pH 5-6. Never-dried samples exhibited the best dispersion. Single rods were observed in all three types of CNCs. Never-dried CNCs had more of the single rods than the others.

Table 2.2 Average length and width of CNC bundles/rod of never-dried samples at pH 3.5 on different type of grids, based on the counting of 200 particles on each type of grid.

CNCs	**Carbon grid**	**Silicon Monoxide grid**	**Formvar grid**
Length	211 ± 70 nm	149 ± 73 nm	250 ± 100 nm
Width	8.8 ± 5.5 nm	5.2 ± 1.6 nm	19.1 ± 6.4 nm

On Figure 2.4 we compared the typical width of the bundles observed in the three samples, as a measure of aggregation. These values are characteristic of what we observed over analysis of dozens of images. Spray-dried CNCs, with a typical CNCs bundle width of 168 nm featured a much enhanced aggregation behavior than both never-dried (29 nm) and freeze-dried (33 nm). This conclusion is actually consistent with the fact that spray-dried CNCs revealed to be more difficult to disperse than freeze-dried or never-dried counterparts. In general, spray-dried CNC suspensions were allowed to be redispersed at room temperature for more than a week before being imaged. Increasing ultrasonication times prior to sampling did not improve dispersion of these samples, demonstrating that drying history impacted irreversibly the dispersion properties of CNCs. These results are also consistent with the work done by Beck *et al.*[20] where they observe difference in aggregate sizes due to the different drying history of CNCs.

Upon varying the sampling conditions and samples, we did observe one other kind of structure, entirely different from the rods or rod bundles discussed above (Figure 2.5, Table 2.1). It looked like patches, of between 100 to 200 nm in size, with a much higher contrast than the rods. This type of morphology was exclusively observed when we used spray-dried samples. It happened on formvar grids, or on carbon grids when the dispersion was not complete, namely when the suspensions were prepared only a day before sampling and not a week. Note that if silicon monoxide coated grids were used instead of formvar coated grids, the spray-dried CNCs were always observed to be rod-like. These results are consistent with the idea that the patches are constituted of dense pockets of CNCs brought together during the drying process on the grid. Formvar is

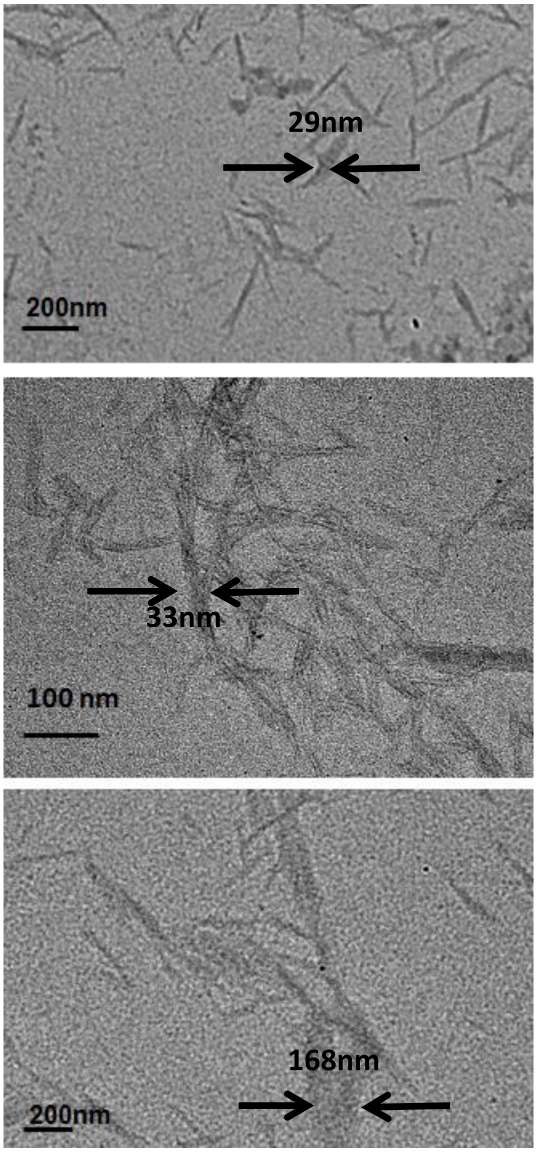

Figure 2.4 Types of CNCs at pH 5-6, carbon grid: never-dried CNCs (top); freeze-dried CNCs (middle); spray-dried CNCs (bottom).

hydrophobic and can encourage the formation of water nano-droplets rich in CNCs, causing aggregation.

Aggregation of CNCs, either caused by drying method (spray-dried vs other samples), or by poor resuspension, favored a similar mechanism. These structures have been observed by others and referred to as mushrooms. Previous reports established that never-dried and freeze-dried CNCs were fibre/rod-like whereas spray-dried CNCs were spherical or mushroom-shaped.[15] While we did observe the mushroom structures, our results demonstrate that such a structure is an artifact of sampling, caused by poor distribution on the TEM grid. All CNC samples, regardless of drying history are clearly rod-shaped. This example illustrates the importance of a careful selection of TEM grid coating.

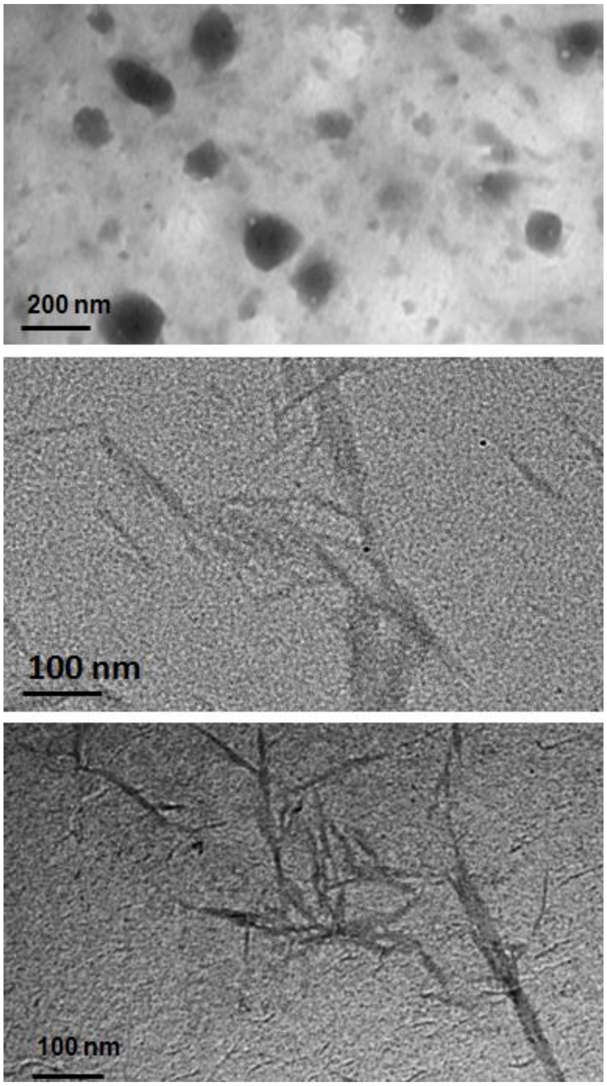

Figure 2.5 Spray-dried CNCs (at pH 5-6) onto a formvar grid (top), carbon grid (middle) and silicon monoxide (bottom).

2.4.3 Comparison of TEM images of CNCs under high resolution and low dose microscopy

It is a common practice to carry out a low dose TEM when the sample is an organic polymer, so that the electron beam does not destroy the sample. CNCs may burn under the high density electron beam while performing HR-TEM. There are two ways to save the sample from getting destroyed: (1) use of low dose TEM using preinstalled software in the microscope, and, (2) playing with the intensity of the electron beam on HR-TEM; so that the sample is prevented from burning. As seen in Figure 2.6, obtaining good images from both methods was possible, as long as the electron beam did not damage the sample.

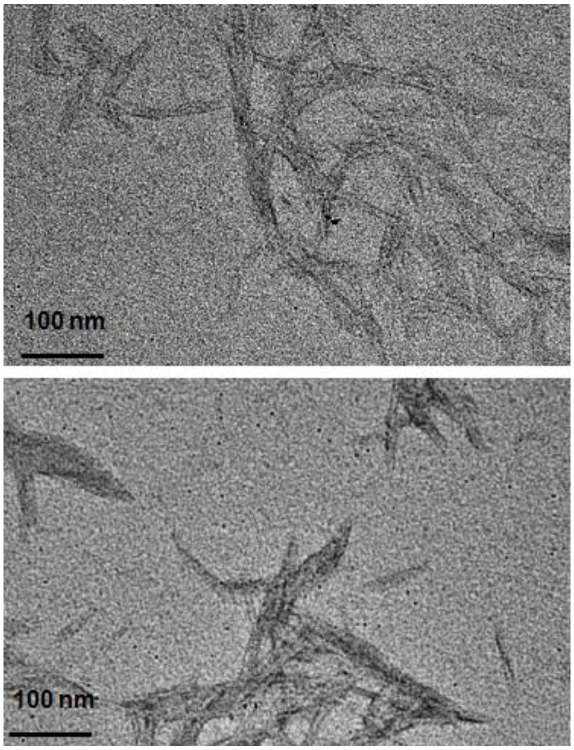

Figure 2.6 Freeze-dried CNCs (pH 5-6 and carbon grid): high resolution TEM (top) and low dose TEM (bottom).

2.4.4 Morphology of modified/decorated CNCs with palladium nanoparticles (PdNPs@CNCs)

In this case, CNCs were used as support for palladium nanoparticles. It is difficult to characterize the nanocrystals when stained with heavy metal salt, because staining would also hide the metal nanoparticles when imaging the modified CNCs.[10] Figure 2.7 shows a TEM image of PdNPs@CNCs without any staining. Here, it was important to take the image at lesser acquisition times and a large defocus value. This is important for preventing the damage of CNCs under the electron beam. Under these conditions, both the CNCs and the Pd NPs were clearly visible. A close examination of this image revealed that, as published before,[10] Pd NPs are mostly present onto CNCs. It is important to note, however, that because of the need to defocus the image to observe the CNCs, the size of Pd NPs, as seen on the image, is over-estimated. Some particles appear white, as a consequence of the same effect.

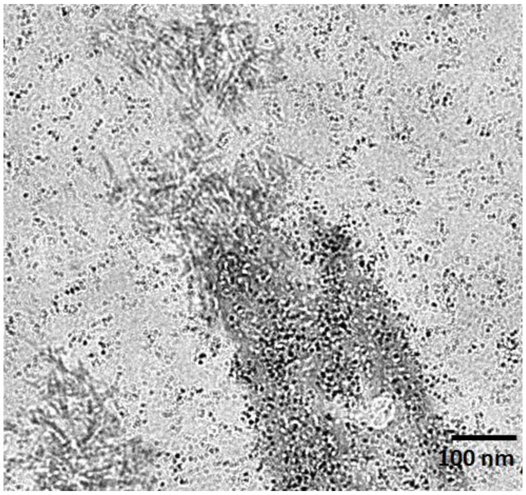

Figure 2.7 TEM image of modified CNCs, PdNPs@CNCs.

2.5 Discussion

Transmission electron microscopy is a convenient technique for imaging CNCs by passing electrons across a grid on which a dried sample rests. In the case of dry materials, a reliable and representative image can be obtained, one that describes the system accurately. However, when the aim is to study systems such as colloidal suspensions, it becomes important to take surface energies into consideration as the specimen dries. As shown above, CNCs are optimally imaged when the sample has never been dried and deposited onto a hydrophilic grid, ideally silicon monoxide-coated. The more common and affordable carbon-coated grids also provided reliable results in the majority of cases. Besides, these results showed that never-dried samples were the easiest to disperse on the grid, followed by freeze-dried and then spray-dried. Freeze-drying is less likely to strongly bind individual CNC nanorods together than spray-drying. In any case and regardless of the history of the CNCs, the material itself is always a rod-like high aspect ratio nanoparticle. As a general trend, the population of individual rods decreases with increasing pH, increasing hydrophobicity of the grid coating and increasing particle packing upon drying (Table 2.1). Never-dried CNCs are better-dispersed and single rods are more numerous in these samples. For freeze-dried CNCs, single rods, small clusters and large aggregates are present. For freeze-dried samples, aggregation depends on the concentration of suspensions used while freeze drying, as discussed by Cervin *et al*.[21] Thanks to the high quality and resolution of the images observed, we were able to size individual rods of CNCs (Figure 2.8). 1000 single rods were counted for never-dried CNCs at pH 3.5 on a carbon grid. We measured them to be 9.7 ± 4.4 nm in width and 216 ± 82 nm in length, consistent with reported values.[4]

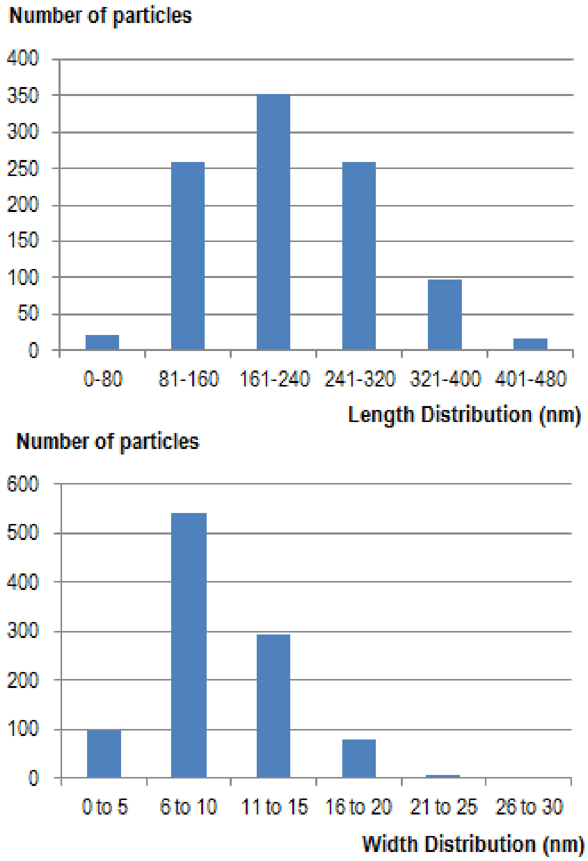

Figure 2.8 Histograms of CNCs single rods length (top) and width (bottom) measured on 1000 particles for never-dried particles on carbon grids at 3.5 pH.

We also demonstrated that never-dried, freeze-dried and spray-dried are all rod shaped. If dispersed properly, never-dried, spray-dried as well as freeze-dried CNCs appear very similar. The mushroom-structure is occasionally observed, but we showed it is an artifact of drying; as improved dispersion sufficed to break them apart and reveal the presence of rods. This result is also in accordance with the TEM studies done with carbon nanotubes[22, 23] and various types of inorganic nanoparticles, such as ZnO[24] and Au nanoparticles,[25] where the importance of dispersion of the sample is stressed while imaging these nanoparticles. The type of morphology observed by TEM depends on how well the sample has been dispersed in the suspension, which in turn depends upon the drying history of the CNCs, interaction between the CNCs and the surface of the grid, and the rate of evaporation.

In this work, we demonstrated that that negative staining with heavy metals can be avoided by a careful tuning of TEM parameters and clear indications and details are provided. We also showed that good images could be obtained on either of the voltages: 120kV or 200kV, a low voltage being recommended for sample conservation during long exposure. An increased potential did not allow for greater contrast or sharpness. The most important part of the procedure is to prepare the samples with diligence and thoroughness. Appropriate dispersion of the CNC sample is critical to get high quality and reproducible images, which is, in turn, important to carry out statistical measurement on size and morphology of the CNCs. Silicon monoxide grids are better for sample preparation as they are hydrophilic and prevent aggregation on the grid itself. Nevertheless, the work shows that the carbon grids can be used with success as well.

2.6 Conclusions

This work emphasizes the importance of a well-established methodology for electron microscopy imaging of CNCs. These results clearly demonstrate the importance of controlling the sampling method, especially during sample drying on the TEM grid. We provide in this article a clear methodology to perform TEM of CNCs in a reliable and reproducible fashion by controlling the pH, the grid properties and the sample suspension. This work revealed that never-dried, freeze-dried and spray-dried all exist as rod structures, with a size of 9.7 ± 4.4 nm in width and 216 ± 82 nm in length, in the case of never-dried samples. An important conclusion to draw from this work is that expensive and toxic heavy metal stains are unnecessary for imaging. Low-dose and high resolution TEM were also compared and discussed.

2.7 References

1. B. G. Rånby, *Acta Chem. Scand.*, 1949, **3**, 649.
2. D. Klemm, F. Kramer, S. Moritz, T. Lindström, M. Ankerfors, D. Gray and A. Dorris, *Angew. Chem. Int. Ed.*, 2011, **50**, 5438.
3. G. Morandi, L. Heath and W. Thielemans, *Langmuir*, 2009, **25**, 8280.
4. Y. Habibi, L. A. Lucia and O. J. Rojas, *Chem. Rev.*, 2010, **110**, 3479.
5. K. Kümmerer, J. Menz, T. Schubert and W. Thielemans, *Chemosphere*, 2011, **82**, 1387.
6. T. Kovacs, V. Naish, B. O'Connor, C. Blaise, F. Gagné, L. Hall, V. Trudeau and P. Martel, *Nanotoxicology*, 2010, **4**, 255.
7. J. F. Revol, H. Bradford, J. Giasson, R. H. Marchessault and D. G. Gray, *Int. J. Biol. Macromol.*, 1992, **14**, 170.
8. A. Dufresne, *Molecules*, 2010, **15**, 4111.
9. E. Kloser and D. G. Gray, *Langmuir*, 2010, **26**, 13450.
10. C. M. Cirtiu, A. F. Dunlop-Brière and A. Moores, *Green Chem.*, 2011, **13**, 288.
11. S. Padalkar, J. R. Capadona, S. J. Rowan, C. Weder, Y.-H. Won, L. A. Stanciu and R. J. Moon, *Langmuir*, 2010, **26**, 8497.
12. I. Kvien, B. S. Tanem and K. Oksman, *Biomacromolecules*, 2005, **6**, 3160.
13. M. Nakakoshi, H. Nishioka and E. Katayama, *J. Electron Microsc.*, 2011, **60**, 401.
14. Y. Peng, D. J. Gardner and Y. Han, *Cellulose*, 2012, **19**, 91.
15. Y. Peng, Y. Han and D. J. Gardner, *Wood and Fiber Science*, 2012, **44**, 448.
16. Y. Peng, D. J. Gardner, Y. Han, A. Kiziltas, Z. Cai and M. A. Tshabalala, *Cellulose*, 2013, **20**, 2379.
17. P. Ramanen, P. A. Penttila, K. Svedstrom, S. L. Maunu and R. Serimaa, *Cellulose*, 2012, **19**, 901.
18. X. M. Dong, J.-F. Revol and D. G. Gray, *Cellulose*, 1998, **5**, 32.
19. E. H. Qua, P. R. Hornsby, H. S. S. Sharma and G. Lyons, *Journal of Material Science*, 2011, **46**, 6029.

20. S. Beck, J. Bouchard and R. Berry, *Biomacromolecules*, 2012, **13**, 1486.
21. N. T. Cervin, C. Aulin, P. T. Larsson and L. Wågberg, *Cellulose*, 2011, **19**, 401.
22. A. R. Boccaccini, J. Cho, J. A. Roether, B. J. C. Thomas, E. Jane Minay and M. S. P. Shaffer, *Carbon*, 2006, **44**, 3149.
23. Z. L. Wang, P. Poncharal and W. A. de Heer, *Pure Appl. Chem.*, 2000, **72**, 209.
24. X. L. Hu, Y. Masuda, T. Ohji and K. Kato, *Key Eng. Mater.*, 2010, **445**, 123.
25. S. L. Westcott, S. J. Oldenburg, T. R. Lee and N. J. Halas, *Langmuir*, 1998, **14**, 5396.

2.8 Appendix

This section consists of additional images acquired for the project.

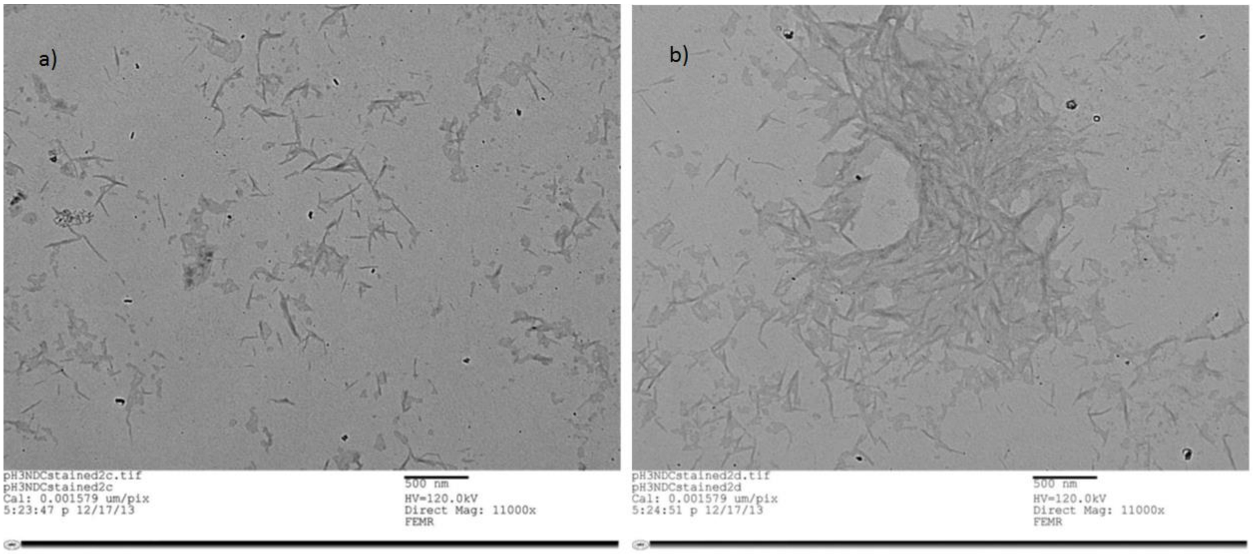

Figure 2.9 Never-dried CNCs at pH 3.5, stained with uranyl acetate: a) on carbon grid, and b) on formvar grid.

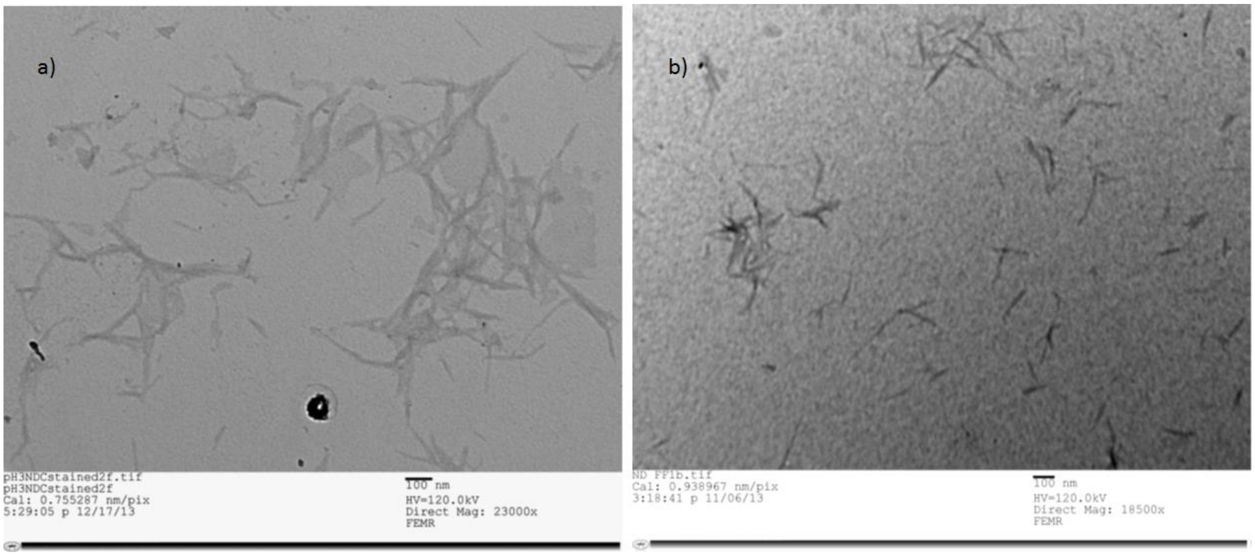

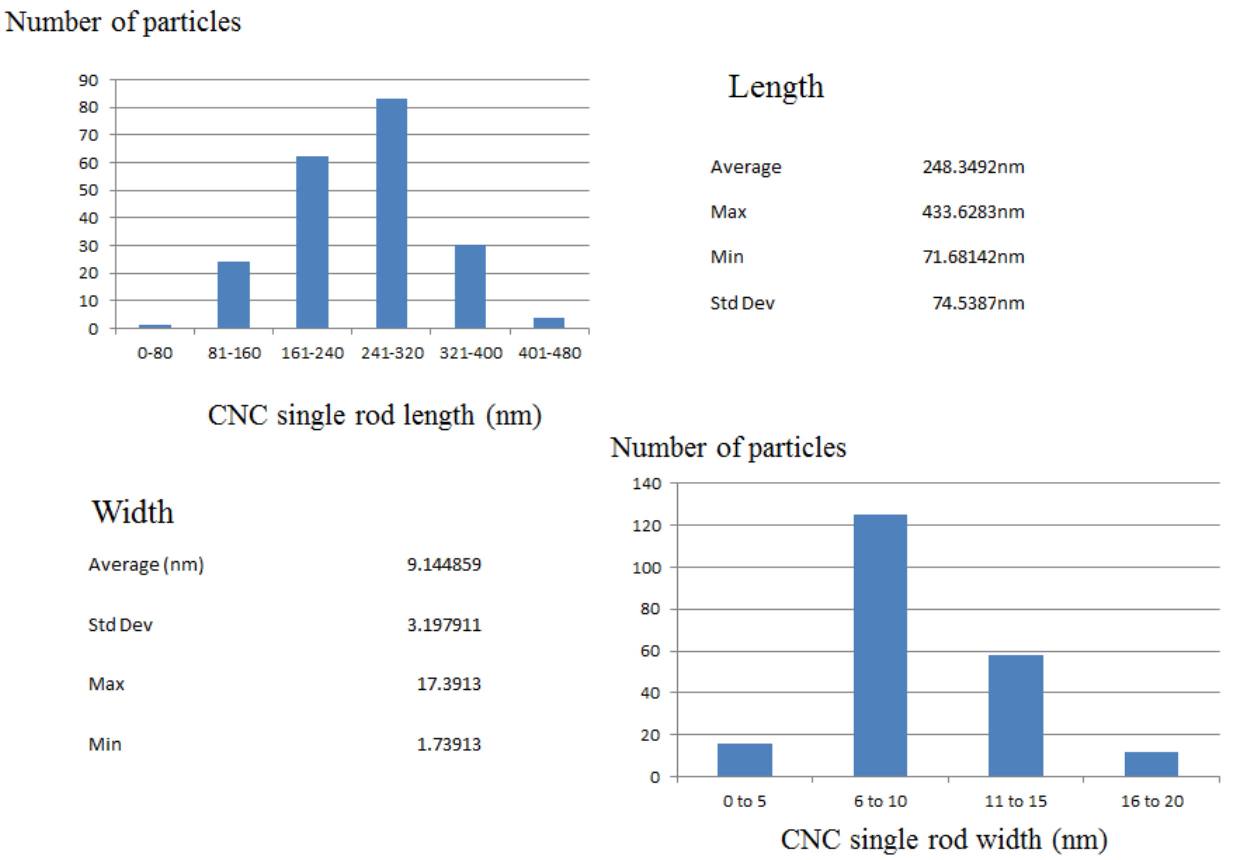

Length

Average	248.3492nm
Max	433.6283nm
Min	71.68142nm
Std Dev	74.5387nm

Width

Average (nm)	9.144859
Std Dev	3.197911
Max	17.3913
Min	1.73913

Figure 2.10 Length and width histograms of never-dried CNCs on carbon grid at pH 3.5, stained with uranyl acetate.

Figure 2.11 a) Never-dried CNCs on silicon monoxide grid at pH 3.5, and b) Spray-dried CNCs on carbon grid at pH 3.5.

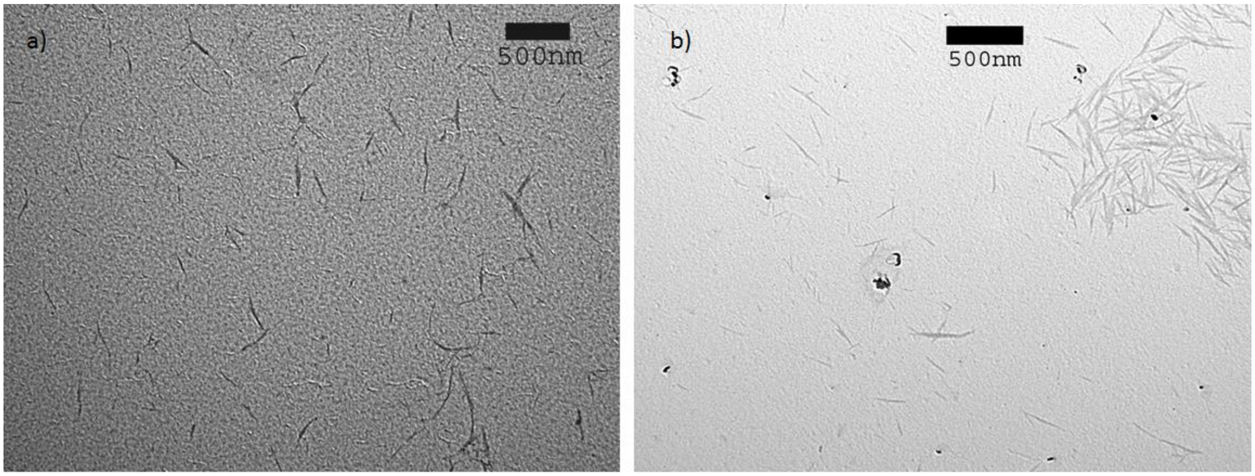

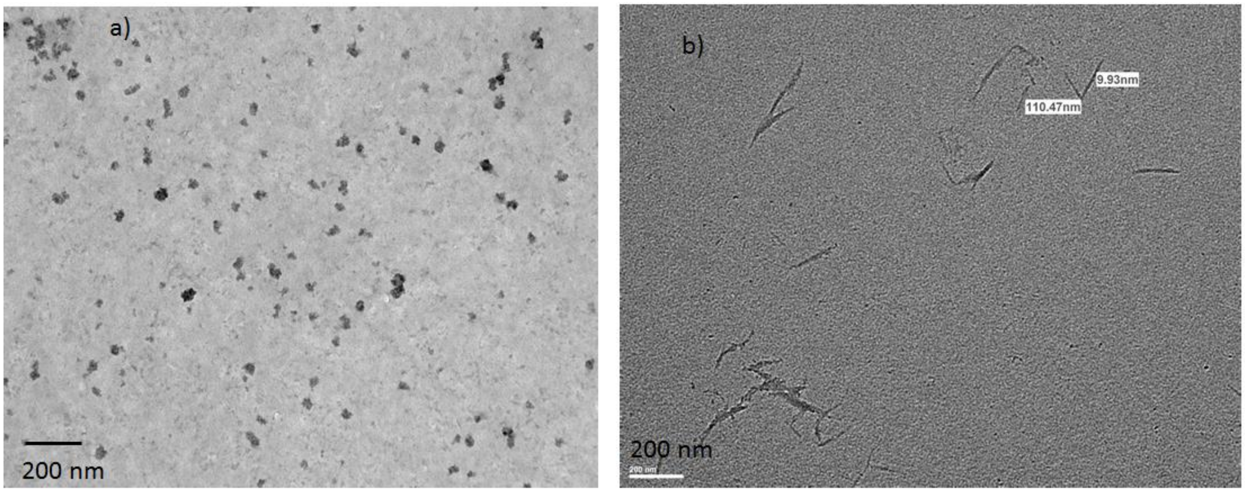

Figure 2.12 a) Spray-dried CNCs on formvar grid at pH 3.5 (mostly artefacts observed), and b) Spray-dried CNCs on silicon monoxide grid at pH 3.5.

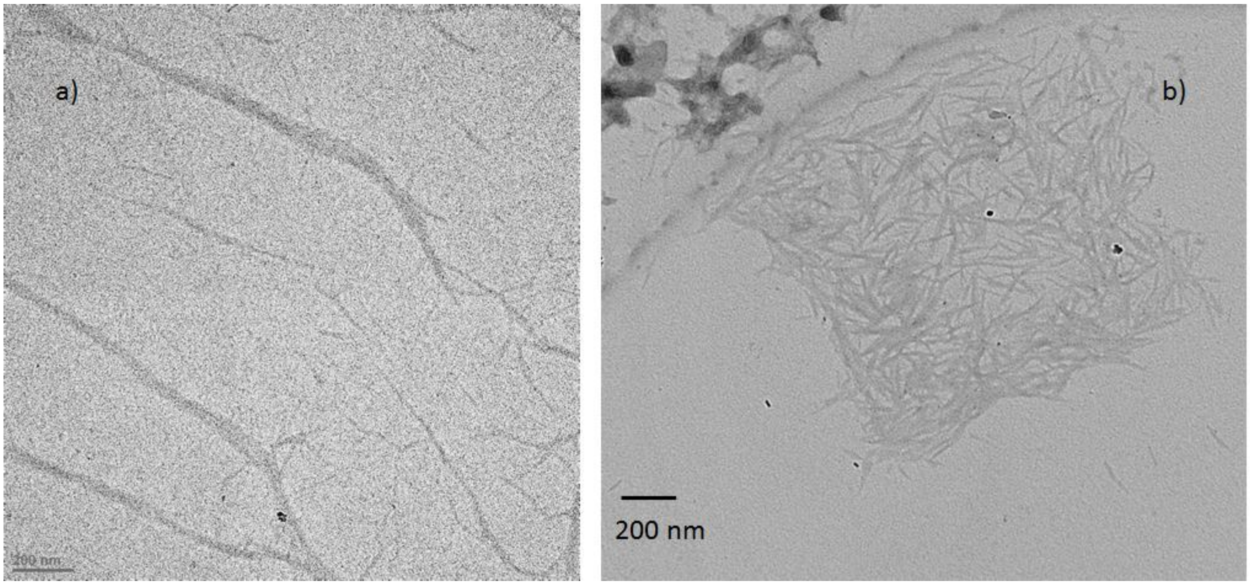

Figure 2.13 a) Freeze-dried CNCs on carbon grid at pH 3.5, and b) Freeze-dried CNCs on formvar grid at pH 3.5.

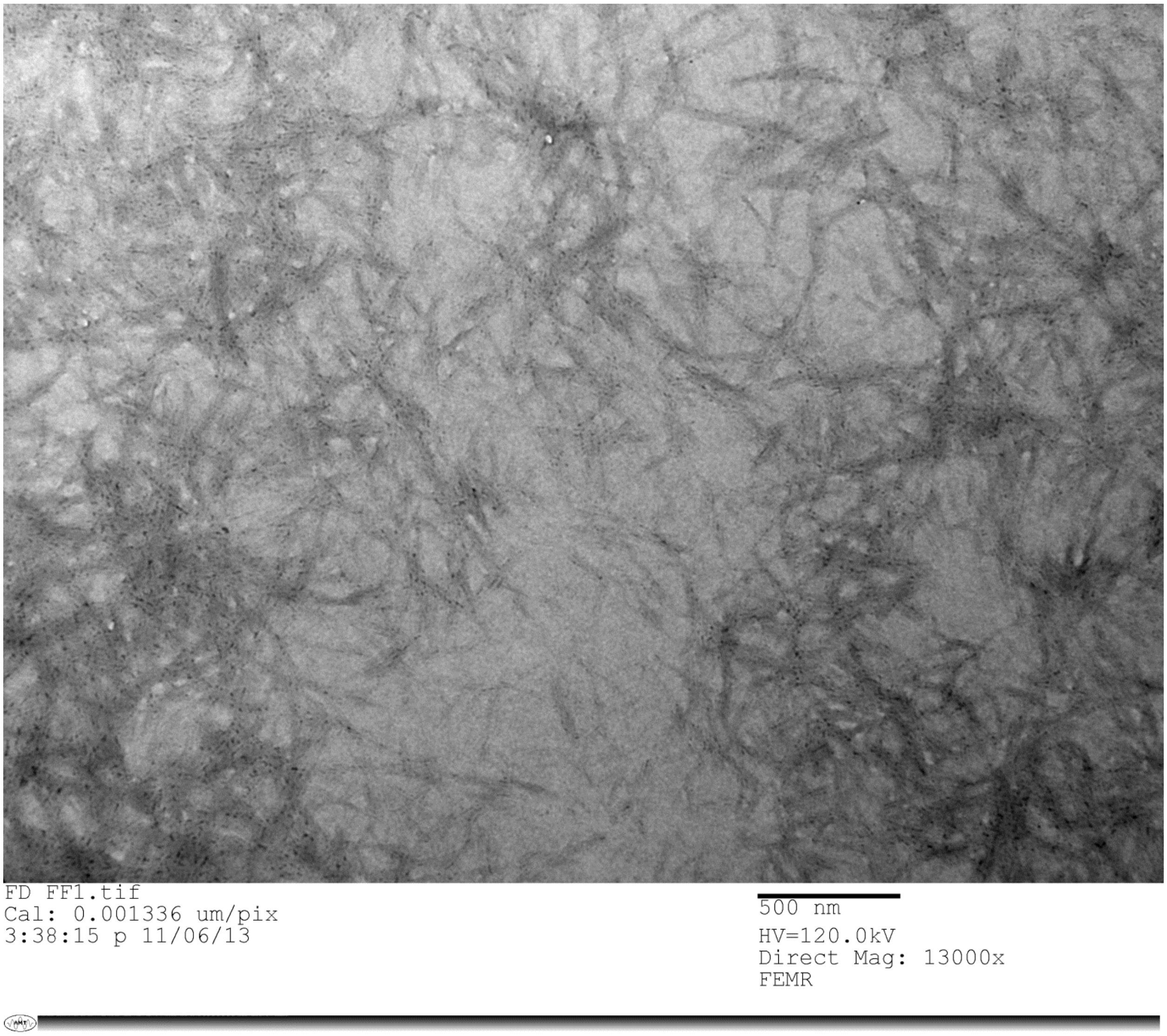

Figure 2.14 Freeze-dried CNCs on formvar grid at pH 5-6.

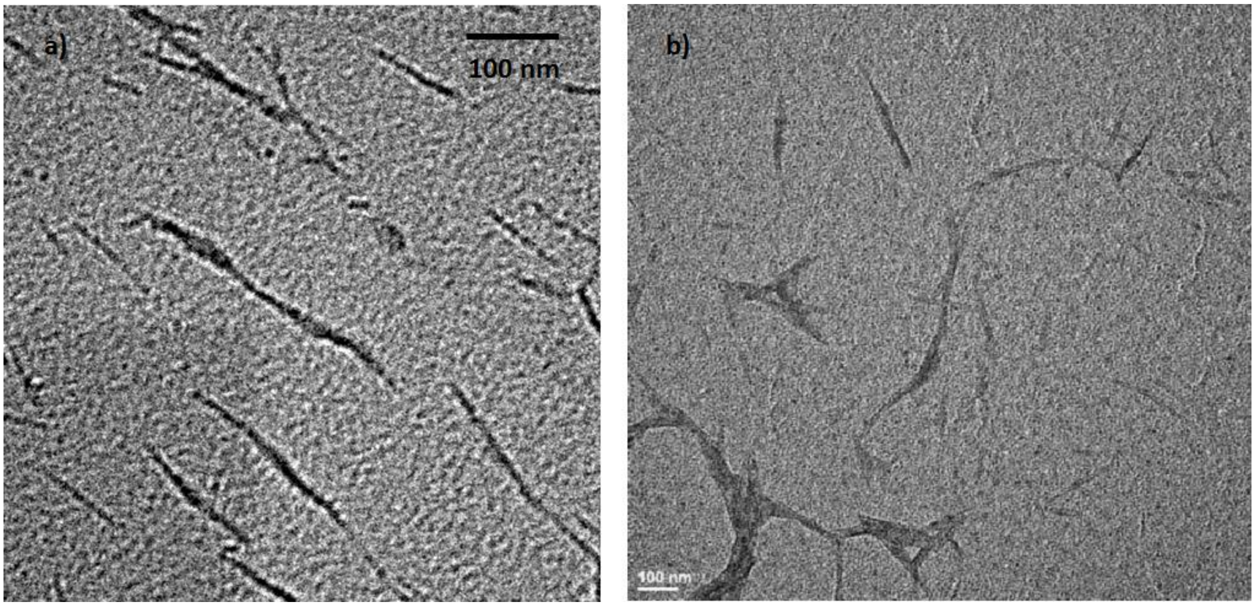

Figure 2.15 a) Freeze-dried CNCs on silicon monoxide grid at pH 3.5, and b) Freeze-dried CNCs on silicon monoxide grid at pH 5-6.

3 Cellulose nanocrystals as chiral inducers

The CNCs possess multiple levels of chirality. Moreover, the surface of CNCs is covered with the primary hydroxyl groups in a regular and organised fashion. We hypothesized that these features of CNCs could be used for inducing chirality. We tested our hypothesis by performing enantioselective hydrogenation reaction on a set of prochiral substrates using Pd NPs supported onto CNCs as catalysts. Here the Pd NPs were essential for activating the hydrogenation reaction and the CNCs imparted the enantioselectivity.

This chapter is adapted from a published article, whose citation appear below, which is reprinted with permission from the American Chemical Society and all co-authors.

Madhu Kaushik, Kaustuv Basu, Charles Benoit, Ciprian M. Cirtiu, Hojatallah Vali and Audrey Moores. Cellulose Nanocrystals as chiral inducers: Enantioselective cataly-sis and Transmission Electron Microscopy 3D Characterization. *JACS*, 2015, 137, 6124-6127.

3.1 Abstract

Cellulose nanocrystals (CNCs), derived from cellulose, provide us with an opportunity to devise more sustainable solutions to current technological challenges. Enantioselective catalysis, especially heterogeneous, is the preferred method for the synthesis of pure chiral molecules in the fine chemical industries. Cellulose has been long sought as a chiral inducer in enantioselective catalysis. We report herein an unprecedentedly high enantiomeric excess (ee) for Pd patches deposited onto CNCs used as catalysts for the hydrogenation of prochiral ketones in water at room temperature and 4 bars H_2. Our system, where CNCs acted as support and sole chiral source, achieved an ee of 65% with 100% conversions. Cryo-electron microscopy, high resolution transmission electron microscopy and tomography were used for the first time to study the 3D structure of a metal functionalized CNC hybrid. It established the presence of sub nanometer thick Pd patches at the surface of CNCs and provided insight into the chiral induction mechanism.

3.2 Introduction

Biomaterials are being intensely researched as replacements for existing, non-sustainable systems used in fields such as, optics, electronics, environmental science and catalysis.[1-3] Modern bioresources blend applicability with sustainability-linked properties including non-toxicity, earth abundance, bio-degradability. Among them, cellulose nanocrystals (CNC) constitute an exciting example, featuring applications in the polymer and paper industry,[4-7] as super capacitors,[8, 9] pH-responsive reversible flocculants,[10] hydrogels,[11] aerogels[12] and chiral materials.[13-19] They are readily available from cellulose of both vegetal and bacterial origin, through strong acid hydrolysis or mechanical defibrillation.[20] CNCs exciting properties arise from their well-defined size and morphology, high specific surface area, high aspect ratio, high crystalline order and chirality, superior mechanical strength, and controllable surface chemistry.[5, 21, 22] Each CNC is a high aspect-ratio nanocrystal of a homopolymer, which repeat unit is a dimer of glucose known as cellobiose (Figure 3.1a). Recently, a deeper understanding of this nanomaterial was made possible *via* transmission electron microscopy (TEM) based tomography.[23]

Enantioselective catalysis has been the method of choice to synthesize pure chiral molecules in the pharmaceutical and agrochemical industry.[24] This is largely achieved using homogeneous catalysis, notably organocatalysis.[25] The “chiral pool”, provided by nature, is a classical resource for chiral induction.[26] For industrial applications, however, developing heterogeneous versions of enantioselective catalysts is essential,[24] because of the importance of their easy separation and recycling in this context,[27-30] and nanoscience has been an important contributor to creativity in this area.[31-35]

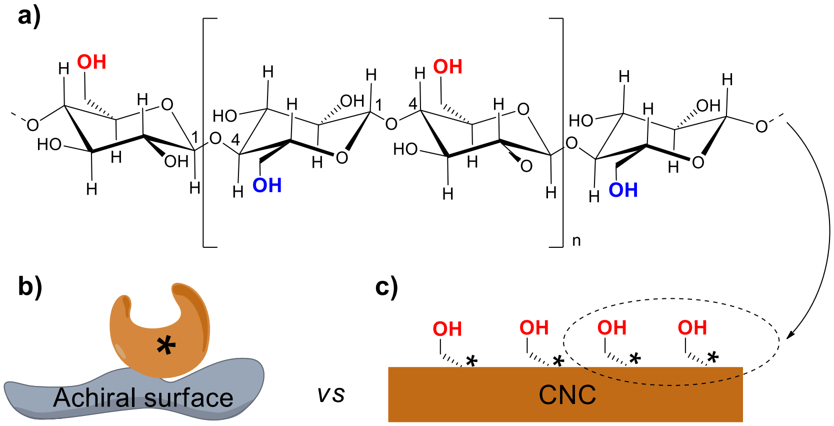

Figure 3.1 a) Molecular structure of cellulose nanocrystals (CNCs); b) scheme of a 3D chiral molecule-modified surface; c) scheme of the 2D surface of a CNC featuring hydroxyl groups oriented in a chiral fashion.

A typical, and very successful, strategy to induce chirality relied on the use of 3D chiral molecules supported onto 2D material acting as spectators (Figure 3.1b).[36-38] The alteration of metal surfaces with strongly interacting chiral modifiers also afforded powerful catalysts.[39, 40] In all these cases, enantioselectivity originated from a three dimensional, chiral molecular arrangement. The ability to use a 2D chiral structure, especially bio-based, to afford enantioselectivity has remained a challenge until today, because the flat nature of such structures typically limited their ability to interact effectively with incoming substrates (Figure 3.1c). In the literature, such 2D chiral materials of natural origin, including quartz, silk fibroin, and cellulose,[41-44] were used as supports for metal or metal oxide catalysts yielding very poor enantioselectivities. The best-known example of this route was reported in the 1950s as a silk-supported Pd catalyst affording a 25% enantiomeric excess (e.e.) in the hydrogenation of benzylidene oxazolidone.[41] Harada and Yoshida used modified cellulose-palladium catalyst for asymmetric hydrogenations, where they could not obtain e.e. above 10% and the results were irreproducible.[44, 45]

While amorphous chiral polymers have a limited ability to be used directly as chiral inducers, highly crystalline and well-defined CNCs have demonstrated interesting chiral properties, mostly exploited in the framework of material science. CNCs in concentrated aqueous suspensions adopt a chiral nematic ordered phase. The formation of this anisotropic phase is interesting as the molecules in these suspensions possess no structural chirality. This property was exploited for producing iridescent films,[46-48] chiral mesoporous silica[15] and carbon[16], chiral plasmonic films by gold nanorods,[13] and chirality-specific hydrolysis of amino acid substrates.[14] In the field of catalysis, CNCs were used as supports for Pd and Au nanoparticles (NPs).[49] Pd NPs deposited onto CNCs were used for hydrogenation and heck coupling reactions by us and others,[50-53] while the Au counterparts showed activity towards 4-nitrophenol reduction.[54] Ag NPs were also deposited onto CNC and demonstrated antibacterial activity.[55] CNC composites, however, had so far never been applied in enantioselective catalysis.

3.3 Materials and methods

CNCs synthesised by sulphuric acid hydrolysis of wood pulp were provided by FPInnovations. For the manipulation of pH, hydrochloric acid (0.01M) was provided by Fluka Analytical. To redisperse dried CNC samples in suspension, the Sonics & Materials Inc. Vibra-Cell VC1500 ultrasonicator (220V, 15A, 1500W, 20 kHz) was used. The Metrohm Titrando (836 base, 804 Ti stand, and 802 stirrer) autotitrator was used for attaining various pH values. The transmission electron microscopy (TEM) samples were deposited on 200 mesh carbon coated copper grids supplied by Electron Microscopy Sciences. The analyses were performed on the Tecnai 12 microscope (FEI electron optics) equipped with a Lab6 filament at 120kV, equipped with Gatan 792 Bioscan 1k x 1k Wide Angle Multiscan CCD Camera (Gatan Inc.); and FEI G2 F20 Cryo-S/TEM microscope (FEI, Inc) at 200kV, equipped with Gatan Ultrascan 4k x 4k Digital (CCD) Camera System at different magnifications corresponding to different pixel size (defocus level ranging from − 2.5 to − 4.5 μm). All hydrogenation reactions were carried out in a Parr Instruments 5000 Series Multiple Reactor System. The monitoring of catalytic hydrogenation and determination of enantiomeric excess were performed using an Agilent 7890A series gas chromatograph equipped with a MS detector (5975C) on a Agilent Cyclodex-B column. Cyclohexanol (reagentplus grade, 99%, Sigma Aldrich) was used as internal standard for quantification of all hydrogenation reactions. All reagents, solvents and substrates were procured from Sigma Aldrich.

3.3.1 Preparation of catalyst

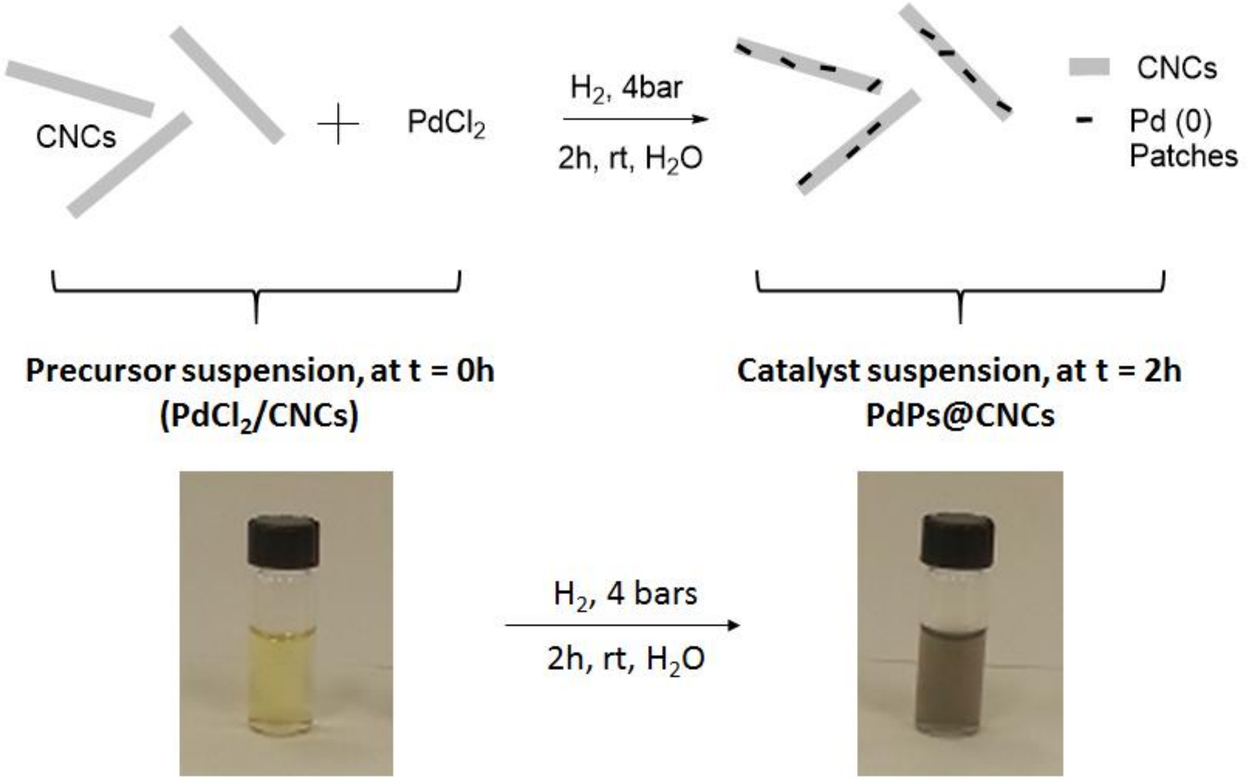

Figure 3.2 Preparation of the catalyst, PdPs@CNCs.

This method was adapted from Cirtiu *et.al*.[50] A suspension of 500 mg of CNCs in 50 mL HCl solution at pH 2 was mixed with 50 mL of saturated $PdCl_2$ acidic solution (pH adjusted to 2 with dilute HCl). The mixture was stirred for 10 min to homogenize the suspension. The final concentration of $PdCl_2$ was $0.75x10^{-3}$ M, while the CNC concentration in the mixture was 0.5% w/w. Then, the mixture was placed under 4 bars of hydrogen gas for 2 hours at room temperature to obtain PdPs@CNCs (Figure 3.2).

3.3.2 Hydrogenation of Substrates

Substrate (0.1 mmol) was added to the catalyst suspension prepared above, PdPs@CNCs, (5mL). To this mixture was added cyclohexanol (0.1 mmol) as internal standard. Then, the mixture was placed in a PARR multiple reactor system under H_2 pressure, 4 bars, 1000rpm, for 2 h at room temperature (Scheme 3.1). Afterwards, reaction mixture was extracted with diethyl ether and then injected on the GC-MS for monitoring the conversion. Please note that the yields reported are for the alcohol. In each hydrogenation reaction, the conversion of the substrate was 100%. The rest was the corresponding side-product obtained due to hydrogenolysis, shown in Scheme 3.1.

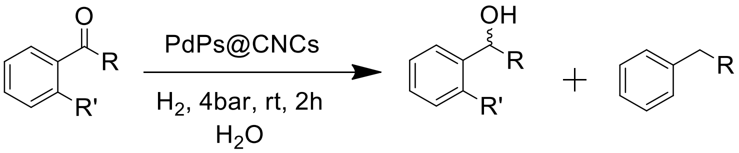

Scheme 3.1 Hydrogenation of prochiral ketones.

3.3.3 Poisoning Experiments

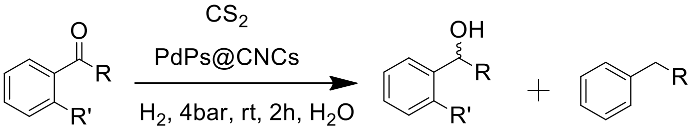

Scheme 3.2 Poisoning experiments.

Substrate (0.1 mmol) was added to the catalyst suspension prepared above, PdPs@CNCs, (5mL). To this mixture was added cyclohexanol (0.1 mmol) as internal standard. 0.5 equivalents of CS_2 with respect to palladium was added to the mixture. Then, the mixture was placed under 4 bars of hydrogen gas for 2 hours at room temperature (Scheme 3.2). Afterwards, reaction mixture was extracted with diethyl ether and then injected on the GC-MS for monitoring the conversion.

3.3.4 Blank Experiments

Three types of blank experiments were conducted for the substrate, 5 under exactly similar conditions of temperature, pressure, metal loading and no. of equivalents used for the substrate and catalyst (Table 3.1). The CNCs alone were not active. In the second experiment, unsupported Pd, made from $PdCl_2$ by the method used for synthesizing the catalyst. The unsupported Pd resulted in 0% conversion. In the third experiment, the commercially available catalyst, PdNPs@C, was used, which gave a conversion of 78% after 24h (in 2h, no conversion was observed). In this, 38% yield of the corresponding alcohol was obtained, with 0% ee. The rest was the side-product obtained due to hydrogenolysis.

3.3.5 Recycling Experiments

Substrate (0.1 mmol) was added to the catalyst suspension prepared above, PdPs@CNCs, (5mL). To this mixture was added cyclohexanol (0.1 mmol) as internal standard. Then, the mixture was placed in a PARR multiple reactor system under H_2 pressure, 4 bars, 1000rpm, for 2 h at room temperature. Afterwards, reaction mixture was extracted with diethyl ether and then injected on the GC-MS for monitoring the conversion. The remaining water suspension, having the catalyst, was then used for the next cycle. The process was repeated upto five cycles.

3.3.6 Monitoring the Hydrogenation Reactions

The monitoring of catalytic hydrogenation and determination of enantiomeric excess were performed using an Agilent 7890A series gas chromatograph equipped with a MS detector (5975C) on an Agilent Cyclodex-B column. Response factors for all compounds were calculated using cyclohexanol as the internal standard. The response factor was calculated by running a standard solution containing known substrate and internal standard concentrations on the GC-MS to determine the area of the two compounds:

Response Factor, R = (concentration of substrate/ concentration of internal standard)*(peak area of internal standard/ peak area of substrate)

3.3.7 Cryo-electron microscopy

3 μl of sample was added to C-flat holey carbon sample support grids R2/2 for cryo-TEM (Protochips, USA). Excess fluid was blotted and the sample was flash frozen hydrated by plunging into a bath of liquid ethane using FEI Vitrobot Grid Plunging System (FEI electron optics). The grids were then stored in liquid nitrogen until observation. Images were acquired usingFEI Titan Krios 300kv CryoS/TEM microscope (FEI, Inc) equipped with Falcon 2 Direct Detection Device (DDD)(FEI) at a magnification of 59kx corresponding to a pixel size of 1.41 Å, defocus level ranging from −2.0 to −3.0μm, under low dose conditions.

3.3.8 3-D Imaging under cryo condiitons

3.3.8.1 Data Acquisition

Tomograms of $PdCl_2$/CNCs and PdPs@CNCs were collected using a Titan Krios TEM (FEI, Einhoven) operated at 300kV and equipped with Falcon 2 Direct Detection Device (DDD) (FEI) using FEI Batch Tomography Software. Cryo-tilt series were collected at a magnification of 37kx for the $PdCl_2$/CNCs and PdPs@CNCs respectively, over a tilt range of ± 60 degrees with an angular increment 2 degrees. The nominal pixel size was 2.24 Å, the defocus ranged from 4 to 6 μm and total dose per tomogram was about 100 $e^-/Å^2$.

3.3.8.2 Image Processing

All tomograms were aligned, filtered and reconstructed using IMOD.[56] Simultaneous iterative reconstruction technique (SIRT) was used. 3D visualization and volume was done using Chimera.

3.4 Results and discussions

Herein, we show that CNCs could be successfully used as 2D chiral inducers and report an unprecedented 65% ee for the hydrogenation of a prochiral ketone using palladium patches deposited onto CNCs (PdPs@CNCs) in water. We also used TEM tomography to establish the structure of the catalyst and provided insight into the potential chiral induction mechanism. In order to test the ability of CNC to serve as an enantioselective support, we deposited Pd (0) at the surface of CNCs, following procedure developed by our group.[50] CNCs, in freeze-dried form, were resuspended in water and exposed to an aqueous acidic $PdCl_2$ solution (Figure 3.2).

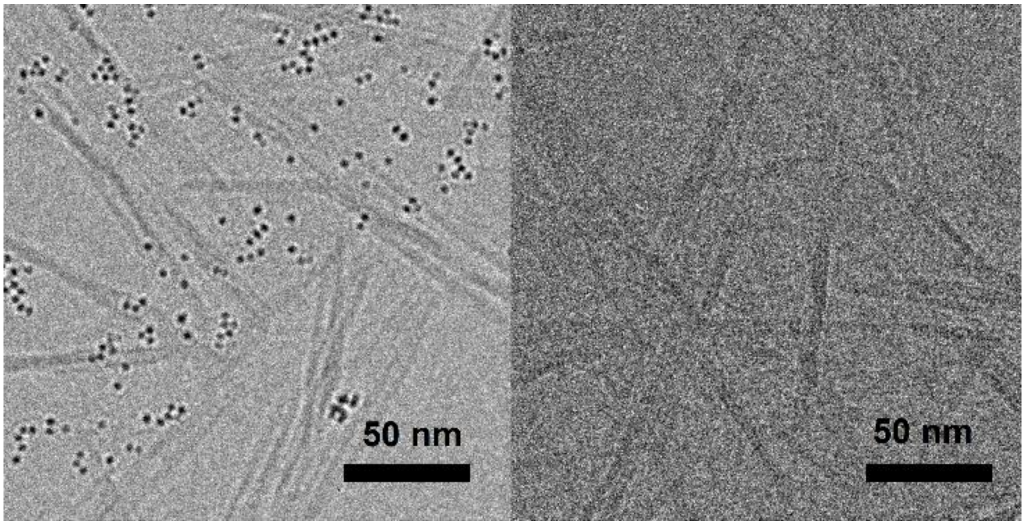

Figure 3.3 Cryo-TEM images of $PdCl_2$/CNCs (left) and PdPs@CNCs (right).

$PdCl_2$ could interact with both hydroxyl groups at the CNC surface as well as the sulfate ester groups introduced during CNC extraction from cellulose. The solution was then exposed to mild H_2 pressure, causing Pd reduction and deposition onto the CNC surface, affording PdPs@CNCs.[50] The resulting hybrid material was active for the hydrogenation of phenol and the Heck reaction. For the present work, we turned to hydrogenation of prochiral ketones. The reaction proceeded well under mild conditions, using 4 bars of hydrogen at room temperature in water. Under these conditions, acetophenone (**1**) was 100% converted in 2 h, with a yield of 87% for 1-phenylethanol (Scheme 3.3). Interestingly, an ee of 7% was measured. Although very low, this ee demonstrated that the CNC surface had some chiral induction activity, as it was the only chiral source present. We selected 4 more ketones with different substitution schemes and steric bulk, in hope to achieve more exciting ees. **2-5** also gave 100% conversions and excellent yields. **2** and **3**, like **1**, gave low enantiomeric excess (ee) between 5 to 7%. Hydrogenation of the bulkier substrate **4**, gave an increased ee of 21%. Interestingly, **5**, with an additional ether functionality susceptible to H-bond with the CNC surface, afforded a high 65% ee, an unprecedented ee for 2D chiral induction.

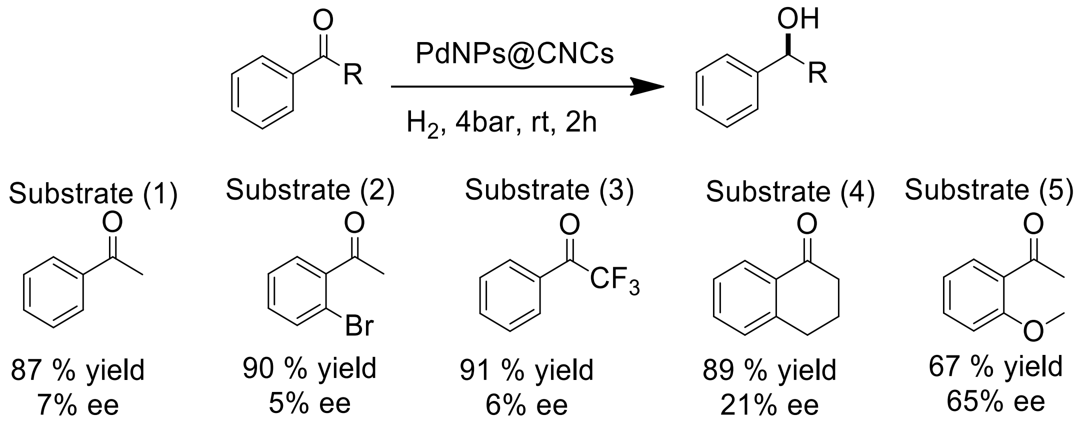

Scheme 3.3 Enantioselective ketone hydrogenation using PdPs@CNCs as catalyst.

To evaluate the stability of this catalyst, recycling tests were performed and demonstrated that the aqueous suspension of PdPs@CNCs could be reused by simple phase separation up to 3 times with no loss of activity and enantioselectivity. The 4th and 5th cycle did lead to a drop in activity, but the enantioselectivity was preserved (Figure 3.4).

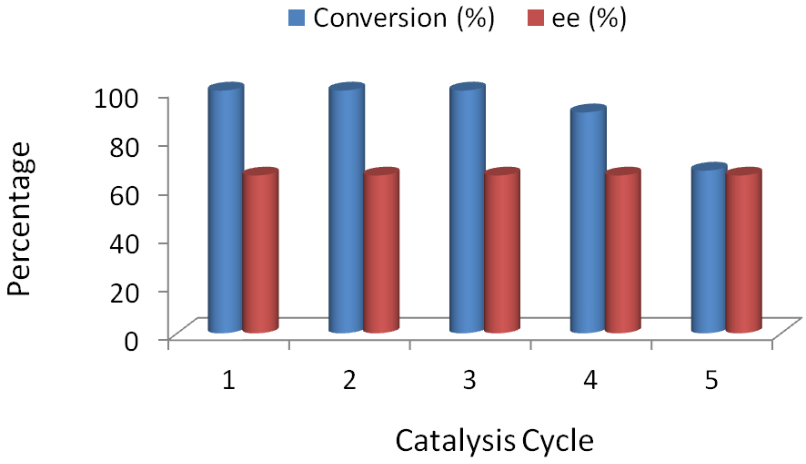

Figure 3.4 The results of recycling the catalyst up to 5 cycles.

Besides, no conversion was measured when using unmodified CNCs or unsupported Pd NPs, which tended to grow and form palladium black (Table 3.1). To determine whether the catalysis was truly heterogeneous, a poisoning experiment using CS_2 was also performed (Scheme 3.2).

Table 3.1 Comparison of blank tests with PdPs@CNCs.

Catalyst	Conversion (%)	Yield (%)	ee (%)
CNCs (40 mg)	0	0	NA
Bulk Pd (0) (0.2 mg Pd)	0	0	NA
5% PdNPs@C (0.2 mg Pd)*	78	38	0
0.5% PdPs@CNCs (0.2 mg Pd)	100	67	65

** Reaction time had to be increased to 24 h, as there was no conversion in 2 h*

The addition of 0.5 equivalents of CS_2 to the reaction mixture made the catalyst totally ineffective under the reaction conditions used.[57] These results confirmed that i) the reaction of hydrogenation happened heterogeneously and that palladium metal was the active catalyst; ii) CNCs were not just a mere support to the Pd catalyst but participated actively in the reaction. The CNC surface is lined with hydroxymethyl groups at the sugar cycle C6 position (Figure 3.1). These primary hydroxyl groups are pointing outwards in an organized, periodic and chiral fashion, assigning a level of molecular preorganization to the CNC surface (Figure 3.1a and Figure 3.1c). Remarkably, in this system, only CNCs possessed the chirality necessary to explain the ee obtained, as large as 65% with substrate **5**. It is interesting to note as well that bulk around the hydrogenated C=O double bond was critical and justified an ee enhancement from 7% to 25%, between substrates **1** and **4**. The results also suggested that an increased interaction of the substrate with the CNC surface resulted in an increased ee. Substrate **5** possessed an additional ether functionality susceptible to improve interaction with polar surfaces such as CNC, but also with metal surfaces.[58] A complete morphological characterization of the catalyst was performed to gain further insight into the potential chiral induction mechanism.

The catalyst was thus imaged by TEM without heavy metal staining. Imaging in cryo-TEM was carried out to investigate the structure of the composite nanomaterial PdPs@CNCs under conditions as close to native as possible. In 2014, cryo-TEM and tomography were already used by Ikkala and coll. to obtain the 3D structure of unmodified CNC.[8] In the present work, a thin vitrified layer of an aqueous suspension of PdPs@CNCs was imaged in a cryo-STEM with a direct detection device (DDD) at an accelerating voltage of 300 kV. In order to have a comparison stand point, we also analyzed under the same conditions a CNC suspension exposed to $PdCl_2$, without H_2 reduction ($PdCl_2$/CNCs). Although $PdCl_2$/CNCs is the precursor to PdPs@CNCs, it is not active for hydrogenation catalysis.[19a] Cryo-TEM images of both samples are presented in Figure 3.3 (and in the appendix from Figure 3.7 to Figure Figure 3.13) and all show well dispersed and well defined CNC whiskers of 150-200 nm in length and 4-6 nm in width, which is in agreement with values reported in the literature.[2b] Surprisingly, no Pd nanoparticles could be seen at this resolution for PdPs@CNCs suspensions, the active catalyst in this study. A tilt series from -60° to +60° was acquired on PdPs@CNCs and its 3D structure was analyzed from the reconstructed tomograms (Figure 3.5, in appendix: Figure 3.16, Figure 3.17 and movie available on: http://pubs.acs.org/doi/suppl/10.1021/jacs.5b02034). In both tomograms and movies,

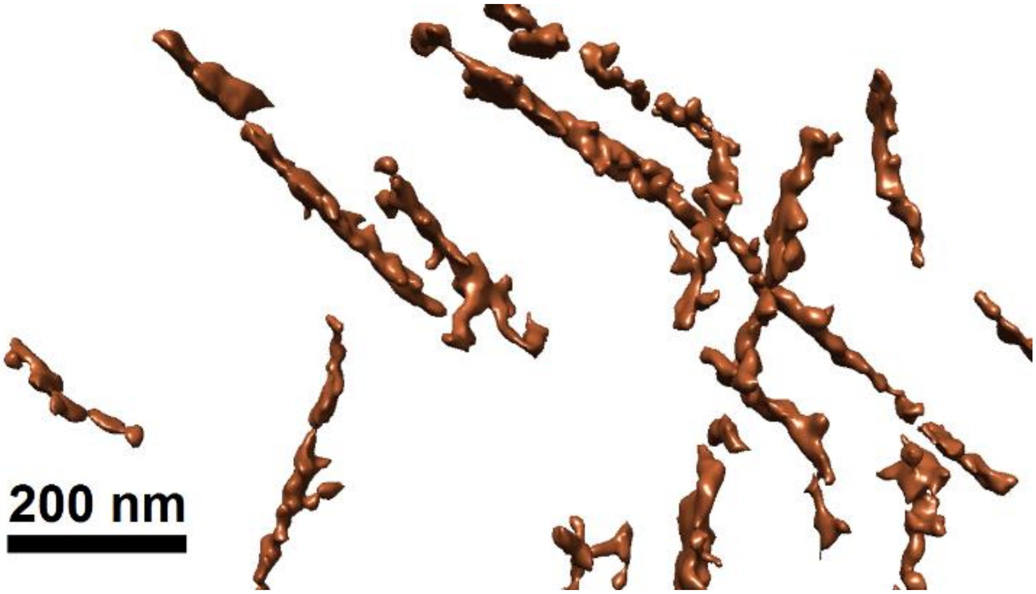

Figure 3.5 TEM tomogram of PdPs@CNCs in cryo conditions.

CNC whiskers can be seen as individual rods, consistent with the observations of Ikkala and coll.[8] On the other hand, for the $PdCl_2$/CNCs sample, well-defined, high-contrast nanoparticles of 2.7 nm ± 0.4 in diameter were observed. These particles did not appear to be correlated to the presence of CNCs. The reconstructed tomograms of $PdCl_2$/CNC (in appendix: Figure 3.14, Figure 3.15 and movie available on http://pubs.acs.org/doi/suppl/10.1021/jacs.5b02034) showed that these particles were segregated at the surface of the vitrified ice layer, and could be caused by $PdCl_2$ precipitation.

To complement these findings, both samples were air-dried on Cu TEM grids and imaged at room temperature using DDD and a phase plate at 300kV, enabling higher resolution images in comparison to the images collected in cryo-TEM. Interestingly, nanoparticles were observed in both samples, but in far greater amounts for the precursor, $PdCl_2$/CNCs. More importantly, on PdPs@CNCs sample grids, patches of Pd were seen on the surfaces of the CNCs (Figure 3.6, in appendix: Figure 3.18, Figure 3.19, Figure 3.20). These patches appeared as parallelepipeds, of 2 to 5 nm in width and 5 to 20 nm in length (Figure 3.6). Their very low contrast suggest that they are possibly only a few atoms in depth. The quality of the images obtained in terms of contrast for both the metal and the organic phase simultaneous was remarkable. An Energy dispersive

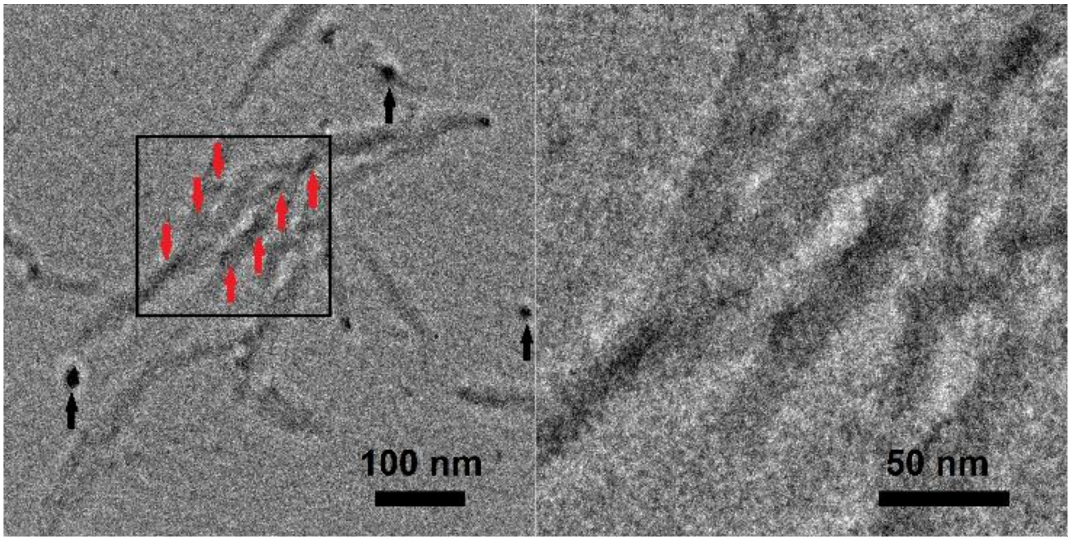

Figure 3.6 TEM images of PdPs@CNCs recorded using a DDD. On the left, few isolated CNCs featuring plates (red arrows) on their surface. Larger NPs (black arrows) are very few and not physically linked to CNC; on the right, a close up view of the area indicated by the box on the left and revealing Pd patches.

spectroscopy (EDS) was carried out on both samples, and revealed the presence of Pd in PdPs@CNCs and Pd and Cl in $PdCl_2$/CNCs (in appendix: Figure 3.21 and Figure 3.22). These results suggest the active catalyst, PdPs@CNCs, was composed of CNC and Pd (0) originated from the reduction of $PdCl_2$, as established from EDS and the catalytic activity. This metal was present as subnanometer thick patches deposited on CNC as observed in high resolution TEM, but too thin to be observed in cryo-TEM.

3.5 Conclusion

In this investigation, we have established the role of CNCs in chiral induction in hydrogenation of prochiral ketones. Pd patches are important for activating the hydrogenation reactions, whereas the CNCs brought in the enantioselection. Cryo-TEM and tomography in conjunction with DDD technology demonstrated the direct contact between the Pd patches and their low-density support. Conceptually, these results offer an opportunity to use cellulose, in the form of the highly crystalline CNC, directly in asymmetric catalysis. Our future work will focus on expanding the scope of the reaction and improving enantioselectivity by achiral surface modification of CNCs, and kinetic investigations to establish further reaction mechanism(s).

3.6 References

1. M. S. Peresin, Y. Habibi, J. O. Zoppe, J. J. Pawlak and O. J. Rojas, *Biomacromolecules*, 2010, **11**, 674.
2. V. K. Thakur, M. K. Thakur, P. Raghavan and M. R. Kessler, *ACS Sustainable Chem. Eng.*, 2014, **2**, 1072.
3. M. J. Rak, T. Friscic and A. Moores, *Faraday Discuss.*, 2014.
4. R. J. Moon, A. Martini, J. Nairn, J. Simonsen and J. Youngblood, *Chem. Soc. Rev.*, 2011, **40**, 3941.
5. D. Klemm, F. Kramer, S. Moritz, T. Lindström, M. Ankerfors, D. Gray and A. Dorris, *Angew. Chem. Int. Ed.*, 2011, **50**, 5438.
6. E. C. Ramires and A. Dufresne, *TAPPI Journal*, 2011, **10**, 9.

7. S. BelHaaj, A. Ben Mabrouk, W. Thielemans and S. Boufi, *Soft Matter*, 2013, **9**, 1975.
8. S. Y. Liew, W. Thielemans and D. A. Walsh, *J. Phys. Chem. C*, 2010, **114**, 17926.
9. S. Y. Liew, D. A. Walsh and W. Thielemans, *RSC Adv.*, 2013, **3**, 9158.
10. K. H. M. Kan, J. Li, K. Wijesekera and E. D. Cranston, *Biomacromolecules*, 2013, **14**, 3130.
11. J. Yang, C.-R. Han, J.-F. Duan, M.-G. Ma, X.-M. Zhang, F. Xu, R.-C. Sun and X.-M. Xie, *J. Mater. Chem.*, 2012, **22**, 22467.
12. X. Yang and E. D. Cranston, *Chem. Mater.*, 2014, **26**, 6016.
13. A. Querejeta-Fernández, G. Chauve, M. Methot, J. Bouchard and E. Kumacheva, *J. Am. Chem. Soc.*, 2014, **136**, 4788.
14. T. Serizawa, T. Sawada, H. Okura and M. Wada, *Biomacromolecules*, 2013, **14**, 613.
15. K. E. Shopsowitz, H. Qi, W. Y. Hamad and M. J. MacLachlan, *Nature*, 2010, **468**, 422.
16. K. E. Shopsowitz, W. Y. Hamad and M. J. MacLachlan, *J. Am. Chem. Soc.*, 2011, **134**, 867.
17. H. Qi, K. E. Shopsowitz, W. Y. Hamad and M. J. MacLachlan, *J. Am. Chem. Soc.*, 2011, **133**, 3728.
18. M. Giese, L. K. Blusch, M. K. Khan and M. J. MacLachlan, *Angew. Chem. Int. Ed.*, 2015, **54**, 2888.
19. M. K. Khan, A. Bsoul, K. Walus, W. Y. Hamad and M. J. MacLachlan, 2015.
20. B. L. Holt, S. D. Stoyanov, E. Pelan and V. N. Paunov, *J. Mater. Chem.*, 2010, **20**, 10058.
21. Y. Habibi, L. A. Lucia and O. J. Rojas, *Chem. Rev.*, 2010, **110**, 3479.
22. N. Lin, J. Huang and A. Dufresne, *Nanoscale*, 2012, **4**, 3274.
23. J. Majoinen, J. S. Haataja, D. Appelhans, A. Lederer, A. Olszewska, J. Seitsonen, V. Aseyev, E. Kontturi, H. Rosilo, M. Österberg, N. Houbenov and O. Ikkala, *J. Am. Chem. Soc.*, 2013, **136**, 866.

24. K. Ding and Y. Uozumi, *Handbook of asymmetric heterogeneous catalysis*, John Wiley & Sons, 2008.
25. P. I. Dalko, *Enantioselective organocatalysis*, Wiley Online Library, 2007.
26. T. Katsuki and K. B. Sharpless, *J. Am. Chem. Soc.*, 1980, **102**, 5974.
27. D. J. Cole-Hamilton, 2003, **299**, 1702.
28. D. J. Cole-Hamilton and R. P. Tooze, *Catalyst separation, recovery and recycling: chemistry and process design*, Springer, The Netherlands, 2006.
29. C.-H. Pélisson, A. Denicourt-Nowicki, C. Meriadec, J.-M. Greneche and A. Roucoux, *ChemCatChem*, 2014.
30. *Catalyst Separation, Recovery and Recycling*, Springer, Netherlands, 2006.
31. D. Astruc, F. Lu and J. R. Aranzaes, *Angew. Chem. Int. Ed.*, 2005, **44**, 7852.
32. V. Polshettiwar and R. S. Varma, *Green Chem.*, 2010, **12**, 743.
33. V. Polshettiwar, R. Luque, A. Fihri, H. Zhu, M. Bouhrara and J.-M. Basset, *Chem. Rev.*, 2011, **111**, 3036.
34. D. Wang and D. Astruc, *Chem. Rev.*, 2014, **114**, 6949.
35. D. Astruc, *Nanoparticles and catalysis*, John Wiley & Sons, 2008.
36. C. E. Song and L. Sang-gi, *Chem. Rev.*, 2002, **102**, 3495.
37. A. Baiker, *J. Mol. Catal. A: Chem.*, 1997, **115**, 473.
38. M. Heitbaum, F. Glorius and I. Escher, *Angew. Chem. Int. Ed.*, 2006, **45**, 4732.
39. V. Demers-Carpentier, G. Goubert, F. Masini, R. Lafleur-Lambert, Y. Dong, S. Lavoie, G. Mahieu, J. Boukouvalas, H. L. Gao, A. M. H. Rasmussen, L. Ferrighi, Y. X. Pan, B. Hammer and P. H. McBreen, *Science*, 2011, **334**, 776.
40. G. Kyriakou, S. K. Beaumont and R. M. Lambert, *Langmuir*, 2011, **27**, 9687.
41. S. Akabori, S. Sakurai, Y. Izumi and Y. Fujii, *Nature*, 1956, **178**, 323.
42. R. L. Beamer, C. S. Fickling and J. H. Ewing, *J. Pharm. Sci.*, 1967, **56**, 1029.
43. G.-M. Schwab and L. Rudolph, *Naturwissenschaften*, 1932, **20**, 363.
44. K. Harada and T. Yoshida, *Naturwissenschaften*, 1970, **57**, 131.
45. T. Mallat, O. E. and B. A., *Chem. Rev.*, 2007, **107**, 4863.
46. J.-F. Revol, L. Godbout, X.-M. Dong, D. G. Gray, H. Chanzy and G. Maret, *Liq. Cryst.*, 1994, **16**, 127.

47. G. Picard, D. Simon, Y. Kadiri, J. LeBreux and F. Ghozayel, *Langmuir*, 2012, **28**, 14799.
48. E. D. Cranston and D. G. Gray, 2006, **7**, 2522.
49. E. Lam, K. B. Male, J. H. Chong, A. C. W. Leung and J. H. T. Luong, *Trends Biotechnol.*, 2012, **30**, 283.
50. C. M. Cirtiu, A. F. Dunlop-Brière and A. Moores, *Green Chem.*, 2011, **13**, 288.
51. M. Rezayat, R. K. Blundell, J. E. Camp, D. A. Walsh and W. Thielemans, *ACS Sustainable Chem. Eng.*, 2014, **2**, 1241.
52. P. Zhou, H. Wang, J. Yang, J. Tang, D. Sun and W. Tang, *Ind. Eng. Chem. Res.*, 2012, **51**, 5743.
53. X. Wu, C. Lu, W. Zhang, G. Yuan, R. Xiong and X. Zhang, *J. Mater. Chem. A*, 2013, **1**, 8645.
54. E. Lam, S. Hrapovic, E. Majid, J. H. Chong and J. H. T. Luong, *Nanoscale*, 2012, **4**, 997.
55. R. Xiong, C. Lu, W. Zhang, Z. Zhou and X. Zhang, *Carbohydr. Polym.*, 2013, **95**, 214.
56. J. R. Kremer, D. N. Mastronarde and J. R. McIntosh, *Journal of Structural Biology*, 1996, **116**, 71.
57. K. L. Luska and A. Moores, *Adv. Synth. Catal.*, 2011, **353**, 3167.
58. Z. Hou, N. Theyssen, A. Brinkmann and W. Leitner, *Angew. Chem. Int. Ed.* , 2005, **117**, 1370.

3.7 Appendix

3.7.1 Cryo-electron microscope images

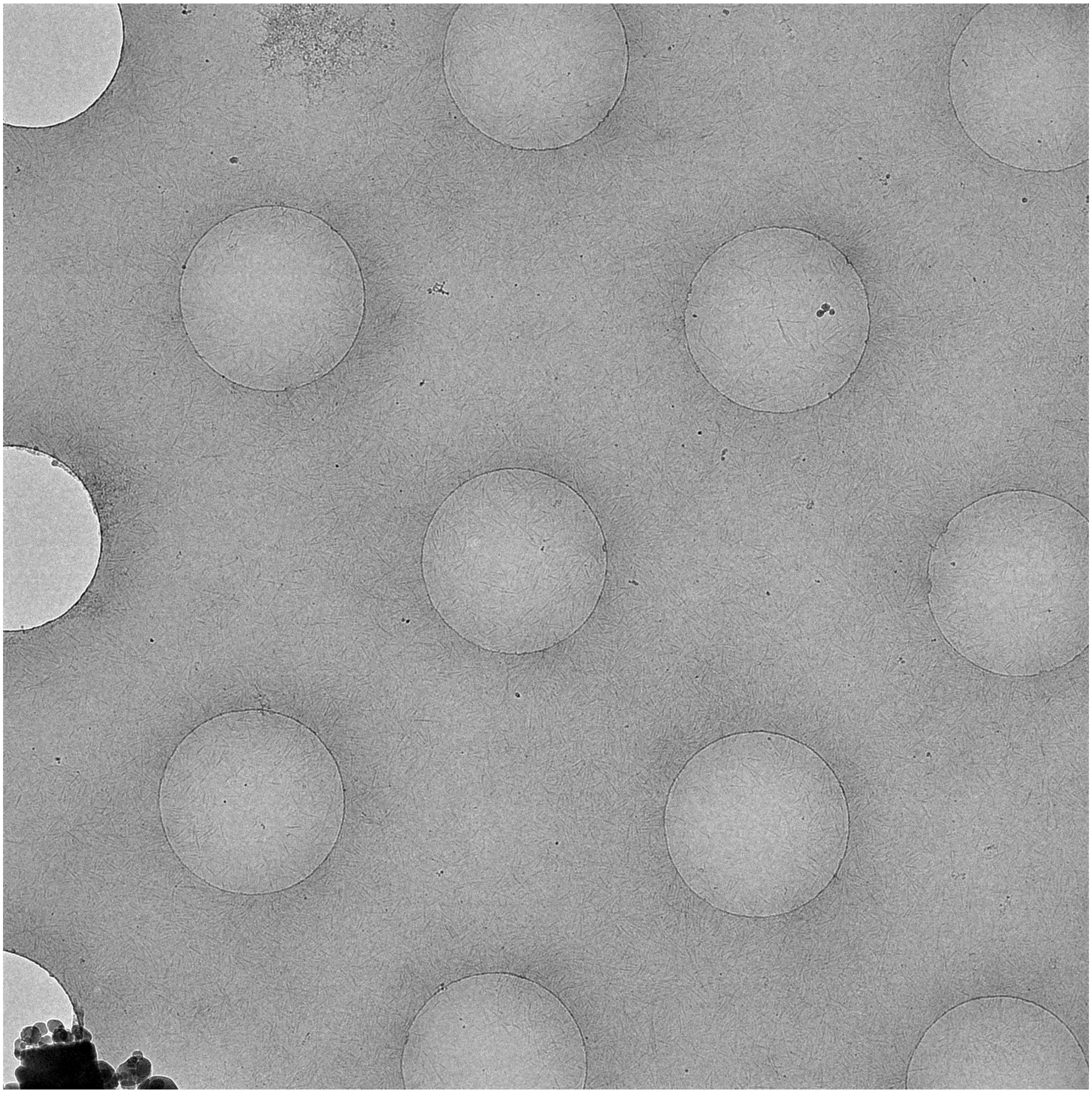

Figure 3.7 Cryo-TEM for precursor suspension, $PdCl_2$/CNCs (t = 0h)

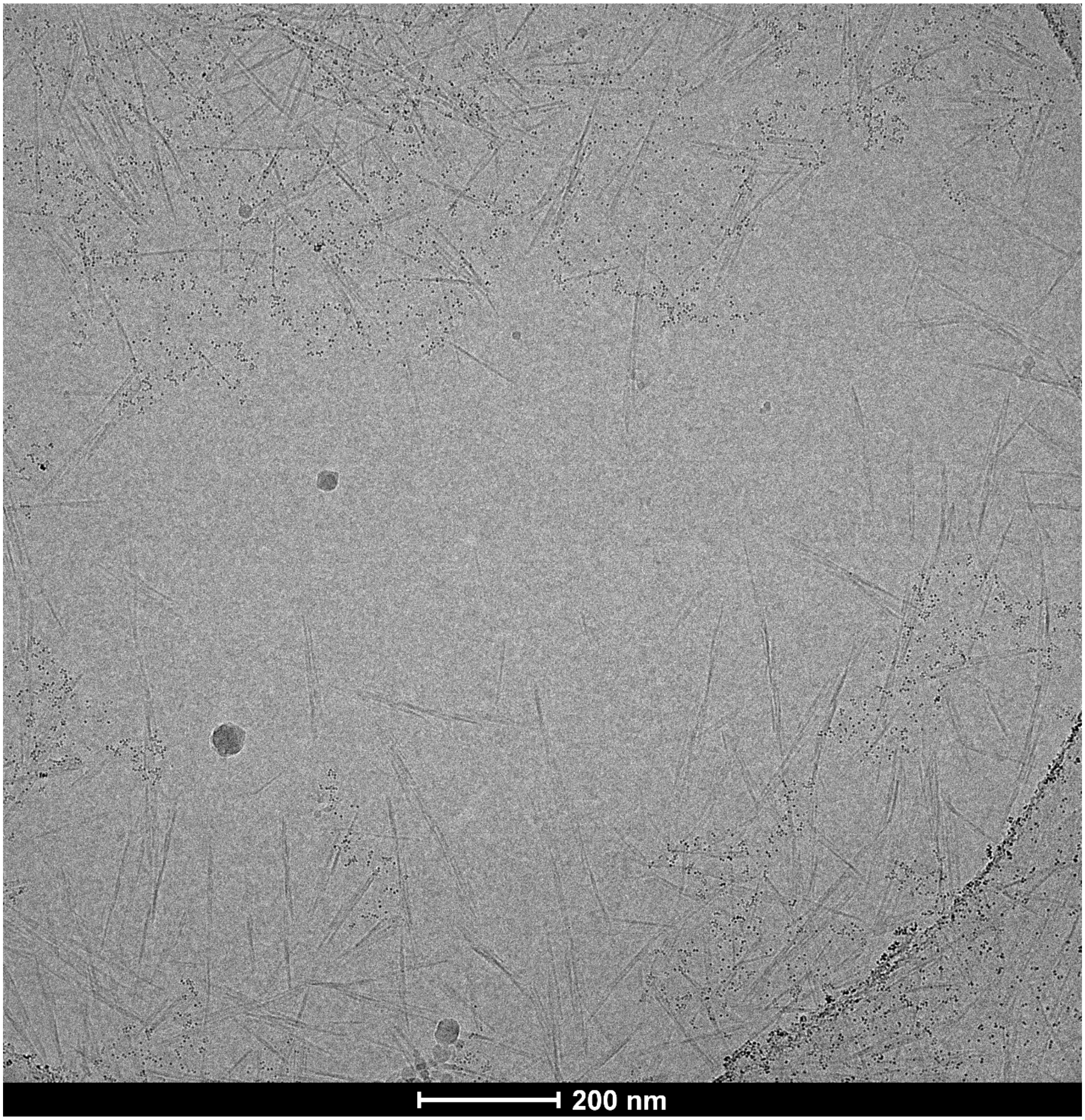

Figure 3.8 Cryo-TEM for precursor suspension, $PdCl_2$/CNCs (t = 0h).

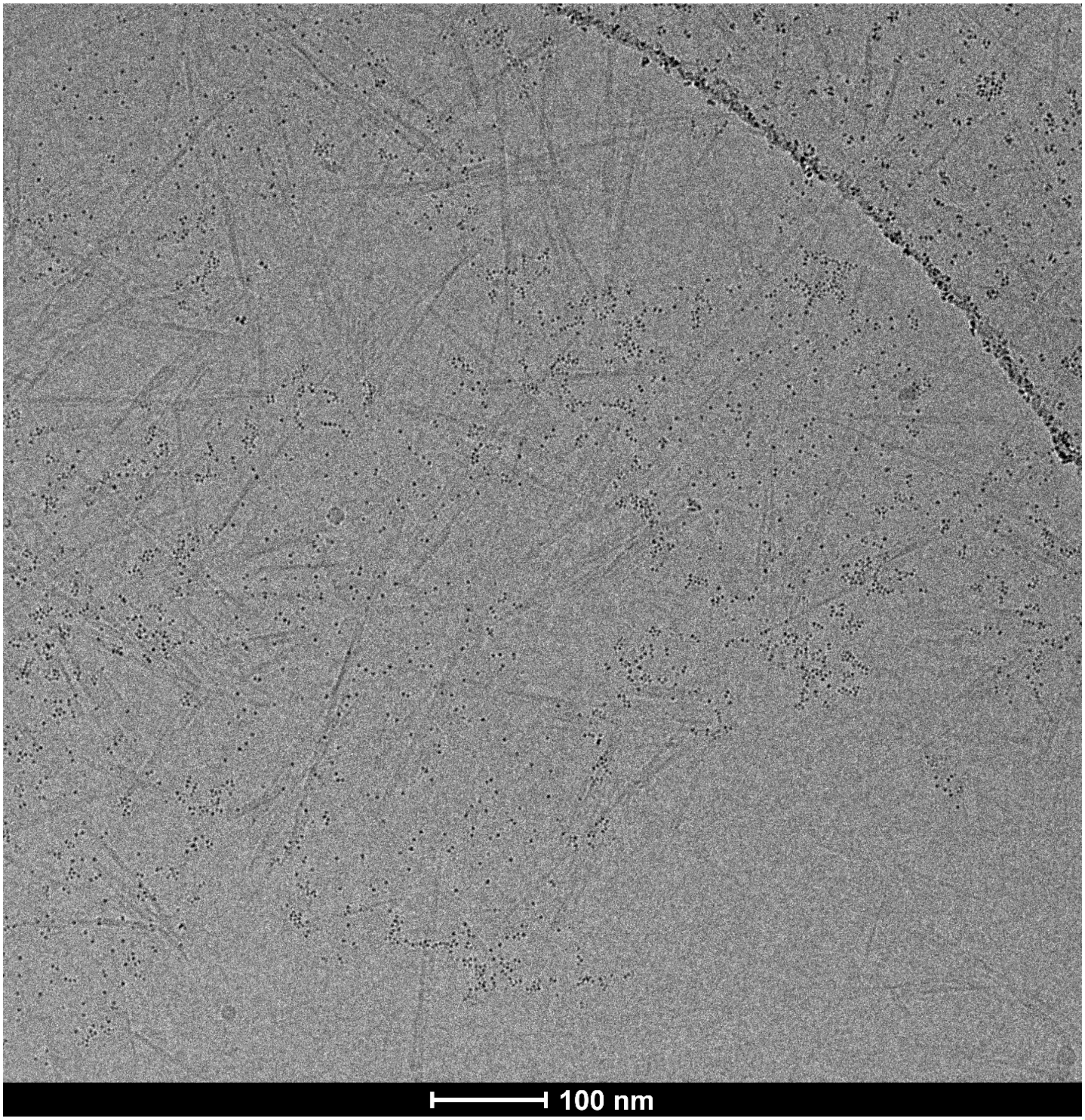

Figure 3.9 Cryo-TEM for precursor suspension, $PdCl_2$/CNCs (t = 0h).

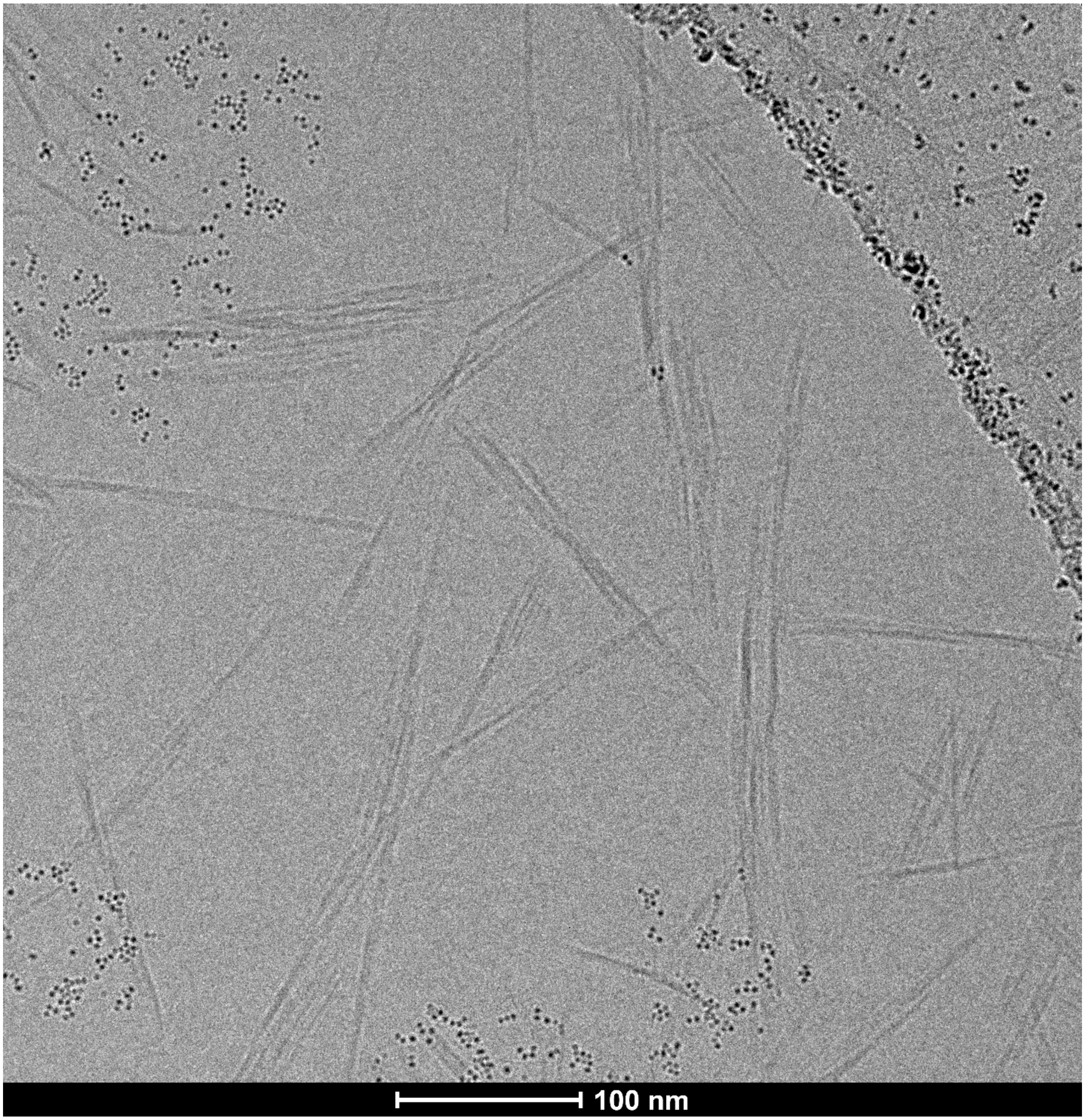

Figure 3.10 Cryo-TEM for precursor suspension, $PdCl_2$/CNCs (t = 0h).

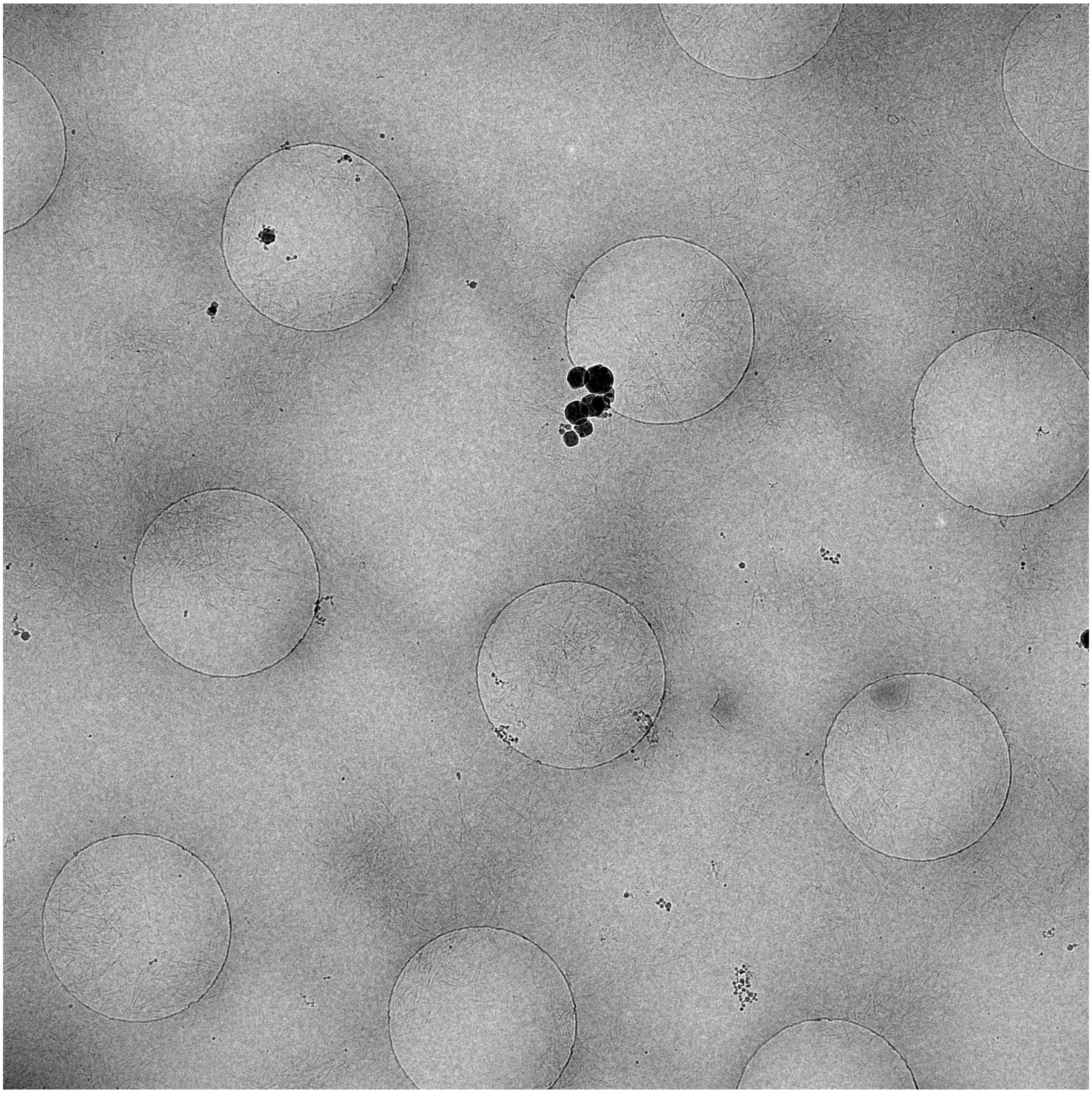

Figure 3.11 Cryo-TEM for catalyst suspension, PdPs@CNCs (t = 2h).

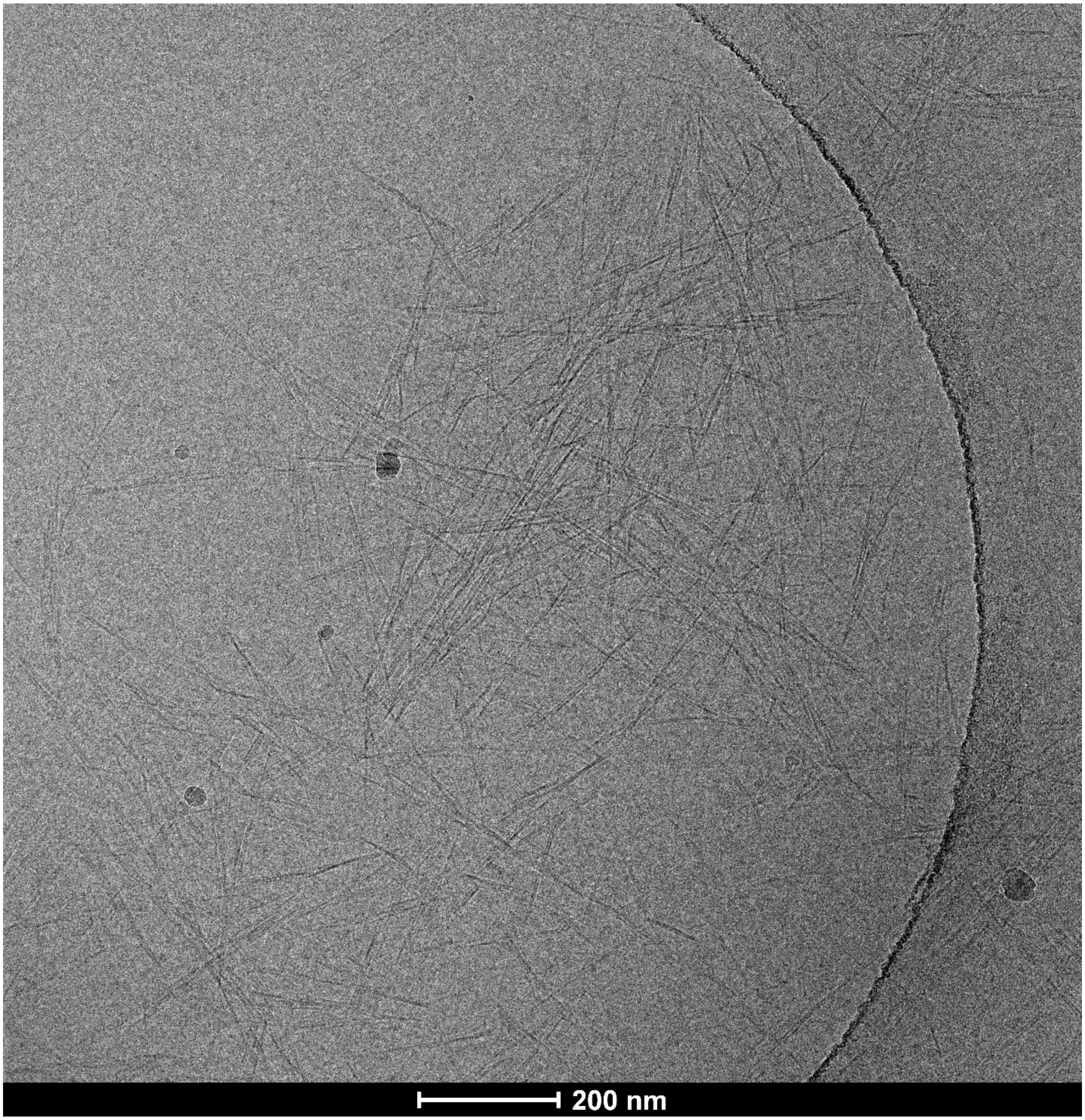

Figure 3.12 Cryo-TEM for catalyst suspension, PdPs@CNCs (t = 2h).

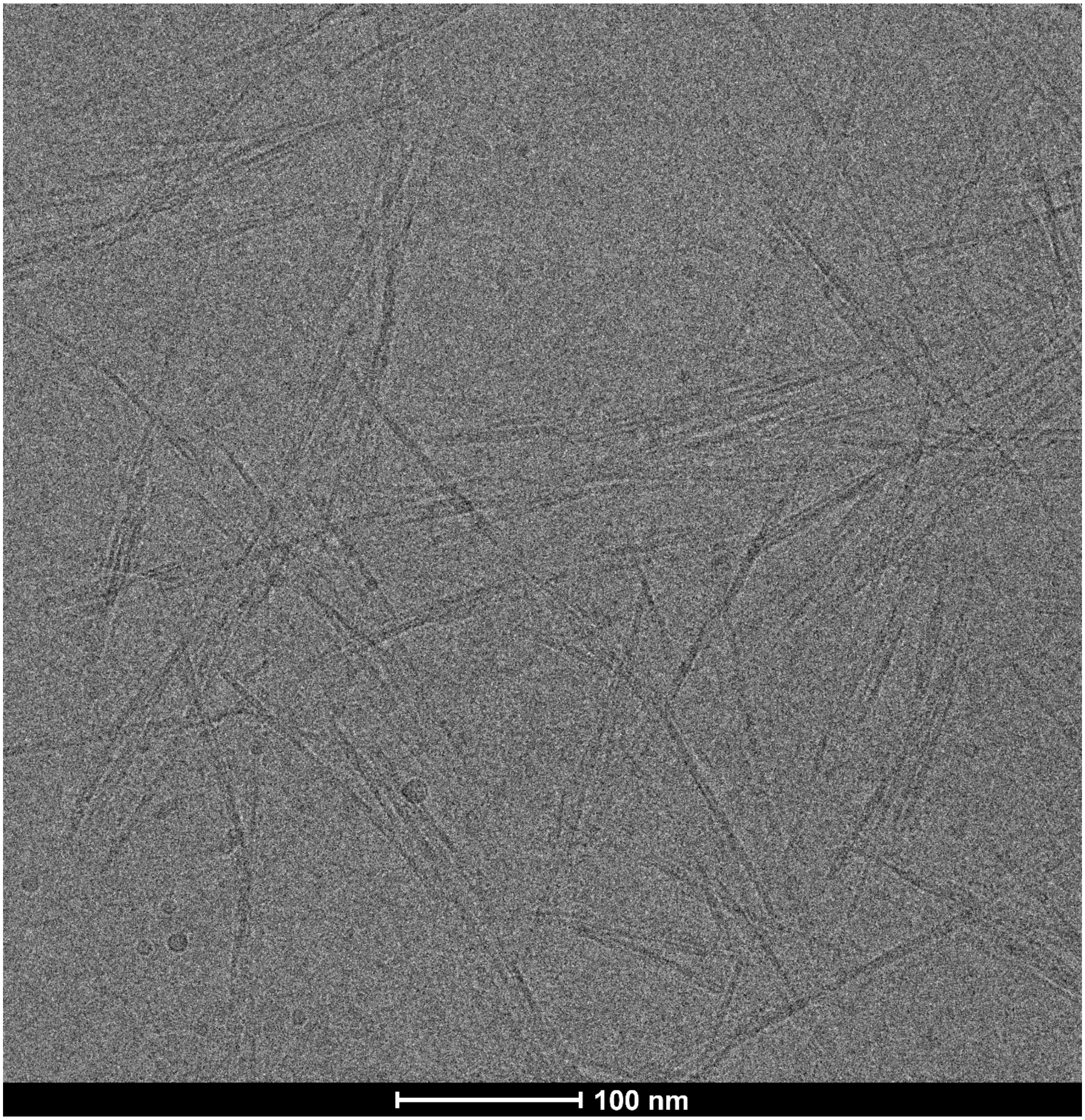

Figure 3.13 Cryo-TEM for catalyst suspension, PdPs@CNCs (t = 2h).

3.7.2 3-D Images under cryo conditons

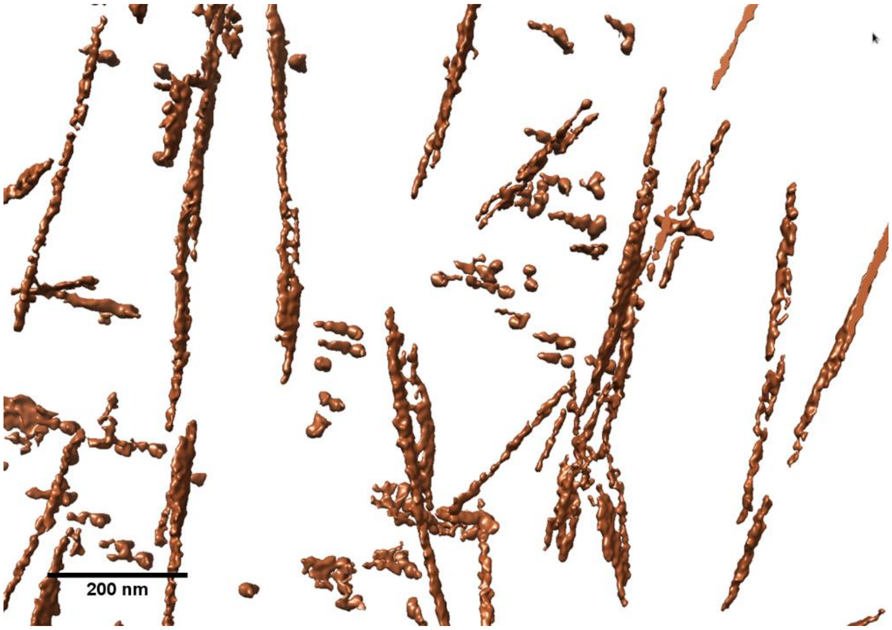

Figure 3.14 Tomogram of $PdCl_2$/CNCs in cryo conditions

Figure 3.15 Tomogram of $PdCl_2$/CNCs in cryo conditions, from a different area.

Figure 3.16 Tomogram of PdPs@CNCs in cryo conditions.

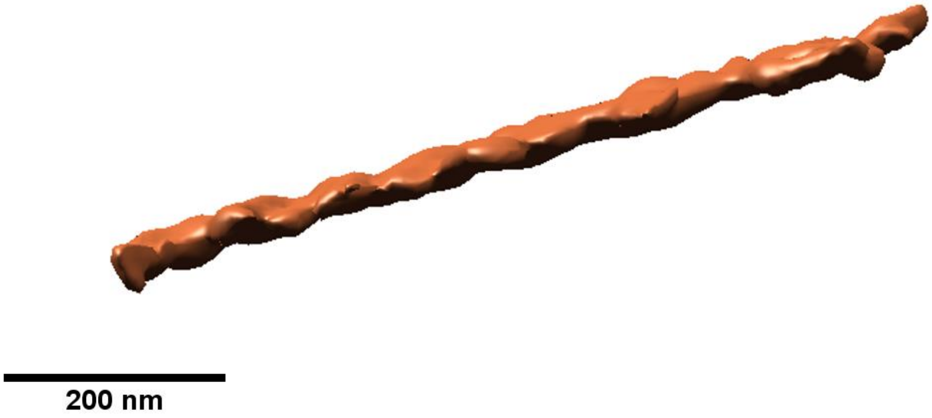

Figure 3.17 Tomogram of PdPs@CNCs in cryo conditions

3.7.3 Images at near focus conditions

To complement the findings from the cryo-TEM, both samples were air dried on TEM grids and observed using an FEI Falcon 2 direct detection device (DDD) and a phase plate on the Titan Krios 300 kV cryo-STEM, enabling near-focus observation, and with higher resolution than what was allowed in cryo-TEM.

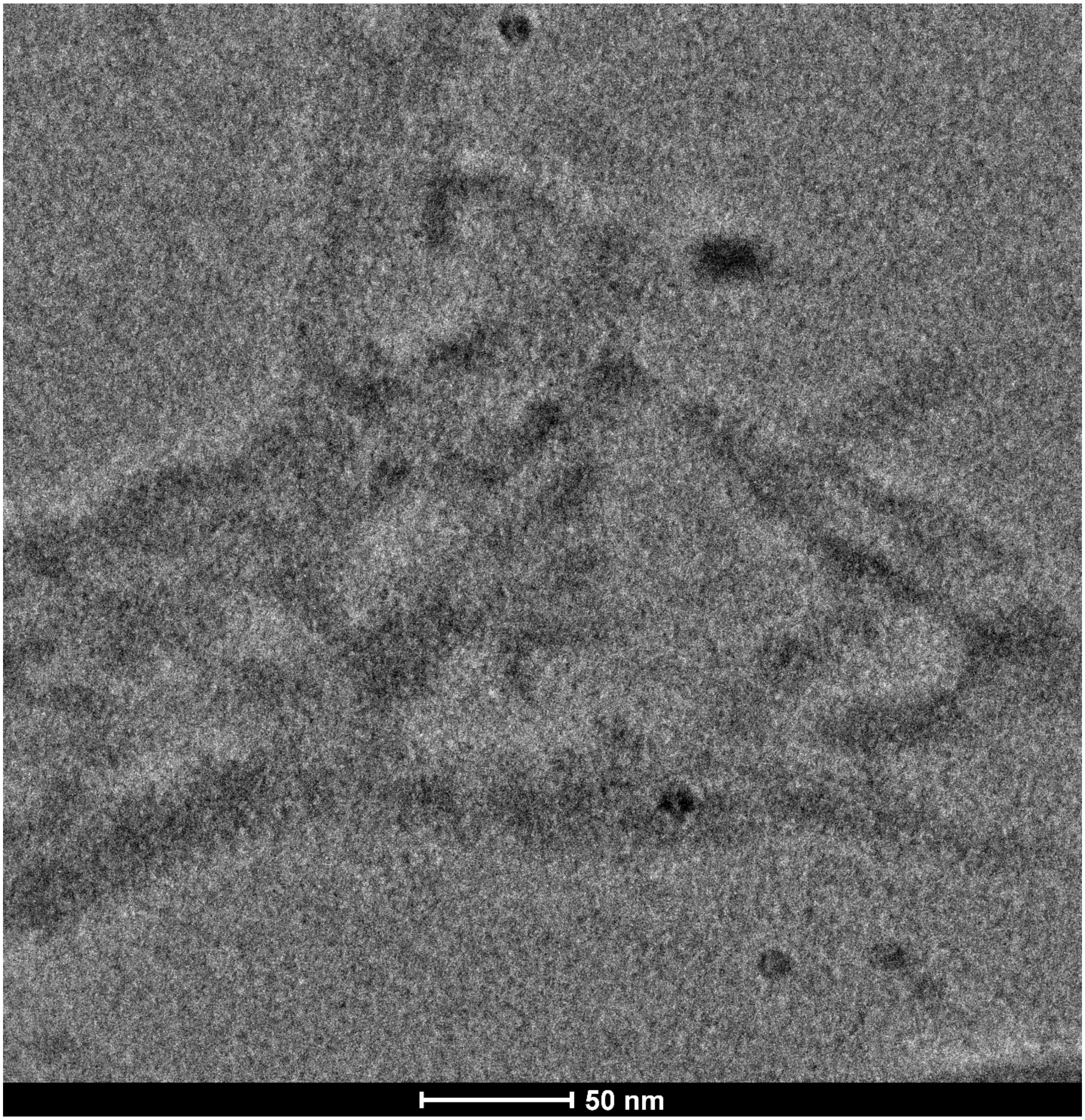

Figure 3.18 TEM images of PdPs@CNCs recorded using a DDD.

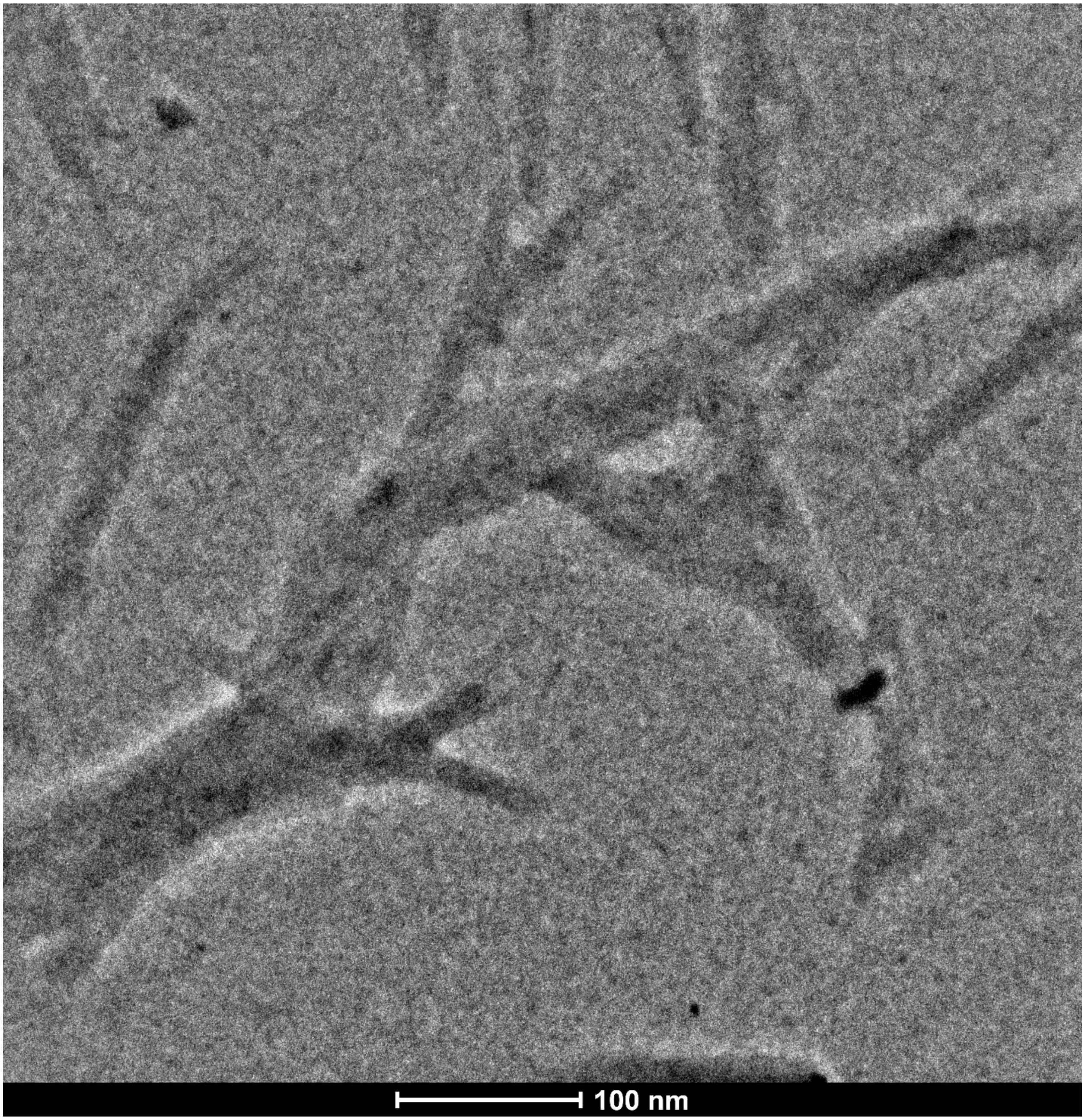

Figure 3.19 TEM images of PdPs@CNCs recorded using a DDD.

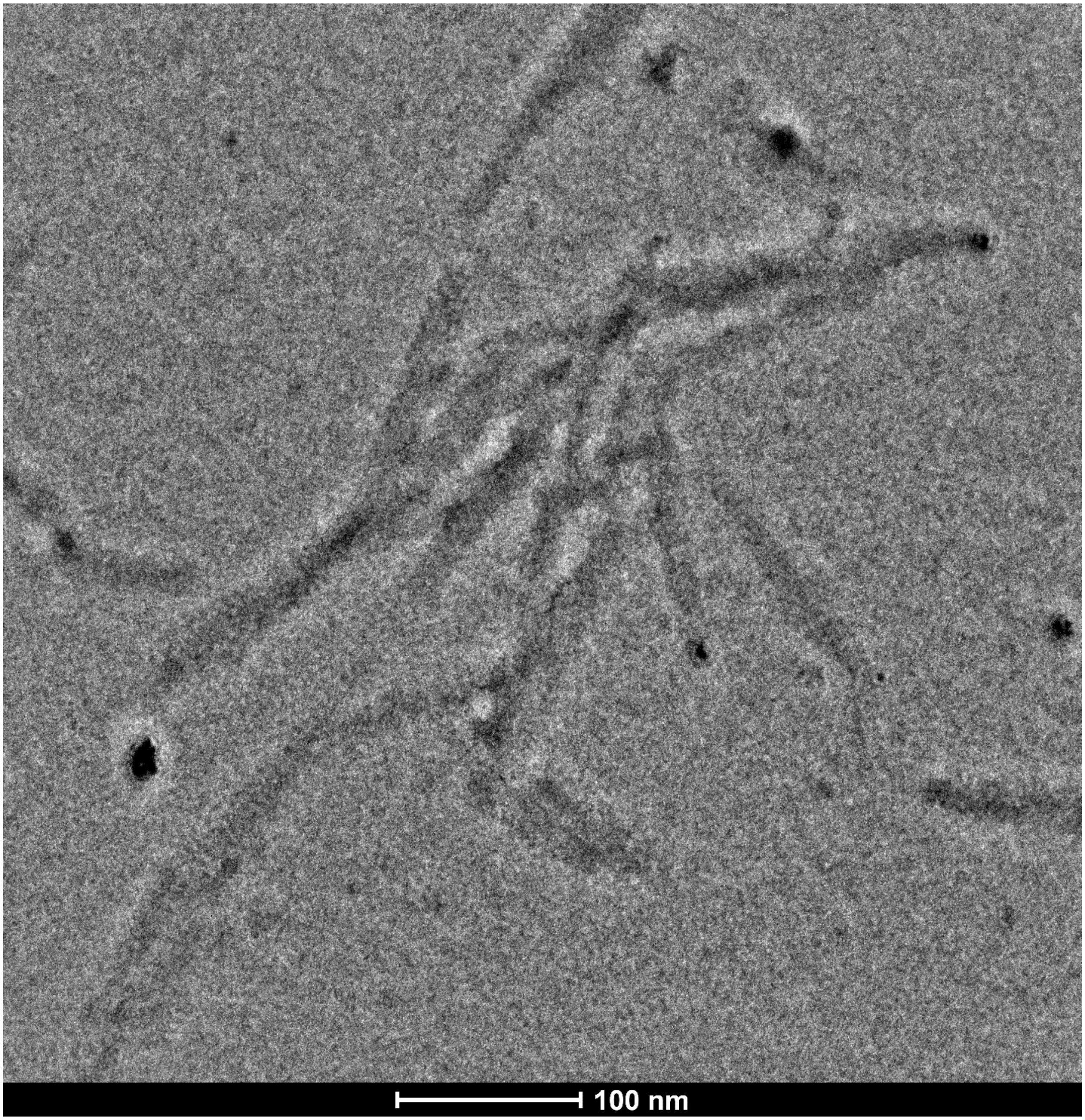

Figure 3.20 TEM images of PdPs@CNCs recorded using a DDD.

3.7.4 EDX analysis

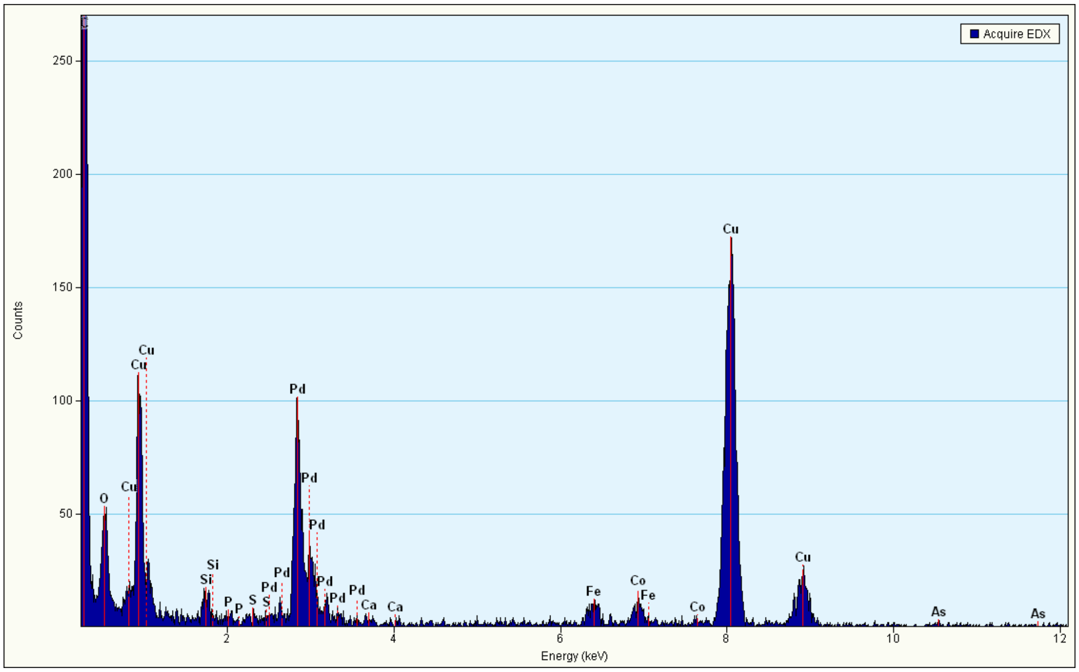

Figure 3.21 EDAX results for the catalyst, PdPs@CNCs, confirming the presence of palladium.

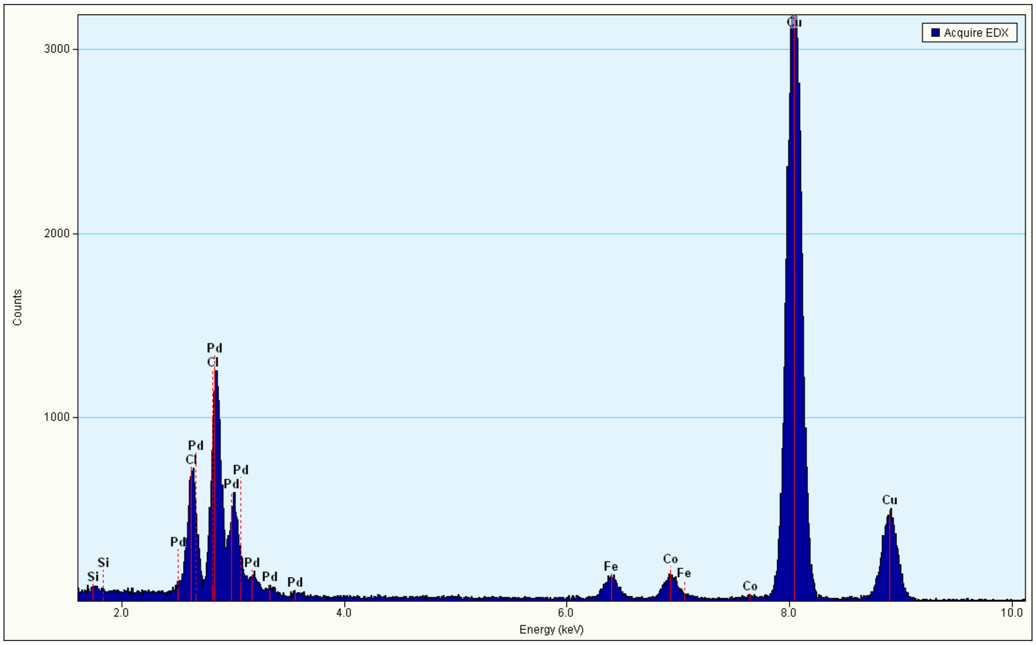

Figure 3.22 EDAX results for the precursor, $PdCl_2$/CNCs, showing both palladium and chloride.

4 Cellulose nanocrystals as reducers for accessing Ag NPs and their applications in hydrogenation of aldehydes, alkenes, alkynes and nitro arenes

In our continued attempt to bring forward innovative application of CNCs in catalysis, we purposed the use of abundant hydroxyl groups on the surface of CNCs for reduction of Ag^+ ions to Ag (0) NPs. A facile synthesis of Ag NPs directly from bulk silver metal is presented in this chapter, where the CNCs act as both support for Ag NPs and as reducers. The Ag NP-CNC hybrid composite is then used for the hydrogenation of aldehydes, alkenes, alkynes and nitro arenes.

This chapter is adapted from a published article, whose citation appear below, which is reprinted with permission from the Royal Chemical Society and all co-authors.

Madhu Kaushik, Alain Li, Reuben Hudson, Mitra Masnadi, Chao-Jun Li and Audrey Moores. Reversing aggregation: Direct synthesis of nanocatalysts from bulk metal. Cellulose nanocrystals as active support to access efficient hydrogenation silver nanocatalysts. *Green Chem*. 2015, DOI: 10.1039/C5GC01281C.

4.1 Abstract

A highly atom-economical synthetic method to access nanocatalysts from bulk metal is described. A water suspension of cellulose nanocrystals was exposed to an Ag wire, under air and light exposure. In 2 weeks, Ag nanoparticles of size 1.3 nm ± 0.3 nm were deposited onto the biopolymer. These species were active for the hydrogenation of aldehydes, 4-nitrophenol, alkenes and alkynes.

4.2 Introduction

Many different synthetic methods have been developed to access metal nanomaterials with well controlled size, shape, aspect ratio and thus properties. However, because metal nanoparticles (NPs) are kinetically stabilized materials, their synthesis often relies on intensive use of solvents, reagents, reducing and capping agents. The concept of atom economy, developed by Trost[1, 2] and adopted within the 12 principles of green chemistry for organic synthesis,[3, 4] remains to be systematically applied to nanosynthesis.[5-8] In recent years, efforts have been made to develop more sustainable synthetic methods to access these high-value materials,[5-8] including solvent-free methods,[9, 10] biomass-based approaches[8, 11] and greener reducers development.[12-15] An interesting avenue relies on by-passing the need to reduce metal salts and use a reduced metal form as starting material. While metal (0) organometallic species have been developed, they often require some synthetic effort and careful handling.[16-19] Bulk metal grinding is also a well-known approach, suffering from poor NP size and shape control.[10] A distinct and potentially milder approach relies on a result recently delineated by Hutchison and his group.[20] Bulk Cu and Ag materials were shown to generate nanoparticles in their surface vicinity, as the results of exposure to moisture, light and air. In this interesting work, no external oxidizing, reducing agents or energy were needed to turn bulk into nanomaterials.

In this article, we present the novel synthetic method to access metal nanoparticles based on this principle, thus bypassing two industrial steps necessary to access such nanomaterials: 1) the need to form metal halide salts produced industrially via reacting pure metals with halohydric acids and 2) the reduction of the resulting halogenide salts, or other derivatives originating from these salts. For this study, we used cellulose nanocrystals (CNCs) as a water suspendable, and mildly reducing support. Ag NPs were produced in days at room temperature, in the presence of light, in water, from a simple Ag wire and without using any other additive than CNCs. Characterization by transmission electron microscopy (TEM) and X-ray photoelectron spectroscopy (XPS), including Auger analysis, was performed to establish that the resulting material was a hybrid composed of CNCs onto which small Ag NPs were deposited (AgNPs@CNC). In this work, we used the resulting Ag NPs in the catalytic hydrogenation of aldehydes to afford primary alcohols in water, at 100^{o}C and 40 bars H_2.[21] We (Li) had recently demonstrated the homogeneous version of this reaction using Ag salts with ligands.[22] AgNPs@CNC were also effective in the hydrogenation of 4-nitrophenol, alkenes and alkynes. The aqueous suspension of AgNPs@CNC served as a biphasically separable catalytic system, recyclable up to 4 times, with negligible leaching.

CNCs are a class of functional nanomaterial readily obtained from cellulose via sulfuric acid hydrolysis.[23, 24] CNCs have well-defined size and morphology, high specific surface area, high aspect ratio, high crystalline order, chirality, high mechanical strength, and controllable surface chemistry. In addition, CNCs are inexpensive, renewable, biodegradable, non-toxic, and accessible industrially in large scale, from a local plant in Quebec.[25, 26] These properties have made CNCs useful in a range of applications, including the production of iridescent and birefringent films, reinforcing fillers in plastics and polymers, chiral materials, hydrogels, aerogels and supercapacitors.[24, 26-36] They have also been shown to act as active and water suspendable support to stabilize NPs of Pd,[37-40] Pt,[41, 42] Au,[43-45] Ag,[43, 46-50] Cu[43] and Se.[51] Specifically, AgNPs@CNCs were previously synthesized from Ag salts, such as $AgNO_3$, using either $NaBH_4$,[43, 46-48] or CNCs themselves as a reducing agent.[49, 50] Ag NPs constitute interesting materials, used for antibacterial applications,[46, 49, 50, 52, 53] 4-nitrophenol reductions,[52, 54-56] oxidation,[57, 58] and alcohols cross-coupling[59] reactions.

4.3 Materials and methods

CNCs synthesised by sulphuric acid hydrolysis of wood pulp were provided by FPInnovations. To redisperse dried CNC samples in suspension, the Sonics & Materials Inc. Vibra-Cell VC1500 ultrasonicator (220V, 15A, 1500W, 20 kHz) was used. The Metrohm Titrando (836 base, 804 Ti stand, and 802 stirrer) autotitrator was used for attaining various pH values. The transmission electron microscopy (TEM) samples were deposited on 400 mesh carbon coated copper grids supplied by Electron Microscopy Sciences. The analyses were performed on the Tecnai 12 microscope (FEI electron optics) equipped with a Lab6 filament at 120kV, equipped with Gatan 792 Bioscan 1k x 1k Wide Angle Multiscan CCD Camera (Gatan Inc.); and FEI G2 F20 Cryo-S/TEM microscope (FEI, Inc) at 200kV, equipped with Gatan Ultrascan 4k x 4k Digital (CCD) Camera System at different magnifications corresponding to different pixel size (defocus level ranging from − 2.5 to − 4.5 μm). ICP measurements were taken using a Thermo ICP-OES to measure Ag content at the elemental wavelength of 328.068nm. XPS was performed on a VG ESCALAB 3 MKII spectrometer (VG, Thermo Electron Corporation, UK) equipped with an Mg Kα source. All hydrogenation reactions were carried out in a Parr Instruments 5000 Series Multiple Reactor System. The monitoring of catalytic hydrogenation was performed using an Agilent 7890A series gas chromatograph equipped with a MS detector (5975C) on an Agilent DB-WAX column and Agilent Cyclodex-B column. Cyclohexanol (reagentplus grade, 99%, Sigma Aldrich) was used as internal standard for quantification of all hydrogenation reactions. All reagents, solvents and substrates were procured from Sigma Aldrich.

4.3.1 Synthesis of Ag NPs

500 mg of CNCs were redispersed in 100 ml water. Ag wire (7 g) was added to the CNC suspension and stirred at room temperature for 20 days (Figure 4.1). For blank comparisons, a silver wire was also immersed in water at stirred at room temperature for 20 days. The Ag content was monitored by ICP-OES. The resulting solution was drying by evaporation and the resulting AgNPs@CNCs was collected as a very light brown powder and fully characterized by XPS, TEM and EDAX experiments.

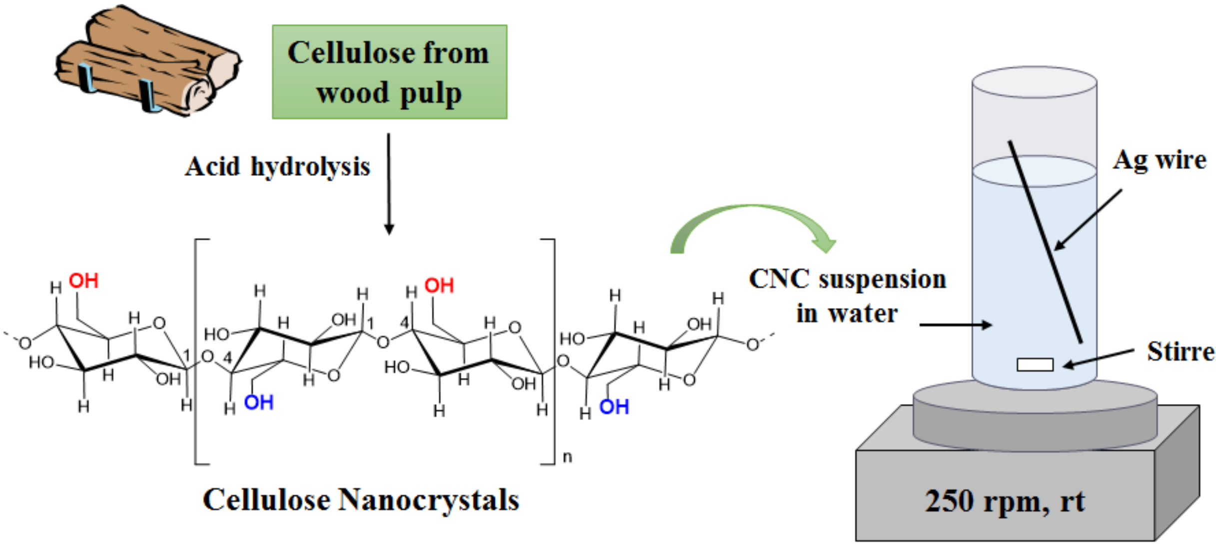

Figure 4.1 Molecular structure of CNCs and the experimental set-up.

4.3.2 ICP measurements

1 ml sample was taken out form the 100 ml CNC suspension being stirred at room temperature with Ag wire at day 3, 7, 10, 15 and 20. The liquid sample was then evaporated overnight in a vacuum oven and the residue was dissolved with 1mL of concentrated HNO_3. 0.25mL of the HNO3 solution was then diluted using deionized water up to 25mL and the sample was tested using ICP-OES.

4.3.3 TEM and EDS

5ul of samples were deposited on carbon film coated 200 Mesh copper EM grids for two minute, followed by blotting off the excess liquid with the edge of a filter paper. The grids were then imaged using FEI G2 F20 Cryo-STEM operated at 200 kV (FEI, Inc). Images were recorded with a Gatan Ultrascan 4k × 4k Digital (CCD) Camera System.

4.3.4 Hydrogenation of substrates

In a typical reaction, substrate (0.1 mmol) was added to the catalyst suspension prepared above, AgNPs@CNCs, (5mL). To this mixture was added cyclohexanol (0.1

mmol) as internal standard. Then, the mixture was placed in a PARR multiple reactor system under H_2 pressure, 40 bars, 1000rpm, for 24 h at 100ºC. Afterwards, the reaction mixture was extracted with diethyl ether and then injected on the GC-MS for monitoring the reaction.

4.3.5 Monitoring the Hydrogenation Reactions

The monitoring of catalytic hydrogenation and determination of enantiomeric excess were performed using an Agilent 7890A series gas chromatograph equipped with a MS detector (5975C) on an Agilent Cyclodex-B column. Response factors for all compounds were calculated using cyclohexanol as the internal standard. The response factor was calculated by running a standard solution containing known substrate and internal standard concentrations on the GC-MS to determine the area of the two compounds:

Response Factor, R = (concentration of substrate/ concentration of internal standard)*(peak area of internal standard/ peak area of substrate)

4.3.6 Recycling experiments

Benzaldehyde (0.1 mmol) was added to the catalyst suspension prepared above, AgNPs@CNCs, (5mL). To this mixture was added cyclohexanol (0.1 mmol) as internal standard. Then, the mixture was placed in a PARR multiple reactor system under H_2 pressure, 40 bars, 1000rpm, for 24 h at 100ºC. Afterwards, reaction mixture was extracted with diethyl ether and then injected on the GC-MS for monitoring the conversion. The remaining water suspension, having the catalyst, was then used for the next cycle. The process was repeated up to five cycles.

4.4 Results and discussions

In an initial set of experiments, silver wires were immersed in CNC suspensions with concentrations of either 0.5 %, 1 % or 1.5 % (w/w) or in pure water. Some vials were exposed to light, while the others were kept in the dark (by wrapping with aluminium foil).

All samples were air-exposed. After 45 days, the Ag content in the samples was measured using inductively coupled plasma – mass spectroscopy (ICP-MS) (Table 4.1).

Table 4.1 Ag content after 45 days in Ag wire exposed CNC suspensions, measured by ICP-MS. All samples were air exposed.

Entry	**CNC concentration (in w/w)**	**Light exposure**	**Ag content (in µg.L^{-1})**
1	0.5	Yes	163.1
2	1.0	Yes	166.3
3	1.5	Yes	144.4
4	No CNC	Yes	5.7
5	0.5	No	4.1
6	1.0	No	4.5
7	1.5	No	4.4
8	No CNC	No	5.1

The results were bimodal. High, and essentially similar, concentrations of Ag were observed when CNCs were present in the suspension and when the suspensions were exposed to light (table 1, entries 1-3). Any other circumstance led to the presence of a baseline quantity of Ag (table 1, entries 4-8). Light proved essential to silver oxidation in accordance with the work of Hutchison.[20] But CNC were also essential, proving their key role in the silver wire depletion. The kinetics of this process was further explored with a 0.5 % CNC suspension exposed to the Ag wire at room temperature (Figure 4.1). Its Ag content was monitored by ICP-MS upon sampling on days 3, 7, 10, 15 and 20. Two sets of experiment were carried out side by side, one in the presence, one in absence of light. Figure 4.2 shows a steady increase of the Ag content in the CNC suspension for the first 10 days with light, after which it reached a plateau around 160 µg.L^{-1}. This value is comparable to results obtained at 45 days, indicating the achievement of an equilibrium state. Again, absence of CNC or light led to no significant increase in Ag concentration (Figure 4.2). The role of air was probed by immersing a silver wire in a degassed CNC suspension, in the presence of light. No significant amount of Ag was observed in this case either.

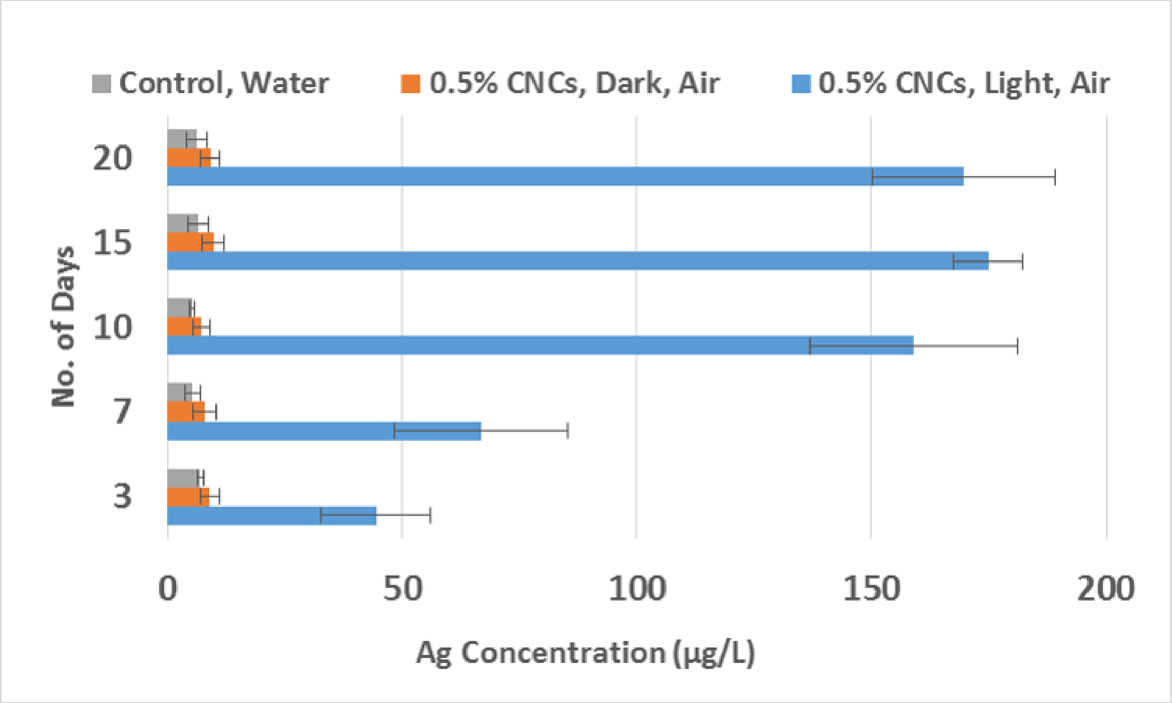

Figure 4.2 Ag content over 20 days by ICP-MS measurements. The values observed are an average of five data points for each type of experiment.

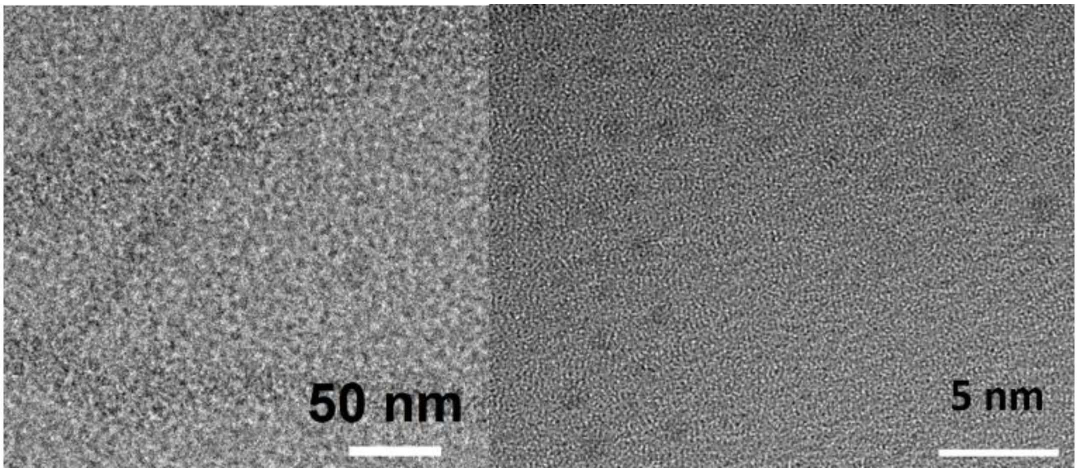

Figure 4.3 TEM images of Ag NPs supported on CNCs.

The ICP-MS measurements were performed after proper Ag digestion and were thus a means to quantify Ag in suspensions in all its possible forms, i.e. Ag salts and suspended Ag colloids. In order to gain more insight into the role of the CNC in the observed phenomenon as well as the nature of the ICP-MS measured Ag, a complete characterization of the resulting suspended material was undergone. A sample of 0.5% CNC suspension, stirred at room temperature for 20 days while exposed to Ag wire, light and air was dried onto a Cu TEM grid. On TEM images, CNCs were observed as well-dispersed, low contrast whiskers and the Ag NPs appeared as darker spots, mostly onto the CNCs, with an average size of 1.3 nm ± 0.3 nm (Figure 4.3, in appendix: Figure 4.7 and Figure 4.8). The presence of Ag was confirmed by EDS (Figure 4.8). A careful selection of focusing conditions allowed to overcome the usual difficulties associated with CNCs/metal hybrid composites imaging.[60, 61] Reduction of Ag under TEM conditions was excluded based on time analysis, Ag NPs size and specific location onto CNC and XPS results (*vide infra*).[62] These TEM results were in agreement to the previously reported CNC images,[26, 60, 61, 63] showing that the CNCs did not aggregate in suspension and retained both their high surface area and rod-like form.

Next, XPS experiments were performed to gain insight into the Ag oxidation state. Differentiation between Ag (I) and Ag (0) was not as predominant in the photoelectron region, because both species have similar binding energies and their peaks are not as distinct. XPS in the Auger region was performed in addition to the XPS in the photoelectron region. Luckily, in the Auger region, Ag (I) and Ag (0) each produce an individual peak, at 355.7 eV and 357.21 eV respectively. They were both observed in AgNPS@CNCs samples (Figure 4.4). XPS being a surface technique, sputtering was performed on the samples for 15 seconds and led to Ag (I) peak disappearance, leaving the Ag (0) peak alone (Figure 4.4). Standards for this method were obtained using Ag metal (Figure 4.9).

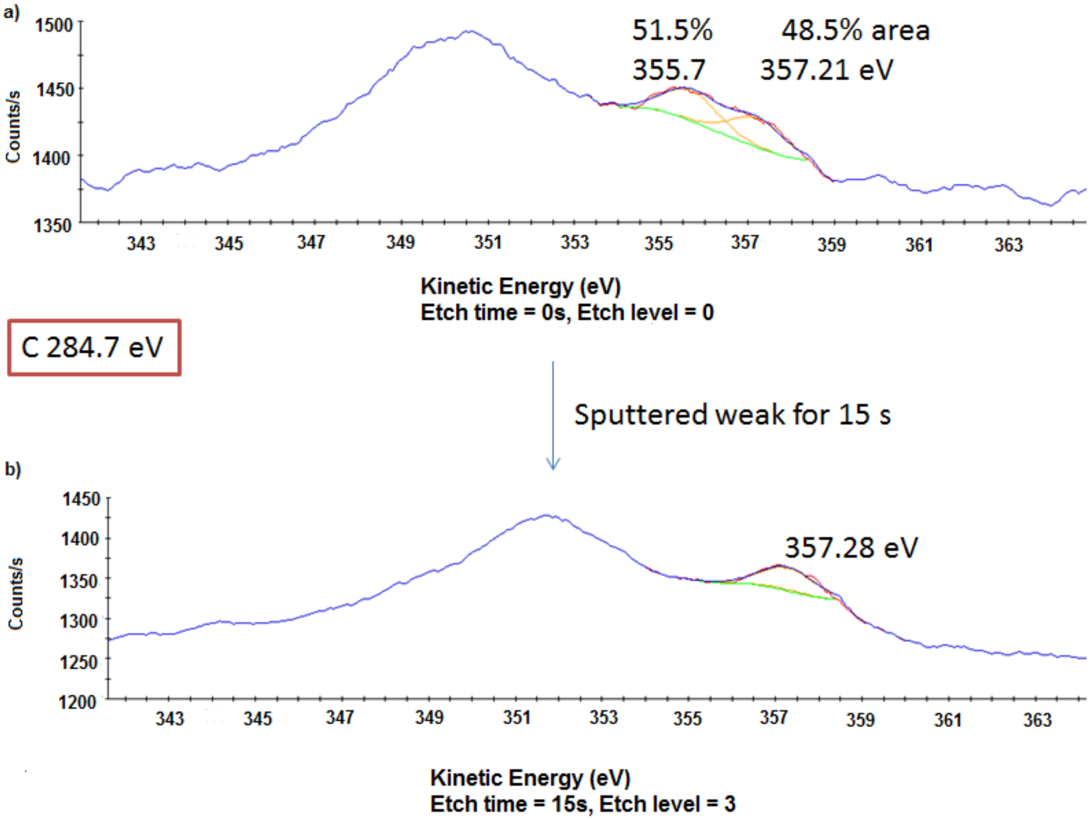

Figure 4.4 XPS spectrum in the Ag Auger region: a) AgNPs@CNCs, b) after sputtering an AgNPs@CNCs sample for 15 s.

This study thus proved that: 1) Ag (0) NPs (with partially oxidized surface) were produced at the surface of CNCs upon immersing a Ag wire in a CNC suspension; 2) both CNCs and light were necessary for this reaction to proceed. A proposed mechanism is depicted in Figure 4.5. According to the study of Hutchison and coll., light, moisture and air are able to oxidize the Ag wire into Ag (I) salts.20 In absence of CNCs, the reaction stops at this stage and the Ag concentration in suspension remains marginal. In fact, in absence of potential support, Ag NPs tend to dissolve in pure water.[64] When CNCs are in suspension, the Ag salts are consumed towards the growth of Ag NPs at the CNC surface, causing more Ag depleting from the wire and a sharp Ag concentration increase. CNCs are nanowhiskers composed of cellulose strings packed in a crystalline fashion. Cellulose itself is a polymer of cellobiose, a dimer of glucose. Therefore, the surface of

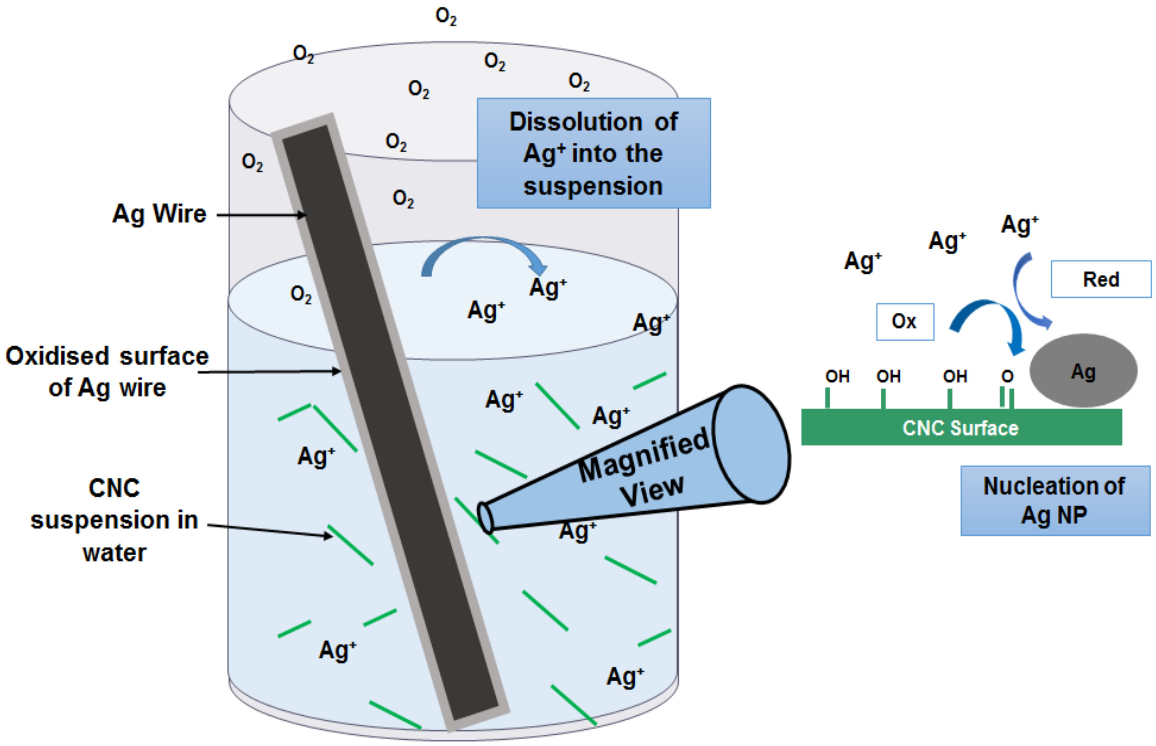

Figure 4.5 Pictorial representation of the mechanism for the generation of Ag NPs from Ag wire in aqueous CNC suspensions.

CNCs is lined with of hydroxyl groups, which has been shown before to enable the reduction of Ag (I) back into Ag (0).[65] Cellulose was also shown to allow this reduction under microwave conditions.[66] In the CNC synthesis process, by strong sulfuric acid hydrolysis, some hydroxyl groups are turned into sulfate esters (sulfur content = 3%). These sulfate groups have been proven to favour stabilisation and nucleation of Ag NPs in a recent research.[47] A recent review on the evaluation of Ag NPs synthesis according to sustainable principles may be used to access this novel method.[8] Over the 8 evaluation criteria used, this method ranks very high on 7 of them (reducing agent, capping agent, solvent, local resources used, reaction temperature, equipment and size range).

Beyond its key role in the Ag NPs synthesis, the CNC suspension also acted as a stabilizing medium for the nanocatalysts, which were stable as non-aggregated, small NPs, and a readily usable and separable catalytic system. The AgNPs@CNCs suspension obtained was tested as catalysts for the hydrogenation of unsaturated compounds, including aldehydes, alkenes, alkynes and nitro, in water (Table 4.2). To start with, benzaldehyde was chosen as the model substrate for optimisation of temperature and pressure conditions (Table 4.3). At 100°C and 40 bars H_2, benzaldehyde was successfully hydrogenated to benzyl alcohol with a yield of 96% (Table 4.2, entry 1).

Table 4.2 Hydrogenation of unsaturated compounds using AgNPs@CNCs[a]

Entry	Substrate	Product	Yield [b]
1	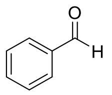	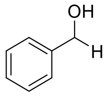	96%
2	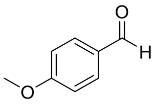	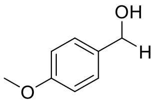	72%
3	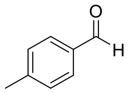	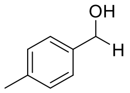	78%
4	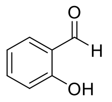	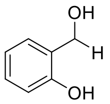	83%
5	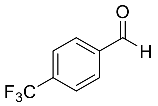	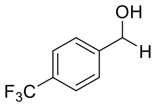	43%
6	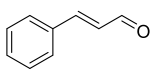	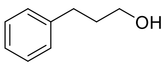	89%
7	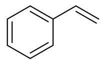	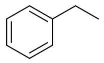	98%
8	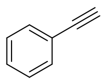	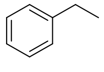	91%
9	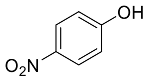	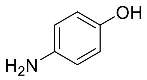	100%
10	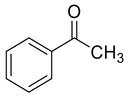	N/A	0%

[a]: *reaction conditions: 100°C, 40 bars H_2, 24 h, water as solvent*
[b]: *determined by GC-MS*

The homogeneous counterpart of this reaction was recently demonstrated by us (Li) under comparable conditions and AgNPs@CNCs offer an appealing means of heterogenizing this process in an atom-economical fashion.[22] Further screening was performed on substituted aromatic aldehydes (Table 4.2, entries 2-5). Methyl and methoxy substitution in para position, as well as hydroxyl in ortho, afforded good yields. Trifluoromethyl however gave poor results, possibly due to solubility issues. Vinyl aldehydes also worked well, with complete reduction of both C=O and C=C bonds (entry 6). Complete reduction of C-C double and triple was also demonstrated on styrene and phenylacetylene (entries 7-8). We were also pleased to see that a nitroarenes (entry 9) could be turned into aniline derivative, in a process that is more atom economical than the classic NaBH4, silver-catalysed reduction. To the best of our knowledge, this is the first example of this reaction being performed with Ag NPs and H_2 as a reducer. Ketones however proved unreactive under these (entry 10). The catalyst could also be easily recycled by addition of an organic solvent followed by phase separation, and the aqueous AgNPs@CNCs suspension were reused in a subsequent reaction. The yields were quantitative in the 4 first cycles, after which the activity reduced drastically (Figure 4.6).

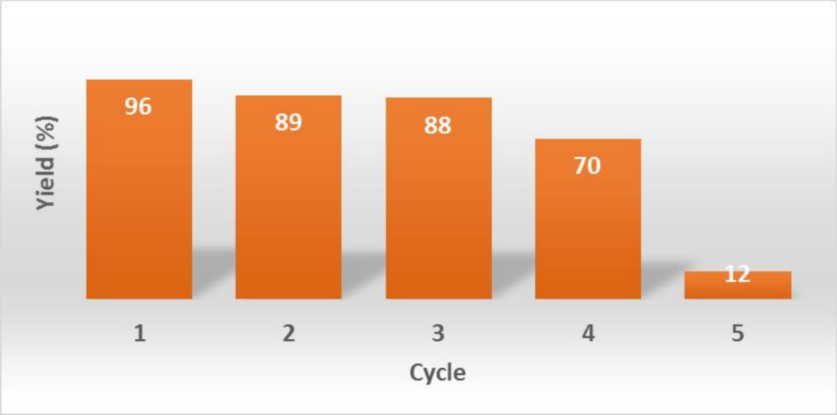

Figure 4.6 Recycling experiments.

This sharp decrease was coincidental with the transformation of the water suspension into a gel, presumably because of water loss upon multiple workups. This gel is likely to lead to a drop in catalytic activity because of diffusion limitation. The leaching of Ag was quantified from the product of benzaldehyde hydrogenation. It was determined that from the 5 mL of a typical catalytic test, 95 ng.L^{-1} of Ag had leached in the product. Compared to the original 168 µg.L-1 concentration of Ag in the same solution, this corresponds to a marginal depletion of 0.056%. As the synthetic method described therein could be considered lengthier than comparable methods, it was checked that AgNO3 salts produced the same outcome as Ag wire exposure. A 175 µg/L aqueous solution of AgNO3 was stirred at room temperature in presence of CNCs (0.5 wt%) for 20 days. The resulting system performed very well for the hydrogenation of benzaldehyde (97% yield). As a control, it was checked that either a CNC suspension or $AgNO_3$ solution alone afforded no conversion for the same reaction (in appendix: Figure 4.10).

4.5 Conclusions

In this article, we described for the first time the direct Ag NPs synthesis from bulk Ag metal in a one-pot setting. This facile, inexpensive synthetic method proceeded in water at room temperature. CNCs played a key role as high surface support and *in situ* reducer to drive the depletion of Ag from a metal wire and afford 1.3 nm ± 0.3 nm Ag NPs. The resulting hybrid were fully characterized by TEM and XPS and tested for their catalytic activity. Their ability to hydrogenate aldehydes, 4-nitrophenol, alkenes and alkynes was shown and they afford a cheap and sustainable alternative for their homogeneous counterparts.

4.6 References

1. B. M. Trost, *Acc. Chem. Res.*, 2002, **35**, 695.
2. B. M. Trost, *Angew. Chem. Int. Ed.*, 1995, **34**, 259.
3. P. Anastas and N. Eghbali, *Chem. Soc. Rev.*, 2010, **39**, 301.
4. P. T. Anastas and J. C. Warner, *Green Chemistry: Theory and Practice*, Oxford University Press, New York, 1998.
5. J. A. Dahl, B. L. S. Maddux and J. E. Hutchison, *Chem. Rev.*, 2007, **107**, 2228.
6. C. J. Murphy, *J. Mater. Chem.*, 2008, **18**, 2173.
7. M. J. Eckelman, J. B. Zimmerman and P. T. Anastas, *J. Ind. Ecol.*, 2008, **12**, 316.

8. M. Cinelli, S. R. Coles, M. N. Nadagouda, J. Błaszczyński, R. Słowiński, R. S. Varma and K. Kirwan, *Green Chem.*, 2015, **17**, 2825.
9. M. J. Rak, N. K. Saadé, T. Friščić and A. Moores, *Green Chem.*, 2014, **16**, 86.
10. M. J. Rak, T. Friščić and A. H. Moores, *Faraday Discuss.*, 2014, **170**, 155.
11. J. Virkutyte and R. S. Varma, *Chem. Sci.* , 2011, **2**, 837.
12. V. Kelsen, B. Wendt, S. Werkmeister, K. Junge, M. Beller and B. Chaudret, *Chem. Commun.*, 2013, **49**, 3416.
13. K. Pelzer, O. Vidoni, K. Philippot, B. Chaudret and V. Colliere, *Adv. Funct. Mater.*, 2003, **13**, 118.
14. C. Pan, K. Pelzer, K. Philippot, B. Chaudret, F. Dassenoy, P. Lecante and M.-J. Casanove, *J. Am. Chem. Soc.*, 2001, **123**, 7584.
15. M. Kaushik, H. M. Friedman, M. Bateman and A. Moores, *RSC Adv.*, 2015.
16. K. Philippot and B. Chaudret, *C. R. Chimie*, 2003, **6**, 1019.
17. B. Chaudret, *C. R. Phys.*, 2005, **6**, 117.
18. S. A. Stratton, K. L. Luska and A. Moores, *Catal. Today*, 2012, **183**, 96.
19. R. Linhardt, Q. M. Kainz, R. N. Grass, W. J. Stark and O. Reiser, *RSC Adv.*, 2014, **4**, 8541.
20. R. D. Glover, J. M. Miller and J. E. Hutchison, *ACS Nano*, 2011, **5**, 8950.
21. D. E. De Vos, P. G. N. Mertens, F. Cuypers, P. Vandezande, X. Ye, F. Verpoort and I. F. J. Vankelecom, *Applied Catalysis A*, 2007, **325**, 130.
22. Z. Jia, F. Zhou, M. Liu, X. Li, A. S. C. Chan and C.-J. Li, *Angew. Chem. Int. Ed.*, 2013, **52**, 11871.
23. D. Klemm, F. Kramer, S. Moritz, T. Lindström, M. Ankerfors, D. Gray and A. Dorris, *Angew. Chem. Int. Ed.*, 2011, **50**, 5438.
24. S. J. Eichhorn, A. Dufresne, M. Aranguren, N. E. Marcovich, J. R. Capadona, S. J. Rowan, C. Weder, W. Thielemans, M. Roman, S. Renneckar, W. Gindl, S. Veigel, J. Keckes, H. Yano, K. Abe, M. Nogi, A. N. Nakagaito, A. Mangalam, J. Simonsen, A. S. Benight, A. Bismarck, L. A. Berglund and T. Peijs, *Journal of Material Science*, 2010, **45**, 1.
25. J. A. C. Gömez, U. W. Erler and D. O. Klemm, *Macromol. Chem. Phys.*, 1996, **197**, 953.

26. Y. Habibi, L. A. Lucia and O. J. Rojas, *Chem. Rev.*, 2010, **110**, 3479.
27. X. Cao, Y. Habibi, W. L. E. Magalhães, O. J. Rojas and L. A. Lucia, *Curr. Sci.*, 2011, **100**, 1172.
28. S. J. Eichhorn, *Soft Matter*, 2011, **7**, 303.
29. H. Koga, E. Tokunaga, M. Hidaka, Y. Umemura, T. Saito, A. Isogai and T. Kitaoka, *Chem. Commun.*, 2010, **46**, 8567.
30. H. Koga, A. Azetsu, E. Tokunaga, T. Saito, A. Isogai and T. Kitaoka, *J. Mater. Chem.*, 2012, **22**, 5538.
31. X. Yang and E. D. Cranston, *Chem. Mater.*, 2014, **26**, 6016.
32. J. Yang, C.-R. Han, J.-F. Duan, M.-G. Ma, X.-M. Zhang, F. Xu, R.-C. Sun and X.-M. Xie, *J. Mater. Chem.*, 2012, **22**, 22467.
33. N. L. Garcia de Rodriguez, W. Thielemans and A. Dufresne, *Cellulose*, 2006, **13**, 261.
34. S. Y. Liew, D. A. Walsh and W. Thielemans, *RSC Adv.*, 2013, **3**, 9158.
35. S. Y. Liew, S. Shariki, A. Vuorema, D. A. Walsh, F. Marken and W. Thielemans, in *ACS Symposium Series*, American Chemical Society, 2012, vol. 1107, pp. 75-106.
36. K. E. Shopsowitz, H. Qi, W. Y. Hamad and M. J. MacLachlan, *Nature*, 2010, **468**, 422.
37. C. M. Cirtiu, A. F. Dunlop-Brière and A. Moores, *Green Chem.*, 2011, **13**, 288.
38. X. Wu, C. Lu, W. Zhang, G. Yuan, R. Xiong and X. Zhang, *J. Mater. Chem. A*, 2013, **1**, 8645.
39. M. Rezayat, R. K. Blundell, J. E. Camp, D. A. Walsh and W. Thielemans, *ACS Sustainable Chem. Eng.*, 2014, **2**, 1241.
40. M. Kaushik, K. Basu, C. Benoit, C. M. Cirtiu, H. Vali and A. Moores, *J. Am. Chem. Soc.*, 2015, **137**, 6124.
41. K. Benaissi, L. Johnson, D. A. Walsh and W. Thielemans, *Green Chem.*, 2010, **12**, 220.
42. F. Coccia, L. Tonucci, D. Bosco, M. Bressan and N. d'Alessandro, 2012, **14**, 1073.

43. S. Padalkar, J. R. Capadona, S. J. Rowan, C. Weder, Y.-H. Won, L. A. Stanciu and R. J. Moon, *Langmuir*, 2010, **26**, 8497.
44. E. Lam, S. Hrapovic, E. Majid, J. H. Chong and J. H. T. Luong, *Nanoscale*, 2012, **4**, 997.
45. J.-L. Huang, D. G. Gray and C.-J. Li, *Beilstein J. Org. Chem.*, 2013, **9**, 1388.
46. Z. Shi, J. Tang, L. Chen, C. Yan, S. Tanvir, W. A. Anderson, R. M. Berry and K. C. Tam, *J. Mater. Chem. B*, 2015, **3**, 603.
47. A. R. Lokanathan, K. M. A. Uddin, O. J. Rojas and J. Laine, *Biomacromolecules*, 2014, **15**, 373.
48. H. Liu, D. Wang, Z. Song and S. Shang, *Cellulose*, 2011, **18**, 67.
49. N. Drogat, R. Granet, V. Sol, A. Memmi, N. Saad, C. Klein Koerkamp, P. Bressollier and P. Krausz, *J. Nanopart. Res.*, 2011, **13**, 1557.
50. R. Xiong, C. Lu, W. Zhang, Z. Zhou and X. Zhang, *Carbohydr. Polym.*, 2013, **95**, 214.
51. Y. Shin and G. J. Exarhos, *Mater. Lett.*, 2007, **61**, 2594.
52. W. Xu, W. Jin, L. Lin, C. Zhang, Z. Li, Y. Li, R. Song and B. Li, *Carbohydr. Polym.*, 2014, **101**, 961.
53. F. Cui, J. Liu, Z. Zhao and H. Feng, *J. Mater. Chem.*, 2012, **22**, 13891.
54. S. K. Das, M. M. R. Khan, A. K. Guha and N. Naskar, *Green Chem.*, 2013, **15**, 2548.
55. H. Liu, H. Liu, S. Yang and C. Nie, *Mater. Lett.*, 2013, **100**, 296.
56. K. Jiang, H.-X. Zhang, Y.-Y. Yang, R. Mothes, H. Lang and W.-B. Cai, *Chem. Commun.*, 2011, **47**, 11924.
57. P. Singh, G. Lamanna, C. Menard-Moyon, F. M. Toma, E. Magnano, F. Bondino, M. Prato, S. Verma and A. Bianco, *Angew. Chem. Int. Ed.*, 2011, **50**, 9893.
58. A. Biabani-Ravandi, M. Rezaei and Z. Fattah, *Chem. Eng. J.*, 2013, **219**, 124.
59. A. Satsuma and K.-i. Shimizu, *J. Jpn. Pet. Inst.*, 2011, **54**, 347.
60. M. Kaushik, W. C. Chen, T. G. M. van de Ven and A. Moores, *Nordic Pulp and Paper Res. J.* , 2014, **29**, 77.

61. M. Kaushik, C. Fraschini, G. Chauve, J.-L. Putaux and A. Moores, in *The Transmission Electron Microscopy*, ed. M. Khan, InTech, 2015, p. Accepted May 25 2015.
62. M. N. Nadagouda and R. S. Varma, *Aust. J. Chem.*, 2009, **62**, 260.
63. D. Klemm, B. Heublein, H. P. Fink and A. Bohn, *Angew. Chem. Int. Ed.*, 2005, **44**, 3358.
64. C. Stephan, K. J. Wilkinson and M. Hadioui, *Nanoscience and nanometrology*, 2015, **1**, 20.
65. P. Raveendran, J. Fu and S. L. Wallen, *J. Am. Chem. Soc.*, 2003, **125**, 13940.
66. M. N. Nadagouda and R. S. Varma, *Biomacromolecules*, 2007, **8**, 2762.

4.7 Appendix

4.7.1 TEM Images

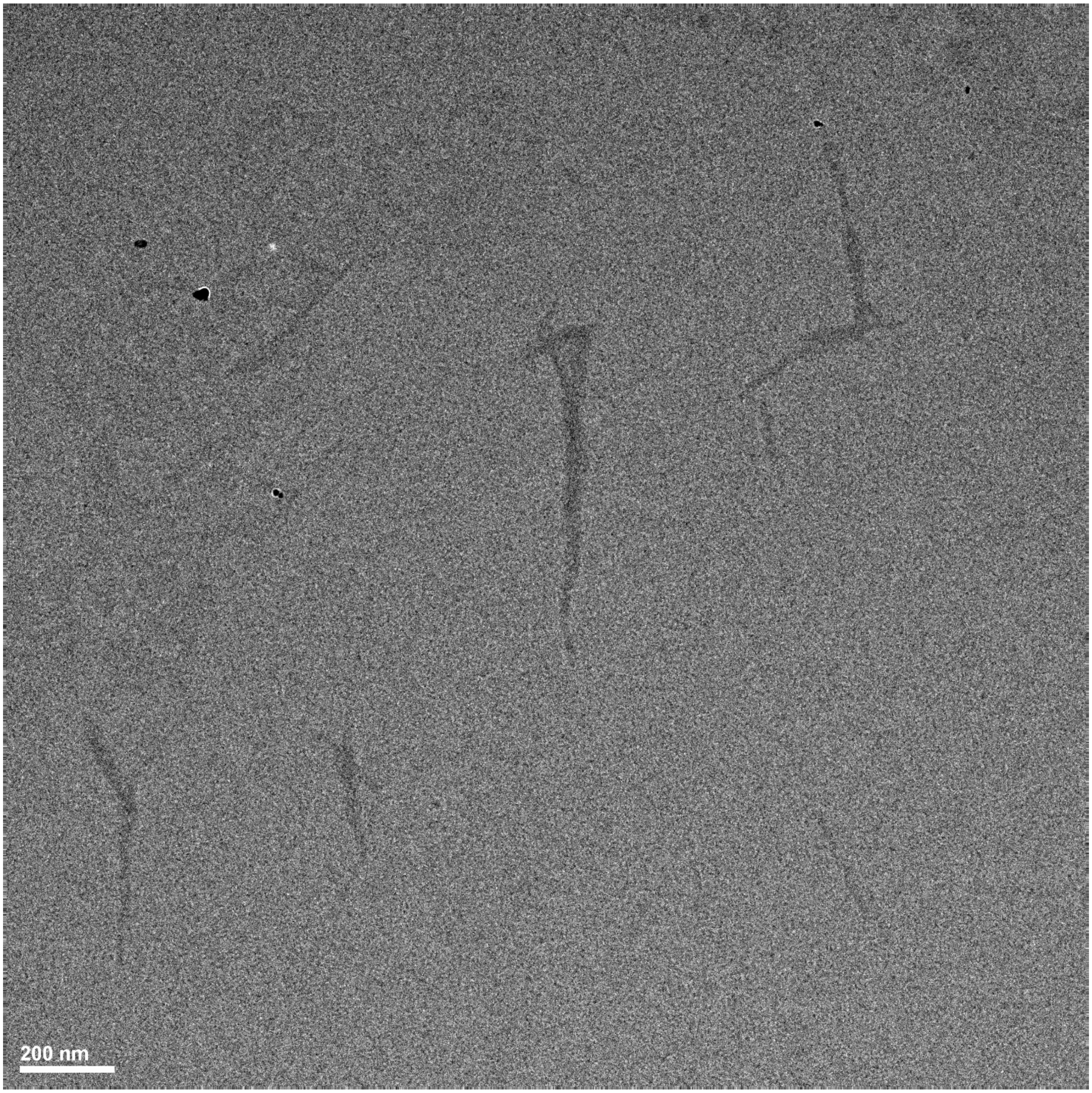

Figure 4.7 TEM of AgNPs@CNCs.

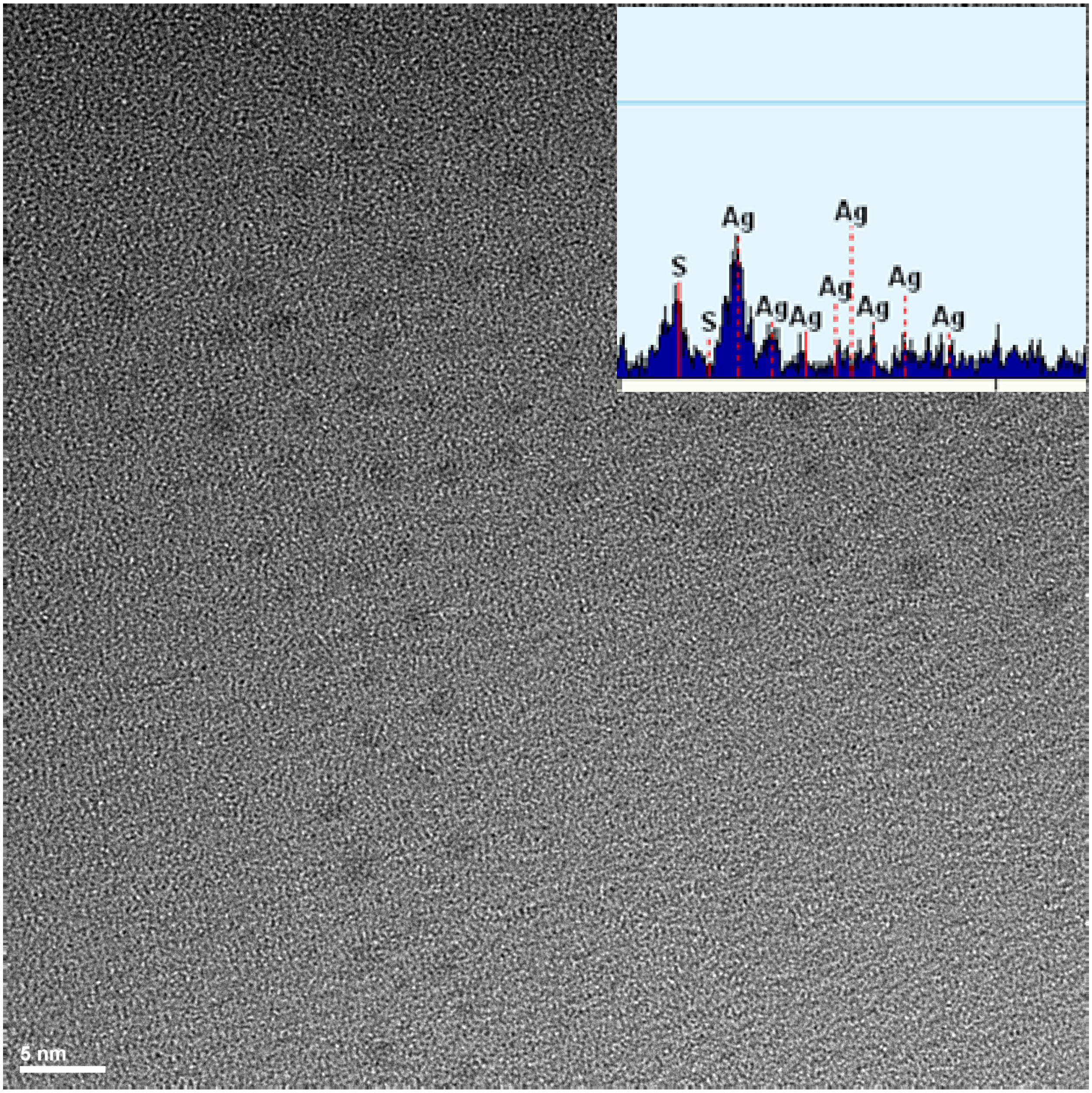

Figure 4.8 TEM of AgNPs@CNCs at higher magnification. The inset (top, right) shows the EDS, confirming the presence of Ag.

4.7.2 XPS: Silver wire standard

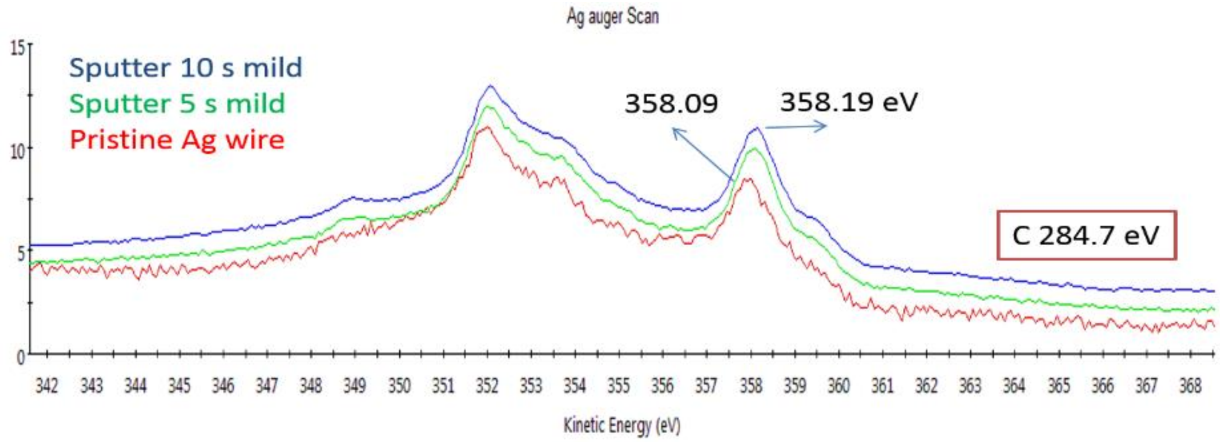

Figure 4.9 XPS spectrum in the Ag Auger region of an Ag wire used as an Ag metal standard.

4.7.3 Optimization of pressure and temperature for hydrogenation reaction

In a typical reaction, substrate (0.1 mmol) was added to the catalyst suspension prepared above, AgNPs@CNCs, (5mL). To this mixture was added cyclohexanol (0.1 mmol) as internal standard. Then, the mixture was placed in a PARR multiple reactor system under various H_2 pressures and temperatures, 1000rpm, for 24 h (Table 4.3). Afterwards, the reaction mixture was extracted with diethyl ether and then injected on the GC-MS for monitoring the reaction.

Table 4.3 Optimization of pressure and temperature for hydrogenation reaction.

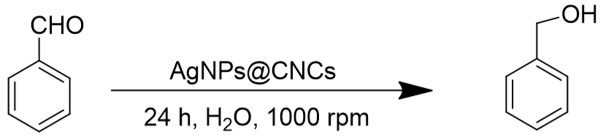

Pressure (H_2)	Temperature (°C)	Conversion
20 bars	100	30 %
	150	33 %
30 bars	100	34 %
30 bars	125	45 %
40 bars	80	25 %
40 bars	100	96%

4.7.4 Control experiments for catalysis

Two types of blank experiments were conducted for benzaldehyde reduction under exactly similar conditions of temperature, pressure, Ag loading and no. of equivalents used for the substrate and catalyst (Figure 4.10). The CNCs alone were not active. In the second experiment, $AgNO_3$ was used in the absence of CNCs resulting in 0% conversion.

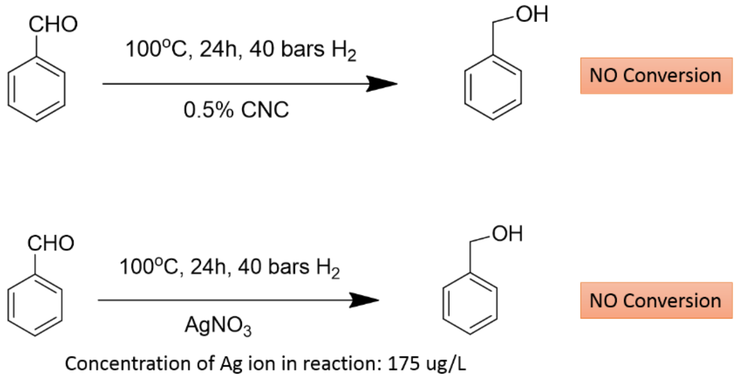

Figure 4.10 Control experiments.

5 Cellulose nanocrystals as non-innocent supports for synthesis of Ru NPs and their applications in arene hydrogenations

In the previous chapter the reducing abilities of the CNCs were demonstrated. Moving forward, here we use CNCs to access Ru NPs from $RuCl_3$ under mild reducing conditions of 4 bars H_2, rt, 24h. This chapter demonstrates the role of CNCs as reducers in conjunction with the H_2 gas for reducing $RuCl_3$ to Ru (0). In the literature, there has been no such instance where the $RuCl_3$ could be reduced without the use of strong reducing agents, such as borohydrides. The prepared Ru NP-CNC hybrid composites were then used for arene hydrogenations under mild conditions, which were competitive with those used for Ru NPs in ionic liquids.

This chapter is adapted from a published article, whose citation appear below, which is reprinted with permission from the Royal Chemical Society and all co-authors.

Madhu Kaushik, Hava M. Friedman, Mary Bateman and Audrey Moores. Cellulose nanocrystals as non-innocent supports for the synthesis of ruthenium nanoparticles and their application to arene hydrogenation. *RSC adv*. 2015, 5, 53207-53210.

5.1 Abstract

Ru nanoparticles were synthesized from $RuCl_3$ under mild H_2 pressure within a suspension of cellulose nanocrystals. X-ray photoelectron spectroscopy and transmission electron microscopy revealed that the small Ru (0) nanoparticles (3.3 ± 1 nm) were deposited onto their cellulosic support. This hybrid proved to be a highly efficient arene hydrogenation catalyst operational at 4 bars and room temperature.

5.2 Introduction

The development of more sustainable synthetic methods to access nanoparticles is an active research field, stimulated by both the interest in the discovery of novel and functional nanomaterials and the ever growing impact of mankind on its environment.[1-4] In this context, biomass derived nanomaterials constitute an opportunity to reduce nanosynthesis footprint, but also to discover unexpected properties and enhanced applications.[5, 6] Cellulose Nanocrystals (CNCs) are easily obtained by strong acid hydrolysis of cellulose and industrially produced from wood pulp.[7-9] This material is renewable, biodegradable and non-toxic.[10] CNCs have well-defined size and morphology, high specific surface area, high aspect ratio: 5 nm in width from 150 to 250 nm in length, high crystalline order and chirality, superior mechanical strength, and controllable surface chemistry.[7-9] CNCs have thus been applied to a variety of fields, including the production of iridescent and birefringent films,[7] chiral templating of silica[11] and carbon[12] materials, reinforcing fillers in plastics and polymers,[7, 13 14-16] flocculants,[17] aerogels,[18] hydrogels,[19] and supercapacitors.[20] As CNCs form stable colloidal suspensions in water and feature a high specific surface area, they are attractive supports for various catalytically active nanoparticles (NPs)[21] including Pd,[22-25] Au,[26] and Ag.[27] Importantly, CNCs are non-innocent supports for metal NPs, as they act as reducers and control metal seeding. Additionally, they were recently shown to act as chiral inducers in the enantionselective Pd-catalyzed hydrogenation reaction of ketones.[6] With these ideas in mind, we envisaged to apply CNCs for the design of catalysts towards the challenging arene hydrogenation reaction.[28] Arene hydrogenation is of prime industrial importance.[29] For instance, benzene hydrogenation to adipic acid is an intermediate step in the production of nylon.

Lately, the increased regulation[30, 31] on the aromatic content of fossil fuels has also triggered interest in more efficient catalytic hydrogenation of aromatics. Conventionally, arene hydrogenations are carried out at high temperatures (~120ºC) and high H_2 pressures (~100 bars).[32, 33] Supported nanoparticles of Rh (0), Ir (0), Ru (0) and Pt (0) have opened avenues to achieve heterogeneous arene hydrogenations under milder conditions.[29, 34-38] The more prohibitive price of Rh, Ir and Pt has made Ru NPs a very appealing candidate for this reaction. Recently, ionic liquid stabilised Ru NPs have demonstrated their ability to hydrogenate arenes under conditions as mild as 4 bars of H_2 pressure and 75°C.[36, 39] Zahmakiran *et al.* and Favier *et al*. have achieved these hydrogenations at room temperatures and 3 bars H_2 pressure, where they use Ru nanoclusters stabilised by nanozeolite framework and 4-(3-phenylpropyl)pyridine respectively.[40, 41] Beyond the study of the catalytic properties of Ru NPs, novel and sustainable synthetic methods to access them have also been an active research field. To replace ruthenium chloride ($RuCl_3$),[40, 42-44] bis(methylallyl)(1,5-cyclooctadiene) ruthenium(II)[45-47] and Ru(1,5-cyclooctadiene)(cyclooctatriene)[44] have been used as precursors, as they do not lead to the generation of salt by-products upon reduction, and also they can be reduced under mild H_2 pressures.[48] They are however expensive, require synthetic skills to prepare and careful handling. RuO_2 was also used as a precursor compatible with H as a reductant.[36, 49] On the other end, typical $RuCl_3$ reduction relies on the use of $NaBH_4$ to afford the desired nanomaterial.[40, 42] $NaBH_4$ is a hazardous substance implying regulated handling and the boron species generated during this reaction may affect the Ru catalytic surface.[50] Recently our group showed that $RuCl_3$ could be effectively reduced and supported by Fe NPs to afford a magnetically recoverable transfer hydrogenation catalysts.[51] Interestingly, very few examples exist where $RuCl_3$ is effectively reduced by mild H_2 pressure. For instance, when cyclodextrins are used as stabilizers, this reactivity is enabled.[52, 53] We present herein a novel approach where CNCs promote the generation of Ru NPs from $RuCl_3$ using mild H_2 pressure as the reducing agens and effectively support the resulting NPs to afford RuNPs@CNCs composite. Subsequently, RuNPs@CNCs were shown to act as powerful arene hydrogenations catalysts under 4 bars H_2 pressure, at room temperature.

5.3 Materials and methods

CNCs synthesised by sulphuric acid hydrolysis of wood pulp were provided by FPInnovations. $RuCl_3.3H_2O$ was purchased from Pressure Chemicals. For the manipulation of pH, hydrochloric acid (0.01M) was provided by Fluka Analytical. To redisperse dried CNC samples in suspension, the Sonics & Materials Inc. Vibra-Cell VC1500 ultrasonicator (220V, 15A, 1500W, 20 kHz) was used. The Metrohm Titrando (836 base, 804 Ti stand, and 802 stirrer) autotitrator was used for attaining various pH values. The transmission electron microscopy (TEM) samples were deposited on 200 mesh carbon coated copper grids supplied by Electron Microscopy Sciences. The analyses were performed on the Tecnai 12 microscope (FEI electron optics) equipped with a Lab6 filament at 120kV, equipped with Gatan 792 Bioscan 1k x 1k Wide Angle Multiscan CCD Camera (Gatan Inc.); and FEI G2 F20 Cryo-S/TEM microscope (FEI, Inc) at 200kV, equipped with Gatan Ultrascan 4k x 4k Digital (CCD) Camera System at different magnifications corresponding to different pixel size (defocus level ranging from − 2.5 to − 4.5 μm). All hydrogenation reactions were carried out in a Parr Instruments 5000 Series Multiple Reactor System. The monitoring of catalytic hydrogenation and determination of enantiomeric excess were performed using an Agilent 7890A series gas chromatograph equipped with a MS detector (5975C) on an Agilent Cyclodex-B column. Cyclohexanol (reagentplus grade, 99%, Sigma Aldrich) was used as internal standard for quantification of all hydrogenation reactions. All reagents, solvents and substrates were procured from Sigma Aldrich.

5.3.1 Synthesis of the catalyst, RuNPs@CNCs

100 mg of CNCs were weighed out in a 5-dram vial, to which 20 mL of deionised water was added. To this solution, 2.6 mg of $RuCl_3.3H_2O$ was added to achieve 0.5 wt% Ru onto CNCs. This solution was then sonicated for 10 seconds in order to completely dissolve the $RuCl_3.3H_2O$ in the water giving a very dark brown solution. After that the reaction mixture was mounted onto the Parr system for 24 hours at room temperature, 4 bars H_2 and 1000 rpm. The resulting suspension of the catalyst, RuNPs@CNCs, was black.

5.3.2 Control Experiments for synthesis of catalyst

Control 1: 100 mg of CNCs were weighed out in a 5-dram vial, to which 20 mL of deionised water was added. To this solution, 2.6 mg of $RuCl_3.3H_2O$ was added to achieve 0.5 wt% Ru onto CNCs. This solution was then sonicated for 10 seconds in order to completely dissolve the $RuCl_3.3H_2O$ in the water giving a very dark brown solution. Then, $NaBH_4$ (25 mg) was added and the reaction mixture was stirred at room temperature for 24 hours (Figure 5.1).

Control 2: 100 mg of CNCs were weighed out in a 5-dram vial, to which 20 mL of deionised water was added. To this solution, 2.6 mg of $RuCl_3.3H_2O$ was added to achieve 0.5 wt% Ru onto CNCs. This solution was then sonicated for 10 seconds in order to completely dissolve the $RuCl_3.3H_2O$ in the water giving a very dark brown solution. The reaction mixture was stirred at room temperature for 24 hours, without adding any external reducing agent (Figure 5.1).

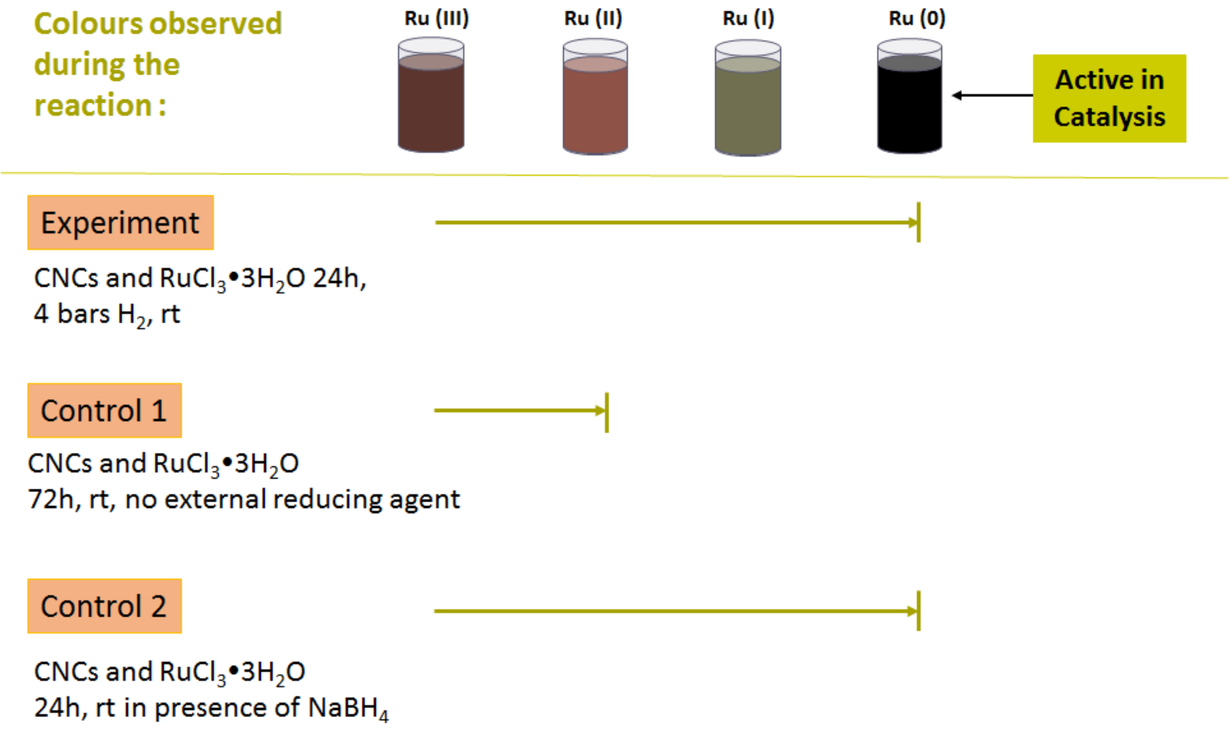

Figure 5.1 The colours observed during the experiments and the controls.

5.3.3 Monitoring the Hydrogenation Reactions

The monitoring of catalytic hydrogenation and determination of enantiomeric excess were performed using an Agilent 7890A series gas chromatograph equipped with a MS detector (5975C) on an Agilent Cyclodex-B column. Response factors for all compounds were calculated using cyclohexanol as the internal standard. The response factor was calculated by running a standard solution containing known substrate and internal standard concentrations on the GC-MS to determine the area of the two compounds:

Response Factor, R = (concentration of substrate/ concentration of internal standard)*(peak area of internal standard/ peak area of substrate).

5.3.4 Optimisation of reaction conditions for arene hydrogenation

Substrate (0.1 mmol) was added to the catalyst suspension prepared above, RuNPs@CNCs, (5mL). To this mixture was added cyclohexanol (0.1 mmol) as internal standard. Then, the mixture was mounted onto a PARR multiple reactor system under various conditions (Table 1 in the manuscript). For time optimization, the reaction was set to 20 bars, rt for 24h. Aliquots of 0.5 ml from the reaction mixture were then analyzed on GC-MS, at time 2h, 4h, 8h and 24h.

5.3.5 Hydrogenation of Substrates

Substrate (0.1 mmol) was added to the catalyst suspension prepared above, RuNPs@CNCs, (5mL). To this mixture was added cyclohexanol (0.1 mmol) as internal standard. Then, the mixture was mounted onto a PARR multiple reactor system under H_2 pressure, 4 bars, 1000rpm, for 24 h at room temperature (optimized conditions). Afterwards, reaction mixture was extracted with diethyl ether and then injected on the GC-MS for monitoring the conversion.

5.3.6 Recycling Experiments

Substrate (0.1 mmol) was added to the catalyst suspension prepared above, RuNPs@CNCs, (5mL). To this mixture was added cyclohexanol (0.1 mmol) as internal standard. Then, the mixture was placed in a PARR multiple reactor system under H_2 pressure, 4 bars, 1000rpm, for 24h at room temperature. Afterwards, reaction mixture was extracted with diethyl ether and then injected on the GC-MS for monitoring the conversion. The remaining water suspension, having the catalyst, was then used for the next cycle.

5.3.7 TEM and EDS

5ul of samples were deposited on carbon film coated 400 Mesh copper EM grids for two minute, followed by blotting off the excess liquid with the edge of a filter paper. The grids were then allowed to dry under air before being imaged using FEI G2 F20 Cryo-STEM operated at 200 kV (FEI, Inc). Images were recorded with a Gatan Ultrascan 4k × 4k Digital (CCD) Camera System.

5.4 Results and discussions

The synthesis of RuNPs@CNCs proceeded very easily by the addition of $RuCl_3$ to 20 ml 0.5% CNC (w/w) suspension in water. The resulting mixture, dark brown in colour, was subjected to 4 bars H_2 at room temperature for 24 hours (Scheme 5.1).

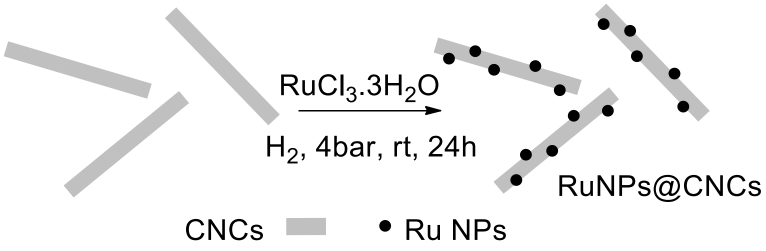

Scheme 5.1 Synthesis of RuNPs@CNCs.

In 24 hours, the complete reduction to Ru (0) was confirmed by both the black colour of the suspension and the XPS $3p_{3/2}$ peak at 461.27 eV (Figure 5.1 and in appendix: Figure

5.7). If stopped after 2 hours, the reduction was not complete and a light brown If stopped after 2 hours, the reduction was not complete and a light brown coloured solution was obtained, corresponding to Ru(II) species[54-56] (Figure 5.1). For comparison, this experiment was performed using $NaBH_4$ instead of H_2 as reducer, which also resulted in the reduction of Ru (III) to Ru (0) in 24 hours. The suspension colour was monitored over time and the following colours were observed in sequence: dark brown, light brown, light green and finally black, corresponding respectively to Ru (III), Ru (II), Ru (I) and Ru (0) (Figure 5.1).[54, 56, 57] When the reaction mixture was stirred at room temperature for over 72 hours, without the use of any external reducing agent, the colour of the suspension changed to light brown. This confirmed that the CNCs have the ability to reduce the Ru (III) partially to Ru (II) but no further.

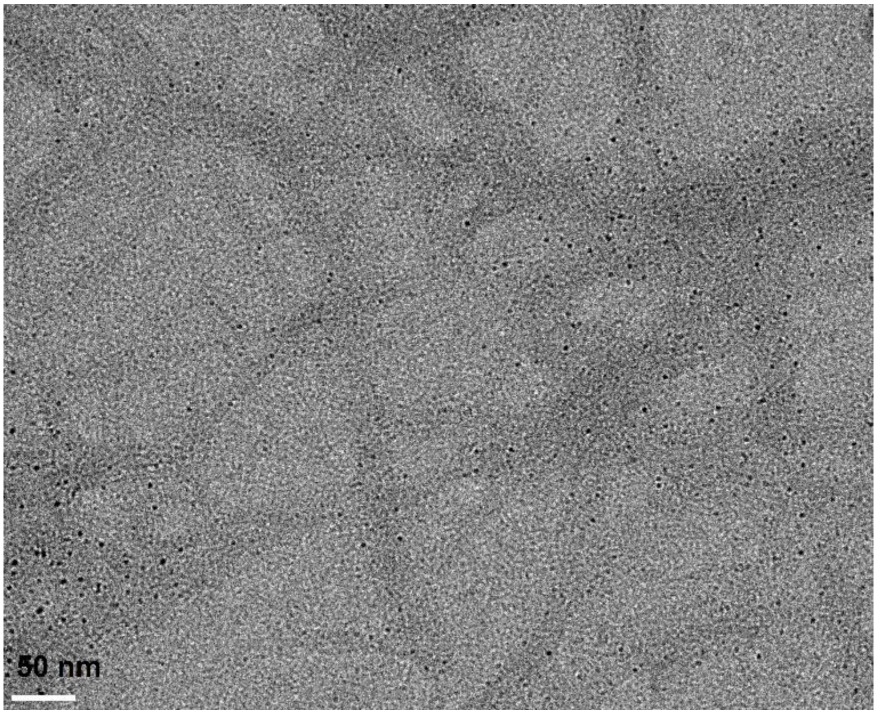

Figure 5.2 TEM of unstained sample of RuNPs@CNCs.

Transmission electron microscopy (TEM) was performed to characterize the material. The imaging of CNC/metal hybrid material is a challenge, requiring conditions where both the organic CNCs and the denser metal are seen with good contrast.[58, 59] With RuNPs@CNCs, good images were acquired. CNCs were observed as low contrast whiskers, as reported before.[7-9, 58] The Ru NPs were present in conjunction with CNCs, revealing that they were deposited onto the CNC surface (Figure 5.2, in appendix: Figure 5.4, Figure 5.5, Figure 5.6). The Ru NPs, seen as darker spots onto the less dense CNCs, featured an average size of 3.3 ± 1 nm, a size where Ru is known to be catalytically active.[36] The TEM also concluded that the CNCs did not aggregate in the catalyst suspension and retain their high surface area and rod-like form. These results show that the CNCs are capable of facilitating the reduction of Ru (III) to Ru (0) in presence of H_2, as a mild reducing agent, at 4 bars and room temperature in water.

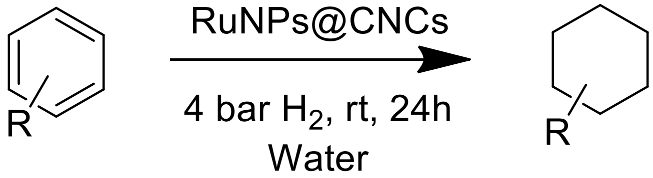

Scheme 5.2 Arene hydrogenation at 4 bars H_2 pressure, rt, 24h, in water, using RuNPs@CNCs as catalyst.

Additionally this reaction affords a Ru NP-hybrid composite of CNC useful to sustain the catalytically active Ru under a reactive environment. RuNPs@CNCs, were thus tested for the catalytic hydrogenation of arenes (Scheme 5.2, Table 5.1). At first, we started with hydrogenation conditions used by Schwab *et al*. at 20 bars H_2 pressure and 100ºC.[39] After 2h, 100% conversion of toluene to methylcyclohexane was achieved (entry 1). The reaction was carried out in the water suspension of the catalyst, with no addition of any other solvent, allowing biphasic extraction for workup. In an attempt for using milder conditions, the same reaction was carried out at room temperature, instead of 100ºC and only afforded a mere 16% conversion to methylcyclohexane (entry 2). At room temperature, 20 bars of H_2 pressure, the time of reaction was increased from 2 hours to 24 hours. Aliquots of the reaction mixture were taken out at times 2h, 4h and 8h and analysed by GC-MS. Conversions ramped up to 91% at 8 hours and 24h afforded 100% conversions (entries 2-5). Next, H_2 pressure was reduced, at 24h and room temperature, to 10 bars, 4 bars and 2 bars, giving conversions of 100%, 100% and 11% respectively (entries 6-8). Therefore, the mildest reaction conditions providing complete conversion are 4 bars H_2, 24 h at room temperature in water. These reaction conditions are milder than the ones usually reported for the arene hydrogenations including the Ru NPs are stabilised by ionic liquids.[39, 46]

Table 5.1 Optimisation of reaction conditions for toluene hydrogenation with RuNPs@CNCs (3mol% in Ru).

S. No.	Time (h)	Pressure (bars)	Temperature	Yield (%)
1.	2	20	100°C	100
2.	2	20	rt	16
3.	4	20	rt	40
4.	8	20	rt	91
5.	24	20	rt	100
6.	24	10	rt	100
7.	24	4	rt	100
8.	24	2	rt	11

Hence, CNCs are a powerful catalyst support for Ru NPs to achieve both easy synthesis and reactivity. In order to check the scope of the reaction, other aromatic substrates with varied substitutions were also hydrogenated at the optimised conditions (Table 5.2). Styrene (2) hydrogenation provided a 96% yield for completely hydrogenated product, ethylcyclohexane and 4% yield for partially hydrogenated product, ethylbenzene. Acetophenone (3) gave 76% of ethylcyclohexane, and the rest were a mixture of partially hydrogenated product. Excellent results for a heterocyclic aromatic (4) were also observed, giving 90% yield for the completely hydrogenated product.

Table 5.2 Arene hydrogenations of different substrates using RuNPs@CNCs.

Substrate	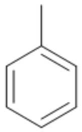 (1)	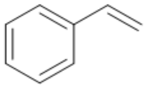 (2)	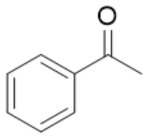 (3)	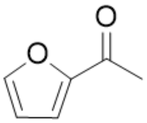 (4)
Yield (%)	100	96	76	90

The catalyst was checked for recyclability, and it was recyclable for six cycles. After that the conversion rates dropped significantly (Figure 5.3).

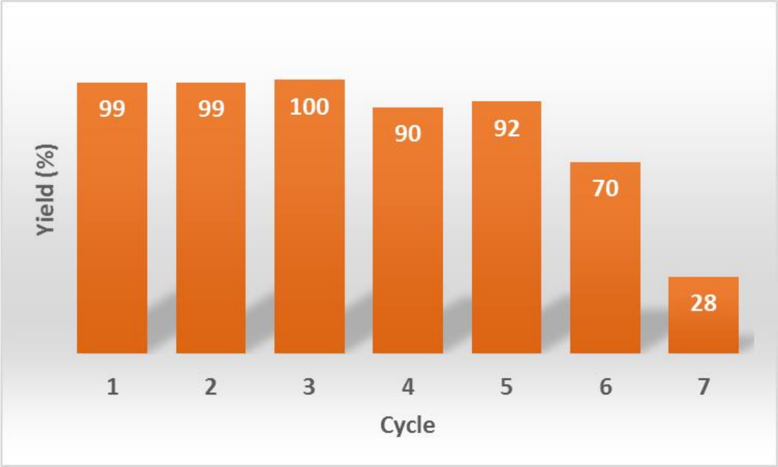

Figure 5.3 Recycling of toluene hydrogenation at 4bars H_2, rt, 24h using RuNPs@CNCs.

In addition, as a control experiment, when using just $RuCl_3.3H_2O$ for the reaction, no conversion was observed. To determine whether the catalysis was truly heterogeneous, a poisoning experiment using CS_2 was also performed. The addition of 0.5 equivalents of CS_2 to the reaction mixture made the catalyst totally ineffective under the reaction conditions used.

5.5 Conclusions

These results conclusively show that the role of CNCs as a non-innocent support for catalytically active NPs. In the synthesis of Ru NPs, the CNCs and H_2 gas synergistically achieve the reduction of Ru (III) to Ru (0) at just 4 bars and room temperature. Furthermore, the catalyst, RuNPs@CNCs was successfully applied to arene hydrogenations under mild conditions of 4 bars H_2, room temperature in water. The product is easily extracted in a biphasic system, and the catalysts can be recycled up to 6 times with no loss of activity. These reaction conditions are competitive with the best results in the field.

5.6 References

1. J. A. Dahl, B. L. Maddux and J. E. Hutchison, *Chem. Rev.*, 2007, **107**, 2228.
2. C. J. Murphy, *J. Mater. Chem.*, 2008, **18**, 2173.
3. M. J. Eckelman, J. B. Zimmerman and P. T. Anastas, *J. Ind. Ecol.*, 2008, **12**, 316.
4. J. M. Campelo, D. Luna, R. Luque, J. M. Marinas and A. A. Romero, *ChemSusChem*, 2009, **2**, 18.
5. S. Iravani, *Green Chem.*, 2011, **13**, 2638.
6. M. Kaushik, K. Basu, C. Benoit, C. C. M., H. Vali and A. Moores, *J. Am. Chem. Soc.*, 2015, **137**, 6124.
7. D. Klemm, F. Kramer, S. Moritz, T. Lindström, M. Ankerfors, D. Gray and A. Dorris, *Angew. Chem. Int. Ed.*, 2011, **50**, 5438.
8. S. J. Eichhorn, A. Dufresne, M. Aranguren, N. E. Marcovich, J. R. Capadona, S. J. Rowan, C. Weder, W. Thielemans, M. Roman, S. Renneckar, W. Gindl, S. Veigel, J. Keckes, H. Yano, K. Abe, M. Nogi, A. N. Nakagaito, A. Mangalam, J. Simonsen, A. S. Benight, A. Bismarck, L. A. Berglund and T. Peijs, *Journal of Material Science*, 2009, **45**, 1.
9. Y. Habibi, L. A. Lucia and O. J. Rojas, *Chem. Rev.*, 2010, **110**, 3479.
10. T. Kovacs, V. Naish, B. O'Connor, C. Blaise, F. Gagné, L. Hall, V. Trudeau and P. Martel, *Nanotoxicology*, 2010, **4**, 255.
11. K. E. Shopsowitz, H. Qi, W. Y. Hamad and M. J. MacLachlan, *Nature*, 2010, **468**, 422.
12. K. E. Shopsowitz, W. Y. Hamad and M. J. MacLachlan, *Angew. Chem. Int. Ed.*, 2011, **50**, 10991.
13. K. M. Z. Hossain, R. M. Felfel, C. D. Rudd, W. Thielemans and I. Ahmed, *React. Funct. Polym.*, 2014, **85**, 193.
14. K. M. Z. Hossain, I. Ahmed, A. J. Parsons, C. A. Scotchford, G. S. Walker, W. Thielemans and C. D. Rudd, *J. Mater. Chem.*, 2012, **47**, 2675.
15. X. Cao, Y. Habibi and L. A. Lucia, *J. Mater. Chem.*, 2009, **19**, 7137.
16. M. A. Hubbe, O. J. Rojas, L. A. Lucia and M. Sain, *BioResources*, 2008, **3**, 929.
17. K. H. M. Kan, J. Li, K. Wijesekera and E. D. Cranston, *Biomacromolecules*, 2013, **14**, 3130.

18. X. Yang and E. D. Cranston, *Chem. Mater.*, 2014, **26**, 6016.

19. J. Yang, C.-R. Han, J.-F. Duan, M.-G. Ma, X.-M. Zhang, F. Xu, R.-C. Sun and X.-M. Xie, *J. Mater. Chem.*, 2012, **22**, 22467.

20. S. Y. Liew, D. A. Walsh and W. Thielemans, *RSC Adv.*, 2013, **3**, 9158.

21. E. Lam, K. B. Male, J. H. Chong, A. C. W. Leung and J. H. T. Luong, *Trends Biotechnol.*, 2012, **30**, 283.

22. C. M. Cirtiu, A. F. Dunlop-Brière and A. Moores, *Green Chem.*, 2011, **13**, 288.

23. X. Wu, C. Lu, W. Zhang, G. Yuan, R. Xiong and X. Zhang, *J. Mater. Chem. A*, 2013, **1**, 8645.

24. P. Zhou, H. Wang, J. Yang, J. Tang, D. Sun and W. Tang, *Ind. Eng. Chem. Res.*, 2012, **51**, 5743.

25. M. Rezayat, R. K. Blundell, J. E. Camp, D. A. Walsh and W. Thielemans, *ACS Sustainable Chem. Eng.*, 2014, **2**, 1241.

26. E. Lam, S. Hrapovic, E. Majid, J. H. Chong and J. H. T. Luong, *Nanoscale*, 2012, **4**, 997.

27. R. Xiong, C. Lu, W. Zhang, Z. Zhou and X. Zhang, *Carbohydr. Polym.*, 2013, **95**, 214.

28. R. C. Larock, *Comprehensive organic transformations, A Guide to Functional Group Preparations*, Wiley-VCH, 1986.

29. J. A. Widegren and R. G. Finke, *J. Mol. Catal. A: Chem.*, 2003, **191**, 187.

30. G. Karavalakis, T. D. Durbin, M. Shrivastava, Z. Zheng, M. Villela and H. Jung, *Fuel*, 2012, **93**, 549.

31. M. Fang and R. A. Sanchez-Delgado, *J. Catal.*, 2014, **311**, 357.

32. R. L. Augustine, *Heterogeneous catalysis for the synthetic chemist*, CRC Press, New York, 1995.

33. J. G. Donkervoort and E. G. M. Kuijpers, in *Fine Chemicals through Heterogeneous Catalysis*, eds. R. A. Sheldon and H. v. Bekkum, Wiley-VCH Verlag GmbH, Weinheim, 2001, ch. Catalytic hydrogenation and dehydrogenation, pp. 351-470.

34. S.-C. Qi, X.-Y. Wei, Z.-M. Zong and Y.-K. Wang, *RSC Adv.*, 2013, **3**, 14219.

35. A. Gual, C. Godard, S. Castillón and C. Claver, *Dalton Trans.*, 2010, **39**, 11499.

36. L. M. Rossi and G. Machado, *J. Mol. Catal. A: Chem.*, 2009, **298**, 69.
37. S. A. Stratton, K. L. Luska and A. Moores, *Catal. Today*, 2012, **183**, 96.
38. B. Leger, A. Denicourt-Nowicki, A. Roucoux and H. Olivier-Bourbigou, *Adv. Synth. Catal.*, 2008, **350**, 153.
39. F. Schwab, M. Lucas and P. Claus, *Angew. Chem. Int. Ed.*, 2011, **50**, 10453.
40. M. Zahmakıran, Y. Tonbul and S. Ozkar, *J. Am. Chem. Soc.*, 2010, **132**, 6541.
41. I. Favier, P. Lavedan, S. Massou, E. Teuma, K. Philippot, B. Chaudret and M. Gómez, *Top. Catal.*, 2013, **56**, 1253.
42. M. Fang, N. Machalaba and R. A. Sanchez-Delgado, *Dalton Trans.*, 2011, **40**, 10621.
43. S. Niembro, S. Donnici, A. Shafir, A. Vallribera, M. L. Buil, M. A. Esteruelas and C. Larramona, *New J. Chem.*, 2013, **37**, 278.
44. J. Llop Castelbou, E. Breso-Femenia, P. Blondeau, B. Chaudret, S. Castillon, C. Claver and C. Godard, *ChemCatChem*, 2014, **6**, 3160.
45. M. H. Prechtl, M. Scariot, J. D. Scholten, G. Machado, S. R. Teixeira and J. Dupont, *Inorg. Chem.*, 2008, **47**, 8995.
46. J. Julis, M. Hölscher and W. Leitner, *Green Chem.*, 2010, **12**, 1634.
47. K. L. Luska and A. Moores, *Green Chem.*, 2012, **14**, 1736.
48. J. D. Scholten, M. H. Prechtl and J. Dupont, in *Handbook of Green Chemistry*, Wiley-VCH, 2012, vol. 8.
49. L. M. Rossi, J. Dupont, G. Machado, P. F. P. Fichtner, C. Radtke, I. J. R. Baumvol and S. R. Teixeira, *J. Braz. Chem. Soc.*, 2004, **15**, 904.
50. X. Yan, H. Liu and K. Y. Liew, *J. Mater. Chem.*, 2001, **11**, 3387.
51. R. Hudson, V. Chazelle, M. Bateman, R. Roy, C. Li and A. Moores, *ACS Sustainable Chem. Eng.*, 2015, **3**, 814.
52. N. T. T. Chau, S. Handjani, J.-P. Guegan, M. Guerrero, E. Monflier, K. Philippot, A. Denicourt-Nowicki and A. Roucoux, *ChemCatChem*, 2013, **5**, 1497.
53. A. Denicourt-Nowicki, A. Ponchel, E. Monflier and A. Roucoux, *Dalton Trans.*, 2007, 5714.
54. E. A. Seddon and K. R. Seddon, *The Chemistry of Ruthenium*, Elsevier, Amsterdam, 2013.

55. A. Bossi, F. Garbassi, A. Orlandi, G. Petrini and L. Zanderighi, in *Stud. Surf. Sci. Catal.*, eds. B. Delmon, P. Grange, P. Jacobs and G. Poncelet, Elsevier, 1979, vol. 3, pp. 405-416.
56. G. Fownes, *A manual of elementary chemistry, theoretical and practical*, Blanchard and Lea, Philadelphia, 1862.
57. A. Bossi, F. Garbassi, A. Orlandi, G. Petrini and L. Zanderighi, eds. B. Delmon, P. Grange, P. Jacobs and G. Poncelet, Elsevier, 1979, vol. 3, ch. Preparation Aspects of Ru-Supported Catalysts and their Influence on the Final Products, pp. 405-416.
58. M. Kaushik, W. C. Chen, T. G. van de Ven and A. Moores, *Nordic Pulp and Paper Res. J.* , 2014, **29**, 77.
59. M. Kaushik, J.-L. Putaux, C. Fraschini, G. Chauve and A. Moores, in *The Transmission Electron Microscope*, ed. M. Khan, Intech, 2015, ch. Transmission Electron Microscopy for the Characterization of Cellulose Nanocrystals, pp. 129-163.

5.7 Appendix

5.7.1 TEM and EDS

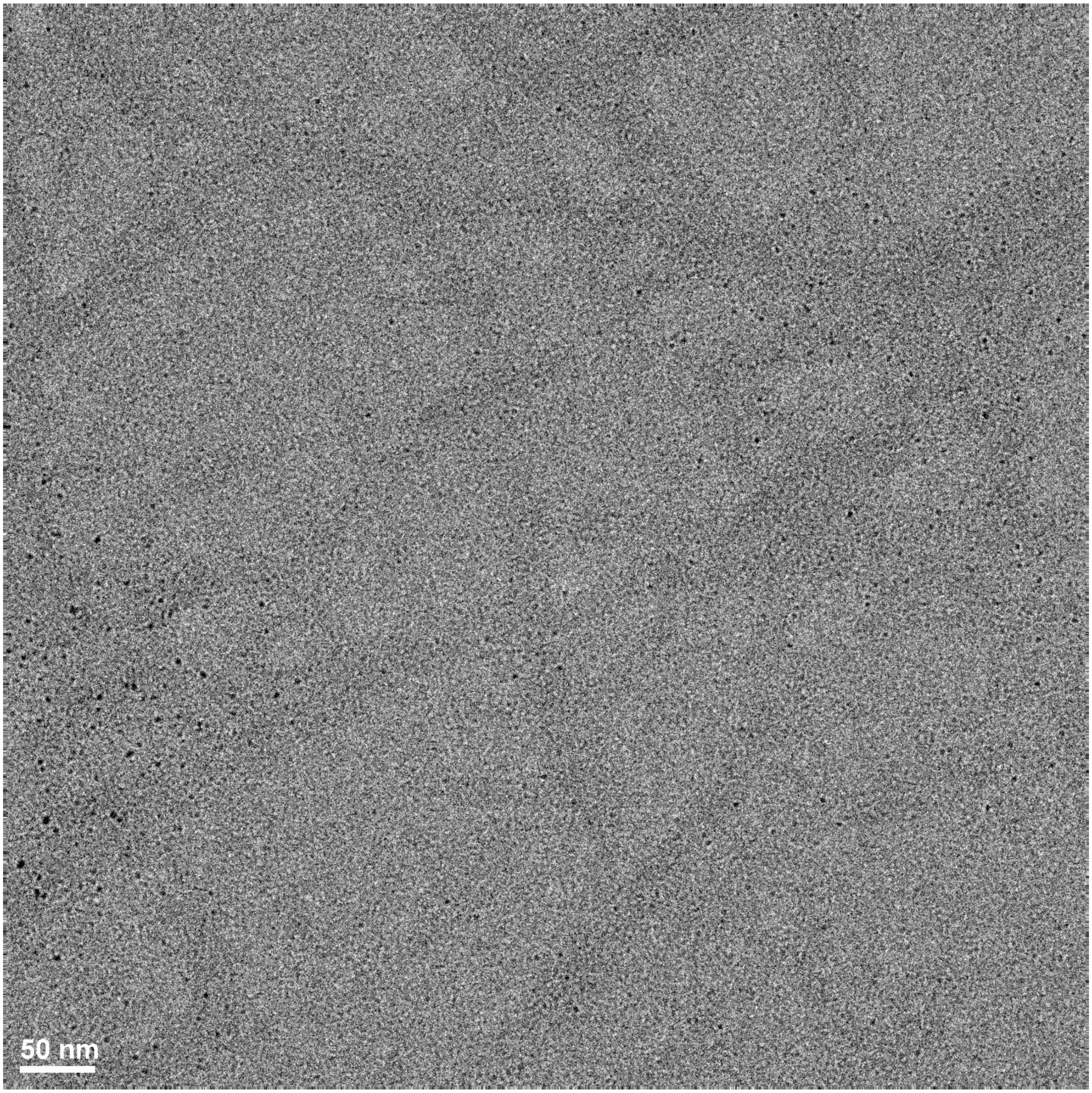

Figure 5.4 TEM of synthesized catalyst, RuNPs@CNCs.

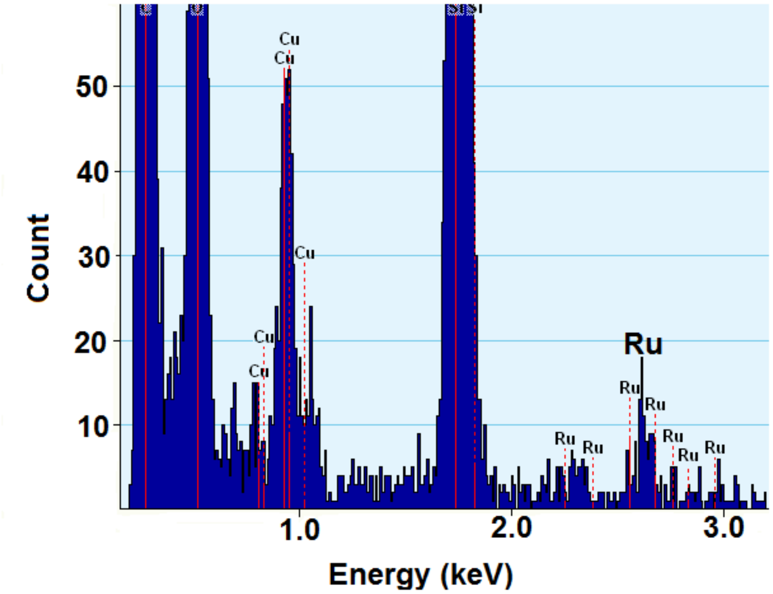

Figure 5.5 EDS confirming the presence of Ru (the darker spots on the TEM).

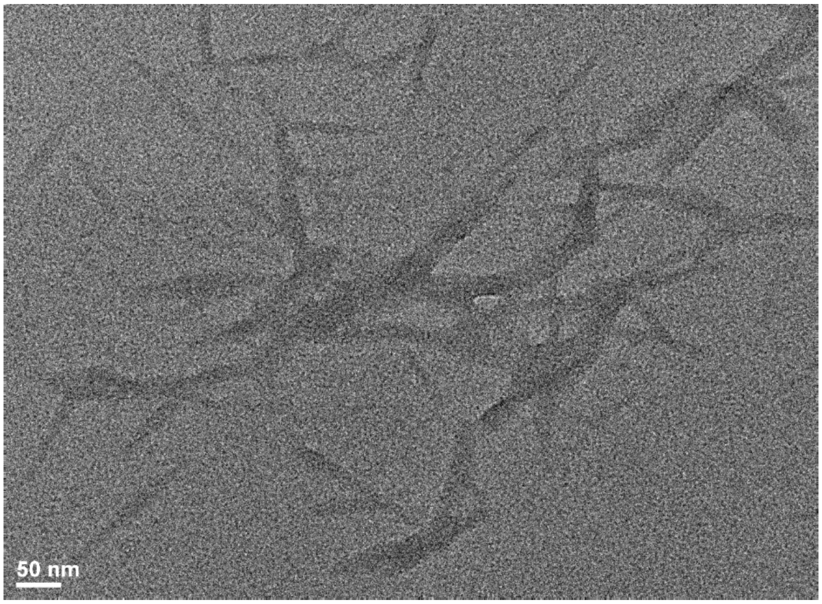

Figure 5.6 TEM of catalyst precursor, a mixture of RuCl3.3H2O and CNCs. The image shows only well-dispersed CNCs, with presence of no Ru NPs.

5.7.2 XPS

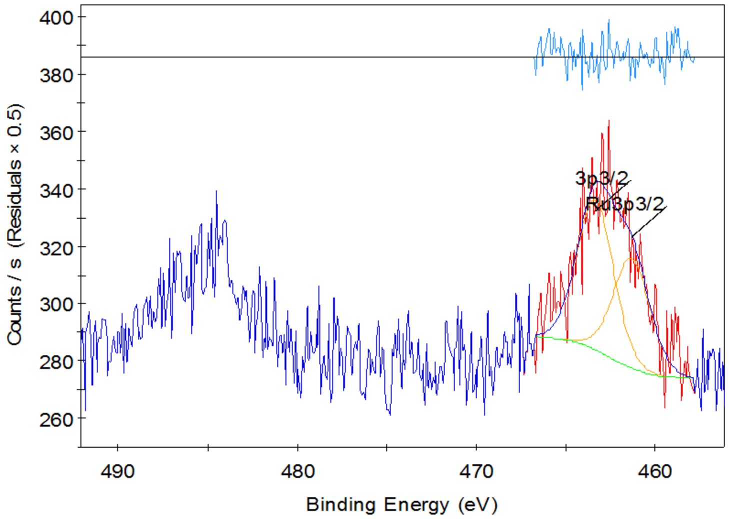

Figure 5.7 Ru 3p$_{3/2}$ peak at 461.27 eV confirms Ru (0).

6 Conclusion and Future Directions

6.1 Conclusion

This dissertation proves that CNCs are a versatile support for metal NPs. Their high surface area, thermal stability, non-toxicity and inexpensiveness provide researchers a sustainable template for metal NPs.[1-4] Moreover, the hydroxyl groups on its surface has been utilised in the recent years for reducing metal precursors, and hence, opening a greener approach for metal NP synthesis, without the use of any external reducing agents.[5-8] The metal NP-nanocellulose hybrid composites have found diverse applications in paper, polymer, plastics, chiral templating, flocculants, aerogels, hydrogels, drug delivery, cosmetics, pharmaceutics and catalysis.[1-4] We specifically focussed on the innovative use of CNCs in catalysis and their characterisation through transmission electron microscopy.

We emphasized the importance of a well-established methodology for electron microscopy imaging of CNCs. Our results clearly demonstrated the importance of controlling the sampling method, especially during sample drying on the TEM grid.[9, 10] Simultaneously, the work provided a clear methodology to perform TEM of CNCs in a reliable and reproducible fashion by controlling the pH, the grid properties and the sample suspension. The work revealed that never-dried, freeze-dried and spray-dried all exist as rod structures, with a size of 9.7 ± 4.4 nm in width and 216 ± 82 nm in length, in the case of never-dried samples. Moreover, the use of expensive and toxic heavy metal stains were unnecessary for imaging. Low-dose and high resolution TEM were also compared and discussed.

Enantioselective catalysis, especially heterogeneous, is the preferred method for the synthesis of pure chiral molecules in the fine chemical industries. Cellulose has been long sought as a chiral inducer in enantioselective catalysis.[11] We reported herein an unprecedentedly high enantiomeric excess (ee) for Pd patches deposited onto CNCs used as catalysts for the hydrogenation of prochiral ketones in water at room temperature and 4 bars H_2. Our system, where CNCs acted as support and sole chiral source, achieved an ee of 65% with 100% conversions. Cryo-electron microscopy, high resolution transmission electron microscopy and tomography were used for the first time to study the 3D structure of a metal functionalized CNC hybrid. It established the presence of sub nanometer thick Pd patches at the surface of CNCs and provided insight into the chiral induction mechanism.

Thereafter, we described for the first time the synthesis of Ag NPs directly from bulk Ag metal in a one-pot setting.[6] This facile, inexpensive synthetic method proceeded in water at room temperature. CNCs played a key role as high surface area support and *in situ* reducer to drive the depletion of Ag from a metal wire and afford 1.3 nm ± 0.3 nm Ag NPs. The resulting hybrid were fully characterized by TEM and XPS and tested for their catalytic activity. Their ability to hydrogenate aldehydes, 4-nitrophenol, alkenes and alkynes was shown and they afford a cheap and sustainable alternative for their homogeneous counterparts.

Following the demonstration of the reducing ability of the hydroxyl groups on the surface of CNCs in the generation of Ag NPs, we used CNCs in synthesis of Ru NPs. Here, we conclusively showed that the role of CNCs as a non-innocent support for catalytically active NPs.[12] In the synthesis of Ru NPs, the CNCs and H_2 gas synergistically achieve the reduction of Ru (III) to Ru (0) at just 4 bars and room temperature. Furthermore, the catalyst, RuNPs@CNCs was successfully applied to arene hydrogenations under mild conditions of 4 bars H_2, room temperature in water. The product is easily extracted in a biphasic system, and the catalysts can be recycled up to 6 times with no loss of activity. These reaction conditions are competitive with the best results in the field.

6.2 Future directions

Nanocelluloses, comprising the whole class of crystalline celluloses in the nano-domain (CNCs, CNFs and bacterial CNFs) have proved to be a versatile support for metal NPs. Their high surface area, thermal stability, non-toxicity and inexpensiveness provide researchers a sustainable template for metal NPs. The catalysis performed by nanocelluloses has given highly promising results in heterogeneous systems, where the catalysts are recyclable multiple times. Recently, researchers have demonstrated that these nanocelluloses could act as chiral recognition centres in chirality specific hydrolysis of amino acids and in enantioselective hydrogenation of prochiral ketones. Furthermore, the characterisation techniques for these nanocelluloses and their modified hybrids have improved. These development shall open new realms for applications of nanocelluloses in various type of heterogeneous catalysis, and specifically, in enantioselective reactions. An interesting strategy would be to chemically modify the surface of CNCs using the primary hydroxyl groups and then use them to get increased enantioselectivity. To compliment these advances, it would be desirable to conduct mechanistic studies on the reactions where the CNCs were used as chiral inducers or for chiral recognition. Simultaneously, further characterisation of the CNC surface and the metal NP-CNC hybrid composite shall be vital for development of CNCs as a catalytic system comparable to natural enzymes in their selectivity and efficiency.

Also, the hydroxyl groups on CNC surface have been utilised for reducing metal precursors, and hence, opening a greener approach for metal NP synthesis, without the use of any external reducing agents. Notably, the study of mechanism of the reduction in such cases, would further assist in use of CNCs as sustainable reducers. The CNC suspension in water provide us a robust system in which biphasic catalysis can be explored. These suspensions provide an ionic liquid-like environment to the metal NPs and metal salts in them. Based on that, another noteworthy direction to take would be to investigate the ligand exchange reactions using organometallic precursors in the CNC-water suspension. The system, thus obtained, would be interesting to check for catalysis, for example in C-H activations, C-C coupling reactions, etc.

I conclude by saying that the use of nanocelluloses in novel catalytic applications has been founded with the work done in the last few years, and it is now open to researchers to implement nanocelluloses in innovative applications.

6.3 References

1. Y. Habibi, *Chem. Soc. Rev.*, 2014, **43**, 1519.

2. E. Lam, K. B. Male, J. H. Chong, A. C. W. Leung and J. H. T. Luong, *Trends Biotechnol.*, 2012, **30**, 283.
3. D. Klemm, F. Kramer, S. Moritz, T. Lindström, M. Ankerfors, D. Gray and A. Dorris, *Angew. Chem. Int. Ed.*, 2011, **50**, 5438.
4. S. J. Eichhorn, *Soft Matter*, 2011, **7**, 303.
5. Z. Shi, J. Tang, L. Chen, C. Yan, S. Tanvir, W. A. Anderson, R. M. Berry and K. C. Tam, *J. Mater. Chem. B*, 2015, **3**, 603.
6. M. Kaushik, A. Y. Li, R. Hudson, M. Masnadi, C.-J. Li and A. Moores, *Green Chem.*, 2015.
7. L. Chen, W. Cao, P. J. Quinlan, R. M. Berry and K. C. Tam, *ACS Sustainable Chem. Eng.*, 2015, **3**, 978.
8. R. Xiong, C. Lu, W. Zhang, Z. Zhou and X. Zhang, *Carbohydr. Polym.*, 2013, **95**, 214.
9. M. Kaushik, J.-L. Putaux, C. Fraschini, G. Chauve and A. Moores, in *The Transmission Electron Microscope*, ed. M. Khan, Intech, 2015, ch. Transmission Electron Microscopy for the Characterization of Cellulose Nanocrystals, pp. 129-163.
10. M. Kaushik, W. C. Chen, T. G. M. van de Ven and A. Moores, *Nordic Pulp and Paper Res. J.* , 2014, **29**, 77.
11. M. Kaushik, K. Basu, C. Benoit, C. C. M., H. Vali and A. Moores, *J. Am. Chem. Soc.*, 2015, **137**, 6124.
12. M. Kaushik, H. M. Friedman, M. Bateman and A. Moores, *RSC Adv.*, 2015, **5**, 53207.

1 Appendix: TEM Chapter

Transmission Electron Microscopy for the Characterization of Cellulose Nanocrystals

This chapter is adapted from a published book chapter, whose citation appear below, which is reprinted with permission from the Intech pubications and all co-authors.

Madhu Kaushik, Jean-Luc Putaux, Carole Fraschini, Gregory Chauve and Audrey Moores, in The Transmission Electron Microscope, Intech, 2015, ch. Transmission Electron Microscopy for the Characterization of Cellulose Nanocrystals, Published September 2015, (http://www.intechopen.com/books/the-transmission-electron-microscope-theory-and-applications/transmission-electron-microscopy-for-the-characterization-of-cellulose-nanocrystals)

1.1 Abstract

Cellulose nanocrystals (CNCs) are high aspect ratio nanomaterials readily accessible from cellulose *via* strong acid hydrolysis. They feature unique properties stemming from their surface chemistry, their crystallinity and their three dimensional structure. These properties have been exploited in a number of applications, including optically active coatings, polymer-reinforcing agents, aerogels and nanochiral materials. CNC size and shape determination is an important challenge and transmission electron microscopy (TEM) is one of the most powerful tools to achieve this goal. Because of the specifics of TEM imaging, CNCs require special attention. They have a low density, are susceptible to electron beam damage and possess unique supramolecular properties. Specific techniques for both sampling and imaging have been developed over the past decades. In this review, we describe the CNCs, their properties, their applications and the need for a precise characterization of their morphology and size distribution. We also describe in details the techniques used to record quality images of CNCs. Finally, we survey the literature to provide readers with specific examples of TEM imaging of CNCs.

1.2 Introduction

1.2.1 Native cellulose and the production of cellulose nanocrystals

Cellulose, the most abundant biopolymer on Earth, has been extensively used by men, in the form of macro- and micro- structures, as a traditional resource in many aspects of daily life, notably to produce textiles and papers. This polymeric material is biosynthesized by a wide variety of living species such as plants, animals, bacteria and some amoebas. Glucose is polymerized by enzymes in a continuous fashion. The resulting cellulose chains are homopolymers of *β*-1,4-linked anhydro-D-glucose units that associate to form microfibrils, further assembled into macrofibers and fibers. Crystalline and disordered regions alternate along the microfibrils (Figure 0.1a).[1-3]

In the late 1940's, cellulose crystallites were isolated for the first time by chemical treatment of a cotton substrate in hot concentrated sulfuric acid.[4] Soon after, Rånby showed that stable colloidal suspensions of negatively charged cellulose particles could be obtained.[5, 6] During the extraction process, the cellulosic fibrous structure is broken down in the presence of concentrated sulfuric acid (other mineral acids can be used such as HCl). After diffusion of the acid within the substrate, the glycosidic linkages in disordered regions, more accessible and reactive, are preferentially broken. An additional mechanical or ultrasound treatment results in the release of rodlike cellulose crystallites, so-called cellulose nanocrystals or CNCs (Figure 0.1). Consequently, as the hydrolysis proceeds, the degree of polymerization of the cellulose macrostructures decreases while the crystallinity of the non-soluble particles increases.[7]

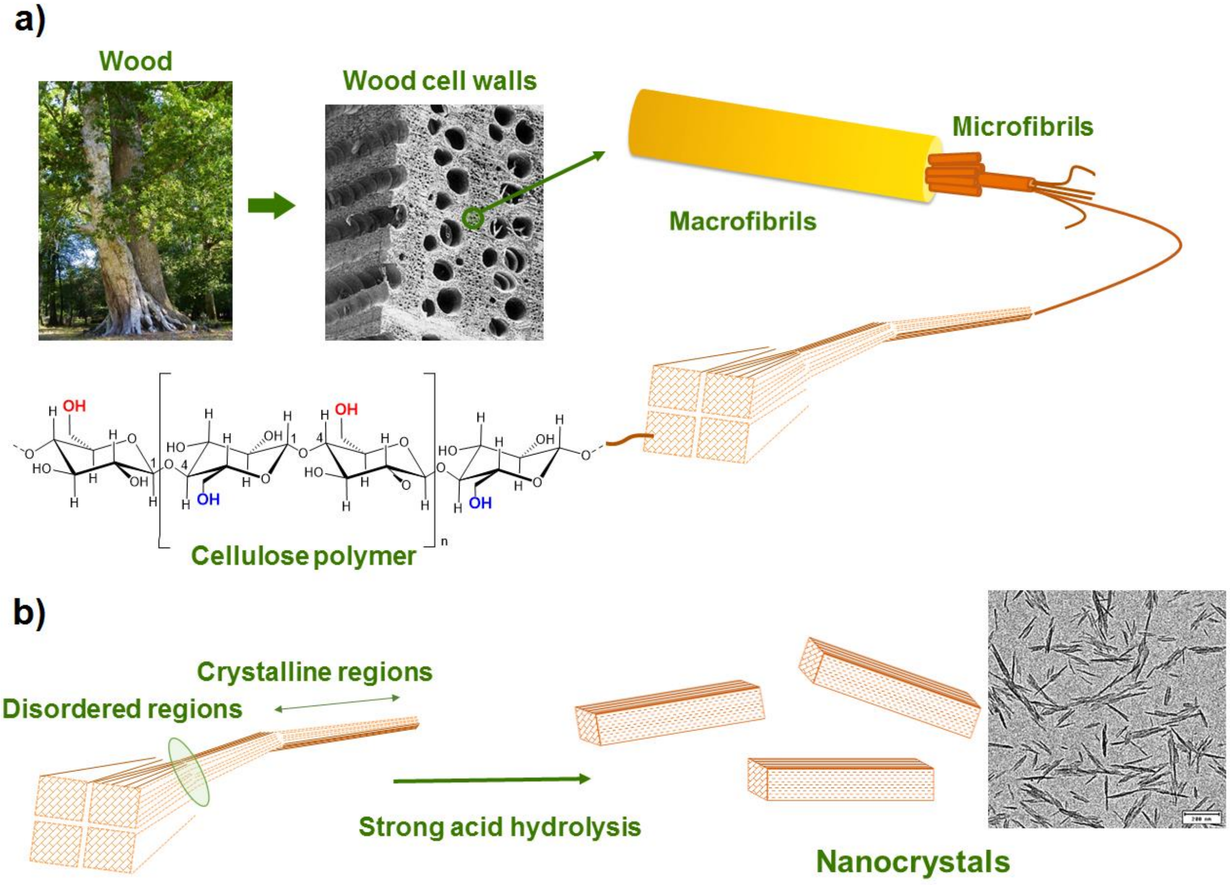

Figure 0.1 a) Structural hierarchy of the cellulose fiber component from the tree to the anhydroglucose molecule. b) Man-made preparation of nanocrystals by selective acid hydrolysis of the disorganized regions of cellulose microfibrils. (SEM image of wood cell structure, courtesy of D. Dupeyre, CERMAV)

1.2.2 Cellulose nanocrystal properties

In the early 1950's, detailed characterizations of the shape and size of various CNCs (cotton, ramie[8] and bacterial cellulose[9]) were proposed from transmission electron microscopy (TEM) images. Since then, CNCs have been produced from a wide (and expanding) variety of sources,[10] such as wood (Figure 0.2a), cotton (Figure 0.2b), bamboo (Figure 0.2c),[11] bacteria (Figure 0.2d),[12] algae (Figure 0.2e), tunicates (Figure 0.2f),[13] eucalyptus,[11] spruce bark,[14] soy husk,[15] etc. The CNC are rodlike objects with a length typically ranging from 50 to 1000 nm and a width varying from 3 to 50 nm (Table 0.1). CNCs thus have high length-to-width (aspect) ratios (10 to 100).[16-21] Their morphology depends on the cellulose source and the conditions of preparation (type and concentration of acid, acid-to-cellulose ratio, reaction time and temperature) (Figure 0.2). The nanoscopic features of the resulting CNCs considerably influence their colloidal and macroscopic properties such as suspension rheology, phase separation concentration, liquid crystal behavior, orientation under electric or magnetic field and mechanical reinforcement ability in nanocomposites.

Table 0.1 Size distribution of CNCs from various sources of cellulose.

Source of Cellulose		Length (nm)	Width (nm)	References*
Plants	Cotton	50 – 300	5 – 10	22, 23
	Rice	50 – 300	10 – 15	24, 25
	Ramie	50 – 250	5 – 10	26-28
	Sisal	100 – 200	3 – 7	29, 30
Microcrystalline cellulose (MCC) from wood		50 – 500	5 – 50	16, 31-33
Tunicates		100 – 3000	10 – 50	22, 23, 34, 35
Bacteria		200 – 3000	10 – 75	36-38

**Proposed references are representative examples and do not constitute an exhaustive list.*

CNCs can be found in several forms. First, CNC can be manipulated in the form of aqueous suspensions resulting from their preparation by strong acid hydrolysis and featuring low pH around 2. CNC suspensions can be neutralized, or CNC's surface modified *via* chemical treatment. Alternatively, several drying methods may be used to afford a solid, fluffy material, with the aspect of white sugar candy.[39]

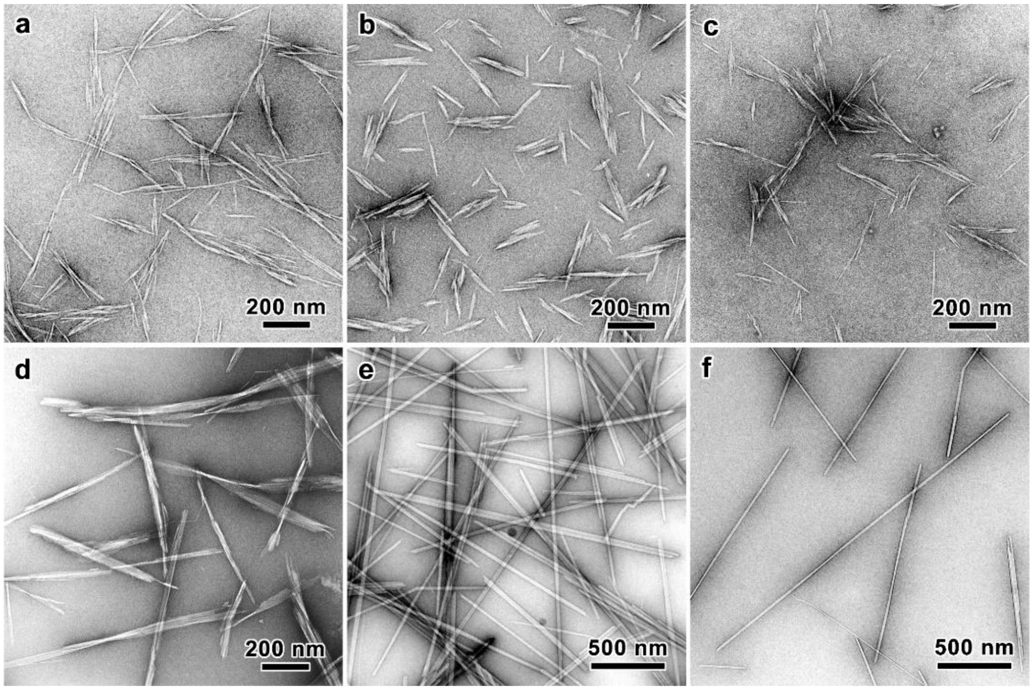

Figure 0.2 TEM images of negatively stained preparations of CNCs of various origins: a) wood; b) cotton (courtesy F. Azzam, CERMAV; c) bamboo (courtesy B. Jean, CERMAV; d) Gluconacetobacter xylinus (courtesy H. Bizot, INRA); e) Glaucocystis (courtesy Y. Nishiyama, CERMAV-CNRS); f) Halocynthia papillosa (courtesy A. Osorio-Madrazo, A. Ludwig University of Freiburg).

In 1959, Marchessault *et al.* showed that CNCs could self-organize into liquid crystalline phases and also revealed that the negative charges, which generate electrostatic repulsions between the particles, originated from the chemical reaction of sulfuric acid with hydroxyl groups of cellulose to form sulfate ester groups.[40]

The sulfuric acid hydrolysis of cellulose has remained confined to academic research laboratories until a big step was made in the mid 1990's, when it was shown that CNCs were efficient reinforcing fillers in latex-based polymer matrices, opening a new potential market for this high-end material.[13] Since then, CNCs has become intensively studied with an accelerating rate of publications released each year.[16-21] Beside mechanical properties, colloidal properties of CNCs in suspension generated a series of studies investigating their ability to form liquid-crystal phases. The colloidal suspensions of CNCs spontaneously organize into a chiral nematic phase above a certain critical concentration. As a consequence, CNCs have been used to produce iridescent and birefringent films,[41-44] chiral mesoporous silica[45, 46] and carbon,[47] gold nanoparticle films with chiral plasmonic properties,[48] enantioselective amino acid hydrolysis catalysts,[49] hydrogels[50] and aerogels.[51] Moreover, the high surface area and controllable surface chemistry of CNCs make them a unique support of metal nanoparticles (NPs) for heterogeneous catalysis. CNCs have been used as supports for nanocatalysts, including Pd[52] and Au[53] nanoparticles. Pd NPs distributed onto CNCs were used for hydrogenation and carbon-carbon bond coupling reactions,[52, 54-56] while the Au counterparts were used for 4-nitrophenol reduction.[57] Ag NPs were also deposited onto CNC to develop an antibacterial activity.[58]

This large panel of high-end applications strongly encouraged industry to seek large-scale production of CNCs. The forest-based industry in North America, Northern Europe and Japan is currently looking into renewing and reinventing itself to extend its activities and guarantee its survival, while renewable materials are being increasingly appealing as fossil-based material replacement. In addition, CNCs are inherently safe, practically non-toxic materials.[59] Nanocellulose-based high added-value materials definitely constitute promising vectors to “turn wood into gold” and revive the forest-based industry. These combined factors led to the opening of the first commercial plant by CelluForce Inc. (Windsor, Québec, Canada), producing 1 ton CNCs per day.[60]

Several review articles or books have been published over the last years that cover in detail the various aspects of the CNC features and applications.[16, 17, 19, 20, 61]

1.2.3 Need for CNC characterization

CNCs possess appealing properties in direct relation with their 3D structure, including well-defined shape, size and aspect ratio. From an industrial perspective, it is essential to collect reliable data on CNCs, especially for quality control, toxicology assessment, R&D and applications.

1.2.3.1 Quality control

The large-scale production of CNCs has become a reality when CelluForce Inc. started up its demonstration plant. Getting reliable, fast and accurate measurement of the particle size is a key to guarantee a consistent production of high-quality CNCs. Several methods exist (*vide infra*) for the determination of size, size distribution and shape of CNCs and they are typically used as research tools and afford a fairly consistent understanding of the materials structure. However, for the moment, no systematic and streamlined method exists for size determination and evaluation of polydispersity for acicular nanomaterial such as CNCs. This question is particularly acute for large scale quality control, for instance in pilot plant production and beyond.

1.2.3.2 Toxicology assessment

Manufactured nanomaterials have recently caused societal concerns about their possible adverse effects on health and safety. Properties of nanomaterials typically differ from those of their parent bulk materials because of their larger surface area, resulting in greater reactivity, their smaller size resulting in their ability to cross natural barriers and intrinsic effects caused by nanometric size, including electronic and plasmonic effects. Since such particles may have a negative effect on biological systems and ecosystems, their toxicological risks must be evaluated and an accurate description of the product in terms of dimensions, chemistry and toxicity is required by the authorities. CNCs have extensively been evaluated using standard ecotoxicological and mammalian test protocols and have, to date, been shown to be practically non-toxic in each of the individual tests.[59] In addition, CNCs have recently obtained regulatory approval under Canada’s New Substances Notification Regulations (NSNR) for unrestricted use in Canada and is the first organic nanomaterial to be added to Canada’s domestic substance list.

1.2.3.3 R&D and applications

To maximize the reinforcing or liquid crystal behavior potential of CNCs, the particles have to be as well-dispersed as possible, especially in nanocomposite applications. An aspect that can lead to aggregation/agglomeration and then affects the further redispersion of the particles is mainly the final drying stage. Drying is one critical process of the large-scale industrial production of CNCs. Aqueous suspension leads to bacterial contamination and precludes long-term storage. In addition, the cost associated to the transportation of suspensions containing up to 90% water is not economically viable. Various drying processes can be used such as freeze-drying, supercritical drying, spray-drying, oven drying, and air drying. Freeze-drying and spray-drying methods are used in the industrial production of CNCs. The resulting solid, hornified macrostructure may be difficult to further redisperse, even in water. Neutralization of the acidic sulfate ester groups prior to drying helps with redispersion.[39]

1.2.3.4 Challenges regarding CNC particle size measurement

The aspect ratio of CNCs dictates the percolation threshold, a key parameter to control mechanical properties in nanocomposites. Knowing the size and morphology of CNCs with precision plays a key role in the development of numerous applications where their morphology directly impacts the final properties of the final product. CNCs prepared by sulfuric acid hydrolysis of cellulose substrates are rigid acicular-shaped and highly crystalline nanoparticles. The geometrical dimensions of these rod-like crystallites exceedingly vary with the source of cellulose (Table 0.1) and with the hydrolysis reaction conditions. For example, CNCs extracted from wood are 3-7 nm in width and 100-200 nm in length while CNCs derived from tunicate are 10-20 nm in width and 500-2000 nm in length.[13] These values are indicative as different reaction conditions and result in different sizes and size distributions. Indeed, size distributions were published as early as 1944 for ramie and cotton CNCs.[62] Lists of the different sizes of CNCs extracted from various sources can be found in recent reviews.[16, 19, 20, 26] CNCs are usually obtained as colloidal aqueous suspensions and the production process induces a batch-to-batch particle size variability. The rheological properties of the suspension and the state of individualization of the particles are strongly affected by external parameters such as nanoparticle concentration, pH, ionic strength, temperature or the presence of an additional compound or impurities.[63-65] The stability of the suspension is due to the electrostatic repulsion forces created by the negatively charged sulfate ester groups located at the surface of the crystals. More generally, its propensity to agglomerate is driven by its surface chemistry. For example, the addition of electrolyte screens the surface charges of the particles, reducing the electrostatic repulsion that prevents CNCs from agglomerating which will result in either an increase or a decrease of the measured particle size by photon correlation spectroscopy (PCS) depending on the amount of electrolyte introduced. Since CNC particles do not undergo swelling or compaction upon the addition of electrolyte, this increase/decrease of the measured particle size is a pure artefact driven only by the laws of physics and thermodynamics. Consequently, for a given sample, particle size variability depends on the sample preparation conditions and the measurement techniques.

Particle size is a good indicator of the quality of the CNC dispersion but the direct observation of nanoparticles remains a challenge and high resolution direct imaging or light scattering techniques are required.

1.2.4 Microscopy and spectroscopy techniques used for CNC characterization

As previously mentioned, CNCs come in a wide variety of length, width and shape depending on the cellulose sources. The cross-sections of CNCs also display a variety of shapes, e.g. square, rectangular, or parallelogram, that are dictated by the arrangements of enzymatic terminal complexes extruding cellulose chains during the biosynthesis. As shown in different cases, the edges of the crystals can be eroded during the acid hydrolysis yielding hexagonal or octagonal cross-sections exposing small surface area of hydrophobic (200) planes.[66]

Many instruments are commonly used for the determination of particle size distribution (PSD) and particle dimension(s), each instrument detecting size through its own physical principle. Numerous techniques based on microscopy, light interactions, electrical properties, sedimentation, sorting and classification exemplify the possibility to get access to the particle size. Depending on the technique, the results are more or less accurate and are related to the nanoparticle shape and its physicochemical features such as chemical composition, heterogeneity, topography, surface charge density, dispersing medium, viscosity, etc. The morphology of CNCs can be accurately revealed either by microscopic methods including transmission electron microscopy (TEM), cryo-TEM, atomic force microscopy (AFM), field emission gun scanning electron microscopy (FEG-SEM), or by scattering techniques such as polarized and depolarized light scattering (DLS and DDLS, respectively) and small- and wide-angle neutron or X-ray scattering (SANS, WANS, SAXS and WAXS, respectively). Each of these techniques has its own advantages and limitations in their application to the study of CNCs. Consequently, care should be taken while comparing particle size data obtained from different techniques.

Light scattering techniques rely on the interaction of light with the hydrodynamic volume of a particle. With anisometric nanoparticles, the response varies as a function of the orientation of each individual particle. The collected data thus needs to be mathematically processed to extract meaningful information. Typically, for acicular particles, such as CNCs, light scattering techniques have not been able to match the precision of microscopy. Microscopy, on the other hand, provides direct images of individual particles and allows characterization of its morphology and size (length, width and thickness). Microscopy techniques having the nanometer scale resolution capabilities to image CNCs are electron microscopy and AFM. Electron microscopy enables the direct observation of the dimensions (*i.e.,* length and width) of a given particle. AFM provides information on morphology, surface topography, mechanical properties and adhesion of CNCs under ambient conditions.[14, 15, 67, 68] While AFM provides reliable information on the thickness of the particles deposited on a flat substrate, the lateral resolution is limited by the convolution of the tip end, whose size and curvature are significantly larger than the dimensions of the nano-objects. However, this so-called "tip-broadening" effect can sometimes be deconvoluted [69]. On the contrary, TEM images provide good nanometric (and often sub-nanometric) lateral resolution, allowing to rapidly screen a large population of particles, thus avoiding major sampling issues. However, as TEM images are projections of the objects along the incident beam direction, it may be difficult to accurately measure the particle thickness. Moreover, the low density of CNCs calls for the use of staining methods. These limitations may be overcome by some of the recent developments described in the following sections, including low-dose microscopy and 3D imaging. When possible, the combination of data from AFM and TEM images, and scattering analyses provides an optimal description of the particle morphology. For instance, a combination of imaging and scattering data was used by Elazzouzi-Hafraoui *et al.*[23] and Brito *et al.*[11] to precisely describe the morphology of CNCs extracted from a variety of sources.

It has to be noted that due to significant technical progress in instrumentation (low-voltage and beam-decelerated imaging, variable pressure) and detector variety and sensitivity, FEG-SEM imaging has become a perfectly valid approach to visualize the surface of CNC assemblies from dried systems[70] or fractured chiral nematic films.[71] CNC suspensions dried on TEM grids can be observed as well in a SEM equipped with a detector located below the specimen. With this so-called scanning transmission electron microscopy (STEM) mode, transmitted and scattered electrons can be collected to reconstitute an image of the specimen very similar to those obtained with a TEM. Although the accelerating voltage is lower (10-30 kV) than that used in a TEM (100-300 kV), the resolution is sufficient to see the fine details of CNCs.[10]

This chapter focuses on TEM approaches. We describe several methods to prepare CNC specimens and emphasize the specific conditions to observe with these highly beam-sensitive nanoparticles, in order to provide images of CNC dispersions allowing to determine reliable size distributions. A thorough description of sample preparation procedures and observation techniques is followed by a review of the literature on CNC imaging by TEM.

1.3 TEM techniques used for the observation of CNCs

1.3.1 Selected milestones in the characterization of nanocellulose by TEM

TEM imaging and electron diffraction played a significant role in the morphological and structural studies of cellulose microfibrils and nanocrystals, complementing data from spectroscopic (Fourier-transform infrared spectroscopy and solid-state NMR) and scattering (of X-ray or neutron) analyses. Important information was obtained at a local scale, allowing to identify mechanisms at work during the biosynthesis and biodegradation of cellulose crystals and characterize some physical properties, with or without additional chemical modification, inside cell walls or, after extraction, in suspension or incorporated in nanocomposites materials.

In 1940, H. Ruska (brother of E. Ruska, inventor of the TEM) published what can be considered to be the first images of microfibrils obtained after HCl hydrolysis of cotton cellulose.[72] During the following two decades, the progress in TEM imaging of cellulose was mostly driven by the motivation to characterize the submicrometer structure of natural cellulose fibers. However, the identification of smaller constituting elements required the disintegration of cell walls and fibers using strong mechanical and/or chemical treatment.[40, 73-77] In particular, images of individual crystalline "fragments" (not yet called CNCs) were recorded after strong sulfuric acid hydrolysis of celluloses from various sources.[8, 9, 78, 79]

In parallel to these morphological studies, important structural information was obtained using electron diffraction. Fiber diffraction patterns were collected from *Valonia* cell wall fragments and CMFs, at room[80] and low[81] temperature, confirming at a local scale the longitudinal orientation of the cellulose chains. The size and distribution of crystallites were determined in *Valonia* microfibrils using diffraction contrast imaging.[82] Later on, electron diffraction was notably used to validate the existence of separate regions of Iα and Iβ allomorphs of cellulose in microcrystals from *Microdictyon* cell wall fragments.[83] TEM imaging and diffraction methods were also combined to demonstrate that the biosynthesis of bacterial cellulose ribbons occurred by addition of the cellulose precursors at the non-reducing end of the chains.[84] A further striking demonstration of the molecular order in cellulose crystallites was provided when Sugiyama *et al.* successfully recorded the first high-resolution images directly showing longitudinal and axial projections of the crystal lattice of *Valonia* microfibrils.[85, 86]

1.3.2 Sample preparation

The sample for TEM imaging has to be extremely thin in order to be transparent to electrons. Sample preparation is thus a crucial step. The limiting thickness depends on the atomic number and density of the observed material and on the energy of the incident electron. Typically, for polymers, the thickness should remain well below 1 µm. For bulk materials, preparing such a thin specimen requires specific sectioning procedures. However, as the thickness of individual CNCs is well below this limit, the preparation of TEM specimens, for instance from dilute suspensions, is a lot easier.

1.3.2.1 Grids, supporting films and homogeneous distributions of nano-objects

In order to be observed by TEM, nanomaterial suspensions are deposited on 3.05 mm-large thin circular metallic grids with typical meshes around a few tens of micrometers, which will be placed in the sample holder for microscopy. There is a huge variety of TEM grids available and the selection of the right kind of grid is a crucial step for acquiring good images. Copper grids are the cheapest and the most widely used. However, when the pH of the suspension is low or high, copper can be degraded, resulting in the formation of artefactual crystallites or dendrites upon drying. In that case, gold or nickel grids have to be preferred. Carbon is by far the most commonly used supporting film. Carbon-coated grids are available commercially but carbon films can also be prepared in the laboratory by evaporating carbon on sacrificial collodion films or cleaved mica. The resulting films are then "fished" on copper grids. Carbon films have a typical thickness of 5-20 nm, depending on whether transparency or mechanical stability is favored. Formvar is also used as supporting film but it is less electron-transparent than carbon and can drift when heated by the electron beam at high magnification.

The main challenge in preparing a specimen suitable for TEM observation is to ensure a satisfying dispersion on the various objects. This is particularly critical for CNCs when one wants to determine the size distribution of a population of CNCs. The supporting carbon film is initially rather hydrophobic so the deposition of aqueous suspensions and subsequent air-drying generally result in locally accumulated material. Glow discharge is considered to be the easiest and most efficient pretreatment of carbon films before sample deposition. The TEM grids are placed in the chamber of a glow discharge unit (*e.g.* automated commercial systems like easiGlow from Pelco or ELMO from Agar Scientific). A pumping system allows to reach a low pressure and the residual air is ionized. The grids are submitted to this mild plasma cleaning during a few seconds, which results in a hydrophilic carbon surface (at least during several minutes) onto which aqueous suspensions easily spread. As charges are also generated on carbon during the treatment, the nano-objects tend to adsorb on the surface. The excess of liquid can thus be gently blotted out without waiting for complete drying and the objects should be homogenously distributed on the grid. Examples of distributions of cotton CNCs prepared afterglow discharge of the carbon film are shown in Figure 0.3. The factory settings of the commercial systems generally promote negative charges and hydrophilic surfaces but, depending on the applications and systems, positive charges and/or hydrophobic surfaces can be produced using additional agents.

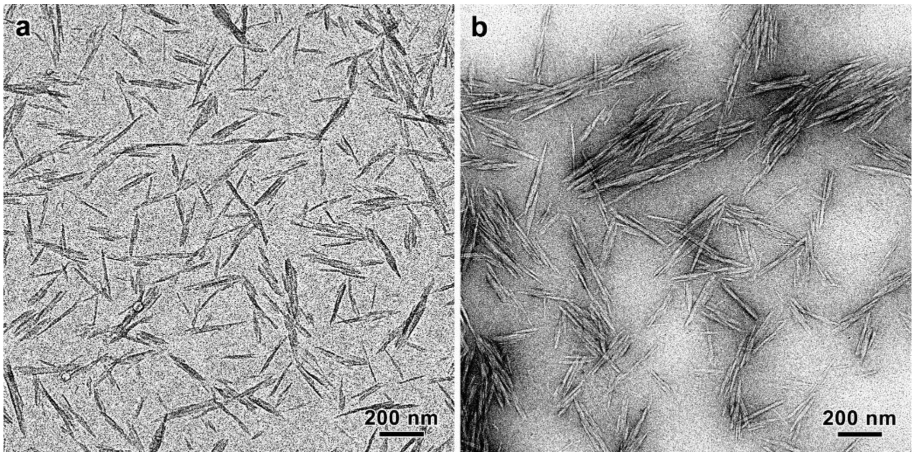

Figure 0.3 Comparison of images of unstained (a) and negatively stained (b) preparations of cotton CNCs. In both cases, the suspensions have been deposited on freshly glow-discharged carbon-coated grids.

Different materials have been tested as supporting films. While hydrophobic formvar promoted aggregation (Figure 0.4a), satisfactory dispersions of individual CNCs were achieved on hydrophilic silicon monoxide (Figure 0.4b).[87] Silica (SiO_2) and silicon nitride (Si_3N_4) films, with or without additional functionalization, are also commercially-available (NanoGrids from Dune Sciences).

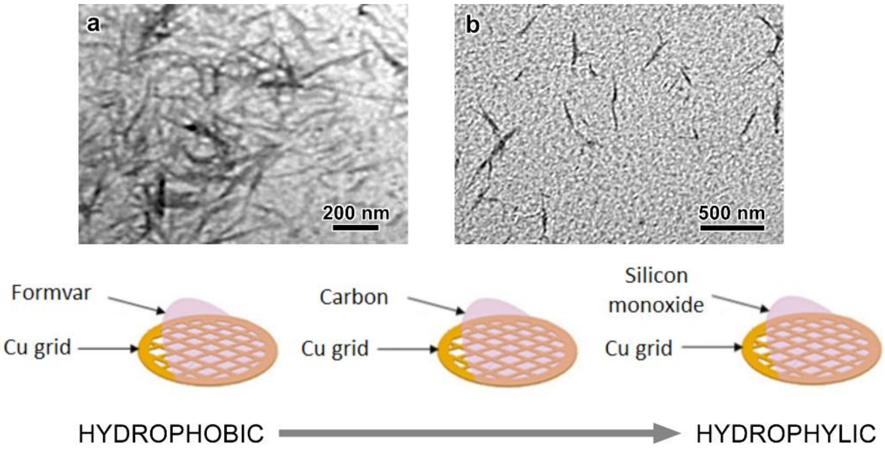

Figure 0.4 Comparison of never-dried CNCs at pH 5-6 on different types of supporting films: a) formvar; b) silicon monoxide.

In addition to the choice of supporting film and the use of addition pre-treatment, the use of very dilute suspensions is recommended, typically 0.001-0.01 % (w/v) for CNC suspensions. The nanocrystals will adsorb more efficiently onto hydrophilic films and particularly those that have been glow-discharged and this effect can be compensated by a higher dilution.

1.3.2.2 Impact of the CNC suspension on the TEM observation

After acid hydrolysis, CNCs occur in the form of suspensions that generally require further purification steps to remove the residual acid and salts. Indeed, residual soluble salts will likely crystallize upon drying on the supporting film of the TEM grid, resulting in the formation of artefactual dendrites. The suspensions are dialyzed against water to reach a pH around 2.5-3. Then CNCs may be used as such – i.e. in the form of an acidic aqueous suspension – or may be neutralized with NaOH to reach pH~7, in the form of neutral aqueous suspension [39]. The drying step of an acidic CNC suspension prevents the CNC to be later redispersed in water because CNC aggregates are created by hydrogen bonds *via* a phenomenon called hornification. Adjusting the suspension to a neutral pH prior to drying allows the dried CNC to be spontaneously redispersed in water, while the specimens dried from acid pH suspensions cannot be properly resuspended.[39]

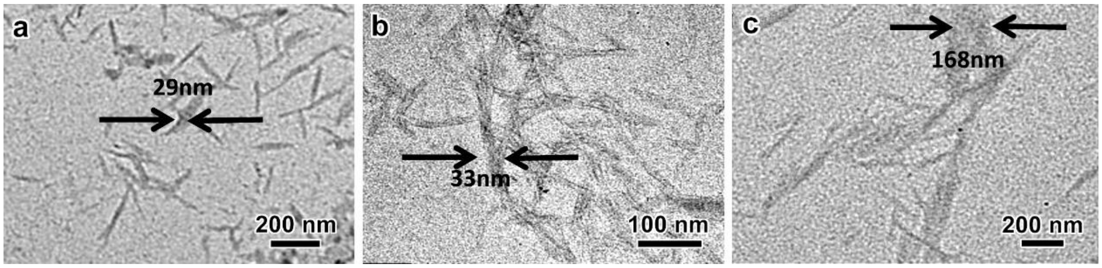

Figure 0.5 TEM images of unstained wood pulp CNCs: a) from a suspension of never-dried CNCs; b) from a freeze-dried suspension of redispersed CNCs; c) from a spray-dried suspension. All suspensions were adjusted to pH 5-6 before deposition onto carbon-coated copper grids.

The impact of the drying step of the CNCs prior to resuspension has been demonstrated by comparing three TEM specimens: 1) “never-dried” CNCs – CNCs suspension resulting directly from cellulose hydrolysis, 2) “freeze-dried” CNCs – CNCs suspension made from dispersing pH-neutralized freeze-dried CNCs and 3) “spay-dried” CNCs – CNCs suspension made from dispersing pH-neutralized spray-dried CNCs.[87] For all three specimens, the pH of the redispersed suspension was adjusted to 5-6 and the suspensions were deposited on carbon-coated grids. As seen in Figure 0.5, dispersions from spray-dried samples featured more CNC aggregates than those prepared from freeze-dried and never-dried samples. More single rods were observed in the latter than in any of the other two. On Figure 0.5a, the typical width of the bundles observed in the three samples is marked as a measurement of aggregation. This conclusion is actually consistent with the fact that spray-dried CNCs are more difficult to disperse than freeze-dried or never-dried counterparts.[39] In addition, a mushroom-like morphology has been exclusively reported for the spray-dried CNCs, which look like patches, of between 100 to 200 nm in size, with a much higher contrast than the rods.[88, 89] However, this morphology was proved to be an artefact from improper dispersion of the sample on the TEM grid.[87] Consequently, the suspensions of previously dried CNCs should be briefly sonicated to promote dispersion before preparing TEM grids.

The pH of CNC suspensions before drying definitively has an influence on the redispersed dried CNC aspect. Furthermore, at pH below 4-5, the CNCs are more negatively charged as the half-sulfate ester groups are in their acidic form. When the CNCs are redispersed in dionized water, the pH is around 5-6. If the never-dried CNCs are observed on carbon-coated TEM grids, at pH 5-6, the images show both individual and aggregated CNCs (Figure 0.6). The dispersion of CNCs from a suspension at pH 3.5 is better.

The particle morphology and aggregation state observed by TEM depends on how the dried CNC sample has been redispersed in water (use of sonication to promote de-agglomeration), which in turn depends upon the drying history of the CNCs (*i.e.* the pH of the suspension before drying). The optimal conditions to image CNCs is to prepare a TEM specimen from a suspension of never-dried CNCs or a pH-neutralized suspension.

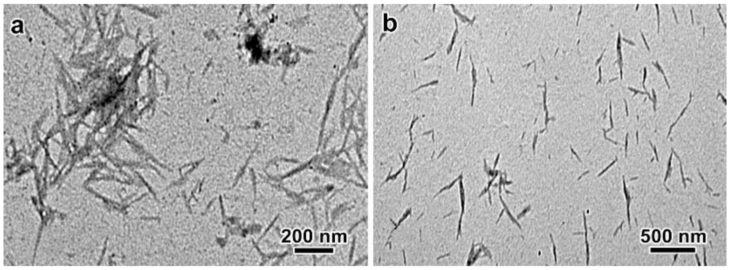

Figure 0.6 Influence of the pH of the CNC suspension on the dispersion on carbon films: a) pH 5-6; b) pH 3.5.

1.3.2.3 Contrast enhancement techniques

1.3.2.3.1 Negative staining

Since the contrast of cellulose specimens is rather low and since using high magnification to see more details will result in a rapid degradation of the particles (hence a loss of contrast), several techniques can be used to enhance the contrast in the images. The most widely used is so-called negative staining. A drop of aqueous solution of heavy atom salt is deposited on the specimen. Upon drying, a thin layer of heavy atoms concentrate around the nanoparticles, creating an electron dense outline.[90] The CNCs thus appear as clear objects on a dark background, hence the negative effect in the image. The preparations can be observed at a higher magnification as, although cellulose is indeed damaged by the electron beam, the heavy atom "imprint" is resistant, revealing fine details of the surface topography. So far, 2 % (w/v) uranyl acetate solutions have been the most commonly used stain but phototungstic acid or ammonium molybdate are sometimes used as well. Uranyl acetate will likely disappear from the catalogues as recent regulations have been enforced regarding the handling of radioactive products, resulting in a significant price increase. Consequently, new commercial ready-to-use stain solutions have been recently proposed, such as Uranyless (that contains lanthanides, from Delta Microscopies) or NanoVan (methylamine vanadate, from Nanoprobes). Practically, a homogenous negative staining of CNCs will be achieved under two conditions: i) the supporting carbon film has to be glow discharged before the nanoparticles and the stain are deposited; ii) the negative stain has to be deposited on the specimen before drying. After a few minutes, the stain in excess can be blotted away with filter paper and the residual thin stain film allowed to dry. It has to be noted that negative staining can partly promote the local flocculation of the CNCs on the supporting film, as can be seen in Figure 0.3b.

1.3.2.3.2 Metal shadowing

The technique has been used very early on to observe nanocellulose. Indeed, in the 1950's, Rånby published images of metal-shadowed preparations of wood and cotton microfibrils,[9] as well as tunicate[9] and bacterial CNCs.[9] Images of ramie and cotton CNCs can also be found in Mukherjee and Woods' paper.[8] Metal (generally gold/palladium or platinum) is vaporized on the sample with a given incidence angle. It thus accumulates on one side of the nanoparticles (electron-dense region) and is absent on the other side (electron transparent region). This results in a shadow-and-light effect that enhances the topography details of the specimen with a very high contrast. Again, it is the metallic layer that is observed even if the cellulose particles are damaged by the incident electron beam. The resolution is limited by the granularity and thickness of the metal film that increases the apparent width of the particles.

In the specific case of concentrated CNC suspensions, freeze-fracture can be used. A drop of the suspension is fast frozen under vacuum and a sharp knife breaks the frozen specimen into two fragments. The resulting surfaces are then directionally shadowed with a thin layer of evaporated metal evaporated, consolidated with an additional layer of carbon. The specimen in then warmed up and the metallic replica washed, deposited on a carbon-coated grid, and observed in the TEM, providing a high-contrast image of the topography of the fractured surface. An example of freeze-fracture replica of a concentrated suspension of cotton CNCs is shown in Figure 0.7a.

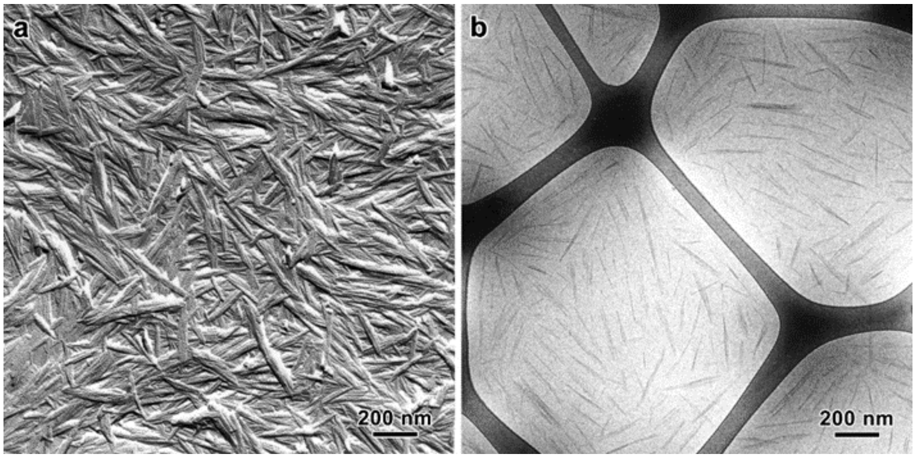

Figure 0.7 Alternative methods to observe cotton CNC dispersions: a) Pt/C replica of a freeze-fractured concentrated suspension; b) cryo-TEM of a dilute suspension. The CNCs are embedded in a thin film of vitreous ice (courtesy S. Elazzouzi-Hafraoui, CERMAV.

1.3.2.4 Cryo-TEM

Cryo-TEM consists in observing nanoparticles embedded in a thin film of transparent vitreous ice, thus avoiding the detrimental effects of drying and/or staining (degradation, deformation, aggregation, agglomeration, coalescence, uniplanar orientation, buffer salt crystallization, etc.). This technique is particularly helpful with dilute suspensions of nano-objects that are soft or liquid at room temperature and whose morphology or structure may be affected by air-drying (deformation due to capillary forces, decrystallization). Droplets of suspensions are deposited on so-called holey or lacey (*e.g.* NetMesh from Pelco) carbon films supported by TEM copper grids. Perforated support foils with predefined hole size and arrangements (*e.g.* Quantifoil from Quantifoil Micro Tools or C-flat from Protochips) can also be used. The liquid in excess is blotted with filter paper and the thin remaining film is quench-frozen in liquid ethane.[90] The frozen specimen is transferred in a cryo-specimen holder precooled with liquid nitrogen and in the microscope, and maintained at low temperature during TEM observation. Temperature and humidity-controlled chambers with automated plungers are commercially available (Vitrobot from FEI, EM-GP from Leica or Cryoplunge from Gatan), ensuring a higher reproducibility of the fast-freezing procedure. Cryo-TEM is not limited to aqueous suspensions and organic solvents can also be used, provided that they can be properly vitrified and that they are not dissolved in liquid ethane.

In the case of CNCs that are rigid crystalline nanoparticles, using cryo-TEM is helpful to prevent the aggregation that may happen upon drying, resulting in unwanted particle superimposition. Indeed, cryo-TEM has only been used in a small number of cases, to observe unstained non-flocculating cotton CNCs (Figure 0.7b)[23, 91] and characterize the 3D shape of dendronized-polymer wrapped CNCs by electron tomography (Section 1.3.3.3).[71]

1.3.2.5 Ultramicrotomy

This preparation technique should be used for bulk materials like plant tissues, cell wall fragments, nanocomposite materials, fibers, etc. When the specimen is affected by air drying, it has to be first fixed in paraformaldehyde / glutaraldehyde, post-fixed with osmium tetroxide, dehydrated by exchange with ethanol and embedded in hardening resins (Epon, LR White, Spurr, etc.).[92] In the case of nanocomposite materials incorporating CMFs or CNCs as reinforcing fillers, small fragments can be used without resin-embedding, provided that the material is sufficiently hard. Ultrathin (50-150 nm) sections of the specimens are then cut at room temperature with a diamond knife in an ultramicrotome.[93] The sections are collected on bare or carbon-coated TEM grids and, if necessary, in order to enhance contrast, may be post-stained with uranyl acetate / lead citrate. When the sample is soft at room temperature, ultrasectioning has to be performed in cryogenic conditions with a dedicated unit.

1.3.3 Observation techniques

Beside the constraints directly related to sample preparation (drying, staining, etc.), the TEM observation of CMFs and CNCs should result in the recording of images with a good signal-to-noise ratio and showing enough fine details of the objects. The various contrasts observed in the images are generated by physical interactions of the incident electrons with the material[94] and these contrasts have to be properly recorded by a sensitive "detector". Although for many years, micrographs were recorded on films, those have been progressively replaced by digital cameras typically equipped with a 1k×1k, 2k×2k or 4k×4k pixel-large CCD or CMOS detectors. These cameras have wide dynamics, good linearity and are very sensitive, allowing to record images with short exposure times and low electron doses. In addition, the software that pilots the camera can process the signal in real time, allowing, for instance, to calculate Fourier transform and correct some aberrations.

1.3.3.1 Contrast

Three main phenomena contribute to the overall contrast of CNCs in an image. Mass / thickness contrast (also called amplitude or diffusion contrast) is generally low for polymer particles as they are mostly composed of light elements that weakly scatter electrons. The proportion of electrons transmitted and scattered by the specimen depends on its density and thickness. By inserting an aperture located in the back focal plane of the objective lens, the operator blocks a certain amount of scattered electrons and form an image with the transmitted (or weakly scattered) electrons. In this so-called bright field image, the dark regions thus correspond to those that scattered most the electrons. As CMFs and CNCs are generally very thin, they generate a low amplitude contrast which, as described in section 1.3.3.1, can be significantly enhanced by using specific staining techniques involving heavy atoms. However, for unstained preparations, large differences in contrast can be observed in hybrid organic-inorganic systems, allowing, for instance, to locate metallic or oxide nanoclusters distributed along cellulose nanoparticles.[52]

Diffraction contrast occurs when the specimen is crystalline or semicrystalline, independently of its chemical nature (light or heavy atoms). Depending on the orientation of the crystal with respect to the incident beam, the electrons will be diffracted away from the optical axis. The set of discrete diffraction angles is defined by the unit cell of the crystal and can be determined using Bragg's relation.[94] When a diffracted beam is stopped by the objective lens aperture, in images with negative defocus, the regions of the particle from which the diffracted beam originates is very dark against the clear amorphous carbon background. This effect is thus important to visualize CNCs in bright field mode as it compensates somewhat the low amplitude contrast. It depends on the crystallinity index of cellulose (low for wood and high for tunicate CNCs, for instance). However, as cellulose is highly sensitive to beam damage, the diffraction contrast lasts for a limited time and disappear as soon as the material becomes amorphous.

Phase contrast is crucial in the case of electron-transparent nano-objects. It results from sharp differences in scattering properties between regions of the specimen. This is the case for CNCs spread on a carbon film (particles in vacuum), and CNC suspensions observed by cryo-TEM (particles embedded in vitreous ice). Phase contrast generates interference Fresnel fringes whose amplitude and distribution depend on the defocus of the objective lens.[94] The effect of phase contrast on the image of unstained CNCs is illustrated in Figure 8a and 8c. High defocus values (positive or negative) increase contrast but also generate larger Fresnel fringes and increase the apparent size of the nanoparticles. Note the complete reverse of contrast between under-focused and over-focused images. In over-focused images, the CNCs are clear with a dark outline which reminds the aspect they would have after negative staining. Close to zero defocus, the contrast is minimal and the specimen is hardly visible. Paradoxically, the operator will be satisfied by images recorded with some defocus as the contrast is higher and as the Fresnel fringes around the particles create an impression of "sharpness". However, this effect is associated with a loss of details. A satisfactory image is thus obtained by balancing the opposing requirements of contrast and ultrastructural details. By convention, the images are recorded in underfocused conditions, the amount of applied defocus increasing with decreasing magnification (typically about -5 µm at 3000x and -1 µm at 10000x). The importance of using underfocused conditions is clear in the case of negatively stained specimens, as seen in Figure 0.8b.

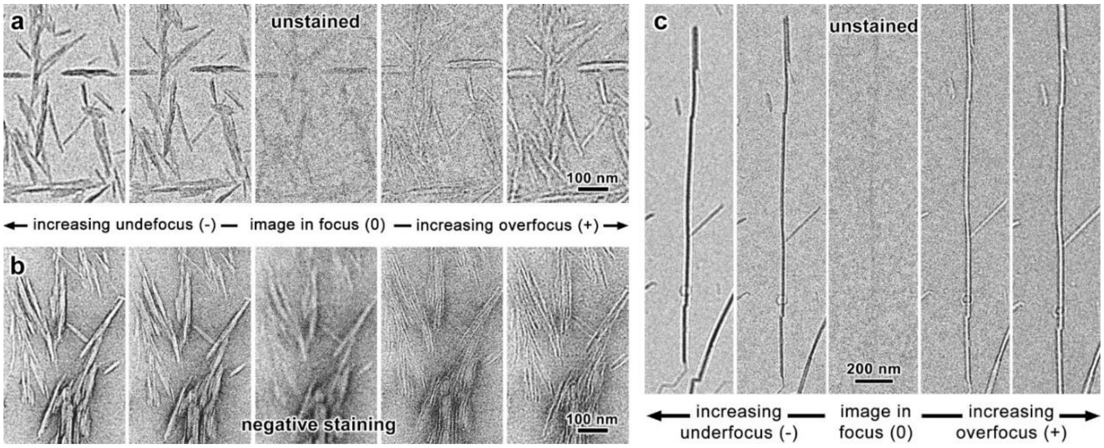

Figure 0.8 Influence of the defocus on the contrast of cotton (a,b) and tunicate (c) CNCs. The preparations are unstained (a,c) and negatively stained with uranyl acetate (b).

In the routine observation of unstained CNC's, the three types of contrast contribute: a weak amplitude contrast due to the small size and organic nature of the particles, a significant diffraction contrast that depends on the crystallinity index of cellulose and orientation of the particles with respect to the incident electron beam, a phase contrast that generate Fresnel fringes along the CNCs controlled by the amount of defocus. As detailed in the following section, all these contributions will be affected by radiation damage.

1.3.3.2 Radiation damage

The most important limitation to observe crystalline polymers by TEM is the significant damage created by the electron beam that rapidly affects the resolution and decreases the contrast of the objects. In such low-density materials, the inelastic scattering of the electrons generate molecular excitations and ionization phenomena, resulting in local heating of the material, breaking of covalent bonds, diffusion of free radicals and emission of volatile species.[95] The consequences can be mass loss, fusion, vaporization, loss of crystallinity, all resulting in a significant decrease of amplitude, diffraction and Fresnel contrasts. For crystalline materials, one can define a "lethal" or "total end point" dose by monitoring the disappearance of the electron diffraction pattern and calculate the electron dose at which crystallinity is irreversibly lost.

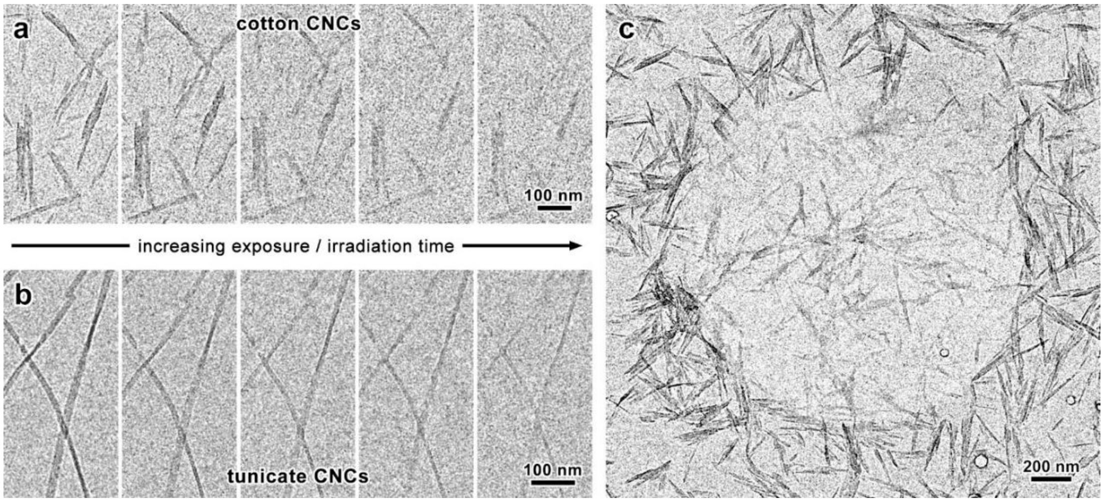

Figure 0.9 Influence of the radiation damage on the contrast of unstained cotton (a) and tunicate (b) CNCs. In (c), the electron beam has been briefly condensed into a smaller disk resulting in a marked damage on a distribution of unstained cotton CNCs.

Even if the selected microscope has the ability to visualize details down to a resolution of 0.1-0.2 nm, the sample itself imposes drastic constraints. Several solutions exist to limit the detrimental effects of beam damage during the observation and image recording. First, contrary to what is done with materials made of heavy atoms, increasing the accelerating voltage of the electrons decreases the interactions with the polymer and thus increases the lethal dose (typically about a factor of 2 between 100 and 200 kV). However, the consequence of a higher accelerating voltage is a decrease in contrast. For instance, individual CNCs observed at 200 kV or a higher voltage tend to become transparent.

Second, the operator has to work with electron doses much lower than the lethal dose, which requires both to use low magnifications and significantly decrease the illumination (e.g. by changing the "spot size" and spreading the surface of illumination). The observation of unstained cellulose specimens thus requires for the operator to make a compromise between image magnification (to see fine details with a sufficient contrast) and electron dose (to have a sufficient signal-to-noise ratio for the detector recording the image). Chanzy has quantified the lethal dose of cellulose by submitting *Valonia* CMFs to increasing electron doses at various accelerating voltages and monitoring the decay of diffracted beam intensity.[96] The average value for the lethal dose was about 4 electrons.Å^{-1} which illustrates the extreme sensitivity of polysaccharides.

Third, the radiation damage can be significantly slowed down (but not suppressed) when the diffusion of free radicals is reduced by maintaining the specimen at low temperature, using a specific specimen holder cooled down with liquid nitrogen. In that case, an increase of the lethal dose by a factor of 3 has been reported in the literature.

The images in Figure 0.9 qualitatively illustrates the cumulative effect of beam damage during the observation of CNCs. Cotton and tunicate CNCs (Figure 0.9a and Figure 0.9b, respectively) have been submitted to increasing electron doses. The three contributions to contrast previously mentioned are affected: diffraction contrast by disruption of the crystallinity, amplitude contrast by mass loss and phase contrast by thinning of the particle and surface damage. The CNCs become transparent and their shape less well-defined. These effects are very fast and irreversible, in particular if the specimen is readily observed at magnifications above 10000x or the beam is inadvertently focused into a smaller disk (Figure 0.9c).

1.3.3.3 3D imaging

TEM images are 2D projections of the 3D objects along the beam direction. Information along this direction is thus lost. One 2D image is generally not enough for the viewer to have a clear idea of the 3D shapes and several images, recorded at different tilt angles of the specimen, are necessary to make a reliable morphological analysis. Electron tomography (ET) can be performed in modern microscopes, thanks to the use of digital cameras and software that can precisely control the specimen orientation and image acquisition. Briefly, series of 2D images containing the data for mass-density distribution in the specimen, are automatically recorded with small angular increments over a large angular range (usually from +70° to -70°). These projections. Using specific software, the collected images are aligned with respect to one another and a back-projection is carried out to obtain a 3D reconstruction of the specimen volume.[97-99] While this technique is now widely used to study the morphology and structure of biological systems (proteins, viruses, membranes, etc.), only one case of CNC analysis can be found in the literature and will be described in section 1.4.3.[71] As explained in section 1.3.3.2, unstained cellulose is highly sensitive to beam damage and will be rapidly degraded and the amplitude contrast will thus decrease during the recording of the tilt series. This imposes to work at low magnification, with extremely low electron doses and a sensitive digital camera. In addition, due to the crystalline nature of CNCs, the contribution of diffraction contrast may fluctuate depending on the tilt angle of the particles.

1.4 Review of cellulose nanocrystal imaging and size analysis

1.4.1 TEM images and size distributions of CNCs

Although AFM is still often used to perform size measurements of CNC populations,[14, 15, 67-69] TEM has been a method of choice to visualize the shape and structure of individual or bundled CNCs.[15, 23, 100, 101] The images are consistent and show that CNCs are rod-like and have a high aspect ratio. Some authors have observed spherical CNC particles[88] but these have been shown to be aggregation-induced artefacts.[87] As seen in Figure 0.2, the CNC aspect ratio and structure greatly vary with the cellulose source. CNCs obtained from plant sources like cotton,[22, 23, 102] rice,[24, 25] ramie,[26-28] sisal[28, 29] or sugar beet[22] have smaller aspect ratios than those of bacterial cellulose,[37, 38] microcrystalline cellulose (MCC)[16, 27, 32, 33, 36, 103] and tunicin[27] (Table 0.1). The significant heterogeneity of the length and width distributions of CNCs for a given source of cellulose can be attributed to the method of preparation: type and concentration of the acid, reaction time, temperature, sonication, method of drying, etc.

To a first approximation, the size measurement of CNCs should not be particularly difficult, provided that the objects are fairly well individualized on the supporting films, not severely damaged by the electron beam section 1.3.3.2, and that a reasonable under-focus was used to record the image (section 1.3.3). Their length and width can be measured from general views recorded at intermediate magnifications (typically 5000 to 10000×) by using a software like ImageJ.[104] Automated procedures are generally difficult to implement with TEM micrographs as the preliminary binarization of the images requires to clearly distinguish the CNCs from a continuous background. As seen in many images presented in this article, this is rarely the case. One thus directly uses the measurement tools of the software or outlines each CNC so that a semi-automatic measurement routine can be run. In addition, a review of the literature shows that the number of counted particles greatly varies (typically from 100 to 1000), mostly depending on the number of individual particles in the images and the patience of the operator. Of course, the number of objects taken into account will influence the reliability of the population statistics.

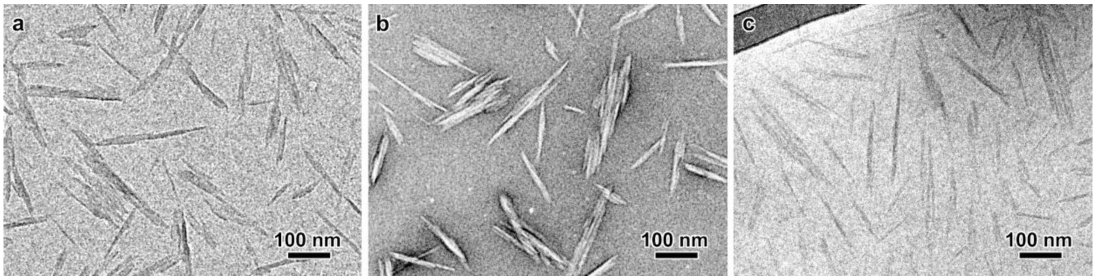

Figure 0.10 TEM images illustrating the diversity of shapes and structures of CNCs prepared by acid hydrolysis of cotton linters: a) dry specimen; b) negative staining (courtesy F. Azzam, CERMAV); c) cryo-TEM (courtesy S. Elazzouzi-Hafraoui, CERMAV).

When higher magnification are used (typically 10000 to 50000×), keeping in mind the potential beam damage of unstained specimens, a better resolution is achieved and more details are revealed, particularly after negative staining. As confirmed by many images found in the literature, the majority of CNCs prepared from various sources are not single crystallites. They are often composed of a few laterally joined rodlike crystallites, as illustrated by Figure 0.10 in the case of cotton CNCs. The same feature has been reported for tunicate,[23] Avicel[23] or bamboo[11] CNCs, to give just a few examples. The images in Figure 0.10 clearly show that cotton CNCs have a high variability in shape and dimensions. They are all different in size and structure, being composed of different numbers of unit crystallites, joined in a different fashion. This association inside individual particles does not result from artefactual flocculation but rather from the fact that the hydrolysis was performed on dry cellulosic substrates in which microfibrils are strongly linked by hydrogen bonds. Neither acid hydrolysis nor sonication (nor any high shearing device) could fully separate the constituting crystallites.

The composite nature of most CNCs, which was validated by a combination of imaging and scattering techniques,[11, 23] will thus influence the measurement of the lateral dimensions that depend on the cross-sectional shape and its regularity along the whole particle, the existence of a longitudinal twist and the specimen preparation method. Considering the acicular morphology of CNCs, their distribution on a supporting film or inside thin vitreous ice favors their planar orientation, allowing to easily measure the length of the rodlike nanoparticles. However, while the particle thickness can be accurately measured from tapping mode AFM images, a choice has to be made regarding the definition of the width in TEM micrographs. As many types of CNCs exhibit a spindle-like shape, the width is generally defined as the largest dimension perpendicular to the particle long axis. Moreover, when the CNCs are ribbon-like, because of the rectangular cross-section of individual crystallites (tunicate CNCs, for instance) or the lateral association of crystallites (cotton CNCs), the drying on a supporting film will generate a strong uniplanarity, the particles tending to lie on their widest face. This propensity to uniplanarity, that brings very useful information of the crystallite orientation in the CNCs, can be easily evaluated by performing complementary WAXS analysis on air-dried films.[11, 23] In addition, some CNCs are longitudinally twisted, which can be detected in TEM images by variations in contrast or stain distribution along the particle (an example on tunicate CNCs can be seen in Figure 0.9b). Therefore, the apparent width of the particle will vary, making the choice of a relevant region to measure more difficult.

Cryo-TEM has been shown to be helpful to prevent particle aggregation/agglomeration due to drying.[23, 91] If the suspension concentration has been chosen with care, and considering the fact that CNCs have charges on their surface, they are conveniently individualized in the embedding film of vitreous ice. As their lateral dimensions are smaller than the typical thickness of the liquid film prior to fast-freezing, they could freely rotate around their long axis. Consequently, the measured width indeed corresponds to the projection of the CNC in a given orientation. Therefore, the width distribution of the population from a cryo-TEM image provides a rotational average of the lateral dimension of the particle and can thus be different from the distribution that is obtained from a specimen prepared by air-drying on a supporting film. The effect will be more pronounced for flat particles, such as cotton CNCs, as shown in Figure 0.10. Using a simple model, Elazouzzi-Hafraoui *et al.* have described the relation that can be made between the distributions obtained with both preparation techniques.[23]

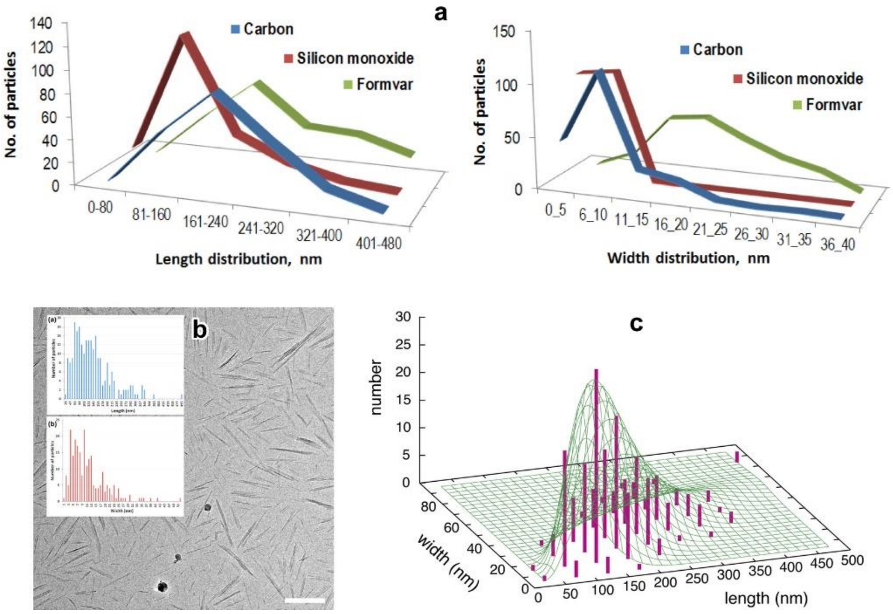

Figure 0.11 Length and width distributions histograms of various CNC systems determined from TEM images: a) never-dried CNCs at pH 3.5 deposited on different types of grids and observed unstained; b) cotton CNCs observed by cryo-TEM; c) 2D histogram from negatively stained cotton CNCs

Determining a size distribution from TEM images thus implies to clearly state the choices that were made in relation with the particle morphology. In addition, length and width distribution can be determined independently (Figure 0.11a and Figure 0.11b)[87, 91] or assuming that there is a correlation between longitudinal and lateral dimensions of the CNCs. In that case, length and width are tabulated for each particle, resulting in a 2D size distribution histogram (Figure 0.11c) which validates (or not) the correlation.[23]

The relevance of the size distribution of a given population of CNCs depends on several factors in relation with the problem that is addressed or the specific property that is investigated. For acicular (and possibly ribbon-like) CNCs, the influence of the statistical errors on the measurements will differ depending on the considered dimension (smaller for the length and larger for the width and thickness). Moreover, the size distributions are always wide, with large standard deviations and asymmetrical shapes (Figure 0.11).[15, 91, 100, 101] Average lengths, widths and thicknesses provide a cylindrical average view of the particles that can be useful to build a preliminary model. However, it is likely that a more complete description of the population, made by fitting the data with suitable functions, will be more relevant for comparisons with X-ray or neutron scattering results,[23] or, for example, to understand the percolation behavior of CNCs inside nanocomposite materials.

1.4.2 TEM of CNC-hybrid composites

Hybrid composites of CNC with metal nanoparticles (NPs) such as Ag, [58, 105] Au,[53] Pd,[52, 106] Pt[107] or Se[108] have been reported. TEM, along with its analytical tools, was used to characterize such composites (Figure 0.12). Due to their high atomic number and possible crystallinity, the metal NPs appear as dark spots in under-focused images. The difficulty to observe such hybrid organic-inorganic systems is that CNCs and metal NPs have very different sensitivity to beam damage. While metallic NPs are very stable, cellulose is rapidly damaged, resulting in a significant loss of contrast and recognizable morphology. Consequently, to have a better visibility, a large defocus is usually applied which causes an overestimation in the size of metal NPs.[87] Additional negative staining can be effective to outline the CNCs more precisely but care must be taken to prevent the layer of stain from overshadowing the contrast of the metallic nanoclusters. Indeed, if the metallic NPs are smaller than 3-4 nm, they will not be distinguished from the granularity of the dry stain. As shown in Figure 0.12f, for larger NPs, CNCs can benefit from the negative staining while the metallic clusters still appears as dark spots.

Alongside visualization of metal NPs, it is very important to validate the chemical nature of the NPs seen in the images. This analysis can be done in a TEM by using energy-dispersive X-ray spectroscopy (EDX) which allows for quantitative measurement of the chemical composition.[52]

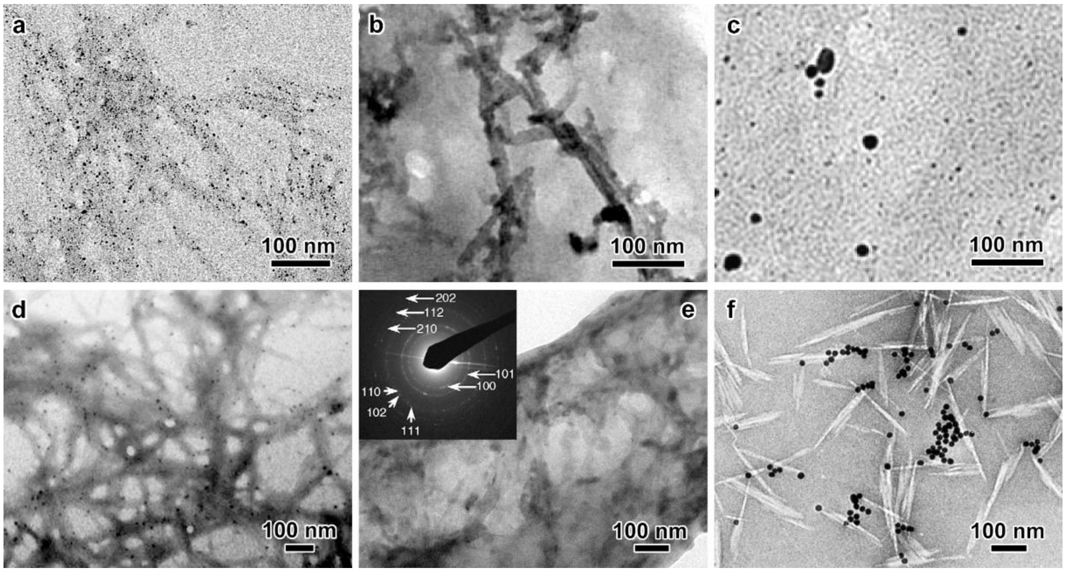

Figure 0.12 Hybrid systems with metallic nanoparticles supported by CNCs: a) Pd on wood pulp CNCs; b) Pt on cotton CNCs; c) Ag on cotton CNCs; d) Au on wood pulp CNCs; e) Se on cotton CNCs. Inset: selected area electron diffraction pattern of the selenium nanoparticles; f) colloidal gold nanoparticles in interaction with cotton CNCs (negative staining) (courtesy B. Jean, CERMAV - unpublished results).

1.4.3 TEM of CNC-polymer nanocomposites

Due to their nanoscale dimensions, high surface area, low density and high mechanical strength, CNCs have been incorporated as reinforcing component into various polymer matrices: styrene-butyl acrylate,[13, 109] polylactic acid,[110, 111] poly(vinylalcohol),[112] polyurethane,[113] epoxides[114] and polyvinylacetate.[29, 115] In order to explain the variation in mechanical properties, these bulk materials have often been characterized by SEM after fracturing, allowing to visualize the distribution of CNCs that emerge at the fracture surface. However, SEM remained limited to the characterization of the topography of the fracture surfaces. TEM was also used to visualize the CNCs inside the material *via* preparation by ultramicrotomy of ultrathin sections of the composites. Figure 0.13 shows examples of images of nanocomposites of CNCs in matrices of styrene-butyl acrylate,[13] polylactic acid[110] and epoxy,[114] respectively. CNCs can be visualized using their intrinsic diffraction contrast[13] but, as they are very sensitive to beam damage, their contrast rapidly decreases to the point where they become hardly visible with the polymer matrix due to the lack of density difference. Additional staining of the matrix can be used, for instance with OsO_4, creating a negative staining effect revealing the embedded CNCs (Figure 0.13c).[114]

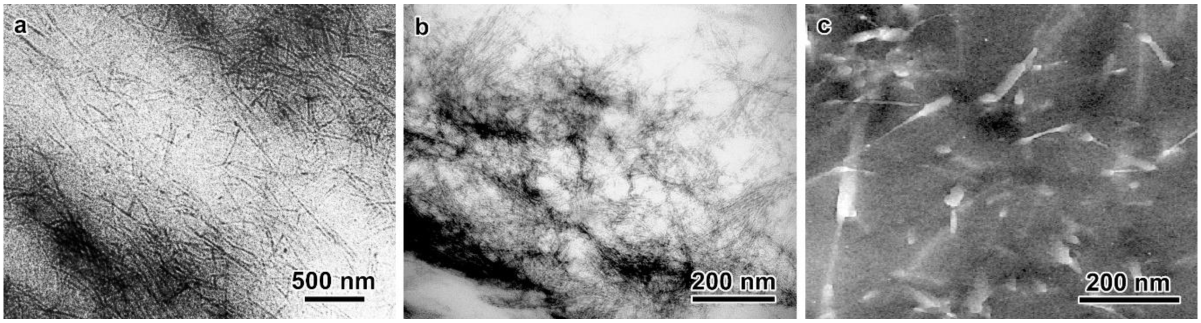

Figure 0.13 TEM images of ultrathin sections of nanocomposite materials incorporating CNCs as reinforcing component: a) tunicate CNCs in a matrix of styrene-butyl acrylate - diffraction contrast in bright field mode; b) CNCs from spruce MCC in PLA - uranyl acetate staining; c) tunicate CNCs in epoxy matrix - OsO4 staining.

1.4.4 3D imaging of CNCs and polymer-wrapped CNCs

Electron tomography (described in section 1.3.3.3) has only very recently started to be used to characterize cellulose-based architectures or individual particles. Ciesielski *et al.* have recently published ET reconstructions of treated plant cell walls, allowing to get 3D information on the microfibril morphology.[116] Majoinen *et al.* studied the morphology of individual CNCs embedded in vitreous ice. Using cryo-TEM conditions, they recorded tilt series and reconstructed tomograms from pristine CNCs (Figure 14a) and from CNCs wrapped up with dendronized polymers (Figure 0.14). This 3D visualization of the CNCs revealed the presence of an helicoidal twist along the rod-like particles. These twists have been proposed to be significant in explaining the cholesteric liquid crystalline assembly[18, 26] and their use in chiral templating.[45, 46]

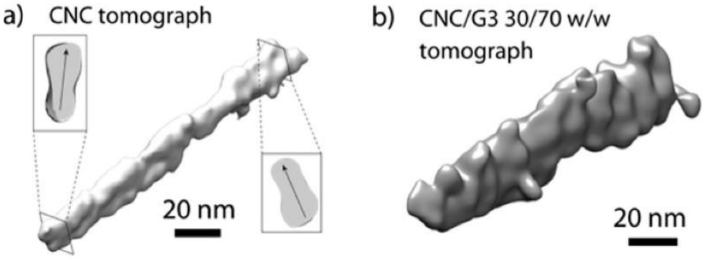

Figure 0.14 Electron tomography reconstitution of initial (a) and dendronized (b) polymer-wrapped cotton CNCs

1.5 Conclusion and perspectives: challenges and solutions in imaging CNCs

CNCs have been extensively studied and many reports can be found in the literature. The particle shape and size vary as a function of the cellulose source and the methodology used to produce the CNCs. In all cases, the CNC populations are polydisperse featuring wide and asymmetrical size distributions. An accurate knowledge of the CNC dimensions and size distribution is crucial to characterize the properties of individual particles and their assemblies in suspension, in dry films or after incorporation into matrices. For instance, morphology and size will influence the phase separation behavior and the formation of liquid crystalline organizations or the percolation properties in nanocomposites. The development of chemical modifications strategies also requires to have a good knowledge of the accessible surface. In addition, CNCs have recently become a new type of industrial nanomaterial with numerous exciting properties and an accurate characterization is important to optimize processes and control their reproducibility.

TEM is a key imaging technique to achieve this goal, thanks to the development of specific techniques to observe beam sensitive polymers. Cellulose is without doubt one of the most beam sensitive materials that can be observed by TEM. Consequently, special care must be taken to record reliable images of CNCs (low dose, low temperature, additional staining). In this article, we have described several sample preparation procedures and observation techniques adapted to the recording of images of CNC populations and carry out reliable size distribution analyses. New approaches have recently been proposed, taking advantage of technical improvements of the microscopes, such as a better control of the stage movements, the use of highly sensitive digital cameras and automatized corrections of several optical aberrations, allowing to record electron tomography image series and reconstruct the volume of the specimens. Although these sophisticated approaches are not routinely used yet in the field of cellulose science, they will certainly rapidly develop. In addition, at a time when the research on CNCs is booming and the range of commercial applications is expanding, TEM imaging will continue to play a central role. Automated particle measurement procedures using TEM image analysis software will be needed to streamline quality control.

1.6 Disclaimer

Mention of trademarks or commercial products in this article is solely for the purpose of providing examples of sample preparation materials and methods and does not imply any affiliation from the authors with the mentioned companies.

1.7 References

1. G. Chinga-Carrasco, *Nanoscale research letters*, 2011, **6**, 1.
2. Y. Nishiyama, *Journal of Wood Science*, 2009, **55**, 241.
3. B. P. D. Klemm, T. Heinze, U. Heinze, W. Wagenknecht, Wiley Online, 1998, vol. 1.
4. R. F. Nickerson and J. A. Habrle, *Ind. Eng. Chem. Res.*, 1947, **39**, 1507.
5. B. G. Rånby, *Acta Chem. Scand.*, 1949, **3**, 649.
6. B. G. Rånby, *Discuss. Faraday Soc.*, 1951, **11**, 158.
7. J. F. Revol, H. Bradford, J. Giasson, R. H. Marchessault and D. G. Gray, *Int. J. Biol. Macromol.*, 1992, **14**, 170.
8. S. M. Mukherjee and H. J. Woods, *Biochimica et Biophysica Acta*, 1953, **10**, 499.
9. B. Ranby, *ARKIV FOR KEMI*, 1952, **4**, 249.
10. C. Fraschini, G. Chauve, J.-F. L. Berre, S. Ellis, M. Méthot, B. O’Connor and J. Bouchard, *Nordic Pulp and Paper Res. J.* , 2014, **29**, 31.
11. B. S. Brito, F. V. Pereira, J.-L. Putaux and B. Jean, *Cellulose*, 2012, **19**, 1527.
12. M. Lopez, H. Bizot, G. Chambat, M.-F. Marais, A. Zykwinska, M.-C. Ralet, H. Driguez and A. Buléon, *Biomacromolecules*, 2010, **11**, 1417.
13. V. Favier, H. Chanzy and J. Cavaille, *Macromolecules*, 1995, **28**, 6365.
14. M. Le Normand, R. Moriana and M. Ek, *Carbohydr. Polym.*, 2014, **111**, 979.
15. H. A. Silvério, W. P. F. Neto, N. O. Dantas and D. Pasquini, *Industrial Crops and Products*, 2013, **44**, 427.

16. S. J. Eichhorn, A. Dufresne, M. Aranguren, N. E. Marcovich, J. R. Capadona, S. J. Rowan, C. Weder, W. Thielemans, M. Roman, S. Renneckar, W. Gindl, S. Veigel, J. Keckes, H. Yano, K. Abe, M. Nogi, A. N. Nakagaito, A. Mangalam, J. Simonsen, A. S. Benight, A. Bismarck, L. A. Berglund and T. Peijs, *Journal of Material Science*, 2009, **45**, 1.
17. Y. Habibi, L. A. Lucia and O. J. Rojas, *Chem. Rev.*, 2010, **110**, 3479.
18. D. Klemm, F. Kramer, S. Moritz, T. Lindström, M. Ankerfors, D. Gray and A. Dorris, *Angew. Chem. Int. Ed.*, 2011, **50**, 5438.
19. R. J. Moon, A. Martini, J. Nairn, J. Simonsen and J. Youngblood, *Chem. Soc. Rev.*, 2011, **40**, 3941.
20. N. Lin, J. Huang and A. Dufresne, *Nanoscale*, 2012, **4**, 3274.
21. C. Salas, T. Nypelö, C. Rodriguez-Abreu, C. Carrillo and O. J. Rojas, *Curr. Opin. Colloid Interface Sci.*, 2014, **19**, 383.
22. L. Heux, G. Chauve and C. Bonini, *Compos. Interfaces*, 2000, **16**, 8210.
23. S. Elazzouzi-Hafraoui, Y. Nishiyama, J.-L. Putaux, L. Heux, F. Dubreuil and C. Rochas, *Biomacromolecules*, 2008, **9**, 57.
24. P. Lu and Y.-L. Hsieh, *Carbohydr. Polym.*, 2012, **87**, 564.
25. N. Johar, I. Ahmad and A. Dufresne, *Industrial Crops and Products*, 2012, **37**, 93.
26. M. S. Peresin, Y. Habibi, J. O. Zoppe, J. J. Pawlak and O. J. Rojas, *Biomacromolecules*, 2010, **11**, 674.
27. Y. Habibi, A.-L. Goffin, N. Schiltz, E. Duquesne, P. Dubois and A. Dufresne, *J. Mater. Chem.*, 2008, **18**, 5002.
28. A. Junior de Menezes, G. Siqueira, A. A. S. Curvelo and A. Dufresne, *Polymer*, 2009, **50**, 4552.
29. N. L. Garcia de Rodriguez, W. Thielemans and A. Dufresne, *Cellulose*, 2006, **13**, 261.
30. G. Siqueira, J. Bras and A. Dufresne, 2008, **10**, 425.
31. J. Araki, M. Wada, S. Kuga and T. Okano, *Colloids and Surfaces A: Physicochemical and Engineering Aspects*, 1998, **142**, 75.
32. J. Araki, M. Wada, S. Kuga and T. Okano, *Journal of Wood Science*, 1999, **45**, 258.

33. D. Bondeson, A. Mathew and K. Oksman, *Cellulose*, 2006, **13**, 171.
34. M. N. Anglès and A. Dufresne, *Macromolecules*, 2000, **33**, 8344.
35. F. Kimura, T. Kimura, M. Tamura, A. Hirai, M. Ikuno and F. Horii, *Langmuir*, 2005, **21**, 2034.
36. J. Araki and S. Kuga, *Langmuir*, 2001, **17**, 4493.
37. M. Roman and W. T. Winter, *Biomacromolecules*, 2004, **5**, 1671.
38. M. Grunert and W. T. Winter, *J. Polym. Environ.*, 2002, **10**, 27.
39. S. Beck, J. Bouchard and R. Berry, *Biomacromolecules*, 2012, **13**, 1486.
40. R. H. Marchessault, F. F. Morehead and N. M. Walter, *Nature*, 1959, **184**, 632.
41. J.-F. Revol, L. Godbout, X.-M. Dong, D. G. Gray, H. Chanzy and G. Maret, *Liq. Cryst.*, 1994, **16**, 127.
42. G. Picard, D. Simon, Y. Kadiri, J. LeBreux and F. Ghozayel, *Langmuir*, 2012, **28**, 14799.
43. D. Liu, S. Wang, Z. Ma, D. Tian, M. Gu and F. Lin, 2014, **4**, 39322.
44. Q. Chen, P. Liu, F. Nan, L. Zhou and J. Zhang, 2014, **15**, 4343.
45. K. E. Shopsowitz, H. Qi, W. Y. Hamad and M. J. MacLachlan, *Nature*, 2010, **468**, 422.
46. K. E. Shopsowitz, J. A. Kelly, W. Y. Hamad and M. J. MacLachlan, *Adv. Funct. Mater.*, 2014, **24**, 327.
47. K. E. Shopsowitz, W. Y. Hamad and M. J. MacLachlan, *Angew. Chem. Int. Ed.*, 2011, **50**, 10991.
48. A. Querejeta-Fernández, G. Chauve, M. Methot, J. Bouchard and E. Kumacheva, *J. Am. Chem. Soc.*, 2014, **136**, 4788.
49. T. Serizawa, T. Sawada, H. Okura and M. Wada, *Biomacromolecules*, 2013, **14**, 613.
50. J. Yang, C.-R. Han, J.-F. Duan, M.-G. Ma, X.-M. Zhang, F. Xu, R.-C. Sun and X.-M. Xie, *J. Mater. Chem.*, 2012, **22**, 22467.
51. X. Yang and E. D. Cranston, *Chem. Mater.*, 2014, **26**, 6016.
52. C. M. Cirtiu, A. F. Dunlop-Brière and A. Moores, *Green Chem.*, 2011, **13**, 288.
53. E. Lam, S. Hrapovic, E. Majid, J. H. Chong and J. H. T. Luong, *Nanoscale*, 2012, **4**, 997.

54. P. Zhou, H. Wang, J. Yang, J. Tang, D. Sun and W. Tang, *Ind. Eng. Chem. Res.*, 2012, **51**, 5743.
55. M. Rezayat, R. K. Blundell, J. E. Camp, D. A. Walsh and W. Thielemans, *ACS Sustainable Chem. Eng.*, 2014, **2**, 1241.
56. M. Kaushik, K. Basu, C. Benoit, C. C. M., H. Vali and A. Moores, *J. Am. Chem. Soc.*, 2015, **137**, 6124.
57. X. D. Wu, C. H. Lu, Z. H. Zhou, G. P. Yuan, R. Xiong and X. X. Zhang, *Environ. Sci. Nano*, 2014, **1**, 71.
58. R. Xiong, C. Lu, W. Zhang, Z. Zhou and X. Zhang, *Carbohydr. Polym.*, 2013, **95**, 214.
59. T. Kovacs, V. Naish, B. O'Connor, C. Blaise, F. Gagné, L. Hall, V. Trudeau and P. Martel, *Nanotoxicology*, 2010, **4**, 255.
60. R. Mohammadi, E. Eidi, M. Ghavami and M. Z. Kassaee, 2014, **393**, 309.
61. H. Charreau, M. L Foresti and A. Vazquez, *Recent patents on nanotechnology*, 2013, **7**, 56.
62. C. A. Husemann E, *Naturwissenschaften*, 1944, **32**, 79.
63. S. Shafiei-Sabet, W. Y. Hamad and S. G. Hatzikiriakos, *Langmuir*, 2012, **28**, 17124.
64. S. Shafiei-Sabet, W. Hamad and S. Hatzikiriakos, *Cellulose*, 2014, **21**, 3347.
65. B. Derakhshandeh, G. Petekidis, S. S. Sabet, W. Y. Hamad and S. G. Hatzikiriakos, *J. Rheol.*, 2013, **57**, 131.
66. W. Helbert, Y. Nishiyama, T. Okano and J. Sugiyama, *Journal of Structural Biology*, 1998, **124**, 42.
67. R. M. dos Santos, W. P. F. Neto, H. A. Silvério, D. F. Martins, N. O. Dantas and D. Pasquini, *Industrial Crops and Products*, 2013, **50**, 707.
68. I. A. Sacui, R. C. Nieuwendaal, D. J. Burnett, S. J. Stranick, M. Jorfi, C. Weder, E. J. Foster, R. T. Olsson and J. W. Gilman, *ACS Appl. Mater. Interfaces*, 2014, **6**, 6127.
69. E. E. Urena-Benavides, P. J. Brown and C. L. Kitchens, *Langmuir*, 2010, **26**, 14263.

70. I. Kalashnikova, H. Bizot, P. Bertoncini, B. Cathala and I. Capron, *Soft Matter*, 2013, **9**, 952.
71. J. Majoinen, J. S. Haataja, D. Appelhans, A. Lederer, A. Olszewska, J. Seitsonen, V. Aseyev, E. Kontturi, H. Rosilo, M. Österberg, N. Houbenov and O. Ikkala, *J. Am. Chem. Soc.*, 2013, **136**, 866.
72. H. Ruska, *Kolloid-Z.*, 1940, **92**, 276.
73. O. Eisenhut and E. Kuhn, *Angew. Chem.*, 1942, **55**, 198.
74. G. Hambraeus and B. Rånby, *Nature*, 1945, **155**, 200.
75. C. A. Husemann E, *Die Markromolecular Chemie*, 1947, **1**, 158.
76. W. G. Kinsinger and C. W. Hock, *Ind. Eng. Chem. Res.*, 1948, **40**, 1711.
77. C. W. Hock, *Textile Research Journal*, 1950, **20**, 141.
78. B. Rånby and E. Ribi, *Experientia*, 1950, **6**, 12.
79. B. Ranby, *ARKIV FOR KEMI*, 1952, **4**, 241.
80. R. Preston and G. Ripley, *Nature*, 1954, **174**, 76.
81. G. Honjo and M. Watanabe, *Nature*, 1958, **181**, 326.
82. A. Bourret, H. Chanzy and R. Lazaro, *Biopolymers*, 1972, **11**, 893.
83. J. Sugiyama, R. Vuong and H. Chanzy, *Macromolecules*, 1991, **24**, 4168.
84. M. Koyama, W. Helbert, T. Imai, J. Sugiyama and B. Henrissat, *Proceedings of the National Academy of Sciences*, 1997, **94**, 9091.
85. J. Sugiyama, H. Harada, Y. Fujiyoshi and N. Uyeda, *Journal of the Japan Wood Research Society*, 1985.
86. J. Sugiyama, H. Harada, Y. Fujiyoshi and N. Uyeda, *Planta*, 1985, **166**, 161.
87. M. Kaushik, W. C. Chen, T. G. M. van de Ven and A. Moores, *Nordic Pulp and Paper Res. J.* , 2014, **29**, 77.
88. Y. Peng, Y. Han and D. J. Gardner, *Wood and Fiber Science*, 2012, **44**, 448.
89. Y. Peng, D. J. Gardner, Y. Han, A. Kiziltas, Z. Cai and M. A. Tshabalala, *Cellulose*, 2013, **20**, 2379.
90. J. R. Harris, in *RMS Microscopy Handbook*, BIOS Scientific Publishers, Oxford, 1997, vol. number 35.
91. T. Abitbol, E. Kloser and D. Gray, *Cellulose*, 2013, **20**, 785.

92. A. M. Glauert, *Fixation, dehydration and embedding of biological specimens*, Elsevier North-Holland/American, 1975.
93. N. Reid, *Practical Methods in Electron Microscopy: Ultramicrotomy*, North-Holland/American Elsevier, 1975.
94. I. M. Watt, *The principles and practice of electron microscopy*, Cambridge University Press, 1997.
95. D. Grubb, *Journal of Material Science*, 1974, **9**, 1715.
96. H. Chanzy, *Commissariat à l'énergie atomique et aux énergies alternatives*, 1975, 55.
97. K. Fridman, A. Mader, M. Zwerger, N. Elia and O. Medalia, *Nat. Rev. Mol. Cell Biol.*, 2012, **13**, 736.
98. J. R. Kremer, D. N. Mastronarde and J. R. McIntosh, *Journal of Structural Biology*, 1996, **116**, 71.
99. J. Frank, ed. J. Frank, Springer Science & Business Media, Second edn., 2008.
100. X. M. Dong, J.-F. Revol and D. G. Gray, *Cellulose*, 1998, **5**, 32.
101. M. A. Henrique, H. A. Silvério, W. P. F. Neto and D. Pasquini, *Journal of Environmental Management*, 2013, **121**, 202.
102. M. Rosa, E. Medeiros, J. Malmonge, K. Gregorski, D. Wood, L. Mattoso, G. Glenn, W. Orts and S. Imam, *Carbohydr. Polym.*, 2010, **81**, 83.
103. X. M. Dong, T. Kimura, J.-F. Revol and D. G. Gray, *Langmuir*, 1996, **12**, 2076.
104. ImageJ, http://imagej.nih.gov/ij/.
105. A. R. Lokanathan, K. M. A. Uddin, O. J. Rojas and J. Laine, *Biomacromolecules*, 2014, **15**, 373.
106. X. Wu, C. Lu, W. Zhang, G. Yuan, R. Xiong and X. Zhang, *J. Mater. Chem. A*, 2013, **1**, 8645.
107. K. Benaissi, L. Johnson, D. A. Walsh and W. Thielemans, *Green Chem.*, 2010, **12**, 220.
108. Y. Shin and G. J. Exarhos, *Mater. Lett.*, 2007, **61**, 2594.
109. V. Favier, G. Canova, J. Cavaillé, H. Chanzy, A. Dufresne and C. Gauthier, *Polym. Adv. Technol.*, 1995, **6**, 351.
110. D. Bondeson and K. Oksman, *Compos. Interfaces*, 2007, **14**, 617.

111. L. Petersson, I. Kvien and K. Oksman, *Composites Science and Technology*, 2007, **67**, 2535.
112. S. A. Paralikar, J. Simonsen and J. Lombardi, 2008, **320**, 248.
113. N. E. Marcovich, M. L. Auad, N. E. Bellesi, S. R. Nutt and M. I. Aranguren, *Journal of Materials Research*, 2006, **21**, 870.
114. M. Matos Ruiz, J. Y. Cavaillé, A. Dufresne, J. F. Gérard and C. Graillat, *Compos. Interfaces*, 2000, **7**, 117.
115. M. Roohani, Y. Habibi, N. M. Belgacem, G. Ebrahim, A. N. Karimi and A. Dufresne, *European Polymer Journal*, 2008, **44**, 2489.
116. P. N. Ciesielski, J. F. Matthews, M. P. Tucker, G. T. Beckham, M. F. Crowley, M. E. Himmel and B. S. Donohoe, *ACS Nano*, 2013, **7**, 8011.